

UNIVERSITA' DEGLI STUDI DI PARMA

Dottorato di ricerca in Scienza e Tecnologia dei  
Materiali

Ciclo XXIX

NANOSTRUCTURED COATINGS FOR  
WETTING CONTROL: DESIGN, FABRICATION  
AND PROPERTIES

Coordinatore:  
Chiar.mo Prof. DALCANALE Enrico

Tutor:  
Dr.ssa RAIMONDO Mariarosa

Dottorando: VERONESI Federico



## SUMMARY

1. INTRODUCTION .....	7
2. WETTING MODELS .....	11
3. CONTACT ANGLE MEASUREMENTS .....	15
4. SUPERHYDROPHOBIC, SOL-GEL HYBRID COATING .....	19
SOL-GEL SYNTHESIS OF ALUMINA NANOPARTICLES.....	20
Synthesis in alcohol medium.....	22
Synthesis in aqueous medium.....	28
COATING DEPOSITION, PROCESSING AND CHEMICAL MODIFICATION .....	31
Dip coating .....	32
Spray coating.....	35
First thermal treatment.....	36
Boiling water treatment.....	37
Chemical modification with fluoroalkylsilane .....	41
WETTING PROPERTIES OF THE HYBRID, NANOSTRUCTURED COATINGS .....	42
Superhydrophobicity.....	42
Oleophobicity .....	45
Durability in aggressive environments.....	46
OTHER CHARACTERIZATIONS: MECHANICAL PROPERTIES AND ROUGHNESS.....	49
Mechanical properties: adhesion.....	50
Surface roughness.....	54
XPS STUDY AND DFT MODELING OF THE HYBRID COATING .....	57
XPS analysis of hybrid-coated aluminum substrates .....	57
DFT modeling of the molecular structure of the coating.....	61
Conclusions .....	64
HYBRID COATING ON COPPER SURFACES: INFLUENCE OF PROCESS PARAMETERS.....	65
Materials and methods .....	67
Results and discussion.....	68
Conclusions .....	83
5. DROP IMPACT STUDIES WITH DIFFERENT LIQUIDS AND SURFACES .....	85
Materials and methods .....	86
Results and discussion.....	87
Conclusions .....	97
6. ASSESSMENT OF ANTI-ICING PROPERTIES .....	99

DROP SHEDDING IN ICING CONDITIONS .....	100
Materials and methods.....	101
Results and discussion .....	103
Conclusions.....	107
DROP FREEZING TIME.....	108
Materials and methods.....	109
Results and discussion .....	110
Conclusions.....	118
7. CONDENSATION ON SUPERHYDROPHOBIC SURFACES .....	119
DROP SHEDDING IN CONDENSING CONDITIONS .....	120
Materials and methods.....	120
Results.....	121
Conclusions.....	125
CONTACT ANGLE MEASUREMENTS IN HIGH HUMIDITY CONDITIONS.....	125
Materials and methods.....	126
Results and discussion .....	128
Conclusions.....	135
8. ANTI-FRICTION PROPERTY IN AXIAL PISTON PUMPS .....	137
DEPOSITION OF THE OLEOPHOBIC COATING ON SLIPPERS .....	137
Slippers properties.....	137
Deposition on smooth slippers.....	139
Deposition on rough slippers.....	140
Spray coating .....	141
ASSESSMENT OF FUNCTIONAL PERFORMANCE IN TEST RIG .....	143
Test rig design.....	143
Tests on standard slippers.....	146
Tests on coated slippers .....	147
Tests in low lubrication regime .....	149
Tests on slippers with different treatments.....	152
Characterization of tested samples.....	156
Tests in real axial piston pump .....	158
TRIBOLOGICAL TESTS.....	161
CONCLUSIONS.....	165
REFERENCES.....	173





## 1. INTRODUCTION

Surface science is a branch of materials science focused on the thin layer of material that forms an interface with the surrounding environment. The behavior and the properties of the surface depends on a large number of variables and can be extremely complex. Therefore, surface science has developed as a discipline of its own, with a large community of scientists devoted to the study and the comprehension of what happens at the outermost part of materials.

A crucial boost to surface science growth was due to the birth and development of suitable characterization techniques. In the last decades, a wide spectrum of surface analyses has been created, allowing for an extremely accurate knowledge of surface chemistry, crystallinity, morphology, roughness and so on. These techniques are complementary to each other, providing different information. Every surface scientist must know how to combine the analyses in order to have a clear picture of the crucial surface properties.

Comprehension and knowledge of surfaces stimulated efforts to modify and tailor them to obtain peculiar properties. Often, the observation of peculiar natural phenomena sparks an idea in the mind of a scientist, who tries to replicate what observed. The relevance of such biomimetic approach has been increasing in the last years and the continuous improvement in the overall comprehension of natural phenomena keeps on fueling this development.

Among the many fascinating natural surface phenomena, the so-called lotus effect may be the most interesting, amusing and therefore the most studied. The leaves of the lotus flower (a genus of aquatic plants called *Nelumbo*) are known for being always clean and spotless, notwithstanding the muddy environments that usually surrounds them. For this reason, many oriental cultures and religions like Hinduism and Buddhism have adopted lotus as a symbol of beauty and purity. Such unspoiled perfection is made possible by the wetting properties of the lotus leaf surface: whenever a water drop hits the surface, it stays spherical and rolls off with no sign of adhesion. In doing so, the dust and dirt particles laying on the surface are dragged away, leaving the leaf perfectly clean. Obviously, this phenomenon has been known for millennia and the first studies about wetting were published in the 19<sup>th</sup> century [1]. Many scientists and industries attempted to recreate water repellence on different surfaces, especially on textiles. Furthermore, authors like Wenzel [2], Cassie and Baxter [3] published their theories between the 1930s and the 1940s, hinting at the role of roughness and surface structure in wetting. However, it was only with the paper published by Barthlott and Ehler [4] in 1977 that a deeper light was shed on this topic. They studied the surface morphology of the lotus leaf surface with a Scanning Electron Microscope (SEM), revealing a peculiar structure [5]. Bumps called papillae, about 10-20  $\mu\text{m}$  tall and 10-

15  $\mu\text{m}$  wide, uniformly covered the surface. At higher magnifications, nano-scale epicuticular waxes were observed on papillae surface. As will be later shown, such dual-scale, hierarchical structures are crucial for the achievement of the property of repelling water, or how it has been called “superhydrophobicity”. Furthermore, surface waxes are chemically stable and do not form any kind of chemical interaction with water. In other words, they provide low surface energy, which is the second requisite for superhydrophobicity. Few years after publication, this paper would be recognized as the cornerstone for the study of superhydrophobic surfaces.

The observation of the lotus leaf surface combined with the pre-existing knowledge about wetting launched a new challenge to scientists: the fabrication of bio-mimicking superhydrophobic surfaces. The list of possible fabrication techniques is almost endless, with only one requirement: it must be possible to control the surface structure and morphology. Two main approaches can be distinguished. The first one [6] [7] is to alter the surface morphology of an intrinsically hydrophobic material, enhancing its water repellence properties. The second one is based on the deposition of a coating on a surface, aiming at the modification of its morphology and/or chemical composition. Chemical [8] [9] [10] or plasma [11] [12] etching, electrochemical deposition [13] [14], polymerization [15] [16], sol-gel coatings [17] [18] [19] [20], Layer-by-Layer assembly [21] [22], Self-Assembled Monolayers [23], vapor deposition [24] [25] are only some of the techniques that can be used and combined to fabricate superhydrophobic coatings.

During my PhD, I focused on a nanostructured hybrid coating obtained via sol-gel synthesis of alumina nanoparticles. I personally performed all the sol-gel syntheses, starting from a procedure published by Minami [26] [27] [28] and adjusting parameters like relative humidity. I also scaled up the synthesis by a factor 10 to assess reproducibility on a quasi-industrial scale. The as-produced sol was characterized in terms of size distribution by Dynamic Light Scattering, then deposited on different substrates either by dip-coating or by spray-coating. Depending on the chosen substrate, the dispersing medium of the sol proved to play a crucial role in the formation of a homogeneous gel film. After few thermal treatments, a ceramic alumina coating with a peculiar flower-like nanostructure was obtained. Once again, substrate material strongly influenced treatment temperatures, as demonstrated by a study on copper surfaces. The final step of the process was the chemical modification by dip-coating in a commercial fluoroalkylsilane (FAS) solution. Such change in surface chemistry caused a steep drop in Surface Energy (SE), therefore a switch from superhydrophilicity to superhydrophobicity. After each step of the process, the surface was characterized in terms of wetting properties to assess the evolution of parameters like Water Contact Angles (WCA), Contact Angle Hysteresis (CAH) and SE. Furthermore, surface morphology and chemical composition were determined via SEM and X-ray Photoelectron Spectroscopy (XPS) analyses. A combination of these techniques allowed for a deeper comprehension of coating



composition and homogeneity, which showed a close correlation with wetting properties. The colleagues at University La Sapienza also performed DFT calculations, which brilliantly showed the formation of an ordered monolayer by FAS molecules.

The scientific community has dealt with superhydrophobicity for many years. However, recently a more challenging pursuit has begun. Water has a very high surface tension ( $\gamma = 72$  mN/m at 298 K), but what happens when a liquid with lower surface tension contacts a superhydrophobic surface? Most of the times, superhydrophobic surfaces are not repellent against low surface tension liquids such as oils and alkanes. The lotus leaf itself is not able to repel these liquids [5]. The property of repelling low surface tension liquids is often defined as oleophobicity [29] [30] [31]. Usually, oleophobic surfaces are harder to fabricate than superhydrophobic ones, as the requisites in terms of surface morphology and chemistry are stricter. In my work, I assessed the oleophobic properties of the previously described coated surfaces by measuring their contact angles with different liquids.

Repellence of liquids implicates a wide variety of possible additional properties and this is what makes superhydrophobic/oleophobic surfaces so relevant. The most straightforward is self-cleaning [32] [33], as observed on the lotus leaf. Impinging drops can roll off the surface, dragging away dust and dirt particles laying on the surface. Self-cleaning properties are highly desirable in many different fields, from building to automotive industry just to name a few. Low CAH is the fundamental requisite for a self-cleaning surface, as the WCA value says nothing about drop mobility on the surface. However, an even deeper comprehension of the dynamic behavior of drops hitting the surface can be obtained by the study of single drop impact events [34] [35] [36]. This was a relevant part of my work, aiming at the research for a criterion of drop rebound on different superhydrophobic surfaces. The study involved water and hexadecane drops to evaluate also the role of liquid properties in determining the impact output.

In the literature, many papers assess the anti-icing properties of superhydrophobic surfaces [37] [38] [39] [40], which could carry a huge breakthrough in industrial sectors like aerospace, communications and renewable energies. In principle, a lack of water adhesion on the surface should lead to a delay in icing (e.g. icing should occur at lower temperatures) as shedding from the surface should be enhanced. However, in many cases it is quite the opposite [41] [42], as surface roughness favors ice adhesion. For this reason, I tested the water drop shedding behavior on superhydrophobic surfaces in icing conditions, e.g. with surface temperature below 0°C.

Furthermore, water drops shedding is often studied in condensing conditions [43] [44] [45] [46], e.g. over the dew point at a certain temperature. The applications range from air conditioning and self-cleaning surfaces to microfluidics and automotive. Behavior of liquids drops depends on the balance

between adhesion forces and external ones (e.g. gravity, airflow). For this reason, I studied water shedding in condensing conditions on different superhydrophobic surfaces, trying to find a correlation between wetting properties in quasi-static conditions and drop shedding behavior.

Another substantial part of my PhD work concerned the application of superhydrophobic coatings for friction reduction in axial piston pumps. Usually, rubbing parts in axial pumps (especially the slippers) are oleophilic, e.g. lubricants easily wet their surfaces. We tried to reverse this approach by depositing the oleophobic coating on those surfaces, looking for any effect on friction. Indeed, a remarkable reduction in friction coefficient was shown, even for quite long-lasting tests. Nonetheless, some aspects remain unclear: why is the coating reducing friction? Why the friction reduction effect remains even when the coating is severely damaged? Notwithstanding these unresolved questions, the observed phenomenon was quite unique (no work in the literature ever reported such behavior), so it deserves to be mentioned and further investigated.

## 2. WETTING MODELS

One of the first studies about wetting belongs to Thomas Young [1] and was published in 1805. However, he never formalized his theory. It was Gauss in 1830 [47] who wrote Young equation for the first time:

$$\cos \theta = \frac{\gamma_{SG} - \gamma_{SL}}{\gamma_{LG}}$$

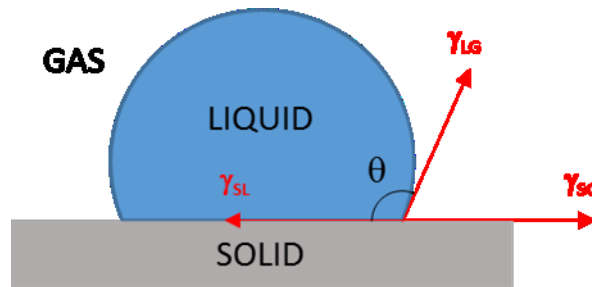


Figure 1. Diagram of the forces at the three-phase contact line of a liquid droplet on a solid.

Figure 1 shows the forces which contribute to define the contact angle  $\theta$ .  $\gamma_{SL}$  is the interfacial tension between solid and liquid phases,  $\gamma_{LG}$  is the interfacial tension between liquid and gas phases (also known as liquid surface tension) while  $\gamma_{SG}$  is the interfacial tension between solid and gas phases (solid surface energy). All the forces interact at the three-phase contact line. The contact angle  $\theta$  is defined as the angle formed by the tangent to the liquid-gas interface at the three-phase contact line [48]. Solid surfaces can be classified in terms of their contact angle: if the liquid phase is water and  $\theta < 90^\circ$ , the surface is termed as hydrophilic, while if  $\theta > 90^\circ$  it is termed as hydrophobic.

However, Young equation is valid only for smooth and homogeneous surfaces. If the surface is rough, the liquid can penetrate the surface features (Figure 2). While studying the wetting behavior of textiles, Wenzel [2] estimated that, in rough surfaces, the solid-liquid interfacial area is increased by a roughness factor  $r$ , defined as the ratio between the actual contact area and the geometric one. Such situation is defined as Wenzel wetting state and the relative Wenzel equation is:

$$\cos \theta_W = r * \cos \theta$$

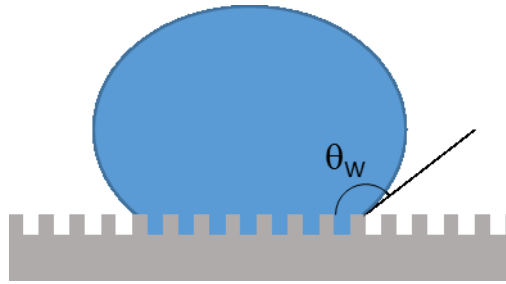


Figure 2. Sketch of a liquid drop resting on a rough surface in Wenzel wetting state.

From Wenzel equation, it is evident how roughness can amplify the wetting behavior of a surface. For example, a hydrophilic smooth surface becomes more hydrophilic if its roughness is increased. This means that the apparent contact angle  $\theta_{app}$ , e.g. the contact angle macroscopically observed, will be smaller than  $\theta$  for a smooth surface of the same material. On the other hand, a hydrophobic material can increase its  $\theta_{app}$  by roughening its surface. Usually, smooth surfaces never show water contact angles higher than  $120^\circ$ . Roughening the surface can lead to  $\theta_{app} > 150^\circ$ , which is the conventional threshold for superhydrophobicity.

If the surface has suitable morphology and chemical composition, water will not be able to penetrate its features. Air pockets will be retained, forming a mixed interface between liquid, solid and gas (Figure 3). This phenomenon can be observed on porous surfaces. Cassie and Baxter [3] described this interface with the following equation:

$$\cos \theta_{CB} = f_1 \cos \theta_1 + f_2 \cos \theta_2$$

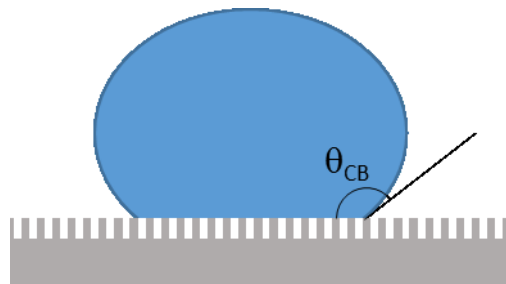


Figure 3. Sketch of a liquid drop resting on a rough surface in Cassie-Baxter wetting state.

In the equation,  $f_1$  and  $f_2$  are the surface fractions with phase 1 and phase 2, respectively.  $\theta_1$  and  $\theta_2$  are the contact angles (as per Young equation) of the liquid on phase 1 and phase 2. If phase 1 is the solid and phase 2 is air, then  $\theta_2 = 180^\circ$ . Furthermore, if no other phase is present and interfaces are planar [49],  $f_2 = 1 - f_1$ . Therefore, Cassie-Baxter equation becomes:

$$\cos \theta_{CB} = f(1 + \cos \theta) - 1$$

As per Cassie-Baxter equation, the smaller the value of  $f$ , the larger the value of  $\theta_{CB}$ . For  $f \rightarrow 0$ , the surface will have  $\theta_{CB} \rightarrow 180^\circ$ . Drops in Cassie-Baxter state usually display very high  $\theta_{app}$ .

Both Wenzel and Cassie-Baxter models have some limits. For example, the latter considers a flat liquid-gas interface beneath the drop, but Herminghaus [50] introduced some corrections accounting for smaller-scale roughness superimposed on the surface structure. This correction is useful to explain the wetting behavior of hierarchically structured surfaces. Milne and Amirfazli tried to reconsider the common use of Cassie-Baxter equation [49], showing that for non-planar interfaces  $f_2 \neq 1 - f_1$ . Spiked surface asperities, high hydrostatic pressure and partial penetration of the liquid in the larger scale features of surface morphology are some of the reasons that lead to non-planarity of liquid-gas and liquid-solid interfaces. The authors suggested using the original form of the Cassie-Baxter equation, in which the sum of the area fractions  $f_1$  and  $f_2$  is greater than or equal to 1:

$$\cos \theta_{CB} = f_1 \cos \theta_1 - f_2$$

Gao and McCarthy even tried to confute Wenzel and Cassie-Baxter models [51]. They brought evidence that the observed contact angle depends on the interplay of tension forces at contact line, rather than contact area. Eventually, much more refined wetting models were elaborated [52]. Nonetheless, Wenzel and Cassie-Baxter models remain the most widely used ones for the description of wetting behavior on solid surfaces.

Transition between different wetting states is highly debated in literature. Many works [49] [53] focus on quasi-static conditions, identifying a critical contact angle  $\theta_{cr}$ :

$$\cos \theta_{cr} = \frac{-f_2}{r - f_1}$$

A surface needs to have intrinsic (Young)  $\theta_i > \theta_{cr}$  to make Cassie-Baxter state thermodynamically favoured over Wenzel state. This criterion shows how a proper design of surface morphology can lead to the desired wetting properties. However, such quasi-static conditions do not represent what happens in real wetting conditions. During operation, liquids drops strike surfaces with non-zero velocity, thus applying a relevant pressure. If we consider a rough surface favouring Cassie-Baxter wetting, air is trapped within its features. One can calculate a related capillary pressure  $P_c$ , which the surfaces opposes against wetting by impacting drops [54] [55]:

$$P_c \propto \gamma_{LG} \frac{-\cos \theta_A}{r_p}$$

In the equation,  $\gamma_{LG}$  is liquid surface tension,  $\theta_A$  is the advancing contact angle (defined in the next section) of the smooth surface and  $r_p$  reflects length scale of the cavities on the surface. The smaller the cavities on the surface, the higher is the anti-wetting pressure exerted by the surface. If impinging drops can overcome this pressure, liquid phase will replace air within surface features and an irreversible Cassie-to-Wenzel transition will occur. Therefore, the wetting state of a surface depends on many aspects, which must be considered while designing the surface.

### 3. CONTACT ANGLE MEASUREMENTS

As already mentioned in the previous chapter, the contact angle  $\theta$  is defined as the angle formed by the tangent to the liquid-gas interface at the three-phase contact line [48]. There are many methods for contact angle measurement [56], but the most widespread one is sessile drop method. This technique is simple and many commercially available, automated systems can perform it in a very short time with good reproducibility. In this technique, a liquid drop of known volume is deposited on the surface. A light source (e.g. a lamp) irradiates the drop from a side, projecting an image in the objective of a camera. In automated systems, a software automatically detects drop profile and fits it with the chosen method. The angle between the baseline and the tangent to the fitting curve in the contact point is the measured contact angle. An example of contact angle measurement is reported in Figure 4.

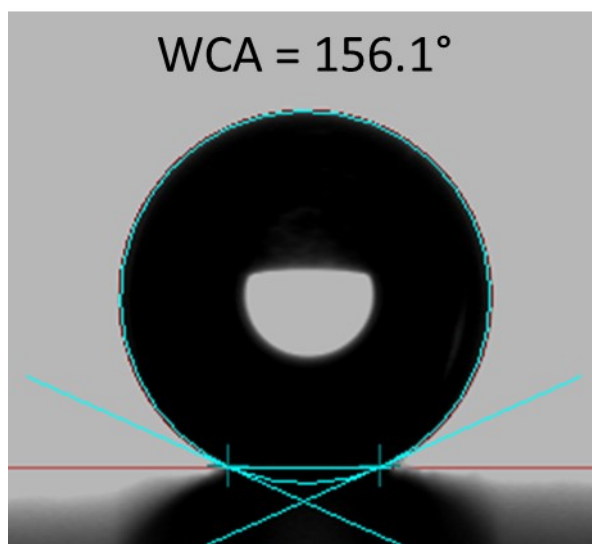


Figure 4. Fitting of a drop profile with ellipse method and calculation of contact angle. The red straight line is the baseline, the blue curve is the fitted drop profile and the blue inclined lines are the tangents of drop profile at the contact points (blue crosses).

The choice of fitting method can affect the calculated contact angle value [57] [58]. Direct goniometric measurement of the tangent usually implies large errors. In case of axisymmetric drop, an automated axisymmetric drop shape (ADSA) analysis allows to obtain drop profile [59]. A theoretical curve described by the Laplace equation is fitted to the experimental profile. Contact angle is calculated from the slope of the theoretical curve at the contact point. This method is the most accurate, as it accounts for gravity-induced deformation in the drop.

For an ideal surface (e.g. homogeneous, rigid, smooth, chemically inert), the contact angle with a certain liquid is constant and depends only on interfacial tensions as described by Young equation. However, real surfaces will always be chemically inhomogeneous and/or rough. For this reason, apparent contact angle will assume different values over the surface. Furthermore, if the drop is inclined or its volume changes in time, two different angles will be observed: the advancing contact angle ACA or  $\theta_A$ , referred to the movement of contact line towards a non-wetted area; the receding contact angle RCA or  $\theta_R$ , referred to the movement of contact line towards a wetted part of the surface [56]. It will always be true that  $ACA \geq RCA$ . The difference  $ACA - RCA$  is called contact angle hysteresis CAH or  $\Delta\theta$  and is related to drop mobility on the surface: the lower CAH, the higher the mobility. Contact angle hysteresis is the main tool to recognize a Wenzel state from a Cassie-Baxter state: in the sooner, the liquid phase penetrates surface structures and is firmly pinned, thus has high CAH. On the other hand, Cassie-Baxter drops are free to move on the mixed solid-gaseous surface, therefore hysteresis will be low, usually below  $10^\circ$ . As already hinted, there are mainly two methods for measuring ACA and RCA. The first one consists in depositing a drop on the surface and tilt it until the drop starts to move. At the onset of movement, the contact angle measured uphill is RCA, the angle measured downhill is ACA. This is the tilted plate technique [60].

However, the most common method for the measurement of CAH is based on a sessile drop still attached to the needle. Drop volume is increased by injection; the  $\theta$  value observed when the contact point starts to move is defined as ACA. This value should be constant as drop volume increases over a certain threshold. Then, drop volume is decreased by suction and the contact line starts to recede. From that moment on, the plateau value of  $\theta$  is RCA. An example of ACA and RCA measurement is reported in Figure 5.

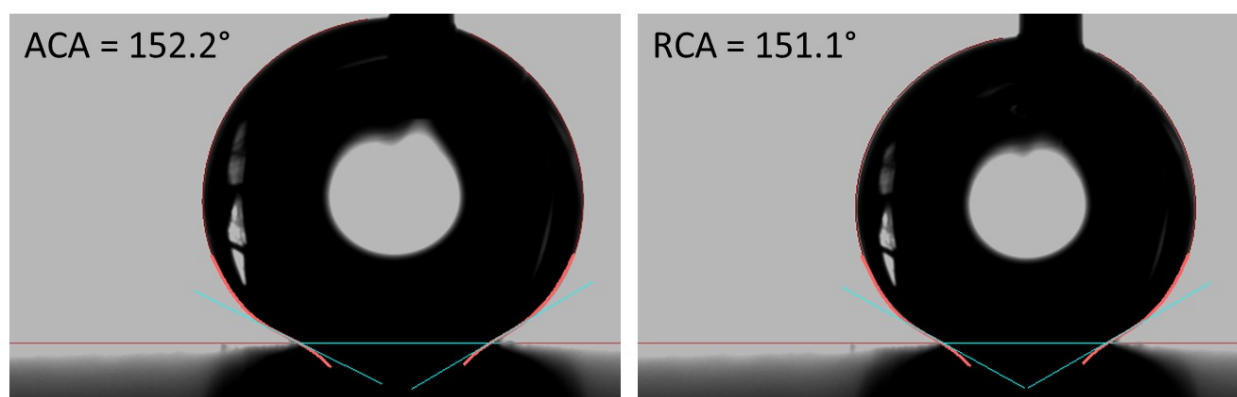


Figure 5. Measurement of advancing (left) and receding (right) contact angle for a water drop on a surface.



The values of RCA can be significantly different depending on the adopted technique [43]. Furthermore, the sliding angle can also be measured from tilted plate method. It is defined as the surface tilting angle at which drop movement starts and it is related to the adhesion force between the drop and the surface [61]. However, tilted plate method requires a specific instrumentation, while contact angle hysteresis can be evaluated with much simpler setups. Therefore, during my activity I only focused on contact angle hysteresis to understand the behavior of drops advancing and receding on surfaces.

Another relevant parameter is surface energy of the solid ( $\gamma_{SG}$  in Young equation), which can be defined as the energy necessary to create a surface from bulk material [62]. In general, the higher the value of  $\gamma_{SG}$ , the smaller the contact angle with a given liquid. Among the different methods for the measurement of surface energy, contact angle measurements are regarded as the simplest, thus the most used [63]. However, the absolute value of  $\gamma_{SA}$  is not sufficient to define surface wetting by a liquid. Indeed, liquid-solid interactions strongly depend on the chemical composition of both phases. For this reason, surface tension is often divided into components to express the relative contributions by different types of interaction. The nature of these components depends on the chosen model. The most common one is Owens-Wendt-Kaelble (OWK) model [64] [65], in which  $\gamma_{SG}$  and  $\gamma_{LG}$  are each divided into a polar component (due to hydrogen bonding and dipole-dipole interactions) and a dispersive component. There is interaction only between correspondent components:

$$\gamma_{SL} = \gamma_{SG} + \gamma_{LG} - 2\sqrt{\gamma_{SG}^d \gamma_{LG}^d} - 2\sqrt{\gamma_{SG}^p \gamma_{LG}^p}$$

Combining this equation with Young equation gives:

$$\gamma_{LG}(1 + \cos \theta)\gamma_{SL} = \gamma_{SG} + -2\sqrt{\gamma_{SG}^d \gamma_{LG}^d} - 2\sqrt{\gamma_{SG}^p \gamma_{LG}^p}$$

In this equation, unknown variables are  $\gamma_{SG}^d$  and  $\gamma_{SG}^p$ . It is necessary to measure  $\theta$  for two liquids with known  $\gamma_{SG}$  components, usually water (large  $\gamma_{SG}^p$ ) and diiodomethane (large  $\gamma_{SG}^d$ ), and solve the system. However, all models for surface energy calculations make many assumptions, for instance the validity of Young equation for the surface. Therefore, these models are valid only for smooth surfaces. For rough surfaces, calculated surface energy values are useful only as an assessment of changes in chemical composition.



## 4. SUPERHYDROPHOBIC, SOL-GEL HYBRID COATING

In the literature, many different techniques have been explored to achieve superhydrophobicity on solid surfaces. Any process able to create a suitable surface structure on the micro- or nano-scale (better if on both scales) can be a potential route to water-repellent surfaces. In addition, the surface must possess an intrinsically low surface energy to avoid interactions with liquid molecules. Thus, chemical modification of the surface is often performed by grafting water-repellent molecules.

Essentially, there are two types of approach to surface structuration [48]. The first one is a top-down approach, in which the surface of the starting substrate is modified by subtraction of material. Depending on the intrinsic wetting properties of the substrate and the characteristics of the treatment, a final chemical modification to lower surface tension might be necessary. For example, a wide range of lithographic techniques has been explored as a route to superhydrophobic surfaces [66] [67] [68]. The main advantage of these techniques is the accurate control of surface structure parameters, while their biggest drawback is the low output rate of these processes. For these reasons, superhydrophobic surfaces by lithography are mainly useful for research studies (e.g. to find correlations between surface structure parameters and wetting) but hardly transferrable to industry. Another top-down approach is based on templates: a material is printed, pressed or grown against the voids of the template, recreating a negative of the pattern that can be then reused to replicate the original structure [69] [70]. Although interesting results can be achieved with this technique, open issues like template removal and accuracy of structure replication remain. To some extent, also etching treatments are top-down approaches, as substrate material is anisotropically removed to create a new surface. Whether etching occurs by plasma treatment [11] [12] or by chemical attack [8] [9] [10], this approach is interesting mainly because of its simplicity and low cost.

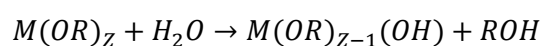
On the other hand, bottom-up approaches start from molecular building blocks that self-organize or self-assemble in different reactive environments. Most of the times, the final product is a structured coating that transfers its properties to the substrate. Such versatility is the main advantage of this approach. On the other hand, adhesion is the main drawback of coatings, which often show mechanical stability issues. The scientific community devoted huge efforts to the optimization of adhesion, which can be improved by adding a primer layer [17] or creating chemical bonds between the substrate and the coating [71]. The literature reports countless attempts of superhydrophobic coatings. Some of the used techniques include electrospinning [72], sol-gel [17] [18] [19] [20], Layer-by-Layer assembly (LbL) [21] [22], anodization [73] [37], electrochemical processes [13] [14], chemical vapor deposition [24] [25] and deposition of colloids or composites [74] [75] [76]. Among these, I chose the deposition of a hybrid coating composed of a ceramic nanostructured layer obtained from sol-gel routes and an organic

monolayer providing low surface energy. Similar approaches have been already explored in the literature [17] [77], but not fully developed in their entire potential. Sol-gel technique is simple, low-cost and provides reproducible results. It is also easily transferrable to industrial scale, as will be demonstrated later. Adopting non-toxic dispersants such as water, it is also an eco-friendly route. Another advantage of sol-gel processes is the wide choice of deposition methods: dip coating [78] [79] [80], spray coating [19] [81], spin coating [82] and so on. Every deposition method has to be tuned to provide controlled film thickness and structure.

This chapter is divided into six parts. The first one deals with the sol-gel synthesis of the ceramic nanoparticles suspension (e.g. the sol), which I performed following two different routes and at different volume scales. The second part deals with the deposition of the coating by dipping the substrate into the sol and the following steps of the process. The third part focuses on characterization of the coating in terms of wetting properties, also assessing its durability in aggressive environments. The fourth section briefly deals with other characterizations, including the assessment of mechanical properties and roughness. The fifth subchapter shows the XPS analyses performed at University La Sapienza (Rome, Italy) on coated aluminum substrates and a modeling of the chemical composition on the coating surface. The last subchapter focuses on the coating of copper surfaces, which requires a tailored processing to achieve the best results in terms of liquid repellence.

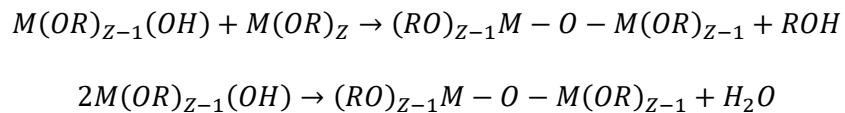
## SOL-GEL SYNTHESIS OF ALUMINA NANOPARTICLES

A sol is a colloidal suspension of solid particles in a liquid [83]. Such particles are so small (diameter < 1  $\mu\text{m}$ ) that gravitational forces acting on them can be neglected. Van der Waals and electrostatic interactions prevail at these length scales and determine the behavior of the particles. Sols of ceramic oxides are obtained from different precursors, either inorganic [84] or organic. Among the latter, metal alkoxides  $M(OR)_z$  [85], where M is a metal or a metalloid (e.g. Si) and OR is an alkoxy ligand, are the most commonly used. These compounds undergo hydrolysis spontaneously with ambient humidity. However, water is usually added to the reaction mixture, possibly with either acidic [86] [87] [82] or basic [19] [88] catalyst.



Not necessarily all OR groups are hydrolyzed. Water content in the mixture, catalysts and chelating agents like acetoacetates [28] [17] [87] are able to influence the degree and the rate of hydrolysis. Specifically, complete hydrolysis is undesired as it leads to sol instability and precipitation of metal hydroxides in a short time [18]. This is true especially for alumina precursors, while silicon alkoxides are much more unreactive and rather need catalysts to hydrolyze [89] [90]. Furthermore, the dispersing medium has a strong influence on the nature of the coating sol. Alcohols are the most widespread media, but water allows for greener routes.

After hydrolysis, condensation reactions lead to the formation of M-O-M bonds and either a water or alcohol molecule. Indeed, condensation is a polymerization reaction, whose product is a macromolecule.



Condensation reactions can go on until hydrolyzable OR groups are available. When the macromolecule reaches macroscopic dimension, a transition from sol to gel occurs [83]. In a gel, the solid phase is continuous and encloses a continuous liquid phase. Also, gel formation (also referred to as gelation) can occur due to attractive dispersion forces between suspended particles, sticking together to form a network. Further, deposition of a sol on a surface followed by rapid evaporation of the solvent leads to a gel film. Gelation times depend on parameters such as pH [91]. Even after gelation, hydrolysis and condensation reactions still happen, involving the sol phase entrapped within the continuous gel phase. This phenomenon is called ageing. Meanwhile, liquid phase evaporates, causing shrinkage and related high capillary pressures. Eventually, the gel collapses, forming a new phase called xerogel. If no precautions are adopted (e.g. supercritical drying to obtain an aerogel), xerogel is the final form observed for gels. Sol-gel syntheses find massive application in ceramic materials science, as they are quite simple to perform, do not require harsh conditions and allow for materials with unique properties [92]. The most common oxides obtained via sol-gel are silica SiO<sub>2</sub> [93] [94], alumina Al<sub>2</sub>O<sub>3</sub> [86] [87], titanium oxide TiO<sub>2</sub> [95] [96] and many others [97] [98].

As previously mentioned, gel films can be prepared on solid substrates to form a coating. There are two ways of preparing sol-gel coatings. The first one is to form the coating *in situ*, on the substrate surface [99]. Typically, the surface is coated with precursors, which react and form a gel film. However, this procedure implies a large waste of chemicals, as the prepared precursor solution must be utilized in a

short time span. Therefore, it is better to synthesize a stable suspension of ceramic oxide nanoparticles which can be used for deposition in a much longer time span, e.g. until the nanoparticles are too aggregated and can no longer form a homogeneous gel film on the surface.

Gel films possess peculiar structures that are not attainable through classic ceramic routes. More specifically, they present a nanostructure when treated in a proper way. For this reason, ceramic gel films have been extensively studied as potential superhydrophobic coatings. An endless list of papers deals with the fabrication of silica gel films and their characterization in terms of surface morphology and wetting properties [71] [19] [20] [82] [88] [78] [81] [100] [94]. Excellent water-repelling properties have been achieved. Nonetheless, almost every aspect of these coatings has been already explored. For this reason, I chose to focus on another ceramic oxide, namely alumina  $\text{Al}_2\text{O}_3$ . Although to a much lesser extent than silica, also alumina gel films have received some interest as superhydrophobic coatings [17] [18] [77] [27] [79]. I followed two different sol-gel routes during my experiments, which are described below.

#### Synthesis in alcohol medium

The first sol-gel synthesis was an alcohol-based one, with isopropyl alcohol (*i*-PrOH) as dispersant. The procedure was inspired by the work from Minami *et al.* [27]. This synthesis is reported in a work published by my group in 2015 [101].

The starting material was aluminum tri-*sec*-butoxide  $\text{Al}(\text{O-}i\text{-Bu})_3$ . It is widely used as alumina precursor in sol-gel synthesis because it is liquid in ambient conditions and provides highly pure and homogeneous products [87]. However, it is extremely sensitive to ambient humidity and promptly forms white  $\text{Al}(\text{OH})_3$  precipitates when exposed to air. Therefore, the presence of a ligand is necessary to stabilize it and allow for a controlled hydrolysis.

Ethyl acetoacetate (EAcAc) was chosen as ligand because past works [87] [28] proved its efficiency in promoting alkoxide stability in water. Specifically, EAcAc forms an extremely stable, six-membered complex with an Al atom (Figure 6) through donor-acceptor interactions, as confirmed by IR and UV spectra of  $\text{Al}(\text{O-}i\text{-Bu})_3$  and EAcAc solutions both in *i*-PrOH and water. Such Al-EAcAc bonds greatly slow down hydrolysis rate. However, this complex is still soluble in the chosen solvent, thus it does not precipitate.

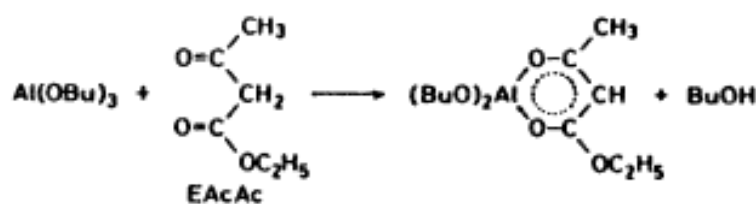


Figure 6. Scheme of the formation of the complex between  $Al(O\text{-}sec\text{-}Bu)_3$  and EAcAc. Image courtesy of Uchihashi et al. [28].

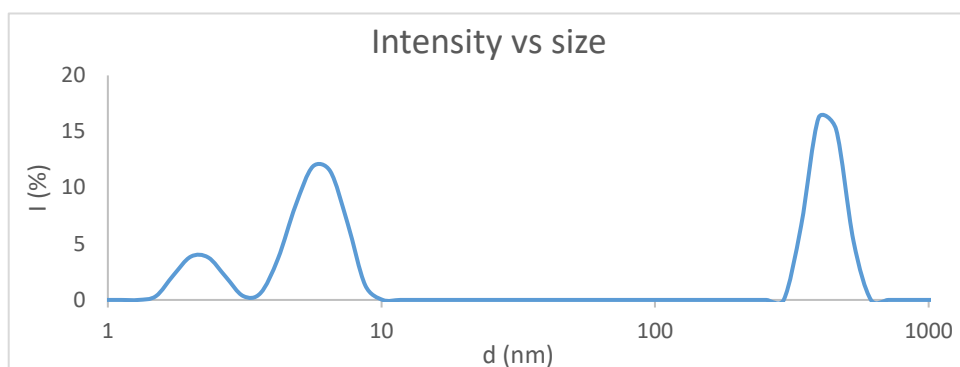
The choice of EAcAc:Al ratio has an influence on the average size of particle size [26]. Specifically, particles become smaller with an increase in this molar ratio since the chelating agent prevents the growth of particles and delays their aggregation.

The synthesis was performed as follows. Aluminum tri-*sec*-butoxide (97%, Sigma-Aldrich) was added to isopropyl alcohol (99%, Sigma-Aldrich) while magnetically stirring to disperse the alkoxide and avoid contact with ambient humidity. After one hour, ethyl acetoacetate (> 99%, Sigma-Aldrich) was added, while stirring continued. After a short time, the mixture turned from transparent to pale yellow, indicating the formation of the chelate complex [28]. After 3 hours, a 1:1 v/v mixture of *i*-PrOH and deionized water was added dropwise to the mixture to start hydrolysis. The molar ratios of EAcAc, water and *i*-PrOH with respect to Al were set to 1, 4 and 20, respectively. The exact quantities of each reagent are listed in Table 1.

Reagent	PM (g/mol)	Purity (%)	$\rho$ (g/mL)	Volume (mL)	Weight (g)	n (mol)	n/n Al	M (mol/L)
EAcAc	130.14	100	1.029	7.5	7.687	0.059	1	0.0005
$Al(O\text{-}sec\text{-}Bu)_3$	246.33	97	0.96	15.6	15.000	0.059	1	0.0005
H <sub>2</sub> O	18.02	100	1	4.3	4.258	0.236	4	0.0020
<i>i</i> -PrOH	60.1	99.7	0.786	90.6	71.212	1.181	20	0.0100
<b>Total</b>				118.0				

Table 1. Molecular weight, purity, density, volume, weight, moles, molar ratio with respect to Al and molarity of every reagent used in the synthesis of alcohol-based alumina suspension.

After 24 hours, the stirring was interrupted and the sol collected for characterization. Average particle size was determined by Dynamic Light Scattering (DLS, Zetasizer Nano S, Malvern Instruments). This technique is based on the scattering of a laser beam by a suspension of nanoparticles. From the analysis of the scattered signal, the distribution of hydrodynamic diameters for suspended particles is calculated [102] [103]. Furthermore, the polydispersity index (*Pdl*) is calculated. The measured distribution is reported in Figure 7, together with the mean size value for each observed peak and its relative area percentage.



<b>PdI</b>	0.883
<b>d (nm)</b>	<b>A (%)</b>
2.2	12.5
5.9	44.3
426.1	43.2

Figure 7. Intensity of scattered light vs size distribution for as-synthesized alumina nanoparticles suspended in *i*-PrOH. In the table, polydispersity index and area percentage under each peak of the distribution are reported.

Three peaks are observed. The largest ones are centered at  $d = 5.9$  nm and  $d = 426$  nm, with very similar area percentages. At small size values ( $d = 2.2$  nm), another peak is observed. However, one must consider that scattered light intensity is proportional to the sixth power of the scattering object diameter [104]. Therefore, size distribution based on scattered light intensity does not reflect the actual number of particles of each size. By using Mie solution to Maxwell's equations [105], it is possible to calculate the volume vs size and number vs size distribution for suspended alumina particles, provided their refraction index  $n = 1.39$ . The resultant size distributions are reported in Figure 8.

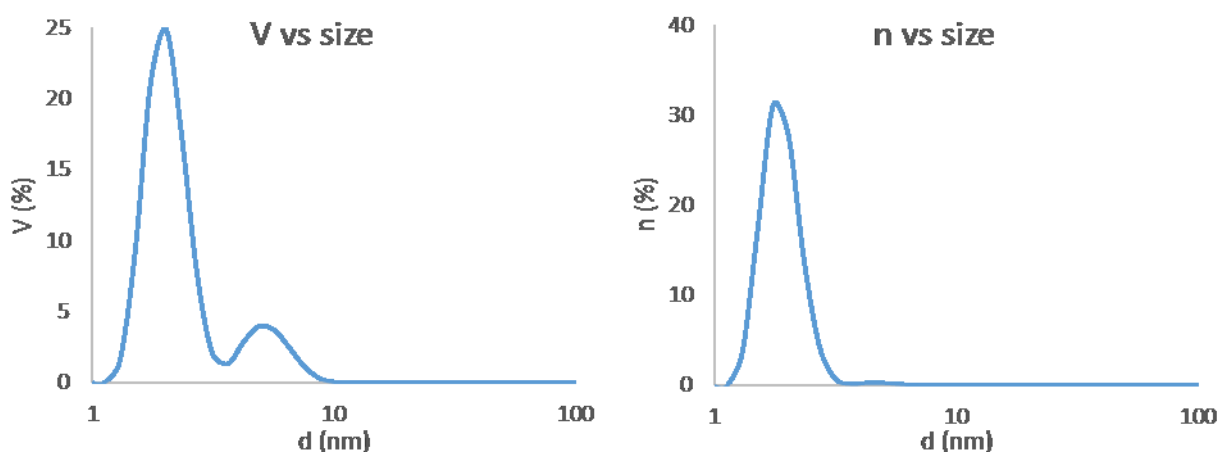


Figure 8. Volume vs size and number vs size distributions for as-synthesized alumina nanoparticles suspended in *i*-PrOH.

From volume and number distributions, it is clear that almost all suspended particles have  $d < 10$  nm. Volume distribution displays two peaks, centered at 2.0 and 4.8 nm, respectively, while the number



distribution had a single peak at 1.7 nm. The same synthesis was performed several times, always providing reproducible results in terms of particle size distribution.

The sol was further characterized in terms of viscosity. A C-VOR 120 rheometer (Bohlin Instruments) was used to measure dynamic viscosity  $\eta$ . Due to the clearly low values of  $\eta$ , a hollow rotating cylinder geometry was adopted for the measurements in order to reach high torque values [106]. The experimental cell is made of two concentric cylinders. A known shear rate is applied to one cylinder, generating a force that is transmitted through the liquid to the other cylinder. Such torque is measured and the relative values of shear stress and viscosity are calculated. In the reported measurements, shear stress was varied in two different fashions: in the first scheme (called “steps”), a shear stress value was set and the system was allowed to equilibrate for 2 minutes, then average  $\eta$  was calculated and shear stress was increased. This procedure allows for a fine control of shear stress. In the second pattern (“ramping”), stress increased constantly and  $\eta$  was measured instantly. This technique is much faster than the previous one, avoiding potential evaporation issues. Shear stress was scanned through three orders of magnitude. Temperature was kept constant at 25.0°C. The results are reported in Figure 9.

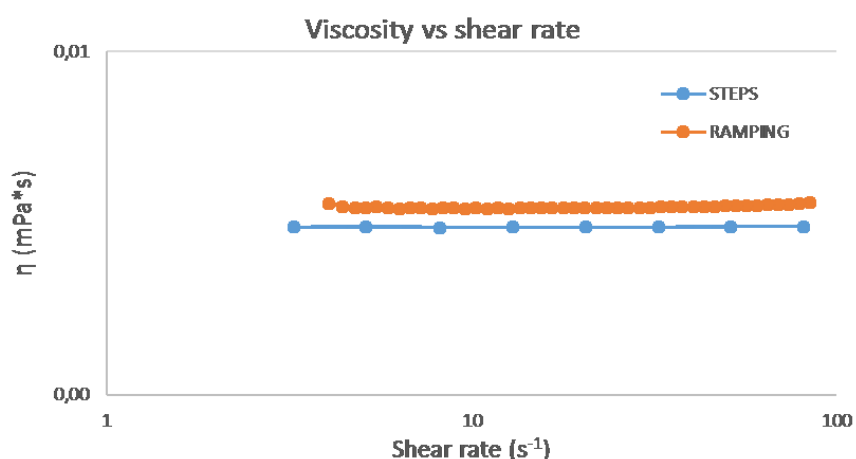


Figure 9. Viscosity versus shear rate for the alcohol-based sol, as calculated from the measured shear stress. Results are reported for both patterns of shear rate variation, namely “steps” and “ramping”.

As shown in the graph above,  $\eta$  remains constant for shear stress values up to 80 s<sup>-1</sup>, indicating a newtonian behavior. At higher shear rates, liquid jets were generated from the sample, causing an increase in measured  $\eta$ . This behavior emerged for both shear rate increase patterns. This increase in  $\eta$  is clearly an artifact, therefore those  $\eta$  values were neglected while averaging and were not reported. Average  $\eta$  values for both methods are reported in the Table 2.

Method	$\eta$ (mPa*s)	St.Dev
Steps	3.08	0.01
Ramping	3.52	0.04

Table 2. Average viscosity for the alcohol-based sol, as computed for "steps" and "ramping" shear stress variation methods. Standard deviations are also reported.

"Steps" method provides a slightly smaller value than "ramping" pattern. However, the values are very close and they are both higher than that of pure *i*-PrOH ( $\eta = 1.96$  mPa\*s at  $T = 25^\circ\text{C}$ ).

Surface tension  $\gamma$  for the nanoparticles suspension was determined via pendant drop method. This technique calculates surface tension for a liquid drop by fitting its profile with a Laplacian curve [107] [108]. The only data needed for this measurement is liquid phase density, which was estimated to be 0.777 g/mL. Seven different drops were used for the measurement of  $\gamma$  and the average value was  $\gamma = 21.3 \pm 0.1$  mN/m at room temperature (about  $23^\circ\text{C}$ ). Isopropyl alcohol has a slightly higher  $\gamma$  (23.3 mN/m), therefore some of the components of the sol caused a small decrease in  $\gamma$ . The responsible for such decrease is uncertain: the only possible responsible could be 2-butanol, which is the side-product of alkoxide hydrolysis. Indeed, 2-butanol has  $\gamma = 22.6$  mN/m at  $25^\circ\text{C}$ , while all other components in the mixture (EAcAc, unreacted water) have higher  $\gamma$  values with respect to *i*-PrOH. However, the contribution of 2-butanol alone is insufficient to explain the actual value of  $\gamma$  for the sol. Furthermore,  $\text{Al}_2\text{O}_3$  nanoparticles should not be responsible for reduced  $\gamma$ : many papers [109] [110] reported the absence of influence of hydrophilic nanoparticles on  $\gamma$  of the pure liquid. Thus, the cause of such small decrease in  $\gamma$  for the alcohol-based sol remained unresolved.

The synthesis described above was a laboratory-scale batch, with a total volume of 118 mL. Aiming at future application on industrial scale, it becomes necessary to assess the scalability of the sol-gel route. The synthesis was replicated with the objective to achieve a volume of 1400 mL. However, with such large quantities of reagents the spontaneous hydrolysis of  $\text{Al}(\text{O-sec-Bu})_3$  during sampling becomes a serious issue. For this reason, this massive sol-gel synthesis was performed in a glove box where relative humidity (RH) was kept at 5%. In those conditions, sampling and handling of  $\text{Al}(\text{O-sec-Bu})_3$  became much easier, with no evidence of  $\text{Al}(\text{OH})_3$  precipitation during operation. A slight excess of EAcAc was used to guarantee total chelation of the alkoxide. Furthermore,  $\text{H}_2\text{O}:\text{Al}$  ratio was increased to provide better hydrolysis and avoid the formation of large particles. The exact quantities of each reagent are listed in Table 3.

Reagent	PM (g/mol)	Purity (%)	$\rho$ (g/mL)	Volume (mL)	Weight (g)	n (mol)	n/n Al	M (mol/L)
EAcAc	130.14	100	1.029	89.2	91.82	0.71	1.03	0.50
Al(O- <i>sec</i> -Bu) <sub>3</sub>	246.33	97	0.96	181.0	173.79	0.68	1.00	0.49
H <sub>2</sub> O	18.02	100	1	50.9	50.85	2.82	4.12	2.02
<i>i</i> -PrOH	60.1	99.7	0.786	1079	848.01	14.07	20.56	10.05
<b>Total</b>				1400				

Table 3. Molecular weight, purity, density, volume, weight, moles, molar ratio with respect to Al and molarity of every reagent used in the scale-up synthesis of alcohol-based alumina suspension.

DLS characterization of the as-synthesized batch showed a slightly different  $I$  vs  $d$  distribution. Three peaks appeared, with mean size of 4.4, 170.0 and 5489 nm, respectively (Figure 10). However, the two peaks at higher  $d$  were ignored as no micron-sized particle was visible in the sol. Probably, air bubbles trapped in the sol were detected by the instrument, causing those unexpected peaks.

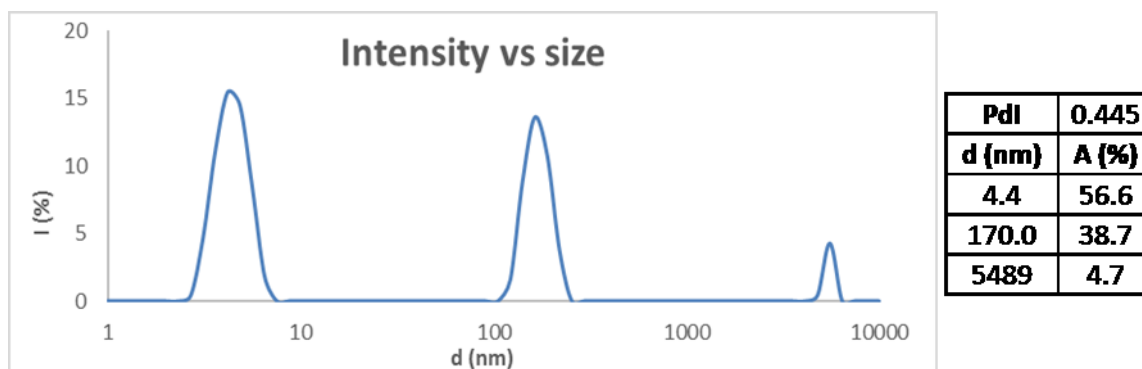


Figure 10. Intensity of scattered light vs size distribution for as-synthesized alumina nanoparticles suspended in *i*-PrOH (scale-up synthesis). In the table, polydispersity index and area percentage under each peak of the distribution are reported.

Volume and number distributions showed that most of the suspended particles had  $d < 10$  nm. They both displayed a single peak centered at 3.6 nm (Figure 11).

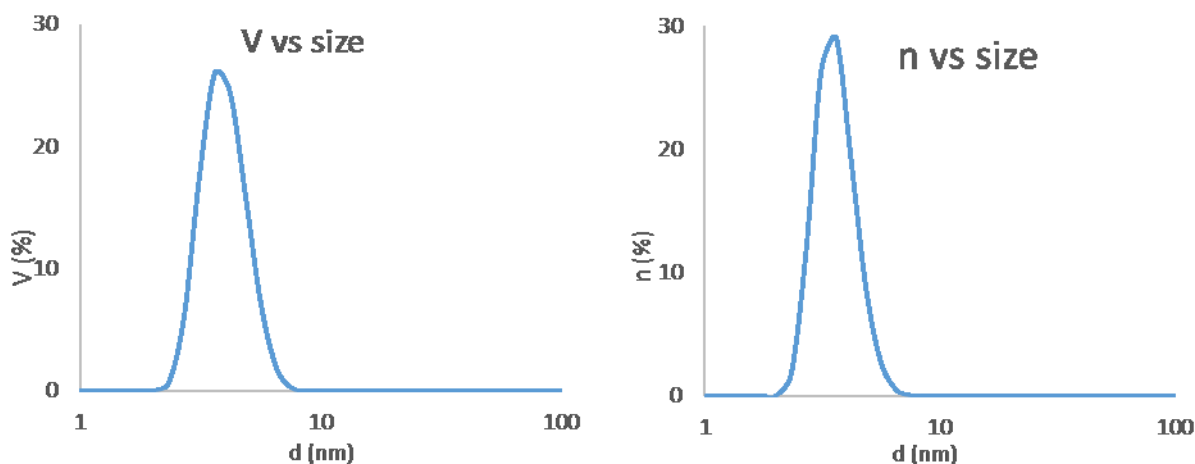


Figure 11. Volume vs size and number vs size distributions for as-synthesized alumina nanoparticles suspended in *i*-PrOH (scale-up synthesis).

These distributions were almost identical to those observed for the lab-scale synthesis. Therefore, it was verified that the alcohol-based sol-gel synthesis of Al<sub>2</sub>O<sub>3</sub> nanoparticles described above could be transferred to a quasi-industrial scale. This evidence opens interesting scenarios for a future large-scale application of these systems.

#### Synthesis in aqueous medium

Despite the excellent results and reproducibility displayed from the previously described synthesis, an alternative sol-gel route was explored. In fact, the use of an organic solvent like isopropyl alcohol can bring health and environmental issues, as it is flammable, skin irritant and potentially explosive. For these reasons, an aqueous sol-gel synthesis is extremely appealing, especially in perspective of a future transfer of the process to industrial scale. The aqueous sol-gel synthesis here described was inspired from the literature [86] [87] and was published in a paper by my group in 2014 [111].

In this water-based route, the same reagents of the previous synthesis were used. EAcAc was added to deionized water and mechanically stirred for few minutes, then temperature was raised to 70°C. Al(O-*sec*-Bu)<sub>3</sub> was dissolved in the mixture, then a 0.5 M HNO<sub>3</sub> aqueous solution was added dropwise to promote peptization by acid catalysis. In aqueous alumina suspensions, HNO<sub>3</sub> induces a charge on the growing particles, generating repulsive forces and eventually allowing for the formation of smaller particles [86]. The molar ratios of EAcAc, water and HNO<sub>3</sub> with respect to Al were set to 1, 50 and 0.3, respectively. The exact quantities of each reagent are listed in Table 4.

Reagent	PM (g/mol)	Purity (%)	$\rho$ (g/mL)	Volume (mL)	Weight (g)	n (mol)	n/n Al	M (mol/L)
EAcAc	130.14	100	1.029	22.3	22.90	0.18	1	0.0008
Al(O- <i>sec</i> -Bu) <sub>3</sub>	246.33	97	0.96	46.6	44.69	0.18	1	0.0008
H <sub>2</sub> O	18.02	100	1	158.4	158.40	8.79	50	0.0381
HNO <sub>3</sub>	63.01	65	1.396	3.7	5.12	0.05	0.3	0.0002
<b>Total</b>				<b>231.0</b>				

Table 4. Molecular weight, purity, density, volume, weight, moles, molar ratio with respect to Al and molarity of every reagent used in the synthesis of water-based alumina suspension.

After 24 hours, the stirring was stopped and the sol collected for characterization. pH was measured with a pH-meter calibrated in the acidic pH range. The average value, calculated for four batches, is pH =  $3.63 \pm 0.05$ . Average particle size was determined by DLS. The measured distribution, the mean size value and area percentage for each peak are reported below in Figure 12.

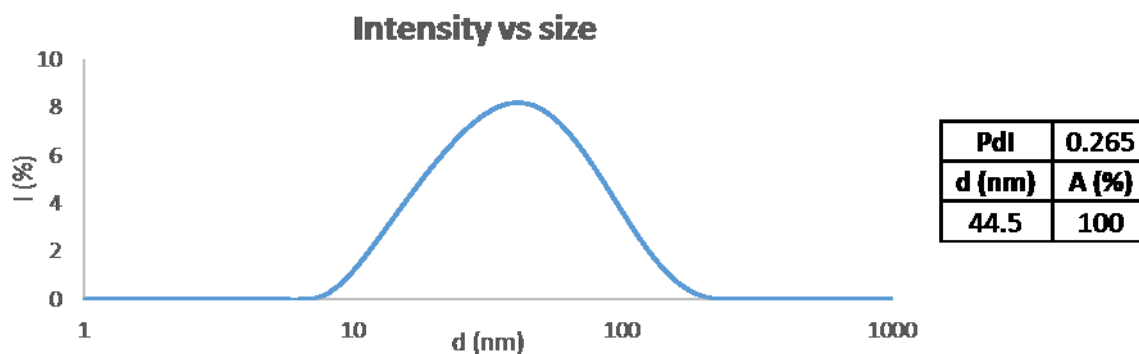


Figure 12. Intensity of scattered light vs size distribution for as-synthesized alumina nanoparticles suspended in H<sub>2</sub>O. In the table, polydispersity index, mean size value and area percentage under each peak of the distribution are reported.

Particle size distribution showed an only peak (monomodal distribution) centered at  $d = 44.5$  nm. However,  $Pdl = 0.265$  was quite high for a monomodal distribution, due to the large width of the peak. Volume and number distribution gave better information about the actual size of suspended particles.

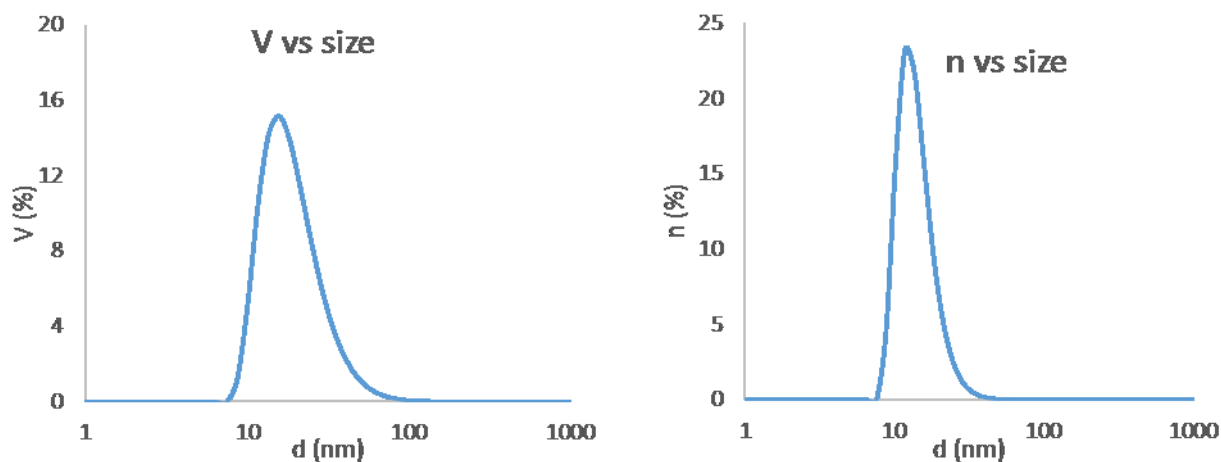


Figure 13. Volume vs size and number vs size distributions for as-synthesized alumina nanoparticles suspended in H<sub>2</sub>O.

From these distributions reported in Figure 13, it is evident that most of the suspended particles had hydrodynamic diameters slightly larger than 10 nm. Volume and number distribution displayed a single peak centered at 15.7 and 13.5 nm, respectively.

Viscosity of the water-based sol was determined in the same way as for the alcohol-based one. The sol was characterized in terms of viscosity. Shear rate was varied only across two decades, as liquid jets started to spurt from the cylinder as explained previously. Moreover, the “ramping” method was limited to three points when it was evident that  $\eta$  was constant. Temperature was kept constant at 25.0°C. Results are reported in Figure 14, while Table 5 reports the calculated average values and standard deviations.

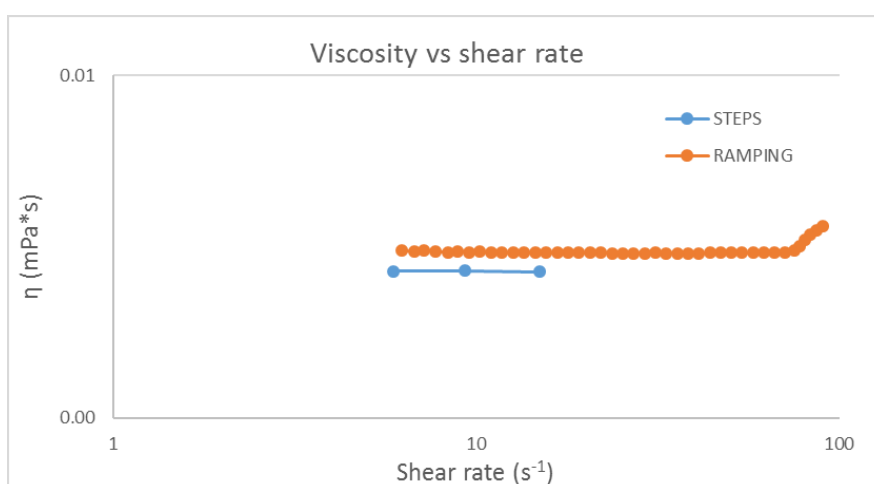


Figure 14. Viscosity versus shear rate for the water-based sol, as calculated from the measured shear stress. Results are reported for both patterns of shear rate variation, namely “steps” and “ramping”.

Method	$\eta$ (mPa*s)	St.Dev
Steps	2.68	0.01
Ramping	3.04	0.02

Table 5. Average viscosity for the water-based sol, as computed for "steps" and "ramping" shear stress variation methods. Standard deviations are also reported.

As observed for the alcohol-based sol, the "steps" method provides a slightly smaller value of  $\eta$ . However, the percent difference between the two average values is almost the same for the two suspensions (around 12% of the largest value). Furthermore,  $\eta$  absolute values for this sol are smaller than for the previous one, as expected from the lower  $\eta$  of water (0.89 mPa\*s at T = 25°C) with respect to *i*-PrOH (1.96 mPa\*s).

Surface tension of the water-based sol was calculated with the pendant drop method. Five drops for each of two as-synthesized batches were used for average calculation. Calculated surface tension was  $\gamma = 29.2 \pm 0.3$  mN/m at room temperature (about 23°C). Compared to water surface tension (72.7 mN/m at 25°C), the difference is remarkable. This strong effect was attributed to the presence of low-surface tension compounds like the chelating agent EAcAc ( $\gamma = 32.3$  mN/m at 25°C) and the side-product of hydrolysis 2-butanol ( $\gamma = 22.6$  mN/m at 25°C).

## COATING DEPOSITION, PROCESSING AND CHEMICAL MODIFICATION

As deposition methods, I mainly explored dip coating and spray coating because of their transferability to industry. In both techniques, there is very small consumption of coating sol and operations can be easily performed by automatic devices. Dip coating is a very simple technique: the substrate is dipped into the coating sol, then is withdrawn after a certain time. Notwithstanding this apparent triviality, it is a complex process in which many parameters must be controlled to achieve reproducible results. Withdrawal speed is the most important parameter, as it strongly influences the gel film thickness. Landau and Levich [112] studied dragging of a liquid by a moving plate and established a relationship between film thickness  $h$  and withdrawal speed  $u$ :

$$h = \frac{0.94\eta^{2/3}}{\gamma^{1/6}(\rho g)^{1/2}} u^{2/3}$$

$\eta$ ,  $\gamma$  and  $\rho$  are sol viscosity, surface tension and density, respectively. This relationship was obtained for withdrawal speeds above 1 mm/s. In such conditions, viscous drag by gravity is the most important factor (viscous regime). For lower speeds (draining regime), evaporation becomes faster than the motion of the drying line, inducing the feeding of coating sol from the reservoir by capillary. Such phenomenon causes deviations from predictions. Indeed, for speeds in the order of 0.1 mm/s the tendency is reversed, as film thickness increases with decreasing speed. Grosso *et al.* [80] [113] published papers to describe this phenomenon and eventually established a more accurate relationship between  $u$  and  $h$ :

$$h = k \left( \frac{E}{Lu} + Du^{2/3} \right)$$

In this equation,  $k$  is a composition constant (proportional to concentration),  $E$  is the evaporation rate,  $L$  is the substrate length and  $D$  contains the physical-chemical characteristics of the coating solution. Both the capillary regime ( $E/u$  term) and the viscous regime ( $Du^{2/3}$  term) contribute to final thickness. As a result, the thickness vs withdrawal speed curve will show a minimum for a certain speed value. This curve can be shifted by changing the surface temperature during deposition or by modifying sol concentration. Control of coating thickness is extremely important for substrates like glass, for which transparency must be unaltered. Thin sol-gel coatings, with thickness smaller than the wavelength of visible light, can maintain or even increase transparency, acting as anti-reflective coatings [88] [99] [100].

As already mentioned, spray coating was also used as coating technique. Its main advantage with respect to dip coating is the need of much smaller sol volumes, as virtually all the sol contributes to film formation. The main drawback is that non-planar surfaces (e.g. with cavities or non-exposed parts) are hardly coated in a homogeneous way. For this reason, I mainly focused on dip coating as deposition technique on most surfaces, while spray-coated samples were fabricated only for preliminary studies.

### Dip coating

All dip coating processes were performed with one of the two automated dip coaters available at CNR-ISTEC (Figure 15). The smallest one is a homemade device composed of a steel arm moving vertically along a screw. The speed of the arm is controlled by adjusting the voltage of a potentiometer. Samples



are attached to the arm, either with a clamp or by any other way suitable for that sample shape, and dipped into the coating suspension.

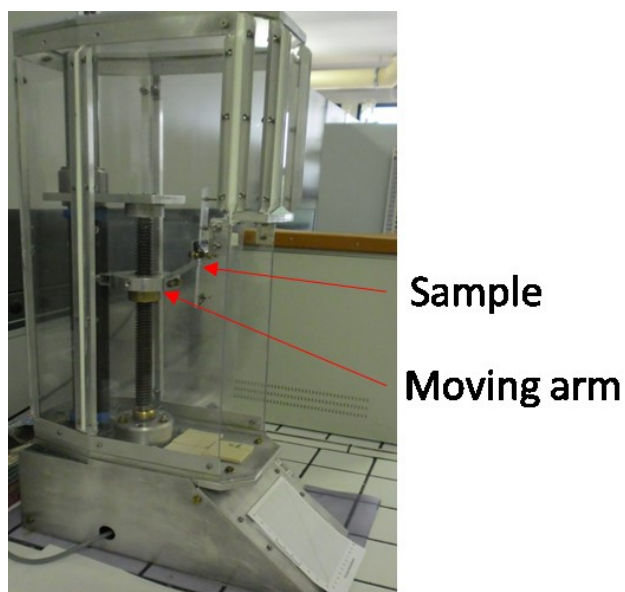


*Figure 15. Small homemade dip coater available at CNR-ISTEC.*

This small device cannot coat samples with any dimension larger than 150 mm. For this reason, a larger dip coater was purchased from Aurel Automation (Modigliana (FC), Italy; see Figure 16). It is a tailored dip coater, designed and developed according to the requests of the research group. This dip coater features a large chamber (internal overall size 1700 x 1000 x 700 mm) and two linked steel arms moved along a rail by an electric engine. A featured clamp can be used to hold samples, but many other setups were adopted depending on the sample shape. All operations are computer-driven and the user can set all crucial parameters, namely: dipping and withdrawal speed; immersion time; starting, intermediate and immersion position; drying time. This allows for maximum repeatability of the dipping process. The limitations in sample size are mainly linked to the chosen vessel, which also determines the necessary volume of coating liquid.

In all cases, we adopted a dipping and withdrawal speed of  $2.0 \pm 0.1$  mm/s in all dip coating processes. The sample was immersed for 5 seconds. Previous experiments at CNR-ISTEC proved that these parameters provide a reasonably thin and uniform alumina nanoparticles coating.

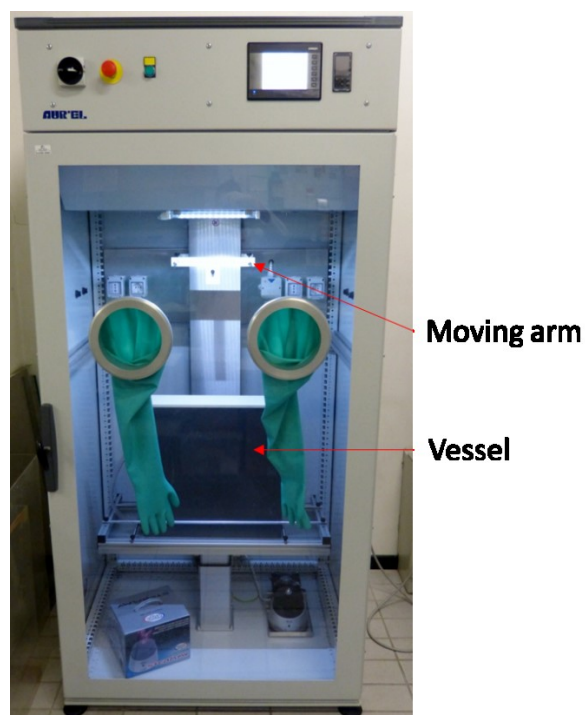


Figure 16. Large automated dip coater designed by Aurel Automation.

After dip coating, the samples were dried in air for a minimum of 3 hours. No significant dependence of coating morphology and properties on drying time was evident. We investigated the coating morphology on a glass substrate after drying with a Field Emission Scanning Electron Microscope (FESEM Gemini Columns, SIGMA Zeiss) and the observed structure is reported in Figure 17. Many pores of sub-micron scale were visible, in addition to randomly oriented, short channels (few hundreds of nanometers wide, few micrometers long). This coating was obtained via dip coating in an alcohol-based sol, but the same morphology was obtained from the water-based dispersion.

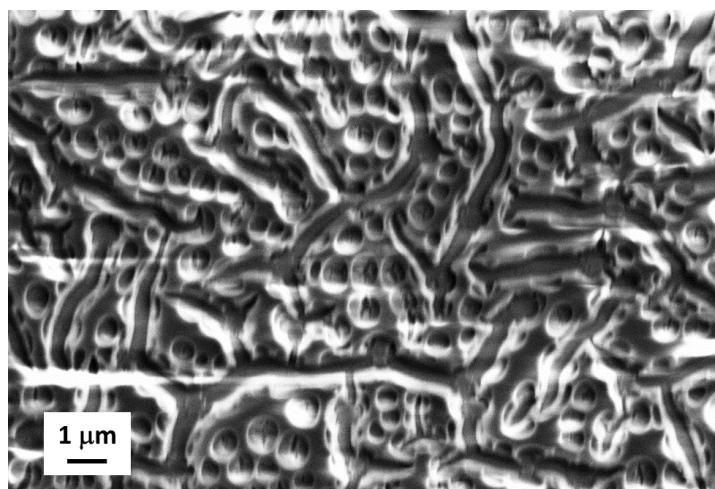


Figure 17. FESEM image of the alumina coating after dip coating on a glass surface and drying in air.

## Spray coating

Spray coating is an extremely widespread deposition technique. An XCel automated spray coater by Aurel Automation (Modigliana (FC), Italy) is available at CNR-ISTEC (see Figure 18), allowing for the control of many deposition parameters. Such repeatable deposition process is unattainable with manual spraying techniques.

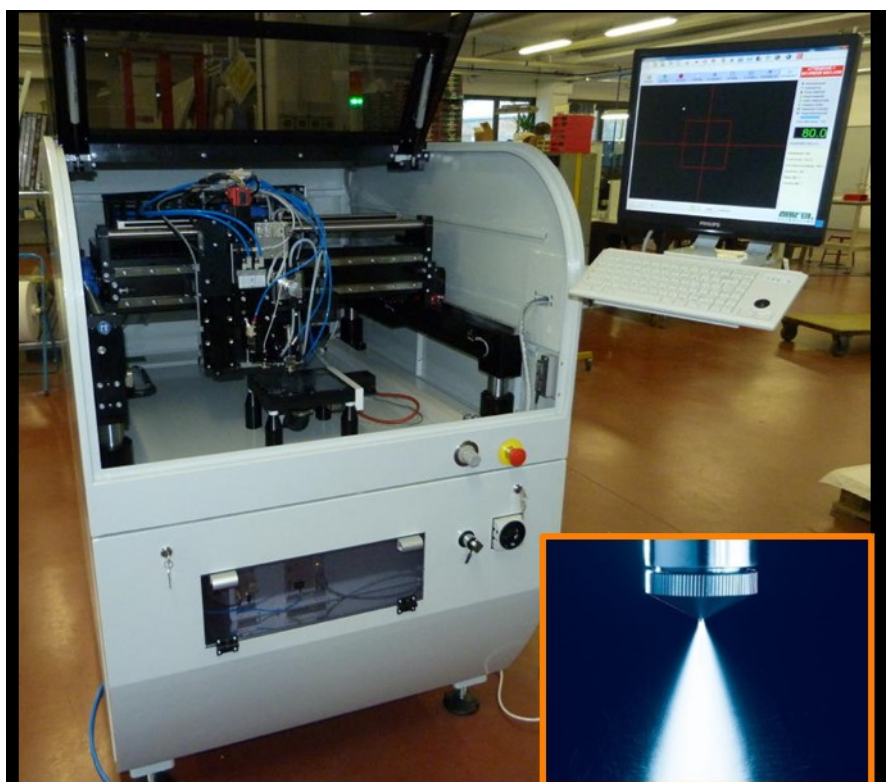


Figure 18. XCel automated spray coater available at CNR-ISTEC. Inset: ejection of a spray from the nozzle.

The spray coater is composed of a three-slot cartridge, able to host two spray nozzles and one ink-jet nozzle. The movement of the cartridge is controlled by a built-in software, allowing for the monitoring of many deposition parameters: spraying pattern (path on the  $xy$  plane and height on the  $z$  axis), atomizing gas pressure, flow rate, drying time between sprays. Moreover, the sample holder is a table whose temperature can be controlled in the  $T = 0 - 80^{\circ}\text{C}$  range. An air suction system sticks the sample to the table.

Spray coating tests mostly involved soda-lime glass microscope slides (75 x 25 mm, Carlo Erba Labware) as substrates. Glass substrates allow for a precise study of coating morphology, as they are perfectly flat and do not change their morphology during all processing steps. Furthermore, they can be easily broken to study coating sections without damaging the coating.

We tested spray coating of both water- and alcohol-based sols. We chose a round nozzle with inner diameter  $\varnothing = 0.36$  mm. Unfortunately, the spray coater does not provide an absolute value of spray flow rate, therefore we attempted deposition with two arbitrary flow rates, namely 6 and 14. Another crucial parameter was the distance between the nozzle and the surface. We attempted two distance values, 7 and 9 cm. Finally, we tried to deposit both the aqueous and the alcohol-based sol.

### First thermal treatment

The air-dried ceramic coatings were heat-treated in a furnace. This annealing step allowed for a complete drying of the film, removal of organic components, completion of condensation and densification, with positive effects on mechanical properties [114]. The choice of treatment temperature is crucial in order to avoid undesired phase transitions and cracking. From an analysis of the literature about alumina films, we inferred that the optimum temperature for the heat treatment of sol-gel alumina treatment was 400°C, in order to guarantee the complete removal of organic ligands [26] and the formation of an amorphous alumina film [28] [115]. Furthermore, keeping T as low as possible is obviously advantageous in terms of energy consumption. As far as cracking is concerned, it is a quite delicate phenomenon and deserves to be considered carefully. Kozuka *et al.* [116] [117] studied the cracking phenomenon in gel films. From their studies, it is evident that the intrinsic stress occurring during heating is maximum when condensation takes place during the treatment. However, in the deposition of a stable nanoparticle suspension, condensation is limited. Thus, cracking will be reduced and will be due mainly to differences in possible thermal expansion coefficients with the substrate (e.g. thermal stress) and capillary pressure caused by solvent vaporization. The same authors emphasized the positive role of chelating agents in diminishing crack formation during heating.

The substrate material has a strong influence on the choice of temperature: as will be further discussed in the last part of this chapter, the substrate can develop structured phases interfering with the coating surface morphology. Therefore, an optimization of thermal processes must be performed for every material on which the coating is deposited. The aforementioned treatment at 400°C proved adequate for a variety of materials including aluminum, soda-lime glass and ceramics. Figure 19 shows the alumina nanoparticles coating after thermal treatment at 400°C for 60 minutes. The coating looked smooth but cracked. This phenomenon could be avoided by adopting lower withdrawal speeds and forming a thinner gel film. However, the results shown in the upcoming sections proved that such cracks do not hinder to achievement of superhydrophobicity.

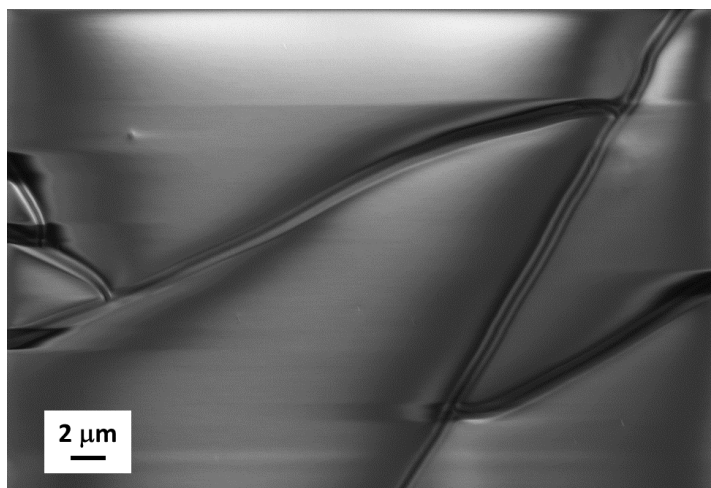
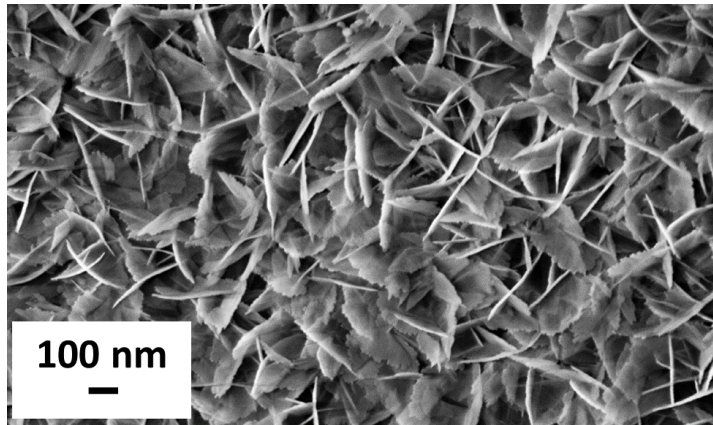


Figure 19. FESEM image of the alumina coating after dip coating on a glass surface, drying in air and thermal treatment at 400°C for 60 minutes.

### Boiling water treatment

The role of the inorganic layer in hybrid superhydrophobic coatings is to provide a suitable surface structure. It is known from the literature [27] that alumina  $\text{Al}_2\text{O}_3$  reacts with hot water to form boehmite  $\text{AlOOH}$  with a peculiar flower-like structure, resembling a desert rose. Such morphology is an excellent candidate for the manufacturing of superhydrophobic surfaces [17] [18] [28] [27], as its nano-scale voids are able to entrap air and develop a high anti-wetting capillary pressure [118]. In this work, we formed boehmite on alumina-coated surfaces by immersion in boiling DI water. We chose to treat the coated surfaces for 30 minutes, which Feng *et al.* [119] suggest to be the optimum for achieving superhydrophobicity on alumina-coated surfaces. A further thermal treatment was performed to complete drying and sinter the coating without losing the flower-like morphology [120] [79]. Treatment temperature was the same as in the previous annealing step, but treatment time was shortened to 10 minutes as no organic species had to be eliminated.

Coating morphology and thickness after such boiling treatment strongly depended on the deposition method. Figure 20 shows the flower-like structure obtained on a dip-coated surface. Lamellae took a random orientation on the surface, creating a huge number of pores or voids with width in the range of tens of nanometers. Lamellae were about 200 nm long on average. The flower-like coating homogeneously covered the entire surface.



*Figure 20. FESEM image of the flower-like boehmite nanostructure obtained on an aluminum substrate by immersion of the alumina-coated surface in boiling DI water for 30 minutes and heat-treatment at 400°C for 10 minutes.*

Figure 21 shows a finer detail of a nanoflake on the boehmite surface. This lamella was expected to be just few nanometers thick.

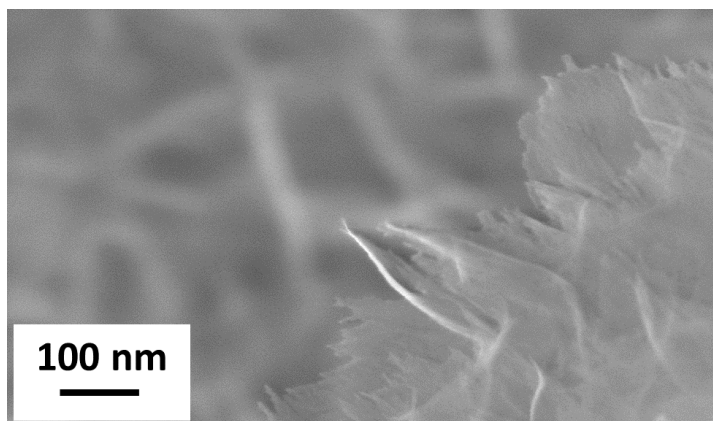


*Figure 21. FESEM image at high magnification of a single lamella in the flower-like boehmite nanostructure.*

Sections of dip-coated glass slides were observed with FESEM to obtain information about thickness. The coating displayed a 200 nm-thick, entirely structured layer (see Figure 22).

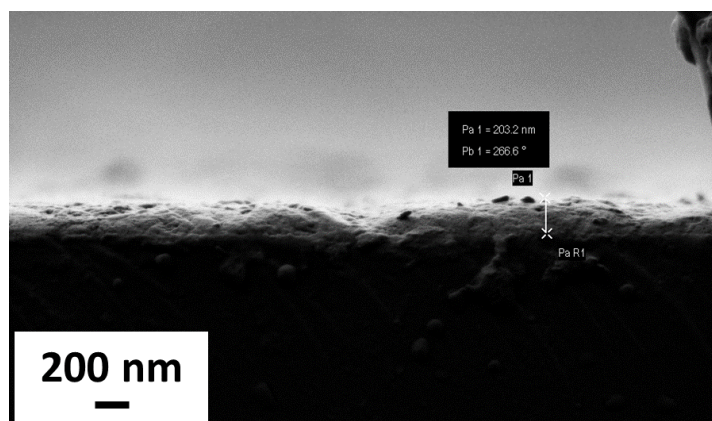


Figure 22. FESEM image of the section of a boehmite-coated glass slide fabricated by dip coating.

When spray coating was adopted as deposition method, both the cross section and the morphology of the coating looked different. First, we compared surfaces sprayed with the same flow rate (6 arbitrary units) and different nozzle-surface distance. Figures 23a and 23b show the surface sprayed from 7 cm, while Figures 23c and 23d are related to the surface sprayed from 9 cm. In the sooner case, the coating looked exfoliated (Figure 23a). Furthermore, the flower-like nanostructure was scarce and not perfectly developed (Figure 23b). For longer spraying distance, the coating looked more homogeneous (Figure 23c), but going into finer details some unstructured areas appeared, juxtaposed to the expected flower-like morphology (Figure 23d). The presence of such discontinuities is detrimental for the wetting properties of the coating.

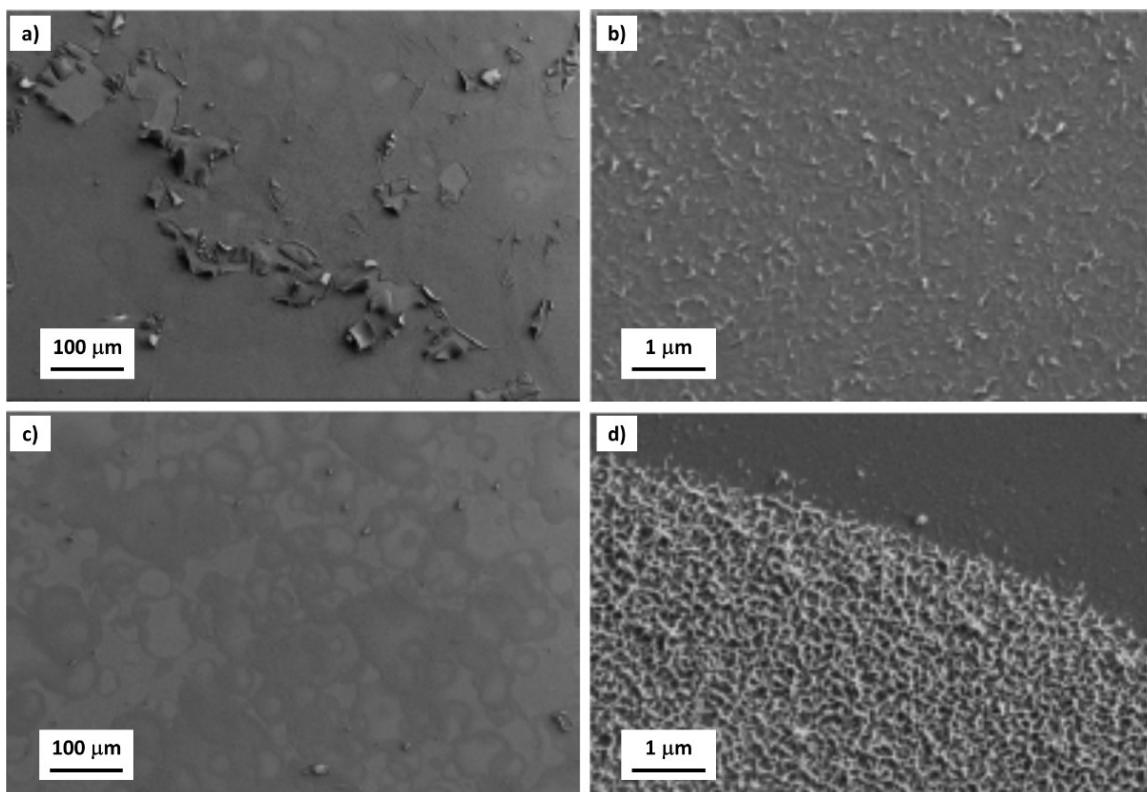


Figure 23. FESEM images of the sprayed alumina coating (flow rate 6 a.u.) after immersion in boiling DI water for 30 minutes and heat-treatment at 400°C for 10 minutes. a) and b) are referred to a surface coated with a nozzle-surface distance of 7 cm, while c) and d) were obtained via spraying from 9 cm. Scale bars are reported.

Similar morphology was observed when flow rate was increased to 14 arbitrary units. The coating formed some large scales (Figure 24a), on which a sparse flower-like morphology was observed (Figure 24b).

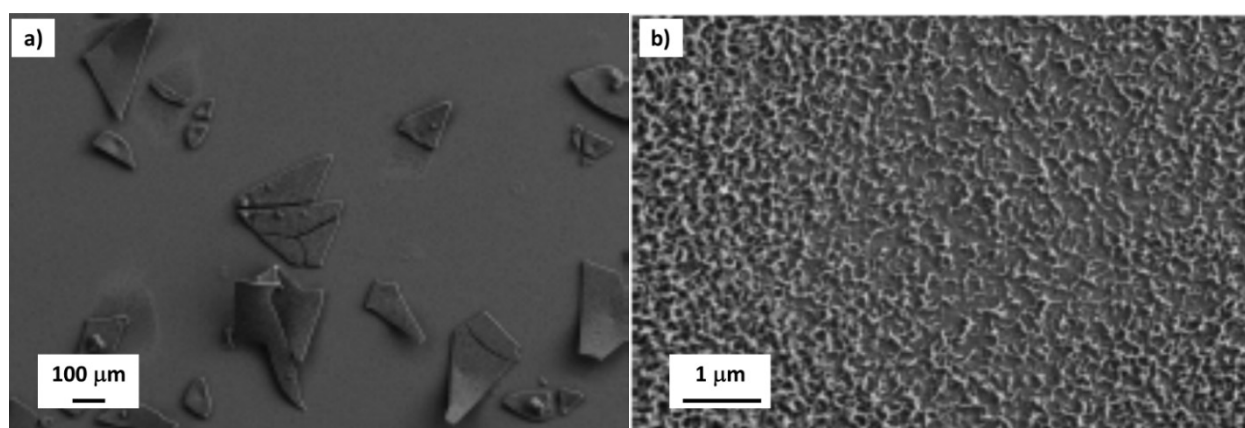


Figure 24. FESEM images at two different magnifications of the sprayed alumina coating (flow rate 14 a.u., nozzle-surface distance 9 cm) after immersion in boiling DI water for 30 minutes and heat-treatment at 400°C for 10 minutes. Scale bars are reported



Regarding the cross section of the sprayed coating, two distinct layers were present: the outer one was about 200 nm-thick and with flower-like structure, as in dip-coated samples. Meanwhile, an additional thicker and non-structured layer was present. Probably such layer could not be reached by the boiling water treatment and did not form boehmite flakes. The thickness of the non-structured layer depended on the number of depositions: Figure 25a shows a 680 nm-thick layer obtained with a single deposition, while Figure 25b shows a 1.2  $\mu\text{m}$ -thick layer fabricated with three depositions. Further investigations are needed to establish whether a longer treatment time would allow for the formation of a thicker boehmite layer. Furthermore, such layer could have positive effects in terms of coating adhesion and mechanical resistance.

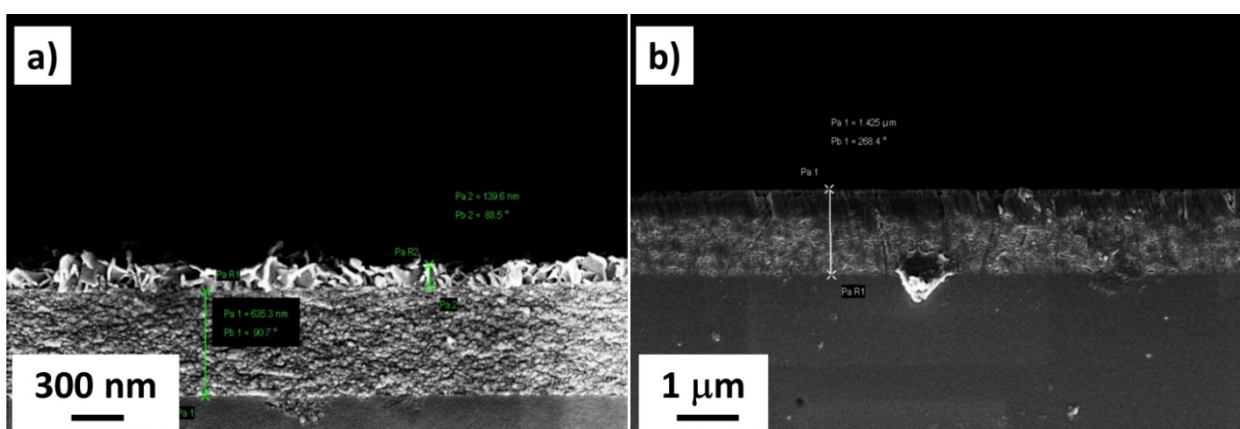


Figure 25. FESEM image of the section of a boehmite-coated glass slide fabricated by spray coating: a) coating obtained with one deposition; b) coating obtained with three depositions.

Notably, the same results in terms of coating morphology and thickness were obtained when the aqueous alumina suspension was used. Therefore, these results are not reported for brevity.

We also characterized the coatings in terms of wetting properties. Whatever the deposition method, the inorganic coating was superhydrophilic: any water drop deposited on its surface instantly spread, thus  $\text{WCA} \approx 0$ . This behavior is due to a combination of hydrophilic surface chemistry (with polar Al-O-Al and Al-OH bonds exposed) and enhanced surface roughness (caused by surface morphology). According to Wenzel [2], this combination leading to superhydrophilicity.

#### Chemical modification with fluoroalkylsilane

On the nanostructured boehmite surfaces, modification of surface chemistry is necessary to achieve superhydrophobicity. In the literature, many molecules have demonstrated to efficiently lower the surface energy, typically by introducing non-polar C-C and C-H bonds or extremely stable C-F bonds. For

example, many authors report successful modification of metal oxides with fatty acids [37] [119] or thiols [121]. However, the interaction between these molecules and the oxides is often too weak, causing poor chemical and mechanical resistance. Meanwhile, silanes proved extremely effective in forming a strong bond with oxides [122], therefore providing more resistant hydrophobization [123]. Fluoroalkylsilanes (FAS), e.g. fluorine-substituted alkylsilanes, establish excellent superhydrophobic properties [9] [10]. Moreover, FAS bestow enhanced repellence against low surface tension liquids on the surface, e.g. oleophobicity [124]. Hence, I chose FAS as low-surface-energy compounds for my superhydrophobic coatings. Furthermore, C-F bonds are extremely strong (the strongest single bonds in organic chemistry [125]), thus allowing for improved thermal stability. FAS can be grafted to the surface through many techniques, but I chose dip-coating for simplicity. Even though FAS solutions can be easily prepared with desired concentration, I used a commercial solution in isopropanol to guarantee reproducibility.

All the boehmite-coated surfaces were chemically modified by dip coating in a commercial solution of FAS in isopropanol, namely Dynasylan SIVO Clear EC (Evonik, Germany). The solute is a long chain FAS with three isopropoxy substituents. Furthermore, an unknown metalorganic catalyst is added into the solution to enhance FAS hydrolysis by air humidity and condensation with surface hydroxyl groups. The dip coating parameters were: dipping and withdrawal speed 2 mm/s, immersion time 2 minutes. In this case, withdrawal speed should not be an important parameter as the coating phase is a solution, not a suspension. We chose a low speed only to avoid turbulence in the solution. Meanwhile, the immersion time was suggested by the retailer. Few tests at longer immersion times showed no improvement in liquid repellence by the surface.

## WETTING PROPERTIES OF THE HYBRID, NANOSTRUCTURED COATINGS

This subchapter will focus on the wetting properties of the hybrid coating previously described. The theoretical aspects of the different contact angle measurements have already been described in Chapter 3. Moreover, we will assess how the liquid-repellent properties of the coating are affected by the exposure to different aggressive environments.

### Superhydrophobicity

The water-repellent behavior of the coating, e.g. its superhydrophobicity, was assessed essentially in two ways. The first one is the measurement of the static water contact angle WCA by the sessile drop

method. As described in Chapter 3, this is an apparent contact angle, whose value can radically change from point to point for a rough and inhomogeneous surface. Nonetheless, WCA is still the most common way to express the wetting behavior of a surface, so it is worth it to measure the average WCA for the coating. Conventionally, a superhydrophobic surface must have  $WCA > 150^\circ$ . For WCA measurements and all other wetting characterizations, we used an OCA 15 Plus optical contact angle system (DataPhysics Instruments). We chose to dispense drops with a volume of  $2 \mu\text{L}$ , which is low enough to avoid excessive shadows and allow for a clear recognition of the contact points. As the chosen fitting method influences the calculated WCA value, we compared the results obtained with the different fitting methods available in the software, namely Laplace-Young, circle, ellipse and tangent. First, we analyzed surfaces obtained via dip coating. Notably, the results were the same regardless of the dispersing medium (isopropyl alcohol or water). Figure 26 reports such comparison for a sessile drop on a sandblasted and hybrid-coated aluminum surface. Table 6 reports the average of 10 measurements for each fitting method on the same surface. In all cases  $WCA > 150^\circ$ , thus the surface was superhydrophobic. The table also reports WCA values on a reference sandblasted aluminum foil. The coating greatly enhanced the observed WCA, transforming a slightly hydrophobic surface into a perfectly superhydrophobic one.

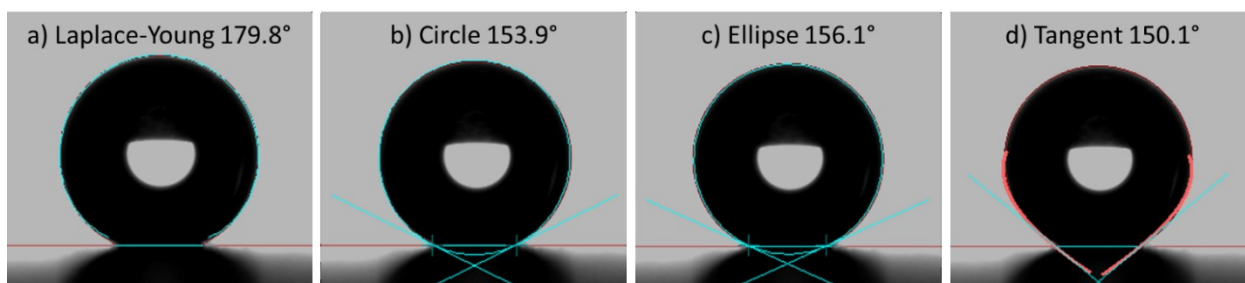


Figure 26. Contact angle measurements for a  $2 \mu\text{L}$  water drop on a sandblasted, hybrid-coated aluminum surface. Drop profile is fitted by the OCA 15 Plus software with four different methods: a) Laplace-Young fitting; b) circle fitting; c) ellipse fitting; d) tangent leaning. For every case, the measured WCA value is reported. The red straight line is the baseline, the blue curve is the fitted profile and the blue line in b), c) and d) is the calculated tangent.

Fitting method	$WCA_{\text{hybrid}} (^\circ)$	$WCA_{\text{ref}} (^\circ)$
Laplace-Young	$179.7 \pm 0.2$	$95.8 \pm 3.1$
Circle	$154.4 \pm 2.3$	$94.2 \pm 2.7$
Ellipse	$155.7 \pm 1.9$	$97.0 \pm 3.2$
Tangent	$152.1 \pm 2.1$	$92.4 \pm 2.2$

Table 6. Average water contact angle values with four different drop profile fitting methods on a sandblasted, hybrid-coated aluminum surface ( $WCA_{\text{hybrid}}$ ) and on a sandblasted, bare aluminum surface ( $WCA_{\text{ref}}$ ). Standard deviations are reported as errors.

The second method for the assessment of superhydrophobicity is the measurement of advancing and receding contact angles, ACA and RCA respectively. Contact angle hysteresis CAH is calculated as the difference between these two values. Conventionally, surfaces with good water repellence properties must show  $CAH < 10^\circ$ . In this case, the tangent fitting method was the only one available. An example of a CAH measurement is reported in Figure 27, while Table 7 reports the average values of ACA, RCA and CAH for a sandblasted, hybrid-coated aluminum surface and a reference sandblasted bare aluminum surface. CAH was much smaller than  $10^\circ$ , indicating excellent anti-wetting properties and very low adhesion of water drops, which in fact rolled off the surface very easily (e.g. with a slight tilting of the sample). On the other hand, a non-coated aluminum surface had very large CAH. Indeed, water drops showed strong adhesion on the surface and could not roll off even when it was tilted by  $90^\circ$ .

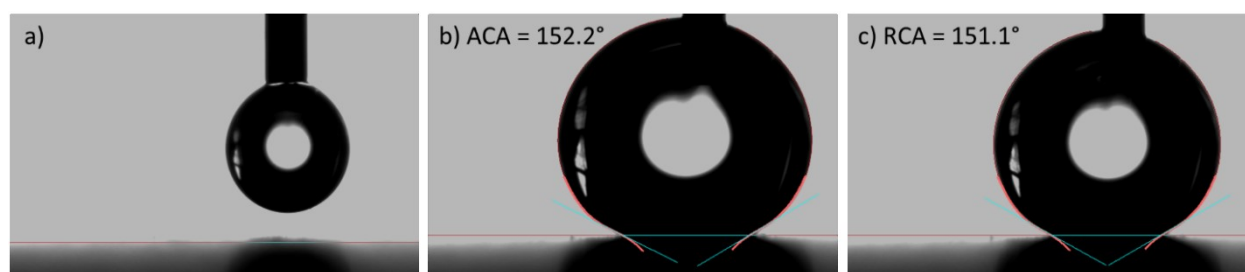


Figure 27. Contact angle hysteresis measurements for a  $2 \mu\text{L}$  water drop on a sandblasted, hybrid-coated aluminum surface: a) starting water drop; b) measurement of advancing contact angle ACA by injecting  $10 \mu\text{L}$  of water inside the drop; c) measurement of receding contact angle RCA after withdrawing  $2 \mu\text{L}$  of water from the drop. Drop profile is fitted by the OCA 15 Plus software with tangent leaning method. The measured CA value is reported. The red straight line is the baseline, while the red thick curve and the blue line in b) and c) are the fitted profile and the calculated tangent, respectively.

	$CAH_{\text{hybrid}} (^\circ)$	$CAH_{\text{ref}} (^\circ)$
ACA	$152.5 \pm 1.2$	$93.5 \pm 2.1$
RCA	$151.5 \pm 0.8$	$53.5 \pm 2.1$
CAH	$1.0 \pm 0.1$	$40.0 \pm 3.2$

Table 7. Average values of ACA, RCA and CAH of water drops on a sandblasted, hybrid-coated aluminum surface. Standard deviations are reported as errors.

Most remarkably, the same wetting properties were obtained on non-sandblasted (e.g. smooth) coated aluminum and on different substrates, like soda-lime glass and ceramics. This means that the coating was applicable to a wide range of materials, no matter their starting wetting properties and surface roughness.

We also investigated the behavior of spray-coated surfaces. Remarkably, none of them was superhydrophobic, as WCA was smaller than  $150^\circ$  in all cases (see Table 8). This result was not surprising, considering the discontinuous flower-like morphology observed on spray-coated samples

(see Figures 23 and 24). These results proved that dip coating was more of a suitable deposition method for the alumina nanoparticles suspensions here described, thus we adopted dip coating as the standard deposition method for the remainder of the activity. All the following results are referred to dip-coated surfaces. Nonetheless, spray coating is a potentially interesting technique that deserves future studies and optimization.

Coating sol	Flow rate (a.u.)	Spraying distance (cm)	WCA (°)
A	6	7	138.9 ± 14.3
A	14	7	118.9 ± 10.5
A	6	9	117.2 ± 9.4
A	14	9	128.0 ± 7.8
B	14	7	132.0 ± 10.2

Table 8. Average water contact angle (WCA) values on spray-coated aluminum surfaces. The type of coating sol (A is alcohol-based, B is water-based), the flow rate (in a.u.) and the spraying distance (in cm) are reported. All drop profiles were fitted with the Laplace-Young method. Standard deviations are reported as errors.

### Oleophobicity

The ability of a surface to repel liquids with surface tension ( $\gamma_G$  or just  $\gamma$  for brevity) lower than water ( $\gamma = 72.0$  mN/m at 25°C) is often defined as oleophobicity [29] [30] [31], due to the low surface tension displayed by common oils. However, oils are mixtures, thus their actual  $\gamma$  is strongly affected by their composition. For this reason, in the literature the oleophobicity of a surface is mostly assessed in terms of contact angle with model compounds like alkanes [31] [126]. Surface tension for linear alkanes varies with their chain length, e.g. the shorter the chain, the smaller the  $\gamma$  value. For this reason, we measured  $\theta$  for linear alkanes with different chain length, from n-hexadecane (16 C atoms) to n-pentane (5 C atoms). Shorter chain alkanes are gaseous at room temperature, while longer chain alkanes are solid.

However, we extended the range of investigation by measuring the static contact angles also for other liquids with low  $\gamma$ . Diiodomethane is an organic compound with relatively large  $\gamma$  (50.8 mN/m at 20°C), but still it is non-polar. Arnica46 (Agip, Italy) is a very common lubricant oil for hydraulic pumps [127], with high kinematic viscosity  $\nu$  (0.45 stokes at 40°C, almost 70 times higher than water) and excellent anti-wear properties. Its exact composition is unknown; we calculated its surface tension at room temperature with the pendant drop method [107] [108] [128] and we obtained  $\gamma = 29.4 \pm 0.1$  mN/m at  $T = 20^\circ\text{C}$ . Average contact angles (CA) with various low surface tension liquids are reported in Table 9. We decided to perform these characterizations only for dip-coated aluminum samples, as spray-coated surfaces were not as homogeneous and performant.

Liquid	$\gamma$ (mN/m)	$CA_{\text{hybrid}}$ (°)	$CA_{\text{ref}}$ (°)
Diiodomethane	50.8	172.0 ± 3.5	57.0 ± 15.4
n-Hexadecane	27.5	141.8 ± 6.2	13.2 ± 2.3
n-Tetradecane	26.6	144.3 ± 2.3	10.6 ± 2.6
n-Dodecane	25.4	123.6 ± 4.4	9.8 ± 4.4
n-Decane	23.8	97.2 ± 8.4	7.7 ± 2.2
n-Octane	21.6	71.5 ± 8.8	5.9 ± 1.7
n-Hexane	18.4	15.1 ± 4.0	3.8 ± 2.7
Arnica46	29.4	150.0 ± 10.0	16.1 ± 1.6

Table 9. Average contact angles  $CA$  for different liquids on a sandblasted hybrid-coated aluminum surface ( $CA_{\text{hybrid}}$ ) and on a sandblasted bare aluminum surface ( $CA_{\text{ref}}$ ). Drop profiles were fitted with Laplace-Young method. Standard deviations are reported as errors. Surface tension  $\gamma$  is measured at  $T = 20^\circ\text{C}$ .

Comparing  $CA$  values for the hybrid-coated ( $CA_{\text{hybrid}}$ ) and bare sandblasted aluminum ( $CA_{\text{ref}}$ ), the role of the coating in enhancing liquid repellence is evident. While bare aluminum had  $CA < 20^\circ$  for all investigated alkanes, hybrid-coated surfaces displayed a clearly oleophobic behavior, with  $CA > 90^\circ$  for alkanes with  $\gamma > 20.6$  mN/m. When  $\gamma$  fell under this threshold, also  $CA$  dropped to small values, e.g. the surface became oleophilic. Moreover,  $CA$  never reached values larger than  $150^\circ$ , thus the hybrid coating could not be defined as superoleophobic, rather as oleophobic [31]. Figure 28 shows three different liquid drops on a SHS. They all looked spherical and did not spread on the surface, notwithstanding their different  $\gamma$ .

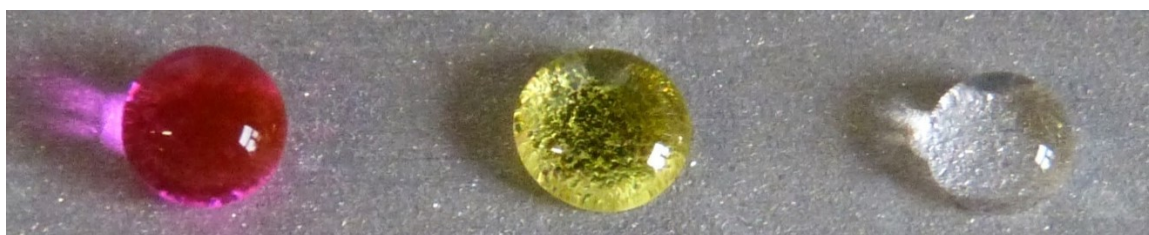


Figure 28. a) Water, b) diiodomethane and c) hexadecane drops on a sandblasted, hybrid-coated aluminum surface.

Provided the combined presence of superhydrophobic and oleophobic behavior, the nanostructured, hybrid coating here described can be defined as amphiphobic [20] [94].

#### Durability in aggressive environments

So far, one of the main issues of superhydrophobic surface is their lack of durability when exposed to harsh operational conditions [129] [130] [131] [132] [133]. Hybrid coatings can lose their

superhydrophobic properties by modification of surface chemistry or by damage to the nanostructure. For this reason, it is necessary to assess the wetting properties of the coating after exposure to different aggressive environments.

We chose an array of so-called ageing tests to simulate many possible aggressive conditions that the coating might face during operation in a hypothetical application. These ageing tests included chemically aggressive environments, UV irradiation, mechanical stress and frosting/defrosting tests in climatic cell. Table 10 describes all the ageing tests performed. The samples consisted in sandblasted aluminum foils (Al1050 H24 99% alloy, 100 x 50 x 2 mm<sup>3</sup>) bearing the hybrid coating previously described. We assessed their wetting properties in terms of WCA, CAH and CA with n-hexadecane before the tests. After the ageing process, we rinsed the samples with DI water and re-measured all the contact angles. The results of these tests were described in a paper published in 2014 [111] and are reported in Figure 29.

Code	Ageing type	Description
A	Acidic solution	Immersion in acetic acid aqueous solution (pH = 3.0) for 60 days
B	Basic solution	Immersion in ammonia aqueous solution (pH = 10.0) for 60 days
S	Saline solution	Immersion in sodium chloride aqueous solution (100 g/L, pH = 7.0) for 60 days
SW	Seawater	Immersion in aqueous solution simulating seawater (pH = 7.9, carbonates 0.230 g/L, sulfates 2.225 g/L, sodium chloride 35 g/L) for 60 days
UV	UV irradiation	Irradiation with an Osram Ultra-Vitalux 300W lamp with I = 5.0 ± 0.2 mW/cm <sup>2</sup> for 150 min
Abr	Abrasion	Abrasion with a rotating felt disk according to UNI EN 1096-2 standard for coated glasses (applied load 4 N, disk diameter 60 mm, rotating speed 60 rpm, test time 30 s)
CC	Climatic cell	20 frosting/defrosting cycles in static climatic cell (T range = -15 ÷ +25°C, rate 2°C/min, relative humidity 30%)

Table 10. Ageing tests performed on sandblasted, hybrid-coated aluminum surfaces.

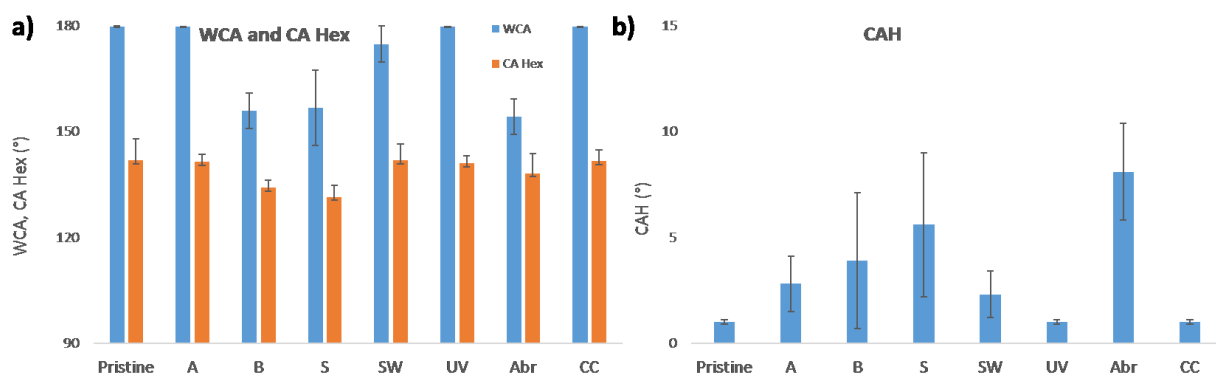


Figure 29. a) Water (WCA, blue) and hexadecane contact angles (CA Hex, orange) and b) contact angle hysteresis (CAH) on as-fabricated hybrid-coated aluminum surfaces (pristine) and after ageing tests (see Table 9 for the codes). Standard deviations are reported as error bars.

Looking at the evolution of contact angles, the response of the coating depended on the ageing test. More precisely, the acid solution, the seawater, the UV irradiation and the exposure to frosting/defrosting cycle did not damage the coating significantly, as the values of WCA, CAH and CA with hexadecane did not change significantly after the tests. However, three conditions seemed to damage the coating, namely the immersion in basic or saline solution and the abrasion. For all these conditions, WCA decreased to about  $150^\circ$ , CA with hexadecane fell under  $140^\circ$  and CAH increased up to almost  $10^\circ$ .

Based on these results, we elaborated some hypotheses about the bonds occurring during the coating process. The FAS layer is stable due to Si-O-Al bonds formed with hydroxyl groups of alumina and further stabilized by the cross-linking bonding among free Si-OH groups, generated by the FAS hydrolysis under environmental humidity. Probably some of these bonds are partially hydrolyzed during the tests, causing weakening of the FAS adhesion and lowering of the hydrophobic performances [134]. After a prolonged immersion, a partial detachment of the fluorinated layer can occur, eventually exposing the naked boehmite coating which is hydrophilic. This phenomenon is further emphasized when samples are immersed in basic ammonia solution: aluminum oxides like boehmite react with alkaline compounds forming aluminum oxide anions ( $\text{AlO}_2^-$ ) and eventually aluminum hydroxide ( $\text{Al}(\text{OH})_3$ ), which is insoluble. Thus, it can either precipitate or react with hydroxyls ions forming hydroxoaluminate like  $\text{NH}_4\text{Al}(\text{OH})_4$  precipitates. All these phenomena enhance the deterioration of alumina oxide layer. Anyway, even after such harsh tests the hybrid-coated surfaces were still superhydrophobic, with  $\text{WCA} > 150^\circ$  and  $\text{CAH} < 10^\circ$ . We further inspected FAS degradation phenomena in basic environment with the XPS investigations reported later.

Moreover, it was interesting to assess the changes in surface morphology induced by the most severe ageing tests (Figure 30). We observed the surface of the hybrid-coated samples after immersion in basic solution, in saline solution and after abrasion. In the first case (Figure 30a), the flower-like nanostructure seemed affected from the test, as the flakes looked slightly aggregated and shortened. Probably the edges are the most reactive of the inorganic layer, thus sensible to attack by hydroxyl ions. Meanwhile, after the saline test (Figure 30b) some glossy aggregates were observed on the surface, probably due to NaCl crystals that cover the nanostructured coating. Even in this case, boehmite nanoflakes were slightly reduced in length and formed sparse aggregates. Abrasion tests also caused limited damages to the flower-like structure, in addition with the formation of coarse grain probably linked to wear debris (Figure 30c).



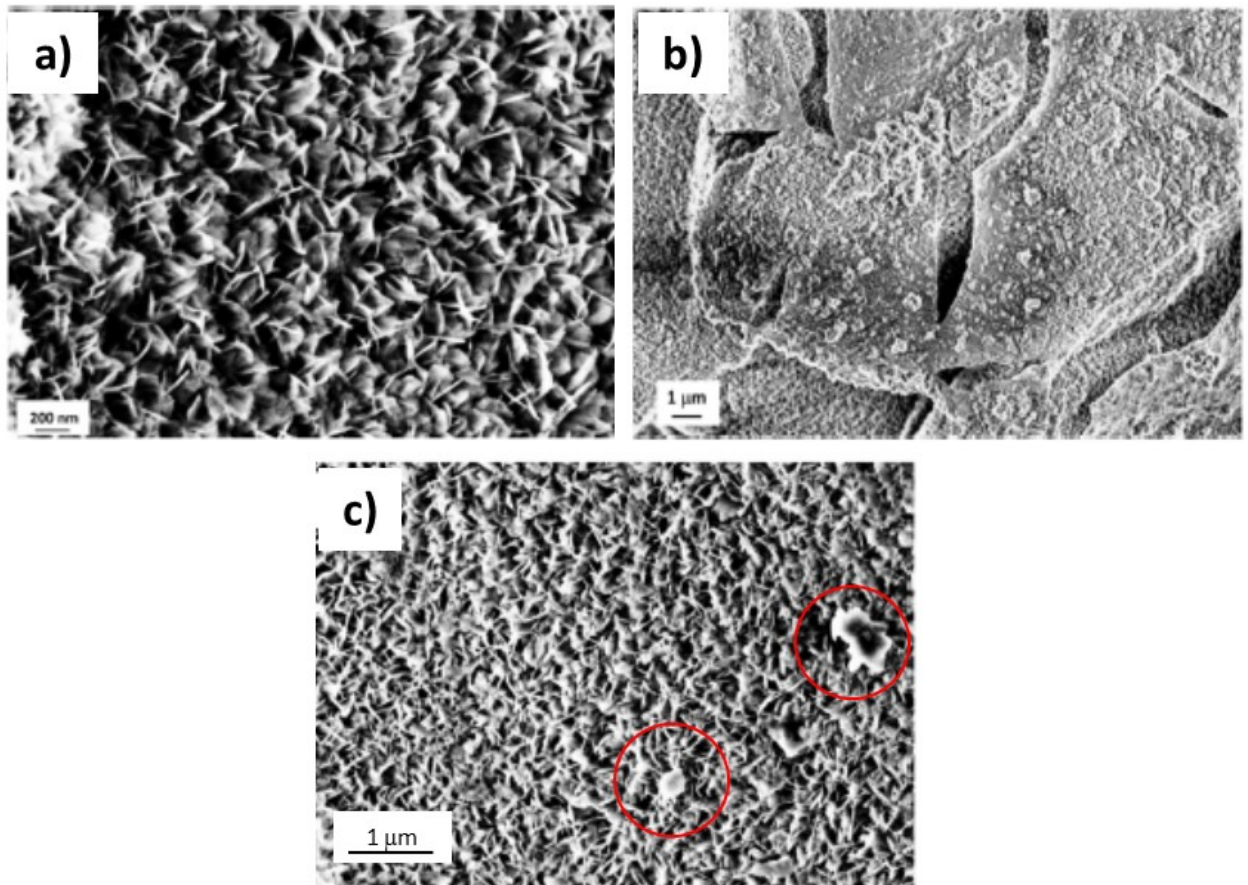


Figure 30. FESEM images of hybrid-coated aluminum surfaces after a) immersion in basic ammonia solution, b) immersion in saline solution and c) abrasion. In c), red circles mark micron-sized aggregates.

In summary, the hybrid coating proved to be resistant to many aggressive environment and mechanical stresses, as it maintained its amphiphobic properties almost unaltered. A slightly higher sensibility was observed for basic and saline environments, as well as for abrasion. However, even in those cases superhydrophobicity was retained after the tests.

#### OTHER CHARACTERIZATIONS: MECHANICAL PROPERTIES AND ROUGHNESS

Wetting properties are obviously the most important features of superhydrophobic coatings. Nonetheless, the assessment of other properties become crucial when we try to apply superhydrophobic coatings in any real device. Depending on the application, the coating must own specific properties. We mainly focused on two aspects, namely adhesion to the substrate and roughness.

The mechanical characterization of thin films is a crucial topic. Many studies have been devoted to this subject [135] [136] [137], highlighting a variety of highly challenging issues. The most important one is to

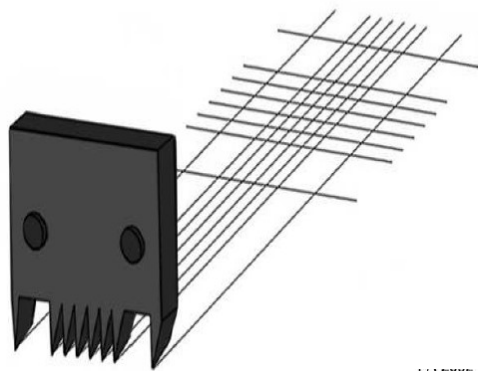
distinguish the signal generated by the film from that generated by the substrate. Obviously, the thinner the coating, the harder it becomes to isolate its properties from those of the underlying material. Many techniques have been developed for the mechanical characterization of thin films. Each method provides information about the behavior of the coating under a specific mechanical stress. However, there is often a lack of standardized methods for the assessment of mechanical properties of coated surfaces. For this reason, many authors designed tailored tests to assess the ability of the mechanical resistance of the coatings, especially in the case of superhydrophobic ones. For my hybrid, nanostructured coating I focused on adhesion properties and its resistance to wear and other mechanical stresses.

Roughness is also a crucial parameter for a wide range of applications, from optics to anti-fogging surfaces[ref.]. There are plenty of techniques for roughness measurement, each with different sensitivity. Moreover, roughness can be described by many parameters, all of which have to be considered for a proper description of the surface asperities.

#### Mechanical properties: adhesion

Adhesion is the ability of the coating to stick to the substrate [138]. Obviously, a coating with high adhesion to many different substrates would ensure excellent versatility and durability through time. For this reason, it is important to assess the adhesion of the coating on different materials, in order to acknowledge the limitations of the actual technology and to orientate the future research for an appealing superhydrophobic coating.

Adhesion can be evaluated according to different standard tests. The first one and most simple is the tape test, which is regulated by the ASTM D3359. In this procedure, a cutter blade is used to create a grid-shaped scratch on the coated surface (Figure 31, left side). Then, a standardized adhesive tape is applied on the scratches and peeled off. The evaluation of adhesion is performed by the user: observing either the sample surface or the peeled tape, the quantity of removed coated is evaluated and the degree of adhesion is determined by comparison with model images (Figure 31, right side). Adhesion ranges from 0B (more than 65% of the coating is removed) to 5B (no coating is removed).



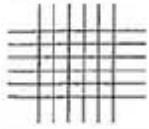
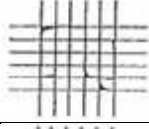
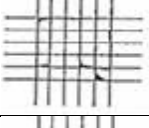
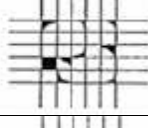
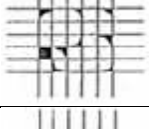
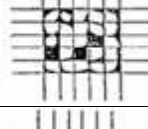
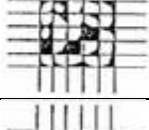
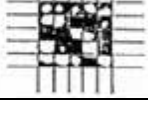
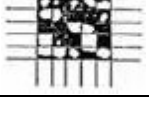
Classification	% of area removed	Surface of cross-cut area from which flaking has occurred for 6 parallel cuts & adhesion range by %
5B	0% - None	
4B	Less than 5%	
3B	5 - 15%	 
2B	15 - 35%	 
1B	35 - 65%	 
0B	Greater than 65%	

Figure 31. (Left) Sketch of the cutter blade and the cross-cut area on the surface and (right) classification of coating adhesion according to % area of coating removed by tape peel-off.

The tape test was performed on coated aluminum surfaces. More specifically, we deposited the coating with the usual process on two different types of aluminum: one with an untreated, smooth surface and one with sandblasted, rough surface. The reason was to assess a possible influence of surface roughness on coating adhesion.

After the test, it was not possible to determine the level of adhesion by looking at the cross-cut area on the surface, as it looked completely unaltered for both types of samples. For this reason, we looked at the peeled tape to see if any residue was visible. For rough aluminum, almost no trace of coating was observed on the tape, corresponding to an adhesion of 4B (Figure 32, left). For the smooth aluminum, a little more coating was removed, so an adhesion level of 3B was established (Figure 32, right). This small difference in adhesion level can be due to micron-scale surface roughness induced by sandblasting: the micron-sized pits can “protect” the coating from the mechanical stress applied by peeling off the tape, resulting in reduced coating removal.

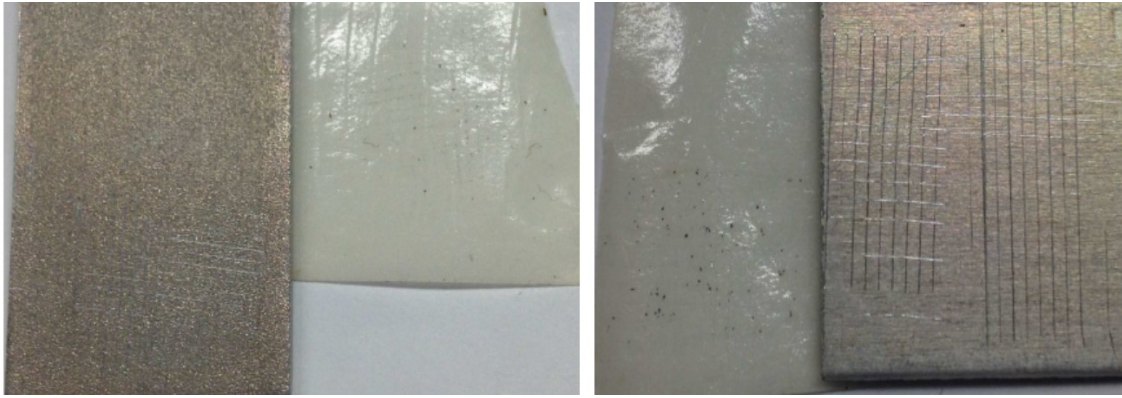


Figure 32. Cross-cut area on (Left) rough and (right) smooth coated aluminum surfaces, together with their relative peeled tapes for the evaluation of coating adhesion.

In addition to tape test, we also assessed coating adhesion with a scratch test. These experiments were performed with a CSM Revetest machine available at CNR-IMAMOTER in Turin, Italy (Figure 33, left). In a typical test, a diamond stylus is drawn across the surface under an increasing normal load until failure of the coating occurs (Figure 33, right). For the duration of the test, a piezoelectric accelerometer detects the acoustic emission (AE) produced as the coating is damaged. Failure is established by both observation of the AE curve and visual inspection of the track using an optical microscope and/or a profilometer. AE is often more efficient in the determination of coating failure because it can detect failures beneath the coating, which are not visible with optical microscopes. More specifically, the adopted test parameters were the following:

- Stylus: Rockwell C diamond with tip radius 200  $\mu\text{m}$
- Track length = 5 mm, speed = 10 mm/min
- Applied load = 1 ÷ 20 N, load increase rate = 100 N/min

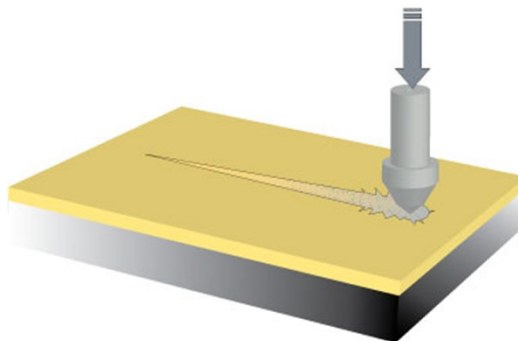
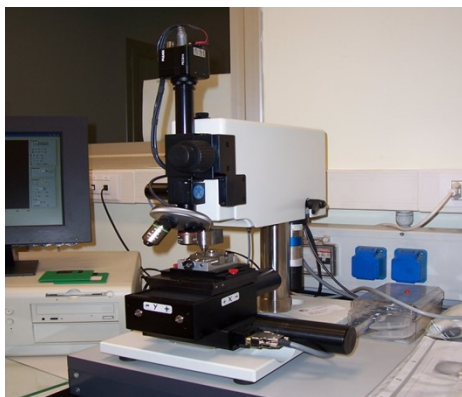


Figure 33. (Left) CSM Revetest machine available at CNR-IMAMOTER in Turin, Italy. (Right) Sketch of the scratch test: the stylus is drawn from left to right with a constant speed and increasing applied load, digging a track on the surface.

We tested two types of coated materials, namely aluminum and soda-lime glass. Moreover, both smooth and sandblasted, rough aluminum were coated and tested. The acoustic emission signals and the test tracks for aluminum and glass samples are reported in Figure 34 and 35, respectively. The wear tracks were observed by a Zeiss Axio.LabA1.m optical microscope equipped with CMOS5Mpx camera and Axiovision SE64 software for image analysis.

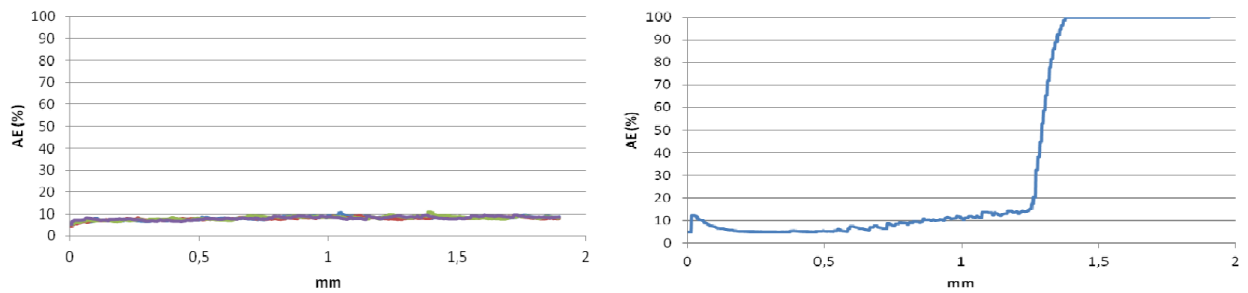


Figure 34. Acoustic emission signals as a function of track length for (left) aluminum and (right) glass coated surfaces.

As displayed on the left side of Figure 34, the AE signal was almost constant for both types of coated aluminum surfaces, suggesting that no failure occurred on those samples. Meanwhile, a steep increase in the AE signal for coated glass samples indicated the presence of coating failure corresponding to a load of about 13 N.

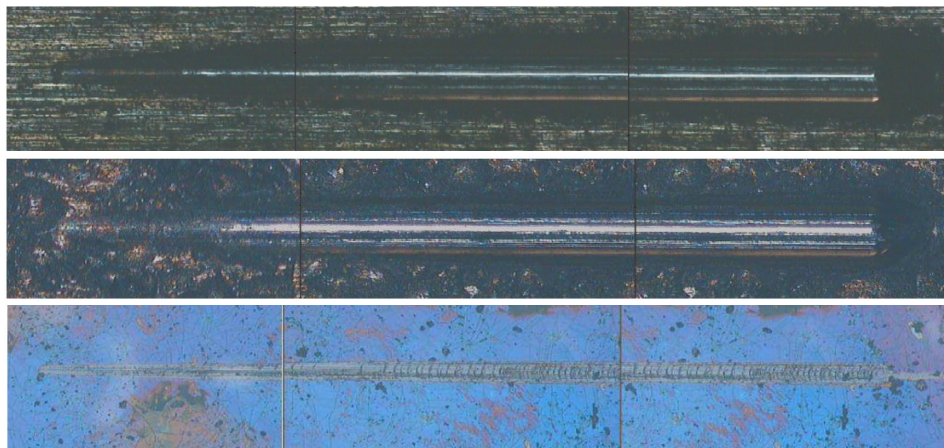


Figure 35. Scratch test tracks for (top) smooth aluminum, (middle) rough aluminum and (bottom) glass coated surfaces.

From Figure 35, it is clear that coating failure occurred also on the aluminum samples. For this reason, we calculated the critical failure loads from optical microscope images. Two critical loads can be distinguished: the first one (CL1) takes place when small fractures are observed on the surface, while the

second one (CL2) occurs when the coating is fully delaminated. An example of the two critical loads is displayed in Figure 36 for a coated, smooth aluminum substrate.

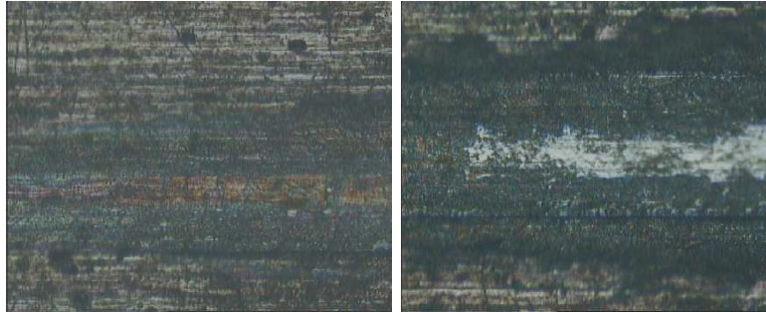


Figure 36. High magnification of the wear track on a coated smooth aluminum surface: (left) first critical load and (right) second critical load.

In Table 11, the average CL1 and CL2 for the three tested types of samples are reported.

Sample	CL1 (N)	CL2 (N)
Smooth aluminum	3.0	5.4
Rough aluminum	3.0	4.7
Soda-lime glass	2.3	7.4

Table 11. First (CL1) and second critical load (CL2) for coated surfaces, as determined from optical microscope images of the wear tracks.

CL1 was identical for the coated aluminum surfaces and very similar also for the coated glass. On the other hand, there is a significant difference in CL2, which is the highest for coated glass. However, the uncertainty in these measurements was very high due to the large error in load estimate. These tests were meant as a very rough approximation of the adhesion of the coating on different substrates. From this data, we can infer that the coating does not have good adhesion on aluminum and glass substrates, leaving room for future improvement of this property.

### Surface roughness

The evaluation of roughness is a key aspect in surface science, as many phenomena are related to the presence of asperities and valleys on the surface. Just to name a few, roughness plays a major role in condensation [139], friction [140], optical properties [141] and, of course, wetting [142]. For these reasons, an evaluation of surface roughness is present in almost all papers related to surface science.

In all roughness measurements, the instrument measures a profile as the variation of topology  $y$  along the selected trace. Roughness can be quantified and evaluated using many parameters. Anyway, the most common is the arithmetic average roughness  $Ra$ , which is the average value of height over a mean line (calculated across the measurement path):

$$Ra = \frac{1}{n} \sum_{i=1}^n y_i$$

However,  $Ra$  does not provide adequate information, especially in terms of topology distribution. Many other parameters can be used to obtain more accurate details. For example, the root-mean-squared roughness  $Rq$  reveals the presence of high peaks and deep valleys better than  $Ra$  does:

$$Rq = \sqrt{\frac{1}{n} \sum_{i=1}^n y_i^2}$$

Other useful parameters are the maximum valley depth  $Rv$ , the maximum peak height  $Rp$  and the relative difference  $Rz$ . Furthermore, parameters like skewness  $Rsk$  and kurtosis  $Rku$  provide enhanced information on height distribution:

$$Rsk = \frac{1}{nRq^3} \sum_{i=1}^n y_i^3$$

$$Rku = \frac{1}{nRq^4} \sum_{i=1}^n y_i^4$$

However, all these parameters refer to a single profile. Thus, it is only a 2D approach with relevant limitations for the characterization of anisotropic surfaces [143]. For this reason, the International Organisation for Standardisation has developed a collection of standards for the analysis of 3D, areal surface texture called “ISO 25178: Geometric Product Specifications (GPS) – Surface texture: areal”. This

standard defines a large number of parameters  $S$ , many of which are the exact areal counterpart of linear  $R$  parameters, i.e.  $Sa$ ,  $Sq$ ,  $Sv$ ,  $Sz$ ,  $Ssk$ ,  $Sku$ . Height values  $y_i$  refer to a mean plane instead of a mean line.

Many techniques are available for the assessment of surface roughness [143]. Essentially two types of methods can be distinguished: contact techniques and non-contact (optical) methods. The sooner use the displacement of a stylus or a tip dragged on the surface to obtain information about surface roughness. Meanwhile, non-contact techniques are mainly based on the interaction of one or more light beams with the surface to reconstruct its asperities. Contact methods have severe constraints in terms of resolution: they cannot resolve features which are smaller than the stylus. Our coating has a nanoscale structure that contact techniques cannot investigate properly. This is why we only used non-contact methods for the measurement of surface roughness in our coating.

A ContourGT-K 3D optical microscope (Bruker Nano GmbH) is available at CNR-ISTEC for the evaluation of surface roughness. This instrument is based on White Light Interferometry (WLI) [144]: a white light beam is split and directed partly at the sample and partly at a defect-free reference surface. The light reflected from these two surfaces is then recombined. The result is a pattern of bright and dark lines that track the surface shape. The microscope objective is scanned along the Z-axis so that each point of the test surface passes through focus. The location of the maximum contrast in the bright and dark lines indicates the best focus position for each pixel, and a full 3D surface map of the surface within the field of view of the microscope is generated. A tailored software is then employed to analyze these data to calculate different parameters of interest, such as surface texture, roughness or other critical geometric dimensional information.

In our case, we focused on the areal roughness parameters to assess the topology of the nanostructured coating. More in detail, we evaluated roughness on a smooth aluminum substrate before and after the deposition of the hybrid coating. Roughness parameters for both surface types are reported in Table 12.

	Bare	Coated
<b><math>Sa</math> (<math>\mu\text{m}</math>)</b>	0.691	1.545
<b><math>Sq</math> (<math>\mu\text{m}</math>)</b>	0.897	1.916
<b><math>Sv</math> (<math>\mu\text{m}</math>)</b>	-39.452	-24.034
<b><math>Sz</math> (<math>\mu\text{m}</math>)</b>	73.929	42.441

Table 12. Areal roughness parameters for an aluminum substrate before (bare) and after deposition of the hybrid coating (coated).  $Sa$ : average roughness,  $Sq$ : root-mean-squared roughness,  $Sv$ : maximum valley depth,  $Sz$ : difference between deepest valley and highest peak. Every value is the average of three measurements. An area of  $10 \times 10 \text{ mm}^2$  was investigated for each measurement.



From the data in Table 12, it is evident that the coating induced major modifications in surface roughness. Both  $S_a$  and  $S_q$  were more than doubled, while  $S_v$  and  $S_z$  were significantly smaller in absolute value. These results suggest that that coating might level the surface by partly filling the valleys.

However, these results were absolutely preliminary. Analysis of surface roughness is an extremely complex subject that requires deep comprehension of characterization techniques and statistical tools. Further studies will be devoted to extend the knowledge about the topology of these nanostructured coating, with the support of more refined data analysis.

## XPS STUDY AND DFT MODELING OF THE HYBRID COATING

X-ray Photoelectron Spectroscopy (XPS) is a powerful analytical technique that provides a deep comprehension of the chemical composition of a surface [145]. It is based on the detection of electrons emitted by a surface after excitation with an X-ray beam. The energy of these photoelectrons is correlated to the electronic structure of the surface. More specifically, the kinetic energy of the photoelectron depends on the electronic energy level from which it is emitted. Therefore, the analysis of the energy of the photoelectrons yields a picture of the electronic energy levels on the surface, thus of the surface atoms. By refining the analysis through deconvolution, it is also possible to infer the oxidation states and the chemical environment of the atomic species. For this reason, XPS investigations are reported in a plethora of papers about superhydrophobic surfaces [17] [29] [146] [147].

However, even XPS falls short in establishing the actual molecular structure on the surface. For this reason, it is necessary to integrate FESEM images and XPS spectra with a theoretical modeling of the surface structure. Density Functional Theory is often used in many papers to achieve this goal [148] [149].

Both XPS analyses and DFT modeling were performed by the group of Professor Robertino Zanoni at the Department of Chemistry of Università “La Sapienza” (Rome, Italy). The results of this collaboration are reported in a paper published in 2015 [150].

### XPS analysis of hybrid-coated aluminum substrates

For the XPS analyses, we fabricated aluminum substrates with suitable size (Al 1050 H24 99%, 10 x 10 mm<sup>2</sup>). We analyzed samples at three different stages of the functionalization process: uncoated aluminum (labelled as U), coated aluminum after boiling water treatment (B), hybrid-coated aluminum

(S). For the two coated samples, we used an aqueous alumina nanoparticles suspension. All coating processing was performed as described previously. Before XPS measurements, the samples were characterized in terms of wetting properties ( $\theta$  with water and hexadecane drops, labelled as WCA and HCA respectively; see Table 13) and surface structure. Both wetting properties and surface morphology were consistent with the previously reported data for samples at that stage of the process.

Sample	WCA (°)	HCA (°)
U	95.8 ± 3.1	4.0 ± 1.1
B	0	0
S	175.5 ± 3.1	144.0 ± 2.1

Table 13. Water and hexadecane contact angles (WCA and HCA, respectively) for the three types of sample analyzed with XPS. WCA and HCA were set to 0 on sample B due to the rapid spreading of liquid drops.

XPS measurements were performed using a modified Omicron NanoTechnology MXPS system available at the Department of Chemistry of University “La Sapienza” (Rome, Italy). The system is equipped with a monochromatic X-ray source (Omicron XM-1000), a dual X-ray anode (Omicron DAR 400), and an Omicron EA-127-7 energy analyzer. Either Al K $\alpha$  photons ( $h\nu = 1486.7$  eV) or Mg K $\alpha$  photons ( $h\nu = 1253.6$  eV) were used as excitation source operating the anode at 14-15 kV and 10-20 mA. For all samples, a survey scan (analyzer pass energy 50 eV) was acquired to locate the photoionization regions. Then, each region was observed in detail using an analyzer pass energy of 20 eV. Take-off angles of 11° and 71° with respect to the sample surface normal were adopted. The measurements were performed at room temperature, while the base pressure in the analyzer chamber was about  $2 \cdot 10^{-9}$  mbar during the analysis. The binding energy (BE) of the Si 2p $_{3/2}$  bulk component at 99.7 eV was used as an internal standard reference for the BE scale (accuracy of  $\pm 0.05$  eV) for FAS-modified samples. The measurements were performed in the shortest time possible (about 5 s) to avoid chemical modification by the X-ray beam (e.g. defluorination of FAS molecules). The experimental spectra were theoretically reconstructed by fitting the peaks to symmetric Voigt functions [151] and the background to either a Shirley [152] or a linear function. XPS atomic ratios between relevant core lines were obtained (with a 10% error) from experimentally determined area ratios corrected for the corresponding Wagner sensitivity factors [153]. Table 14 reports the relative surface atomic composition for the three samples.

Sample	O/Al	C/Al	F/Al	Si/Al
U	3.7	5.2	0.18	0.21
B	3.0	1.5	0.13	-
S	6.3	23	34	2.3

Table 14. Atomic ratios on the surface of the three types of sample analyzed with XPS.

On sample U (uncoated aluminum), a boehmite passivation layer was expected to cover the surface [154]. Al should be in a chemical state between totally oxidized, e.g.  $\text{Al}_2\text{O}_3$ , and totally hydroxylized, e.g.  $\text{Al}(\text{OH})_3$ . Due to boehmite stoichiometry, the expected O/Al ratio for sample U is 2.0, while the experimental ratio was 3.7. The excess of O atoms, together with the unexpected presence of C and F, hinted at the presence of carbonaceous contaminant species on the surface of U. Si is a component of the aluminum alloy substrate. More detailed information about these impurities can be obtained from curve-fitting of the C 1s peak (see Figure 37).

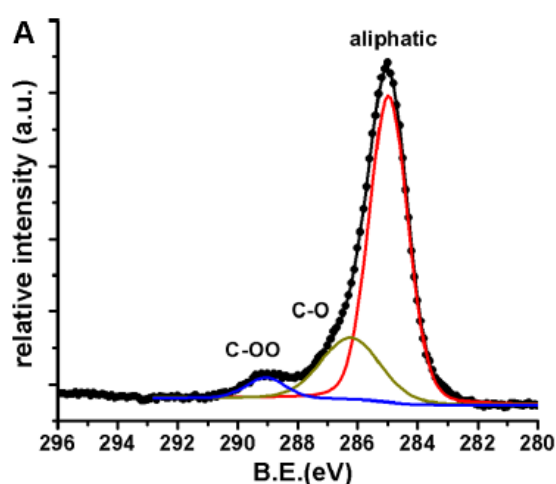


Figure 37. C 1s region of the XPS spectrum for sample U (uncoated aluminum). Black dots and line are experimental points, while red, green and blue lines are the fitted components.

Three components were distinguished: at 284.9 eV the aliphatic backbone, at 286.1 eV and 289.0 eV species containing CO and C(O)O groups, respectively [155]. The relative intensities for the three peaks were 73%, 22% and 5%, respectively. The latter two peaks confirmed the presence of oxidized carbonaceous species adsorbed on the aluminum surface, therefore accounting for the excess O detected. The experimental O/Al ratio could be corrected to the expected value of 2.0. More detailed calculations can be found in the supporting information for the paper [150].

On sample B (boehmite-coated aluminum), surface composition was expected to be similar to that of sample U due to the presence of boehmite. Even in this case, we found an excess of O atoms. Applying the same correction used for sample U, O/Al ratio was adjusted to 2.2. Notably, contaminants were less abundant, as confirmed by reduced C and F signals. Si disappears, due to the new boehmite layer deriving from alumina nanoparticles which are Si-free. The C 1s region of the XPS spectrum for sample B is reported in Figure 38.

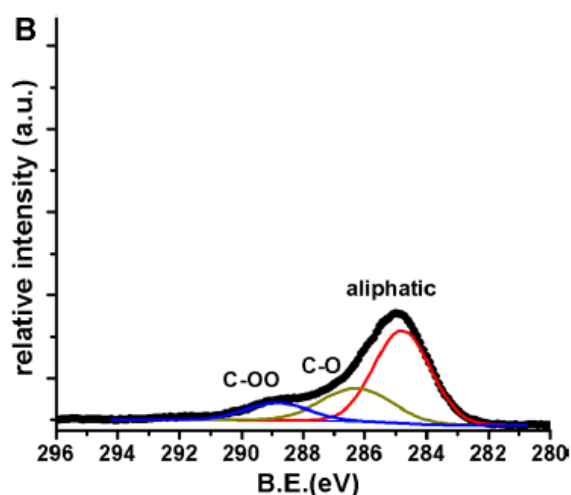


Figure 38. C 1s region of the XPS spectrum for sample B (coated aluminum after boiling treatment). Black dots are experimental points, while red, green and blue lines are the fitted components.

On surface S (hybrid-coated aluminum), the chemical composition was radically different due to the presence of FAS moieties. The survey scan is shown in Figure 39a. Oxygen, carbon, silicon, and fluorine showed an increase. From the experimentally determined relative amounts of C, F, and Si we could calculate the length of the FAS alkyl chains grafted to the surface and their degree of fluorination. The experimental C/Si ratio was  $23/2.3 = 10$ , thus suggesting a ten atom-long alkyl chain. Meanwhile, the F/C ratio ( $34/23 = 1.48$ ) was compatible with seven perfluorinated C atoms.

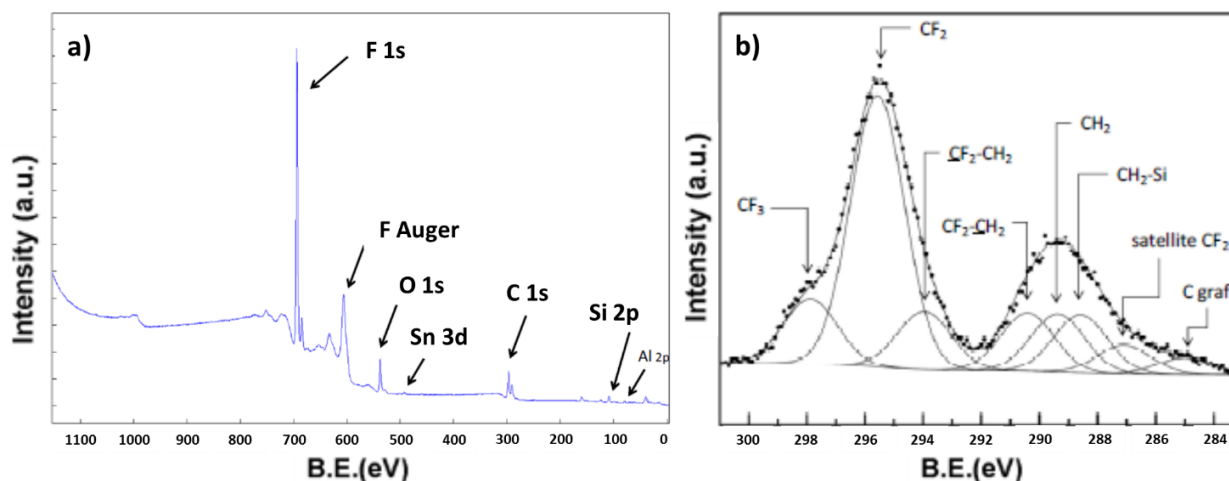


Figure 39. XPS a) survey scan and b) C 1s region for sample S (hybrid-coated aluminum). In b), black dots are experimental points, while solid lines are the fitted components.

The C 1s region was much more complex for sample S (Figure 39b), showing two main composite signals. The C-F components have higher BE, while the alkyl chain signal is at lower BE. By detailed curve-fitting, the C-F signal could be separated into three main components: terminal  $-\text{CF}_3$  at 293.7 eV, internal  $-\text{CF}_2-$  at 291.3 eV, and  $-\text{CF}_2\text{CH}_2-$  at 289.7 eV [155]. Meanwhile, the alkyl chain signal centered at 285.0 eV included three components:  $-\text{CF}_2\text{CH}_2-$ , the internal  $-\text{CH}_2-$ , and  $-\text{CH}_2\text{Si}-$  [155]. At lower BE, satellite peaks due to C-F groups excited by Mg  $\text{K}\alpha_{3,4}$  were added for a better fitting, as well as an additional signal due to carbonaceous contaminants on the sample holder. From the intensity ratios between these components, we could infer the composition of the grafted FAS chains. In particular, a 1:1 ratio was found between the terminal  $-\text{CF}_3$  and the  $-\text{CF}_2\text{CH}_2-$  species (as expected), a 1:5 ratio between the  $-\text{CF}_3$  and the internal  $-\text{CF}_2-$  components, and a 1:3 ratio between  $-\text{CF}_3$  and the alkyl signal. From these data, it was possible to obtain the molecular formula  $\text{CF}_3(\text{CF}_2)_6(\text{CH}_2)_3\text{SiR}_3$  for the FAS molecules grafted to the surface (R are substituents on Si, probably isopropyl groups). It must be considered that this formula does not necessarily correspond to that of the molecules in SIVO Clear EC solution, as many perturbations (e.g. heat-treatment at 150°C, handling, X-ray irradiation, exposure to high vacuum) might have altered the composition of the grafted FAS molecules. The presence of a short non-fluorinated alkyl chain between Si and the fluorinated long chain is likely to allow for a better packing of FAS molecules on the surface, due to the smaller size of H compared to F atoms. Perhaps, a totally perfluorinated chain would hinder formation of the monolayer on the surface.

#### DFT modeling of the molecular structure of the coating

The research group led by Professor Robertino Zanoni at University “La Sapienza” (Rome, Italy) performed DFT-based calculations with the CP2K/Quickstep package, using a hybrid Gaussian and plane-wave method [156]. For further details about DFT calculations, see the published paper [150]. The aim of these investigations was to understand at a molecular level the grafting mechanism of FAS on the surface.

First, the XPS C 1s spectrum of the proposed FAS molecule was simulated and is reported in Figure 40. The simulated spectrum and the experimental XPS peak components are in excellent linear correlation ( $R^2 = 0.98$ ), thus confirming the structure deduced by XPS analysis. Figure 40 also reports the optimized structure of the hydrolyzed FAS molecule, with a helical arrangement of the fluorinated chain due to steric interactions among vicinal  $\text{CF}_2$  groups. This model further suggests that a monolayer of FAS molecules adsorbed on a surface should display a maximum thickness of 15.5 Å, corresponding to the length of a single FAS molecule.

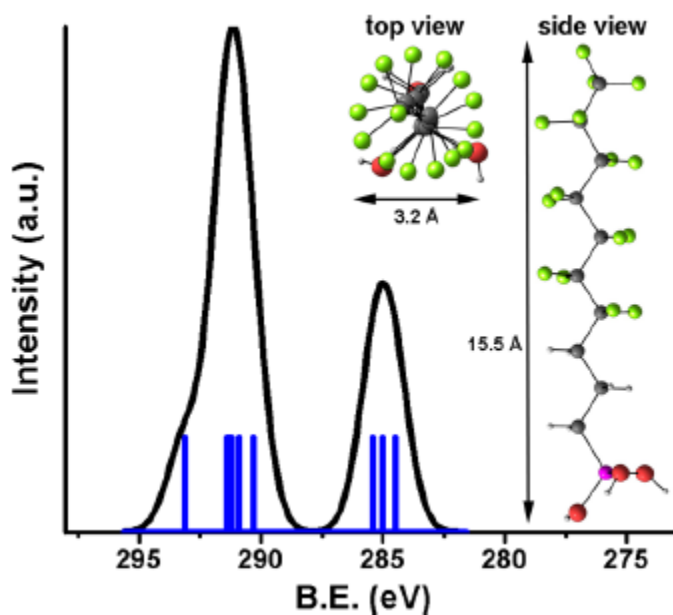


Figure 40. (Left) Gaussian convolution of C 1s orbital energies computed for the model molecule  $\text{CF}_3(\text{CF}_2)_6(\text{CH}_2)_3\text{Si}(\text{OH})_3$ . (Right) Top view and side view of a single  $\text{CF}_3(\text{CF}_2)_6(\text{CH}_2)_3\text{Si}(\text{OH})_3$  molecule.

In a second stage, the process of condensation between a hydrolyzed FAS molecule  $\text{CF}_3(\text{CF}_2)_2(\text{CH}_2)_2\text{Si}(\text{OH})_3$  and hydroxyl groups on the alumina surface was analyzed. Such shorter FAS molecule was chosen to reduce computational costs, but the behavior of the FAS molecule in the hybrid coating should be the same. Notably, the hydrolyzed FAS was chosen as the reactive molecule, because previous calculations showed that the reaction between the surface and the non-hydrolyzed molecule  $\text{CF}_3(\text{CF}_2)_2(\text{CH}_2)_2\text{Si}(\text{OH})_3$  would be energetically unfavored ( $\Delta G = 9.6$  kcal/mol). Furthermore, the chosen substrate was a partially hydroxylated form of alumina, e.g. boehmite, in which the stable (010) plane is exposed. This structural and energetic analysis is represented in Figure 41. In principle, all three Si-OH groups can react with hydroxyl groups at the surface. The first condensation reaction (structure 1 in Figure 41) is almost isoergonic ( $\Delta G = 0.4$  kcal/mol), thus the silane is easily grafted to the surface. A second condensation reaction between the Si-OH terminal group and a surface hydroxyl group can occur (structure 2). Notwithstanding the favorable entropic contribution due to the release of a water molecule, this reaction is unlikely to occur: the large positive enthalpy makes it a highly endoergonic reaction ( $\Delta G = 22.2$  kcal/mol). Perhaps, this effect is due to a mismatch in bond length between Si-OH (2.7 Å) and Al-OH (2.9 Å) [157]. Rather than condensation with a surface-bond OH group, condensation between a second FAS molecule and a surface hydroxyl group followed by condensation between the two vicinal FAS molecules is favored (structure 3,  $\Delta G = -14$  kcal/mol). In this case, the double condensation process is entropy-driven due to the formation of two water molecules.

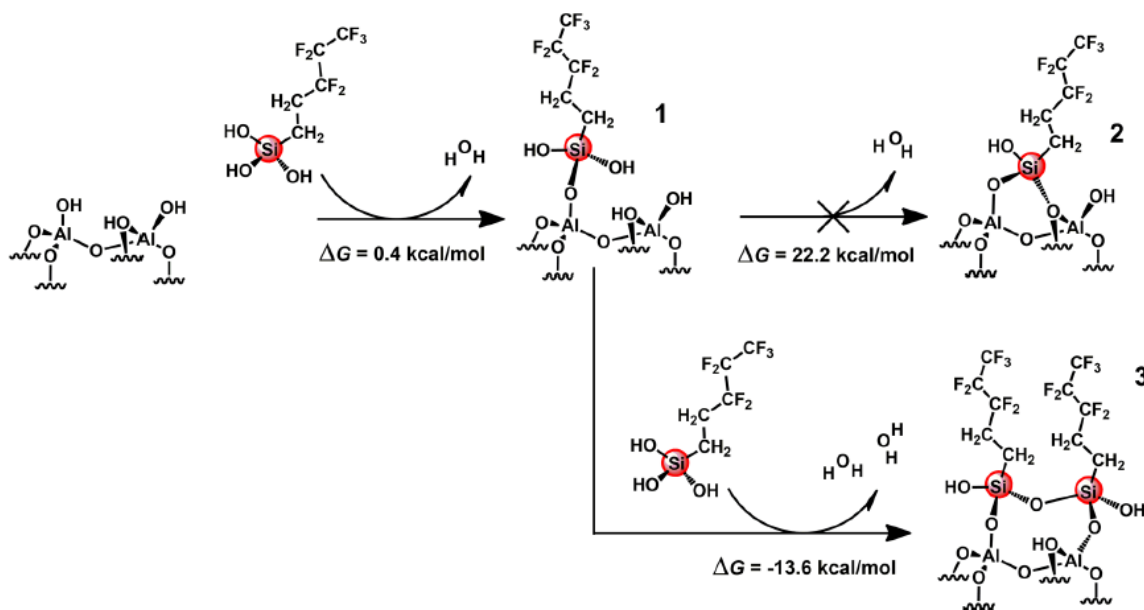


Figure 41. Schematic representation of the possible condensation mechanisms of FAS molecules on an alumina surface.

This result led us to expect that the formation of infinite rows of FAS chains grafted on the surface will be a spontaneous process. Figure 42 shows the calculated surface arrangement of the FAS chains. Consecutive molecules adopt a zigzag configuration along each row, producing a double fluoroalkyl row (Figure 42, left side). This phenomenon produces a very dense packing of alkyl chains on the surface, resulting in a monolayer that covers the entire surface (Figure 42, right side). Given the close distance between fluoroalkyl chains, the contribution of dispersion forces must be relevant. It was calculated that the formation of a monolayer of condensed FAS rows is associated with  $\Delta G = -33$  kcal/mol, which means this process is strongly favored. Furthermore, calculations confirm that the overall thickness of a FAS monolayer on the alumina surface is 1.5 nm. Formation of a multilayer is unlikely, as all the reactive hydroxyls bound to Si undergo condensation, while the exposed  $\text{CF}_3$  terminal groups are extremely inert.

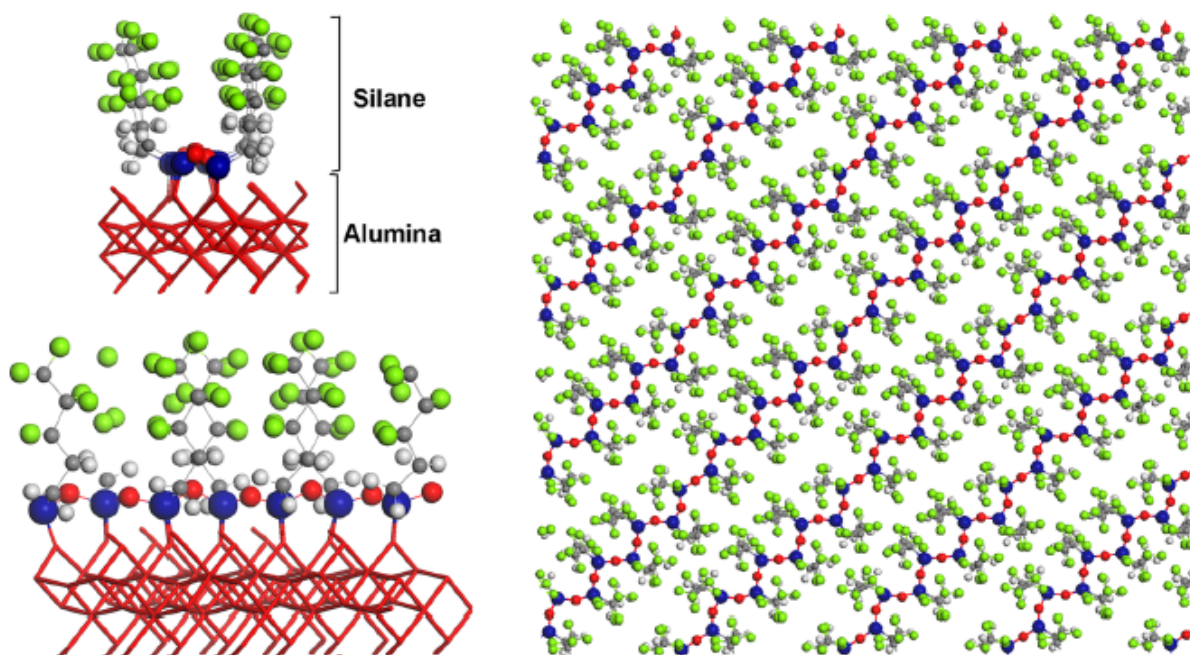


Figure 42. (Left) Side views of a single FAS row grafted on the alumina surface. (Right) Top wide view of the FAS rows, forming a monolayer on the alumina surface (whose structure is omitted for clarity). In both images, C in dark gray, Si in blue, O in red, F in green.

Once a monolayer is formed, only 40% of the surface hydroxyl surface groups react with FAS, due to steric hindrance of the FAS molecules [158]. At the other end of FAS molecules, the terminal  $-\text{CF}_3$  groups are oriented vertically with respect to the surface due to steric interactions between FAS molecules. This result is consistent with past XANES characterization of FAS monolayers grafted to various substrates [159]. The grafted FAS chains are well-ordered and in contact with each other (Figure 42, right), producing a well-packed monolayer on the surface, which can explain the excellent superhydrophobic properties of the FAS-treated surfaces.

Further calculations have been performed to assess the effects of the alkyl portion of the overall FAS chain on the monolayer stability. Indeed, using a totally perfluorinated silane model molecule  $\text{CF}_3(\text{CF}_2)_4\text{Si}(\text{OH})_3$ , monolayer formation is strongly disfavored ( $\Delta G = 52$  kcal/mol) because of the larger steric encumbrance of  $-\text{CF}_2-$  groups compared to  $-\text{CH}_2-$  groups. This proves the previously suggested role of the purely alkyl part of the FAS carbon chain in favoring monolayer formation.

## Conclusions

In summary, the combination of XPS analyses and DFT modeling, together with the previously discussed FESEM images and wetting characterization, defines a much clearer picture of the hybrid coating. FAS molecules had formula  $\text{CF}_3(\text{CF}_2)_6(\text{CH}_2)_3\text{SiR}_3$ , with seven perfluorinated C atoms and three  $-\text{CH}_2-$  units to



allow for optimal packing on the surface. These molecules bond to hydroxyl groups on the alumina substrate by a single Si-O-Al bridge, followed by condensation with vicinal FAS molecules. The propagation of this reaction is thermodynamically favored and leads to a densely-packed monolayer of vertically aligned molecules, with the terminal  $-CF_3$  groups pointing upwards. This can be identified as the cause for the excellent durability displayed by the coating in aggressive chemical environments, as discussed previously.

## HYBRID COATING ON COPPER SURFACES: INFLUENCE OF PROCESS PARAMETERS

Copper is an extremely important material due to its properties: it is recyclable, has good electrical and thermal conductivities, malleability, etc. [160]. Therefore, copper is used in a wide range of applications, from energy conversion and heat exchange to electronic devices [161] [162] [163]. In many of these fields, copper is in contact with liquids, which often cause damage to the devices, e.g. corrosion [71]. Thus, control of copper wetting properties is a crucial topic that deserves deep investigations, aiming at an increase in efficiency and durability of copper-based devices. For example, few papers demonstrated that copper heat exchangers with enhanced water repellence show a significant increase in their efficiency [164] [165]. On superhydrophobic Cu, in fact, vapor condenses in form of droplets (dropwise condensation) instead of spreading on the surface (filmwise condensation). If condensed drops are also able to be removed efficiently, heat transfer between Cu surface and air is faster and more efficient. However, such functionalized copper surfaces are still far from application on industrial scale due to many issues, first of all their durability through time [166]. As a consequence, many efforts are being devoted to fabricate copper surfaces with controlled wetting properties, as confirmed by the increasing number of papers dealing with this topic. Most of these papers deal with organic, inorganic or hybrid coatings able to provide superhydrophobicity to copper surfaces. One of the most common approaches to superhydrophobic copper surfaces is the self-assembled monolayer (SAM) technique [167] [168]. However, the durability of SAMs is often poor. Inorganic and hybrid superhydrophobic coatings are valuable alternatives to SAMs, as thermal treatments are often utilized to provide extended stabilization in the coating (as discussed previously). Usually, the fabrication of inorganic or hybrid copper-based coatings on Cu is based on wet or dry treatments to build up microstructural features made of one or more copper oxides ( $CuO$ ,  $Cu_2O$ ) or hydroxide ( $Cu(OH)_2$ ), with addition of an outer low surface energy layer (mostly fluoroalkylsilane, silanes, long-chain organic acids, etc.) in case of hybrid coatings. The nature of the copper oxide formed on the surface is crucial to determine the nature of the coating. For example, Lee *et al.* [169] created a fully-inorganic superhydrophobic coating by treating copper foils first with an oxidation step, then in reducing atmosphere. They formed cuprous oxide ( $Cu_2O$ ) with a peculiar

morphology and superhydrophobic properties [170], reaching WCAs of about 160°. On the other hand, cupric oxide (CuO) is intrinsically hydrophilic nature, thus chemical modification with an organic compound (hybridization) is strictly necessary to reach superhydrophobicity [171]. The most common method for copper oxides growth is thermal oxidation, while the control of their morphology is achieved by setting temperature, oxygen content and treatment time [172]. In fact, Cu<sub>2</sub>O is observed at 150–200 °C, while CuO is favored above 200–250 °C, but they can coexist at intermediate temperatures. In place of thermal oxidation, a technique called Successive Ionic Layer Adsorption and Reaction (SILAR) can be used to form superhydrophobic copper surfaces [173] [174]. With this technique, Cu(OH)<sub>2</sub> nanoribbons are formed and then easily converted to CuO by isomorphic dehydration. The subsequent hybridization with a low energy compound allows for reaching superhydrophobicity. Whatever the method for oxide formation, many examples of superhydrophobic copper-based hybrid coatings have been reported. Zhang *et al.* [175] prepared CuO nanowires by thermal oxidation of thin porous copper foils, then grafted a fluoroalkylsilane layer to reach superhydrophobicity (WCA=162°). Nam and Ju [176] fabricated superhydrophobic Cu surfaces with WCA=170° by either treating thin copper foils in hot alkali solutions, or subjecting them to thermal oxidation process, followed by spin coating a 2 wt.% Teflon solution. Huang and Leu [177] prepared superhydrophobic Cu (WCA = 150°) by dipping metal foils in a 30 wt.% hydrogen peroxide solution, followed by rinsing in deionized water, drying, heating at 60 °C and spin-coating of Teflon. Zhang *et al.* [178] prepared Cu foils with WCA=161° by immersion in a hot basic solution (0.06M K<sub>2</sub>S<sub>2</sub>O<sub>8</sub>, 3.0 M NaOH) followed by subsequent dipping in a 5 wt.% lauric acid solution in ethanol. Generally, all these methods are more complex and time-consuming than direct wet or dry substrate oxidation and further they imply the use of materials other than copper [179] [180] [181].

Considering the state of the art, we wanted to apply the previously described hybrid coating also on copper surfaces. During the experimental activity, we discovered how crucial it is to finely tune many process parameters to obtain top level superhydrophobicity on copper. More precisely, we investigated the effect of thermal treatment temperature on copper surface, both in terms of morphology and chemical composition, as well as the consequences on coating structuring. Moreover, we tried to deposit the water-based and the alcohol-based sols on copper. We observed substantial differences in coating ability between the two suspensions, with obvious effects on the final wetting properties of coated copper surfaces. The first part of the work was published in 2015 [101], while we are currently working on a second paper dealing with dependence of wetting properties on sol used to fabricate the coating.

## Materials and methods

In our activity, we used the two previously described alumina nanoparticles suspension, one in isopropyl alcohol and one in water medium. Copper foils (Cu 99%, 100 x 50 x 1.5 mm) were used as substrates. First, we sandblasted these foils to obtain micro-scale roughness ( $R_a = 2.3 \mu\text{m}$ , as measured with ContourGT-K optical profilometer by Bruker) for better coating adhesion. Then, we performed two cleaning steps with ultrasounds, one in soapy water and one in ethanol, to decrease the surface from sandblasting residues. Surfaces were coated with either the alcohol-based sol (labeled as A) or the water-based one (B) according to the usual dip coating process (dipping and withdrawal speed 2 mm/s, permanence time 5 s). After drying for few hours in air, the samples were heat-treated at 200°C, 300°C or 400°C for 60 minutes. Immersion of coated samples in boiling water for 30 minutes was performed to create the desired flower-like boehmite nanostructure, then a second heat treatment for 10 minutes was performed maintaining the same temperature adopted in the first one. Finally, fluoroalkylsilane chains were grafted to the surfaces by dip coating them with Dynasylan SIVO Clear EC (Evonik) (dipping-withdrawal speed 2 mm/s, permanence time 2 min), followed by heat treatment at 150°C for 30 minutes. The samples were labeled according to the coating sol and treatment temperature, e.g. A200, A300 and A400 were coated with alcohol-based sol and heat treated at 200, 300 and 400°C, respectively, while B200, B300 and B400 were coated with water-based sol.

In order to achieve a deeper comprehension of copper behavior at different temperature, we also prepared bare copper surfaces with heat treatments at different temperatures and labeled them as U200, U300 and U400.

The as-produced samples were characterized in terms of wetting properties with an optical contact angle system OCA 15Plus (DataPhysics Instruments) equipped with a CCD camera. We measured water static contact angles (WCA) and contact angle hysteresis (CAH). Each measurement was repeated from 5 to 10 times to assess reproducibility.

Surface morphology was investigated with a field-emission scanning electron microscope (FESEM Gemini Columns SIGMA Zeiss), operated at 1.5 keV with a working distance of 4 mm. Information about surface composition was obtained via X-ray Photoelectron Spectroscopy (XPS) performed by Prof. Robertino Zanoni's group at University La Sapienza in Rome with a modified Omicron NanoTechnology MXPS. This system was equipped with a monochromatic X-ray source (Omicron XM-1000), a dual X-ray anode (Omicron DAR 400) and an Omicron EA-127-7 energy analyzer. The primary X-ray beam was constituted of either Al K $\alpha$  photons ( $h\nu = 1486.7 \text{ eV}$ ) or Mg K $\alpha$  photons ( $h\nu = 1253.6 \text{ eV}$ ), both generated operating the anode at 14–15 kV, 10–20 mA. All the photoionization regions were acquired using an analyzer pass energy of 20 eV, except for the survey scan, which was taken at 50 eV pass energy. A take-

off angle of 11° with respect to the sample surface normal was adopted. The measurements were performed at room temperature, and the base pressure in the analyzer chamber was about  $2 \times 10^{-9}$  mbar during the spectra detection. The binding energy (BE) of Al 2p component at 73.7 eV was used as an internal standard reference for the BE scale (accuracy of  $\pm 0.2$  eV). All measurements were conducted in the least possible time after sample preparation. A dependence of the F/C ratio on the exposure time under X-rays was noticed, with a relevant change in the C 1s line shape with time. In order to acquire a less perturbed C 1s spectrum, this region was acquired within the shortest possible time from initial irradiation by X-rays ( $\sim 5$  min). The experimental spectra were theoretically reconstructed by fitting the peaks to symmetric Voigt functions, and the background to a Shirley or a linear function. XPS atomic ratios ( $\pm 10\%$  associated error) between relevant core lines were obtained from experimentally determined area ratios corrected for the corresponding Wagner sensitivity factors. The XPS analysis of samples containing Al and Cu is not straightforward, since Al 2s and Al 2p peaks respectively overlaps with those of Cu 3s and Cu 3p. Special care was taken in curve fitting of the complex envelope of the two above photoemission regions. Parallel to this, the intensity ratio  $(\text{Al } 2p + \text{Cu } 3p)/(\text{Al } 2s + \text{Cu } 3s)$  was measured, following the method reported in the literature, which showed an easy way of XPS quantitation of samples containing the two metals [182]. In addition to the above routes, a fast and independent comparative check for the relative abundance of Cu and Al was performed by collecting the X-ray induced Al Auger signal ( $\text{Al}_{\text{KLL}}$ ) and the Cu Auger signal ( $\text{Cu}_{\text{LMM}}$ ).

We also assessed mechanical stability of the coatings with a simple, home-made test procedure. We immersed A200, A300 and A400 samples in ethanol bath for 30 minutes and activated ultrasounds (25 kHz, 400 W). Then, we compared WCA and CAH values before and after the test. The same durability tests were also run on bare, sandblasted copper samples (U200, U300 and U400) to assess the adhesion of copper oxides on the surface.

Finally, we evaluated the durability of the coating derived from both sol A and sol B by immersing an A200 and a B200 sample in either an acidic ( $\text{CH}_3\text{COOH}$ , pH = 3, sample labelled as A3 and B3) or a basic solution ( $\text{NaOH}$ , pH = 13, labelled as A13 and B13) for 120 hours. After such period, we withdrew the surfaces from the solution, rinsed them with DI water and characterized them in terms of wetting properties, morphology (FESEM) and surface chemistry (XPS).

## Results and discussion

The first set of results focused on the differences in wetting properties bestowed by the two sols on sandblasted copper surfaces after heat treatments at different T and chemical modification with FAS. WCA and CAH values for such samples are reported in Table 15.

Sample	WCA (°)	St.dev	CAH (°)	St.dev
A200	179.8	0.1	3.4	3.0
A300	169.3	10.7	4.0	3.8
A400	174.0	6.0	10.3	4.3
B200	136.6	3.3	16.1	5.5
B300	138.0	3.1	12.6	5.5
B400	135.8	4.6	14.2	4.9

Table 15. Water Contact Angle (WCA) and Contact Angle Hysteresis (CAH) average values and standard deviations for sandblasted copper surfaces with hybrid coating derived from alcohol-based (A) or water-based (B) sol and heat-treated at 200, 300 or 400°C.

From these data, the first remarkable result was that copper surfaces bearing a hybrid coating formed from alcohol-based sol A were much more water repellent than those with a coating from water-based suspension B. WCA values were definitely higher for A samples ( $WCA \geq 170^\circ$ ) than for B surfaces ( $WCA < 140^\circ$ ) and also CAH was totally different (less than  $5^\circ$  for A200 and A300, more than  $12^\circ$  for all B samples). Among A samples, A400 had a higher CAH. This is a first hint at the dependence of final wetting properties on the dispersing medium of coating suspensions.

Moving from these results, we followed two different paths: first, we focused on the effects of difference treatment temperature on surface morphology and wetting properties. Second, we studied the different coating potential of the two alumina suspensions.

Concerning the effects of treatment temperatures, we deeply investigated the morphology of A samples with FESEM. Even a simple visual inspection suggested that there were radical differences among samples treated at different T, as shown in Figure 43. The resemblance of the foils became darker as T increased, which suggests a different oxidation level through the samples.

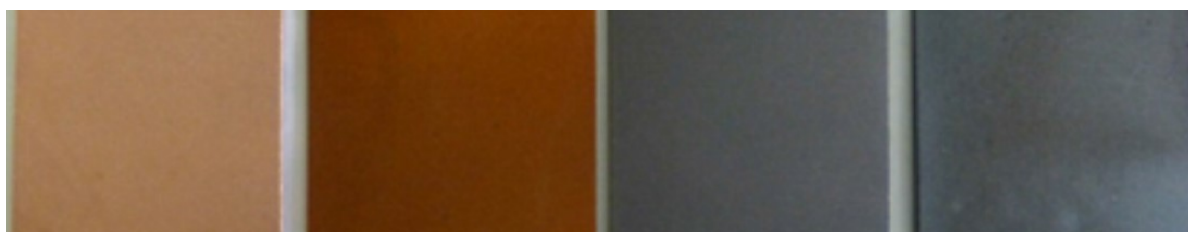


Figure 43. Sandblasted copper foils after treatment at different T. From left to right: untreated, 200°C, 300°C and 400°C.

From FE-SE investigations, A200 and A300 samples showed analogous morphology (Figure 44). They showed a homogeneous, flower-like boehmite coating all over the surface. Few micron-sized structures

were also visible and they were attributed to sandblasting. Such similar surface structures were reflected into very similar WCA and CAH values for these surfaces (see Table 15).

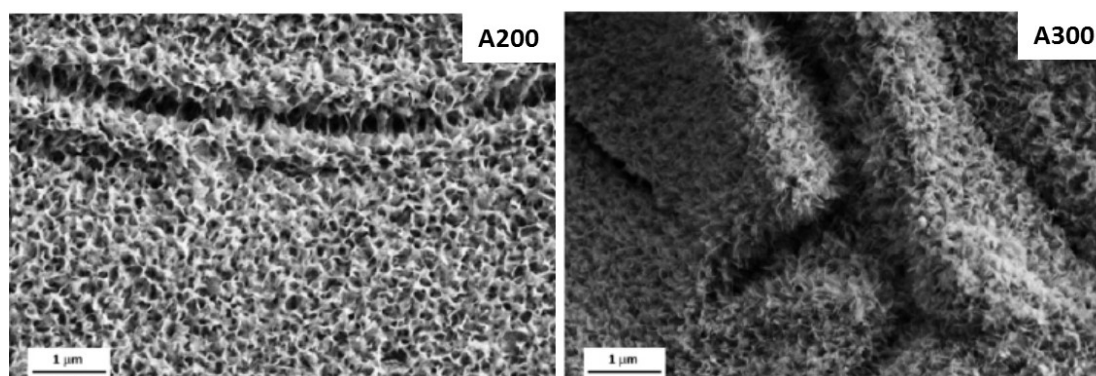


Figure 44. FESEM images from coated samples A200 (left) and A300 (right). Scale bars are reported.

On the other hand, A400 samples showed substantial differences in morphology (Figure 45). While in some areas a clear boehmite flower-like nanostructure was observed (Figure 45a), in other points it was either scarce or absent and replaced by microwires pointing in perpendicular direction with respect to the surface (Figure 45b). At higher magnification, we could notice that smaller sharp needles (e.g. with thickness of few nanometers thick and length ranging from hundreds of nanometers to few micrometers) with a triangular shape and emerging from underlying bumps were also present (Figure 45c). Presumably, these nanoneedles represented early stages in the formation of larger, aggregated microwires visible at lower magnification. The presence of such relevant deviations from the expected flower-like morphology could be responsible for the increase in CAH for A400 samples compared to other coated surfaces. It is well known that the presence of inhomogeneous surface features is one of the main causes for contact angle hysteresis [183].

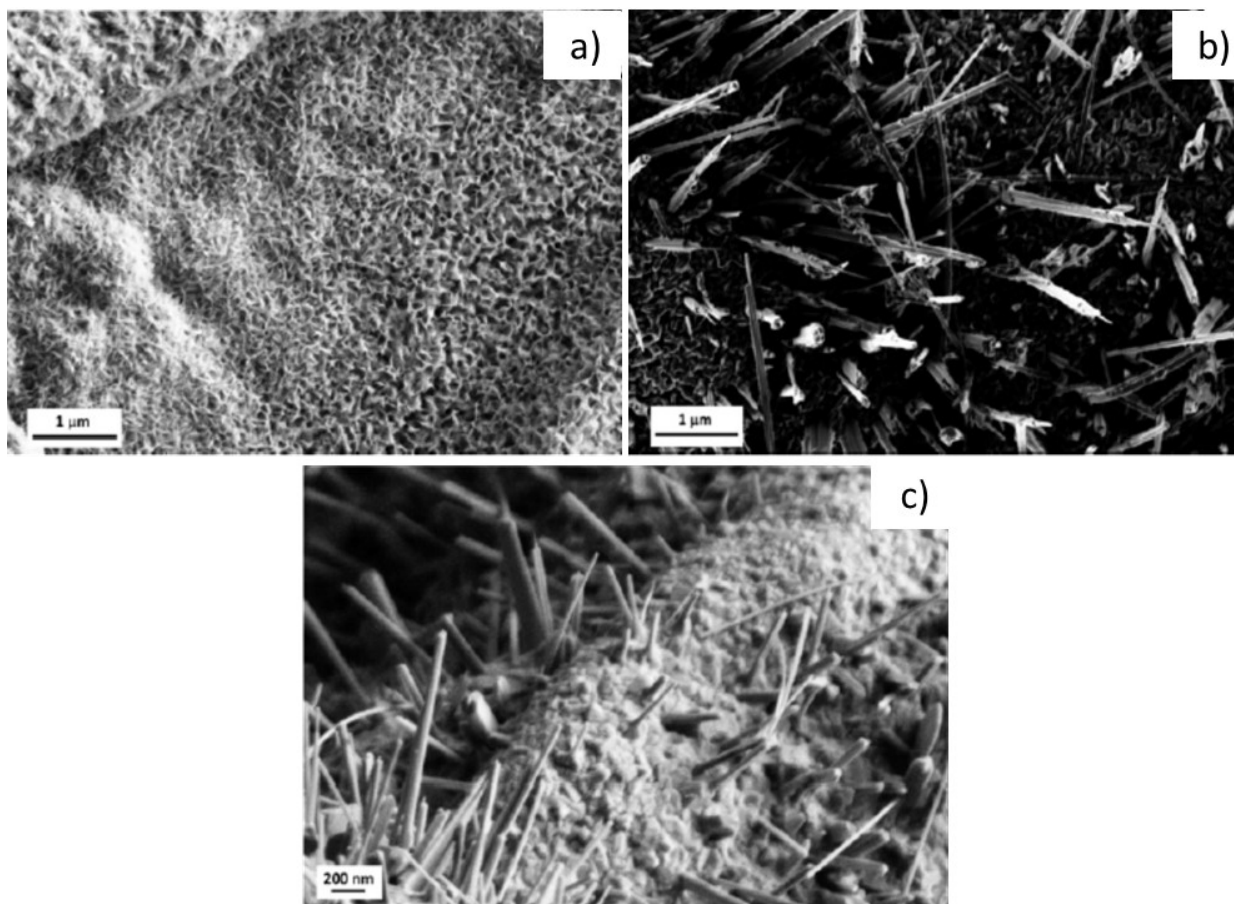


Figure 45. FESEM images from coated sample A400: a) area with flower-like nanostructure; b) area with microwires; c) higher magnification of area B) showing nanoneedles growing on top of micron-sized bumps. Scale bars are reported.

This peculiar morphology is typical of Cu(II) phases like CuO [184] or Cu(OH)<sub>2</sub>. Nanoneedles are an anisotropic feature that is formed as an attempt to minimize the stress generated by volume and structural changes related to thermal oxidation of copper substrate [185] [186]. From the literature, it is known that CuO and Cu(OH)<sub>2</sub> phase cannot be distinguished as the latter converts into the sooner through a topotactic transformation when heated in oxidizing atmosphere, e.g. air [187]. When copper is treated at  $T > 300^{\circ}\text{C}$ , surface hydration and related hydroxide formation are strongly hindered. However, nanoneedles and microwires can promptly rehydrate through time if the surface is stored in ambient conditions, reforming Cu(OH)<sub>2</sub> without changes in morphology.

A deeper comprehension of structural changes in copper surfaces during thermal treatments at different temperatures could be achieved through FESEM observations on bare, sandblasted copper surfaces after thermal treatments. Obtained images are reported in Figure 46.

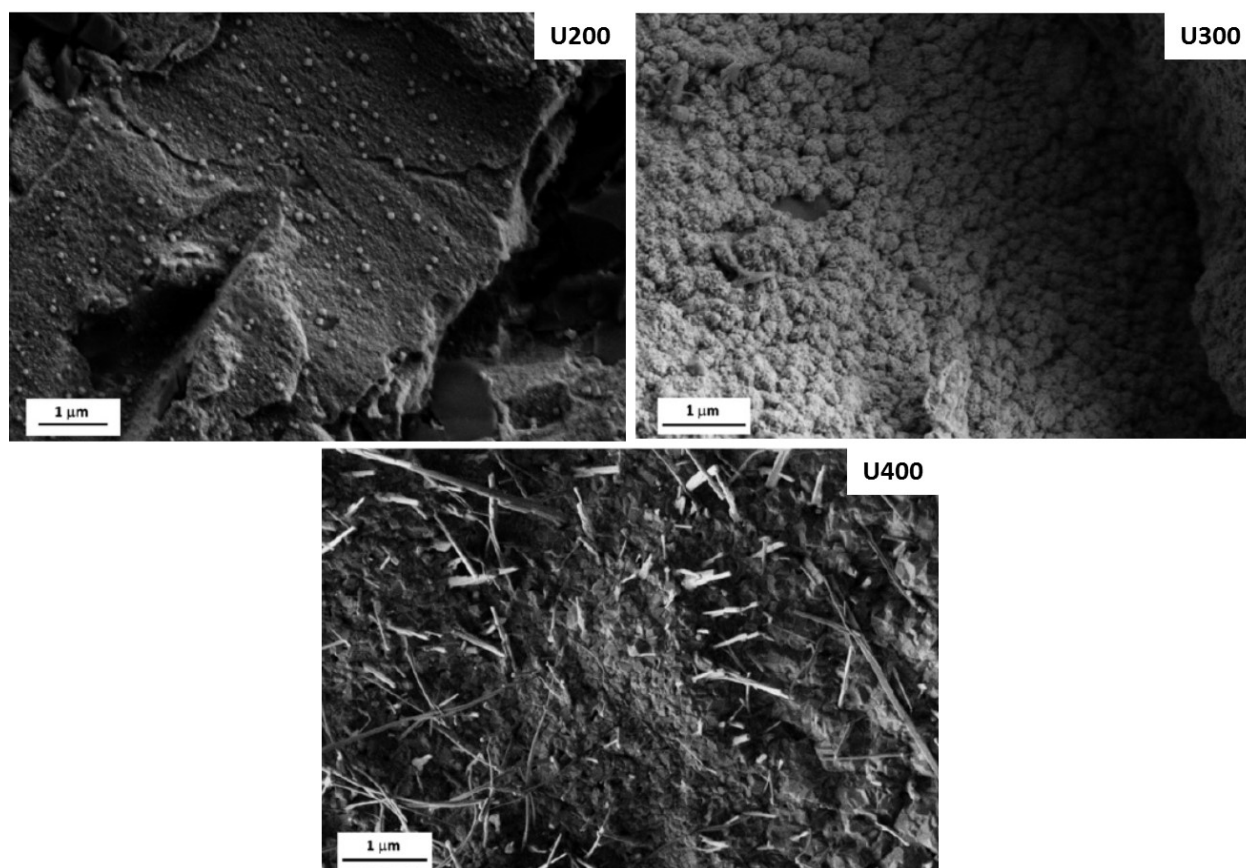


Figure 46. FESEM images from bare sandblasted copper samples U200 (top left), U300 (top right) and U400 (bottom). Scale bars are reported.

U200 sample was very similar to untreated sandblasted copper (not reported) in terms of morphology, with the addition of nanocubes. It is known from the literature that such peculiar shape is typical of  $\text{Cu}_2\text{O}$  [188]. On the other hand, U300 was radically different, since bumps with sizes of few hundreds of nanometers uniformly covered copper surface, which assumed a pitted aspect. This tendency was even more pronounced on U400 surface, on which the same microwires observed in Figure 45b and attributed to Cu(II) phases are clearly visible.

Based on these observations, we could hypothesize a possible sequence for the growth of different copper oxides with peculiar morphologies (Figure 47): at  $T \leq 200^\circ\text{C}$ , superficial copper converts to  $\text{Cu}_2\text{O}$  forming nanocubes; increasing treatment temperature to  $300^\circ\text{C}$  and prolonging treatment time, growth of cubes is faster, thus they coarsen and expand until they cover the entire surface. Furthermore, Cu(I) is further oxidized to Cu(II) and forms sub-micron bumps with the aspect of a desert rose. The edges of these features are probably metastable, thus nanoneedles start to grow from there when temperature is further increased to  $400^\circ\text{C}$ . As already mentioned, such rod-like shape is due to structural and thermodynamic strains in the material when oxidation occurs. It must be remarked that this sequence requires oxidative atmosphere, thus it could not be applicable if such condition was not met. Therefore,



we can claim that surface morphology of copper is strongly dependent on thermal treatment conditions and critically affects the surface structure of the alumina coating.

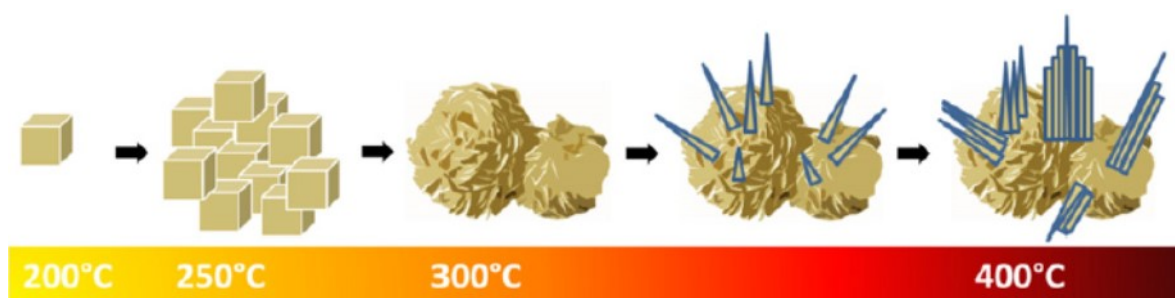
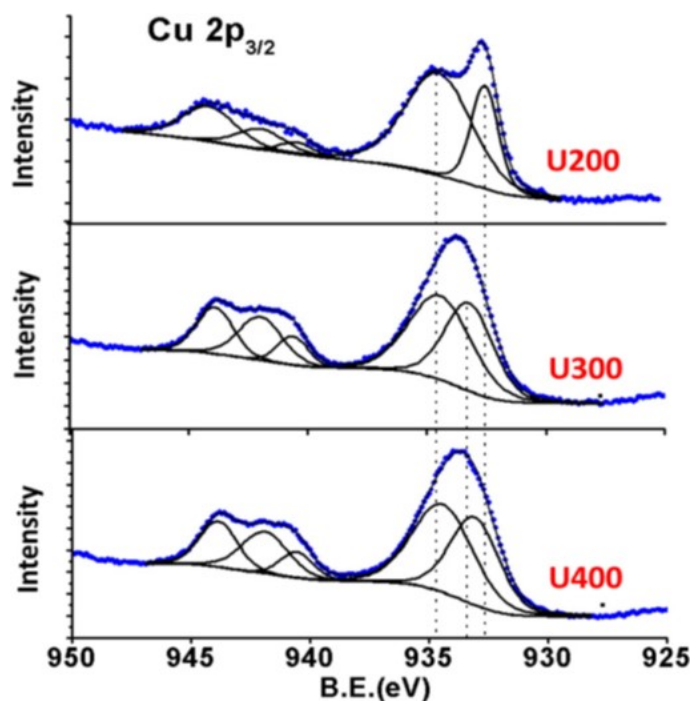


Figure 47. Suggested sequence for the build-up of copper oxide nanostructures with increasing temperature.

XPS of the uncoated and heat-treated samples confirmed what hypothesized so far. Cu  $2p_{3/2}$  regions of the XPS spectra are reported in Figure 48. In U200 spectrum, the peak at lower binding energy (BE) had two components: one centered at 932.3 eV and attributed to Cu(I) (e.g.  $\text{Cu}_2\text{O}$ ), and the other at 934.3 eV related to Cu(II) in form of  $\text{Cu}(\text{OH})_2$ . Moreover, other peaks in the 940-945 eV range were generated by empty valence bands, typical of Cu(II) species. On the other hand, U300 sample displayed the same  $\text{Cu}(\text{OH})_2$  peak at 934.3 eV, while the Cu(I) disappeared and was replaced by a peak at 933.2 eV, which was related to CuO. Remarkably, U400 spectrum was almost identical to that obtained for U300, suggesting that copper oxidation was already complete at 300°C, with CuO as the predominant phase. In the attached table, the elementary composition of uncoated samples is reported. Carbon content diminished as treatment temperature increased, obviously due to desorption of carbonaceous species from the surface. Useful information were derived from O/Cu atomic ratio: it was equal to 2 for U200 sample, hinting at a dominant  $\text{Cu}(\text{OH})_2$  phase. Meanwhile, it was close to 1 for U300 and U400, which suggests that CuO is the main component of sample surface.



Sample	C	Cu	O	F
U200	44.4	17.7	35.0	3.0
U300	28.7	33.3	36.7	1.3
U400	20.9	36.4	39.1	3.6

Figure 48. Cu 2p<sub>3/2</sub> region of the XPS spectra of (top) U200, (middle) U300 and (bottom) U400 samples, respectively. The table reports the atomic elementary composition expressed as percentage for the same samples, as obtained from XPS analyses.

Another crucial aspect for superhydrophobic coatings is their adhesion to the substrate. Therefore, we assessed this aspect by immersion of coated samples heat-treated at different temperatures (namely A200, A300 and A400) in ethanol and treatment with ultrasounds for 30 min. After rinsing with DI water and drying in air, we characterized the samples in terms of wetting properties. Figure 49a shows the vessels containing the samples after the test. Ethanol from tests on A200 samples was still transparent, meaning that no visible trace of material was detached from the samples. On the other hand, A300 and A400 produced a significant loss of surface materials, which precipitated to the bottom of the beakers in form of a black residue. Such black powder was also released from A400 by simply touching it with a finger. Most of this material came from the smooth side of the copper foils, on which copper substrate is clearly exposed (see Figure 49b). On the other hand, the sandblasted faces of A300 and A400 foils seemed less damaged to the naked eye. This confirms the positive effect of sandblasting on hybrid coating adhesion to copper surfaces. The poor mechanical stability of the coating on A300 and A400 was due to the presence of CuO, whose cell parameters are different from those of copper [175], thus causing a mismatch between their structures and inherent brittleness. On the contrary, A200 surface looked completely unspoiled after the test, suggesting a good mechanical resistance of the coating at testing conditions.

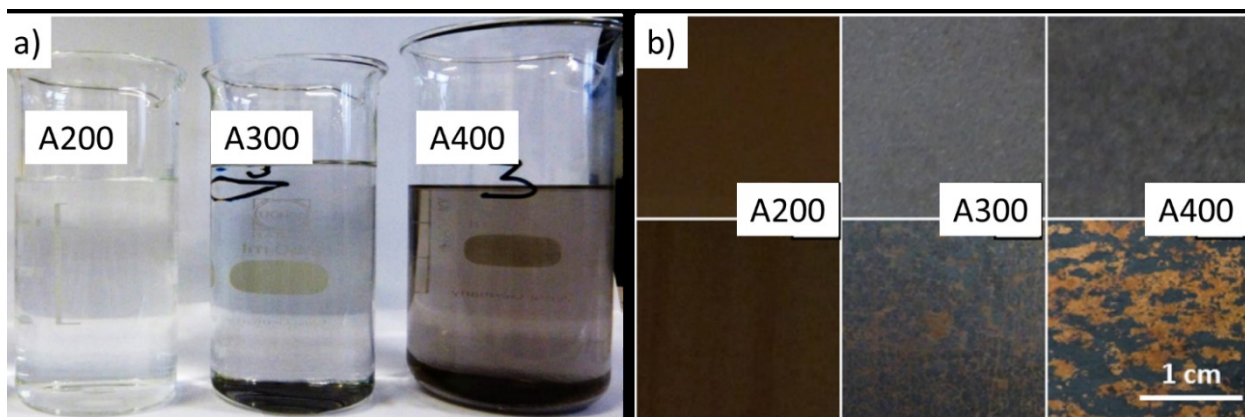


Figure 49. Durability tests by immersion in ethanol bath and sonication. a) vessels containing samples (left) A200, (center) A300 and (right) A400 after the test. b) Images of (top row) sandblasted side and (bottom row) smooth side of (left) A200, (center) A300 and (right) A400 samples after the test.

Figure 50 shows the trends of WCA and CAH for tested samples. Significant reduction of WCA occurred only for A400 samples, falling from values over  $170^\circ$  to about  $150^\circ$ . Meanwhile, CAH increased slightly for A300 and significantly for A400. On the latter surface, water drops adhered tightly and could not be removed by simply tilting the surface. On the other hand, A200 did not lose its extreme water repellence after the tests, showing unchanged WCA and CAH and unaltered rolling of water drops on its surface.

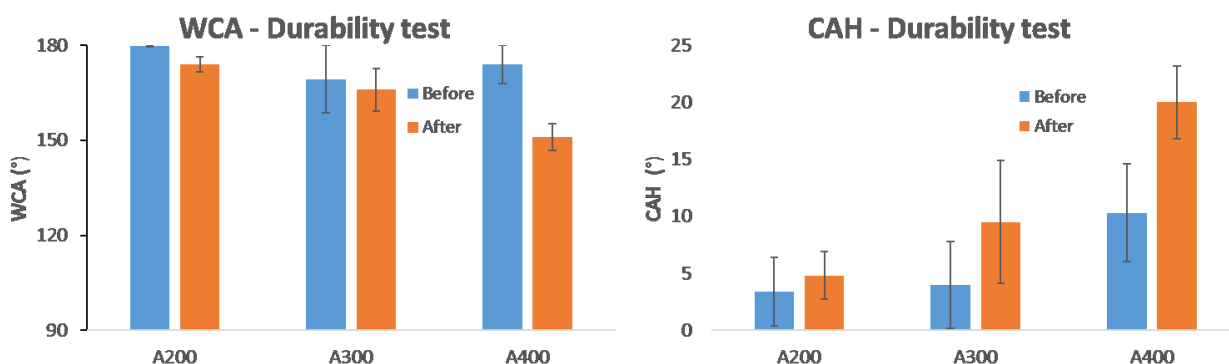


Figure 50. (Left) Water contact angles (WCA) and (right) contact angle hysteresis (CAH) for A200, A300 and A400 samples before (blue) and after (orange) durability test. Standard deviations are reported as error bars.

In the second part of the paper, we went deeper into the different behavior of hybrid coatings obtained from the two alumina suspensions debated so far, namely the isopropyl alcohol-based sol A and the water-based one B. We deposited either one of the two sols on sandblasted copper surfaces with the previously discussed method and investigated wetting properties, morphology and chemistry of the final hybrid coatings. We adopted  $T = 200^\circ\text{C}$  as the chosen temperature for thermal treatments to be

performed on all samples, thus samples were labelled as A200 and B200. As a reference, we also heat-treated a bare sandblasted copper surface, then modified its chemistry by grafting SIVO to the surface. This sample was identical to the aforementioned U200 and served to separate the effects of the coating from those of the underlying copper substrate. U200 had  $WCA = 141.1^\circ \pm 5.2^\circ$  and  $CAH = 18.3^\circ \pm 3.6^\circ$ . These values were very close to those reported in Table 15 for B200 ( $WCA = 136.6^\circ \pm 3.3^\circ$  and  $CAH = 16.1^\circ \pm 5.5^\circ$ ), while A200 was perfectly superhydrophobic ( $WCA = 179.8^\circ \pm 0.1^\circ$  and  $CAH = 3.4^\circ \pm 3.0^\circ$ ).

We observed A200 and B200 surfaces with FESEM to better understand the reason for such different behavior. Figure 51 shows the surface morphology of A200. At low magnifications (Figure 51a), relevant cracks appeared in the coating, forming some “islands” with thicker edges. Cracks were probably due to thermal stresses caused by different thermal expansion coefficients for the alumina coating and copper substrate [117]. However, at higher magnifications (Figure 51b) it is clear that flower-like boehmite was formed also within cracks, therefore the nanostructure is continuous throughout the surface. We hypothesized that the alumina coating was partially dissolved in water during the boiling treatment and was re-deposited as flower-like boehmite even on cracked areas, allowing for better homogeneity [189] [190]. In the future, cracks can be avoided by adopting lower withdrawing speed while dip coating or adopting lower treatment temperatures.

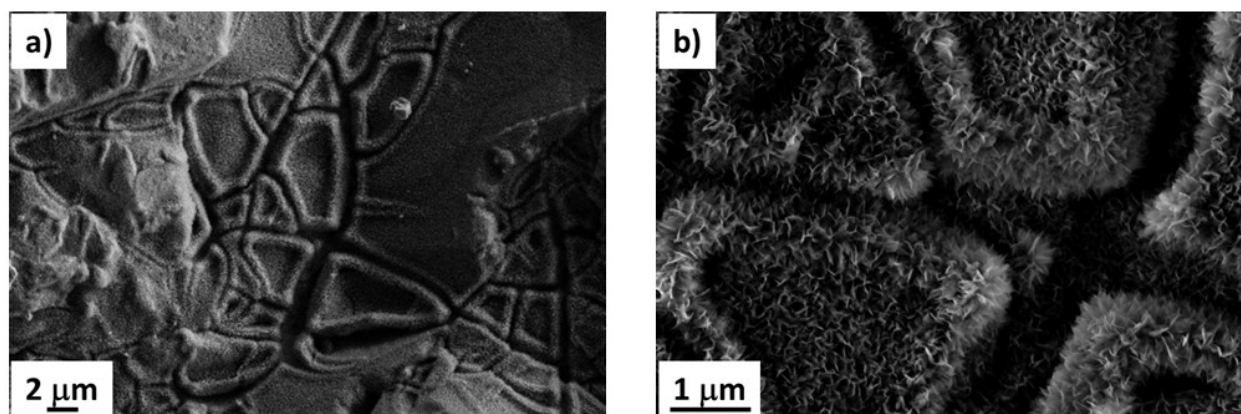


Figure 51. FESEM images from coated sample A200 at a) 10000 X and b) 50000 X magnifications. Scale bars are reported.

Figure J shows the morphology of sample B200. Flower-like morphology was observed, however lamellas looked smaller and less dense compared to those on A200 surface (Figure 52a). Furthermore, some areas were covered by a smooth coating, attributable to unstructured alumina moieties (Figure 52b).

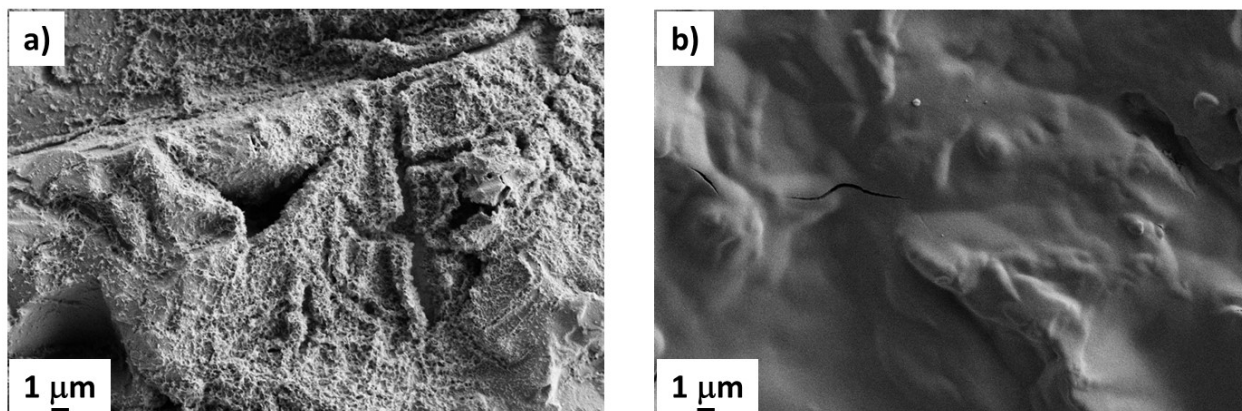


Figure 52. FESEM images from coated sample B200: a) flower-like boehmite coating; b) non-structured alumina coating. Scale bars are reported.

These results confirmed that wetting properties are strictly linked to surface morphologies of the coated and uncoated samples. As previously demonstrated, the flower-like nanostructure proved to be efficient in establishing a Cassie-Baxter wetting state, thus achieving superhydrophobicity. This ubiquitous presence of nanostructured alumina was the cause of the water repellence observed on sample A200. On the other hand, surface morphology of B200 was quite irregular, thus the Cassie-Baxter wetting state could not be achieved and the surface was not superhydrophobic. Water could wet and adhere to unstructured areas, causing lower WCA and higher CAH compared to A200.

XPS analysis was applied to the as produced A200, B200 and U200 samples after FAS grafting. During XPS analysis, the photoemission regions corresponding to Cu, Al, C, O, F and Si were recorded. XPS quantitative analysis is reported in Table 16.

Sample	Al/Cu	O/Cu	C/Cu	F/Cu	Si/Cu
A200	9.3	54.5	102.2	49.7	1.9
B200	5.3	38.4	76.3	69.9	4.6
U200	/	5.7	11.0	20.4	1.0

Table 16. Atomic ratios for the investigated samples (A200, B200 and U200) after FAS deposition, as calculated from XPS spectra. Relative error is  $\pm 10\%$ .

XPS quantitative analysis of the alumina coverage was complicated by the overlap of the Al 2p with Cu 3p regions (and of Al 2s with Cu 3s), but the signal doubling due to the non-conductive nature of alumina allowed to distinguish between the two signals and to calculate the amount of alumina deposited on the surface. Sample A200 was covered with a higher amount of alumina with respect to

B200, as inferred from the Al/Cu atomic ratios respectively equal to 9.3 and 5.0, respectively. A similar trend was observed for oxygen.

Detailed analysis of Cu 2p and O 1s XPS regions is diagnostic of the chemical changing due to the alumina coverage on the copper surface. For this reason, we compared these regions of the XPS spectra for U200, A200 and B200, as shown in Figure 54.

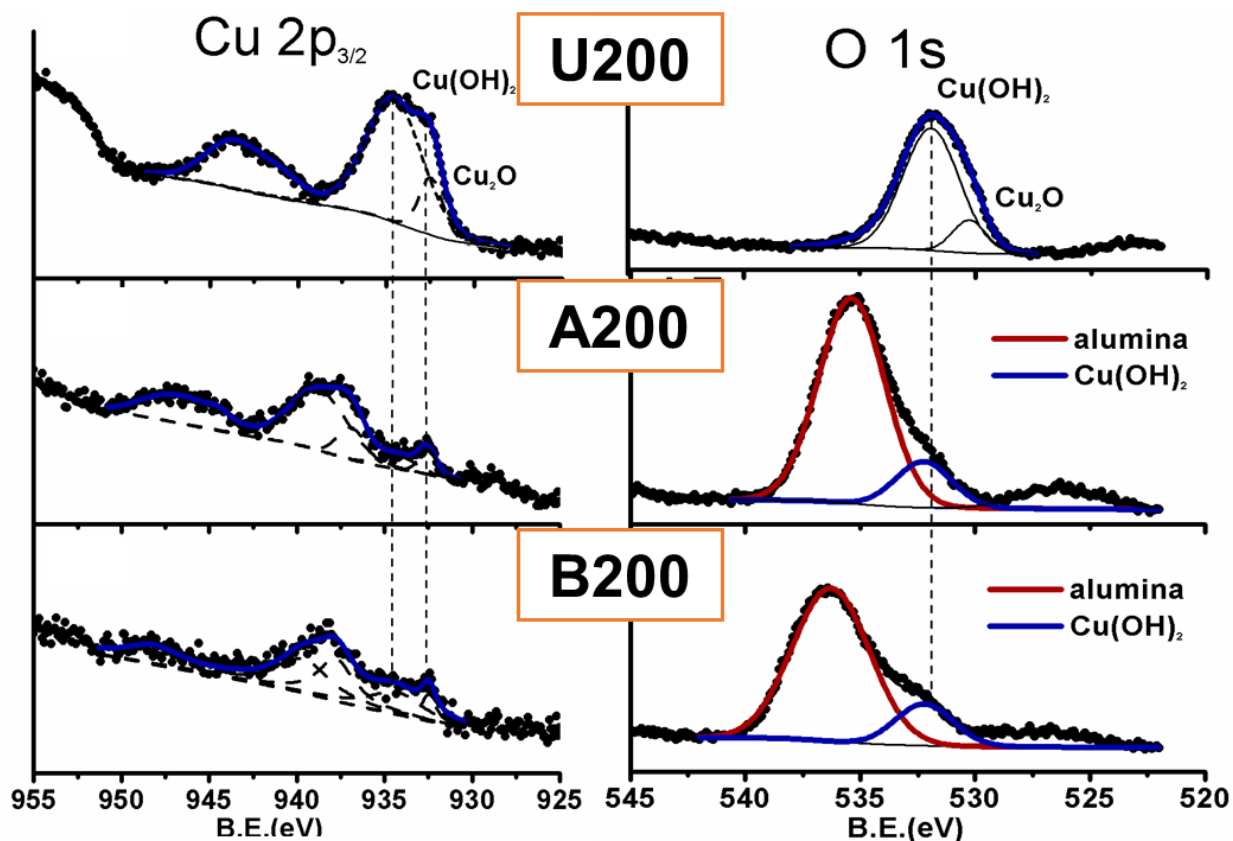


Figure 53. Cu  $2p_{3/2}$  (left) and O  $1s$  (right) regions of the XPS spectra acquired for the samples U200 (top), A200 (middle) and B200 (bottom). In Cu  $2p_{3/2}$  spectra, black dots are experimental points, blue solid line is the fitted spectrum and dashed lines are deconvoluted peaks. The vertical dashed line is a guide to the eye to compare the evolution of different peaks among the spectra. In O  $1s$  spectra, black dots are experimental points, blue solid line is deconvoluted peak related to Cu(OH)<sub>2</sub> and the red solid line is the deconvoluted peak related to alumina.

In the photoemission range of the Cu  $2p_{3/2}$  signal (left column, top), sample U200 showed two different contributions, respectively assigned to Cu(I) oxide (Cu<sub>2</sub>O, BE = 932.3 eV) and Cu(II) hydroxide (Cu(OH)<sub>2</sub>, BE = 934.4 eV). Cu(II) shake-up satellite signals (which are a consequence of electron configuration interaction and appear when electron holes are present in the Cu valence band), visible at 938-947 eV, confirmed the presence of Cu(II) species. The presence of Cu<sub>2</sub>O was confirmed by the corresponding O  $1s$  signal (right column, top), which presented a broad peak encompassing the characteristic signal of a Cu<sub>2</sub>O phase at low binding energies (530.3 eV) plus a main contribution from Cu(II) hydroxide (531.9 eV).

In summary, U200 surface was made of both partially and fully oxidized Cu, as expected because of the relatively low temperature of the thermal treatment (200°C).

Samples A200 and B200 showed a more complicated Cu 2p<sub>3/2</sub> region (Figure 54, left column, middle and bottom). In addition to the Cu(I) and Cu(II) components previously observed for U200, a broad band was also evident, centered at 938.5 eV for A200 and at 939.5 eV for B200, respectively. This signal was assigned to Cu(II) hydroxide and Cu<sub>2</sub>O species coming from sample areas which experience a positive potential shift. Such phenomenon has been widely reported in photoemission from non-conductive samples. The fact that XPS signal related to Cu was still detected even in the presence of alumina coating leads us to think that there is an intimate mixing of the aforementioned Cu species with non-conducting alumina deposits, as sketched in Figure 55. This scenario would lead to the doubling of the Cu 2p<sub>3/2</sub> peaks components. Furthermore, part of this signal could be possibly generated at the cracks. There, the nanostructured alumina coating is supposed to be thinner, thus Cu substrate should be able to generate a detectable XPS signal.

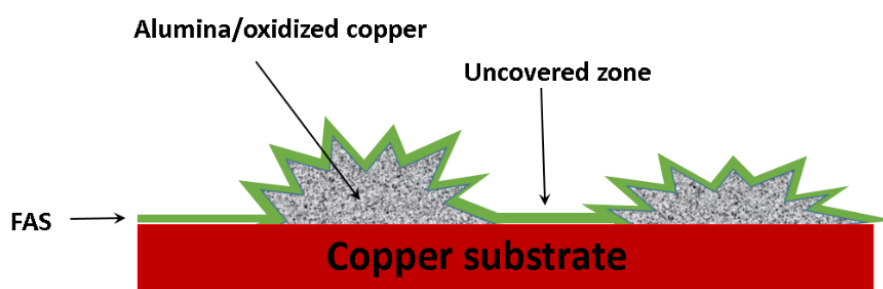


Figure 54. Sketch of the coated AF and BF surfaces, representing discontinuity of alumina coating on copper surface. FAS moieties bind on both coated and cracked areas.

The analysis of the O 1s region for samples A200 and B200 (Figure 54, right column, middle and bottom) confirmed this model. In fact, the peak component centered at 535.5 eV for sample A200 and 536.5 eV for sample B200 could be assigned to species lying on the surface area covered by the alumina, while a second component, centered at 531.3 eV, was assigned to the Cu(II) hydroxide exposed on the uncovered or cracked zones. It is worthy of note that the position of the Cu 2p signal coming from Cu(OH)<sub>2</sub> associated to the alumina covered zones changed on passing from sample A200 to B200, which could be the case when non-conducting effects from the two distinct alumina deposits are operating. In particular, sample B200 showed a larger insulating character compared to A200, e.g. larger BE. The same behavior was observed in the O 1s peaks. By contrast, the peak components associated to the area not covered by alumina (and, therefore, conducting) always fell at the same positions for all investigated samples.

Durability tests by immersion in chemically aggressive solutions provided interesting results. We characterized all tested samples in terms of wetting properties and results are shown in Figure 56. Both surfaces A3 and B3 (yellow columns) did not show any significant change in both WCA and CAH after immersion in acidic solution with respect to the as-prepared coated reference (blue columns). Nonetheless, sample A13 (grey columns) displayed a remarkable loss of superhydrophobicity after immersion in a basic solution for 120 hours. On this surface, WCA drops to 125° and CAH raised to 19°. Such change in the wetting properties could be noticed also on macroscopic scale, as drops adhered to the surface even when it was turned upside down. It must be highlighted that previously reported ageing tests in ammonia solution (pH = 10) gave different results. In that case, after 60 days of immersion WCA and CAH changed only slightly and the surface remained superhydrophobic. Therefore, it seems that harsher conditions (e.g. higher pH) triggered a much faster degradation and damaging of the hybrid coating.

On the other hand, sample B13 did not show any change in its wetting properties after the ageing test, probably because they were quite similar to those of the uncoated copper substrate. Due to the insufficient hydrophobic properties achieved with the water-based coating, we focused only on the isopropanol-based route for the XPS analyses shown below.

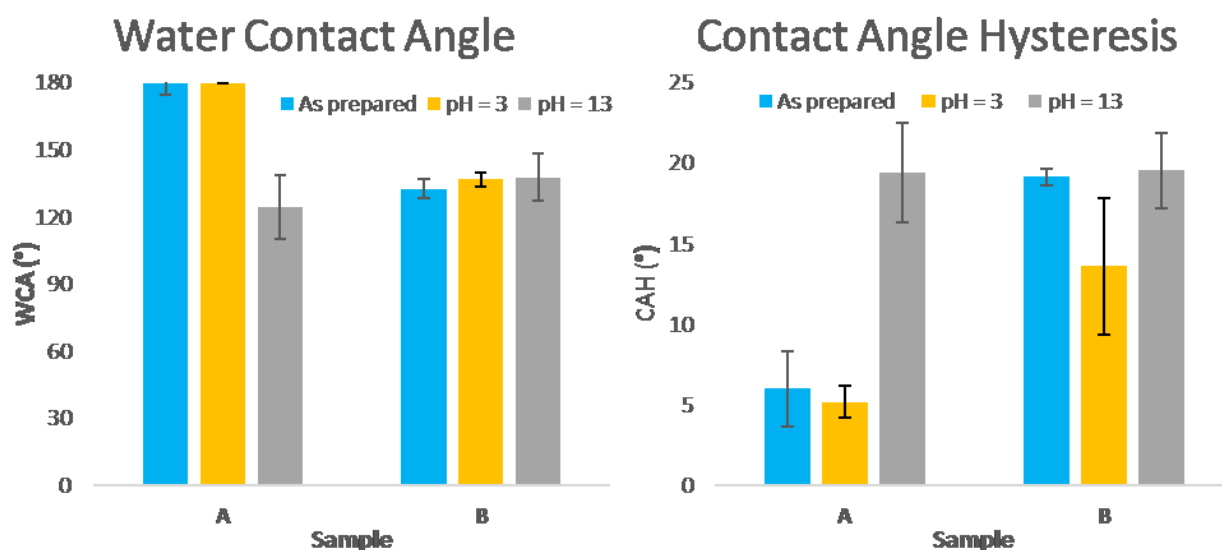


Figure 55. Water Contact Angle and Contact Angle Hysteresis values for as-prepared coated copper surfaces (blue columns) and after immersion for 120 h in either acidic (pH = 3, orange) or basic solution (pH = 13, green). Standard deviations are reported as error bars.



The same XPS analysis of the Cu 2p<sub>3/2</sub> region conducted on sample A200 was repeated on aged samples A3 and A13. Such spectra for as-prepared and tested surfaces are reported in Figure 57, together with the calculated atomic ratios.

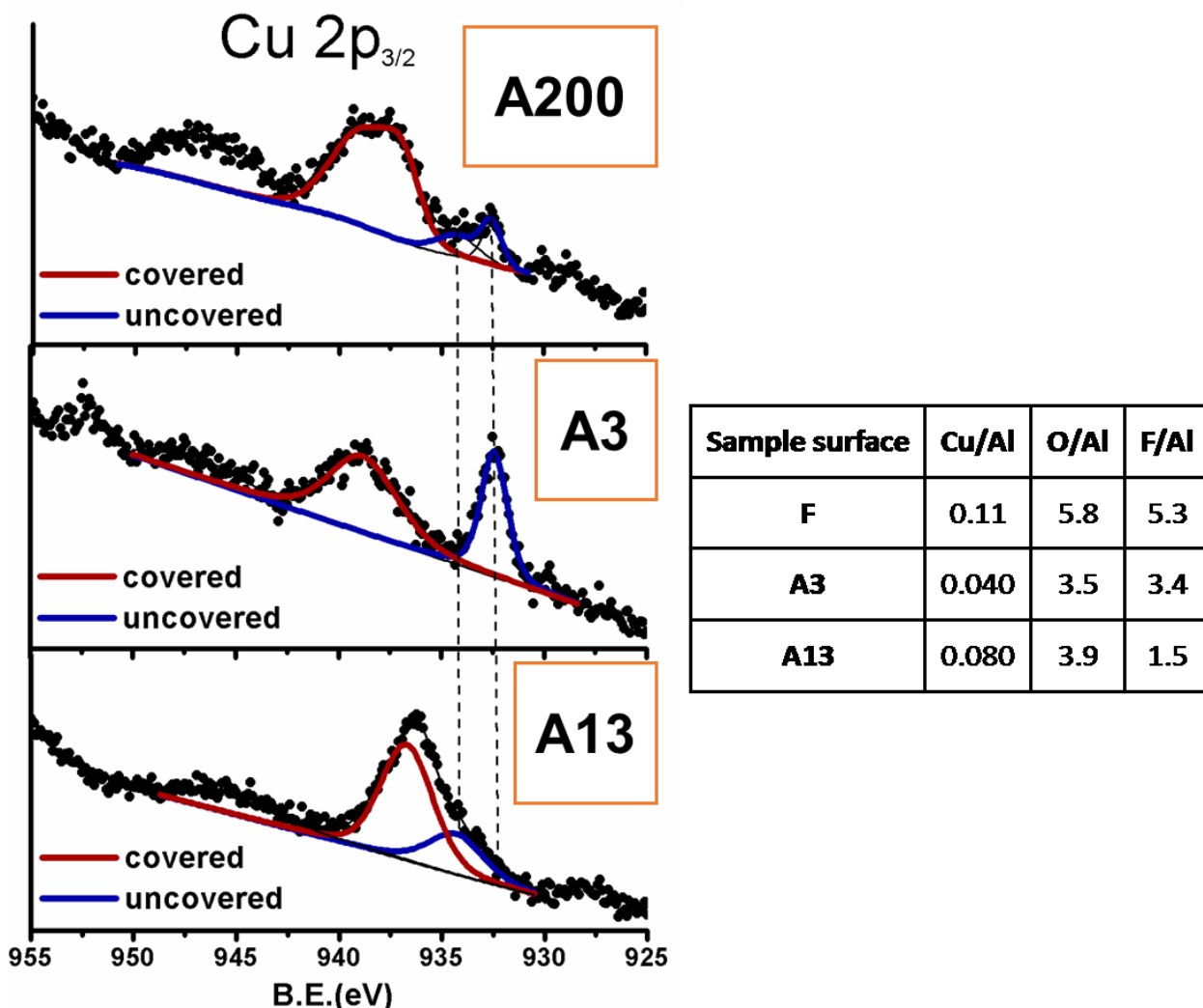


Figure 56. Cu2p<sub>3/2</sub> XPS peaks for as-prepared A200 sample (top) and after treatment in acidic (A3, middle) or basic (A13, bottom) solutions. Black dots are experimental points, blue solid lines are components originated from non-coated Cu, and red solid lines are components originated from alumina-coated Cu. The dashed lines in A200 spectrum show the two components of the peak, namely the one related to Cu(II) at higher BE and the one related to Cu(I) at lower BE. The vertical dashed lines are guides to the eye to compare the evolution of uncoated Cu-related peak components among the spectra. The table reports the atomic ratios as obtained from XPS analyses.

These XPS spectra confirmed the model for the alumina coverage proposed above. Distinct XPS signals were originated from the covered and uncovered areas, as evidenced by different colors in Figure 57. The acidic treatment at pH=3 reduced the total amount of copper at the surface with respect to alumina (see table Figure 57), with Cu/Al ratio dropping from 0.11 to 0.04. The most notable effect is that the Cu(OH)<sub>2</sub> (e.g. the component at higher BE) from the uncovered areas disappeared, and its quantity from

the covered areas was drastically reduced. The main peak component for uncoated areas after acidic treatment was indeed the one associated to  $\text{Cu}_2\text{O}$ . The removal of  $\text{Cu}(\text{OH})_2$  is confirmed also by the reduction of the amount of the related O 1s signal. Even though  $\text{Cu}(\text{OH})_2$  was removed, the FAS layer was only slightly reduced, as revealed by the amount of fluorine (F/Cu ratio from 5.3 to 3.4). Probably, only FAS molecules grafted on  $\text{Cu}(\text{OH})_2$  deposits were removed by the acidic environment. We added SEM observations of A3 surface to achieve a deeper insight (see Figure 58a). As expected, no significant change in surface morphology was observed with respect to the as-prepared sample A200 (see Figure 51), as flower-like alumina still covers the entire surface. This scenario is consistent with the retention of superhydrophobicity displayed by sample A3. The overall picture emerging is that of a “cleaning” of the surface by removal of the  $\text{Cu}(\text{OH})_2$  grown during the preparation.

Treatment in a basic solution produces radically different results. In this case, the amount of copper was only slightly reduced (Cu/Al from 0.11 to 0.08), and on both the covered and the uncovered areas most of the Cu intensity was associated to  $\text{Cu}(\text{OH})_2$  (Figure 57, bottom). On the other hand, the amount of F was severely reduced (F/Cu from 5.3 to 1.5), which suggests that the entire FAS layer on the surface was degraded. Quite surprisingly, SEM image in Figure 58b show that the basic chemical environment did not affect the flower-like surface structure, which was maintained. This is consistent with the results of the ageing tests performed on coated aluminum reported in the previous part of this chapter [111]. Therefore, the loss of superhydrophobicity in basic solution was due to degradation of FAS moieties grafted to the surface, while the alumina nanostructured layer proved resistant to chemical attacks in both acidic and basic environments.

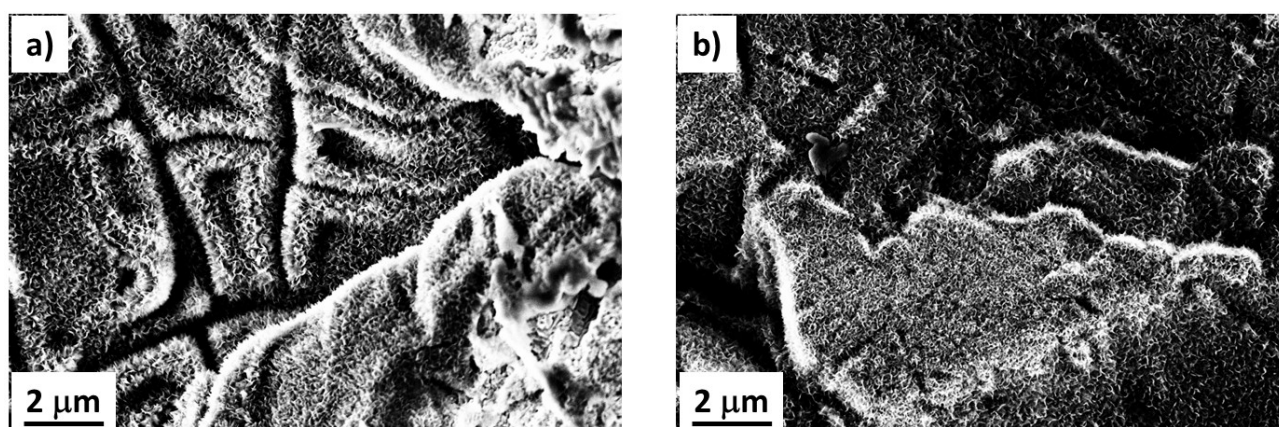


Figure 57. FESEM images of sample a) A3 and b) A13 (coated copper after 120 h of immersion in pH = 3 or pH = 13 aqueous solution, respectively). Scale bars are reported.

## Conclusions

Due to the high relevance of copper as a material for a wide range of applications, we decided to develop a tailored coating process to obtain the best performing superhydrophobic coating on its surface. In the first part of the study, we investigated the relationship between heat-treatment temperature and the final properties of the hybrid coating in terms of morphology, chemical composition and wetting behavior. When treatment temperature exceeded 200°C, copper oxidation to Cu(II) caused the formation of nanowires, which in turn aggregated to extremely brittle microwires with increasing temperature. Even though wetting properties were not substantially different between the samples, 200°C-treated surfaces proved to own much better mechanical stability. Therefore, we adopted 200°C as the chosen temperature for heat treatment of alumina coatings on copper substrates.

In the second part of the study, we assessed the differences in the nanostructured coating when using either an isopropyl alcohol-based sol or a water based suspension for the deposition of alumina nanoparticles. We saw that only the alcohol-based sol could create a homogeneous boehmite flower-like nanostructure after treatment in boiling water. On the other hand, a water-based suspension of alumina nanoparticles left non-structured areas, with detrimental effects on the superhydrophobic properties of the coating.

We further investigated the durability of the hybrid coating in harsh chemical environment, immersing coated copper surfaces in acidic or basic solutions and assessing their morphology, chemical composition and wetting properties after five days. The results show that acidic conditions did not affect the coating significantly, as the only detected change was a removal of  $\text{Cu}(\text{OH})_2$  from the surface. Both the fluorine layer and the nanostructured boehmite were almost unaltered. On the other hand, FAS moieties proved extremely sensitive to basic environment, as fluorine content was drastically reduced after durability tests. Even though surface morphology was not affected by basic environment, the loss of chemical functionalities led to reduced water repellence, e.g. lower WCA and higher CAH.

In summary, these results prove once again the tight relationship between surface morphology, chemical composition and wetting properties. Care must be taken when setting process parameters, as they might severely affect the final properties of the surface, in terms of functionality and stability in severe conditions. Still many more aspects of the process need further exploration, leaving room for future activity aiming at the realization of a superhydrophobic copper surface with appeal for the industry.



## 5. DROP IMPACT STUDIES WITH DIFFERENT LIQUIDS AND SURFACES

So far in this thesis, I have determined the wetting behavior of a surface with the sessile drop method, which is by far the most common method in the literature for the characterization of the wetting properties of materials. This technique uses static or quasi-static drops as a mean to study the interaction between the liquid and the solid surface. However, in many cases drops are not gently deposited on the surface, rather they impact with non-zero velocity. The impact of drops on dry solid surfaces is a phenomenon involved in many industrial applications, e.g. spray cooling, ink-jet printing, spray painting, fuel injection, raindrop erosion, and so on. After impact, the drop can behave in different ways. In other terms, the drop impact output is not easy to determine and depends on a wide set of parameters and forces, like capillarity, viscous forces, and impact momentum. As far as superhydrophobic surfaces are concerned, the repulsive forces between the solid surface and the liquid phase cause the water droplet to bead up on instead of spreading, thus generating a high contact angle. In addition, capillary adhesion forces are low and water drops typically preserve a high mobility on the surface, e.g. contact angle hysteresis is low. However, these values alone do not provide information about the behavior of liquid drops impacting on surfaces. For example, a surface that is only hydrophobic but smoother or with proper topology can be more effective at repelling liquids even for a large value of Weber number ( $We = \rho v 2D_0 / \sigma$ , where  $\rho$  is fluid density [ $\text{kg/m}^3$ ],  $v$  is impact velocity [ $\text{m/s}$ ],  $D_0$  is droplet diameter [ $\text{m}$ ], and  $\sigma$  is surface tension [ $\text{N/m}$ ]) [191]. Thus, investigation of single drop impact [34] [35] [36] is the first step towards understanding and controlling the liquid-solid interactions in complex phenomena.

In the literature, few attempts of finding a correlation between contact angles and drop impact behavior are reported. For example, recently Antonini *et al.* [191] analyzed the impact of water drops on horizontal surfaces and found a correlation between receding contact angle RCA and the occurrence of rebound as impact output. More specifically, rebound was observed only on surfaces presenting with  $RCA > 100^\circ$ , which was thus established as the critical wetting value for water drop rebound. Moreover, they discovered that rebound time decreased as  $\theta_R$  increased. However, in this paper only water drops were considered. Therefore, this criterion for drop rebound might not be necessarily valid also for other liquids.

In fact, if we aim at extending the repellence also to liquids with surface tension lower than that of water (e.g. oils and alkanes), it will be necessary also to assess drop impact behavior with such liquids. Very few papers dealt with this subject [192], especially using oleophobic surfaces as targets for the impacts [193]. In these tests, impact velocity, interfacial tension, viscosity of the liquid, and the chemical

and physical properties of the surface determine the drop outcome as well as the spreading and the retraction dynamics. The most remarkable result of the aforementioned papers was that even oleophobic surfaces (e.g. with high contact angles with low surface tension liquids) might not necessarily lead to a total rebound of impinging drops, especially above a given value of the  $We$ . Eventually, impalement can occur, leading to droplet deposition on the surface.

To better understand the existence of a criterion to predict drop impact outcome for different liquids and the key parameters governing drop-surface interaction, we observed the normal impact of water and hexadecane drops on solid dry surfaces with different wetting properties using a high-speed camera. We compared results from the hybrid-coated surfaces described so far with those from other liquid repellent surfaces. More specifically, we fabricated liquid repellent surfaces according to the so-called SLIPS approach [194] and other SHSs with different surface morphology and chemical composition, as described in a previous paper [9]. The purpose was to establish a relationship between drop impact outcomes and the different parameters concerning both the liquid drop (impact velocity, surface tension, and viscosity) and the solid surface (morphology and roughness, chemistry, and wetting properties).

## Materials and methods

We fabricated four types of SHSs on aluminum foils (size about 100 x 50 x 2 mm):

- Hybrid-coated, sandblasted surfaces prepared from dip-coating with an alumina nanoparticles aqueous suspension, followed by a heat treatment at 400°C for 60 minutes, immersion in boiling water for 30 minutes, heat treatment at 400°C for 10 minutes and finally chemical modification with Dynasylan SIVO Clear EC. These surfaces were labeled as S;
- Liquid-infused surfaces, according to the SLIPS approach. The fabrication was analogous to that of samples S, with addition of a final immersion in perfluorinated lubricant oil Fluorinert FC-43 (3M) which fills the nano-sized pores in the flower-like nanostructure and creates a continuous liquid film on the surface. The lubricant oil is expected to create a liquid-liquid interface with the drops, instead of the mixed air-solid-liquid interface established by SHSs. The advantage of SLIPS approach over SHSs is their resistance in high pressure conditions, which could be helpful in extending the range of conditions in which drop rebound occurs (e.g. avoiding impalement at high  $We$ ). These surfaces were labeled as SI;
- SHSs prepared according to the method described by Malavasi *et al.* [195]. Briefly, aluminum foils were first etched in 37% HCl solution at room temperature for two minutes, then immersed in a lauric acid solution in ethanol (12.7 w/w%) for two hours. These samples were labeled as LAU;

- SHSs prepared with the same etching performed for LAU samples, followed by immersion in an aqueous solution of 1H,1H,2H,2H-perfluorooctyltriethoxysilane [9]. These samples were labeled as FAS.

Sandblasted, uncoated aluminum foils were also tested as a reference and marked as TQ.

For all five surface types, we calculated average values of advancing contact angle ACA, receding contact angle RCA and contact angle hysteresis CAH. Contact angles were measured automatically by an OCA 15plus optical contact angle system (Dataphysics Instruments) with the sessile drop method. Drops with volume of 2  $\mu\text{L}$  were used and their volume was first increased then decreased to measure ACA and RCA, respectively.

Surface topography was evaluated with a Tescan MIRA3 SEM equipment, while roughness measurements were performed with a Contour GT-K (Bruker Nano GmbH) optical profilometer (vertical resolution  $<0.01$  nm, lateral resolution  $0.38$   $\mu\text{m}$ ). We evaluated areal roughness parameters  $S_a$ ,  $S_q$ ,  $S_v$  and  $S_z$ , which were previously defined in Chapter 4. A  $15 \times 15$   $\text{mm}^2$  area was analyzed for every measurement, and a minimum of three measurements were made on the same sample for repeatability.

For drop impact experiments, the experimental setup included a syringe with hydrophobic needle for drop dispensing. The tip of the needle was placed at a fixed height from the dry surface, in a way that the drop was accelerated by gravity. The experimental conditions were the following: impact speed in the  $0.05 < v < 4.2$  m/s range, drop diameter in the  $1.5 < D_0 < 2.6$  mm range, Weber number in the  $0.1 < We < 635$  range, Ohnesorge number ( $Oh = \mu/(\rho\sigma D_0)^{1/2}$ , where  $\mu$  is the liquid viscosity [ $\text{Pa}\cdot\text{s}$ ]) in the  $0.0023 < Oh < 0.0186$  range. Images of drop impacts were recorded using a high-speed camera (PCO 1200-HS) with typical acquisition rates of 1568 and 2477 fps and a spatial resolution of 31  $\mu\text{m}/\text{pixel}$ . Tests were repeated a minimum of 10 times for each condition to guarantee the experimental reproducibility. Images were manually analyzed to identify the drop impact outcome and measure drop rebound time when rebound occurred.

## Results and discussion

SEM images for all tested surfaces are shown in Figure 59. On the sandblasted TQ surface adopted as a reference (first row), abrasion by impacting sand grains produced an irregular microstructure with asperities and cavities, but no nano-scale feature was observed. S and SI samples (second and third row, respectively) showed the well-known flowerlike nanostructure made of crossed, 200-nm-long flakes and nanometric cavities. No difference in morphology was expected between two samples, as the final

infusion steps does not affect surface structure. Meanwhile, LAU and FAS samples (last two rows) displayed a terrace-like structure with submicrometric edges, as expected from the identical etching conditions held for those samples. This structure is a common result of etching processes on aluminum [10].

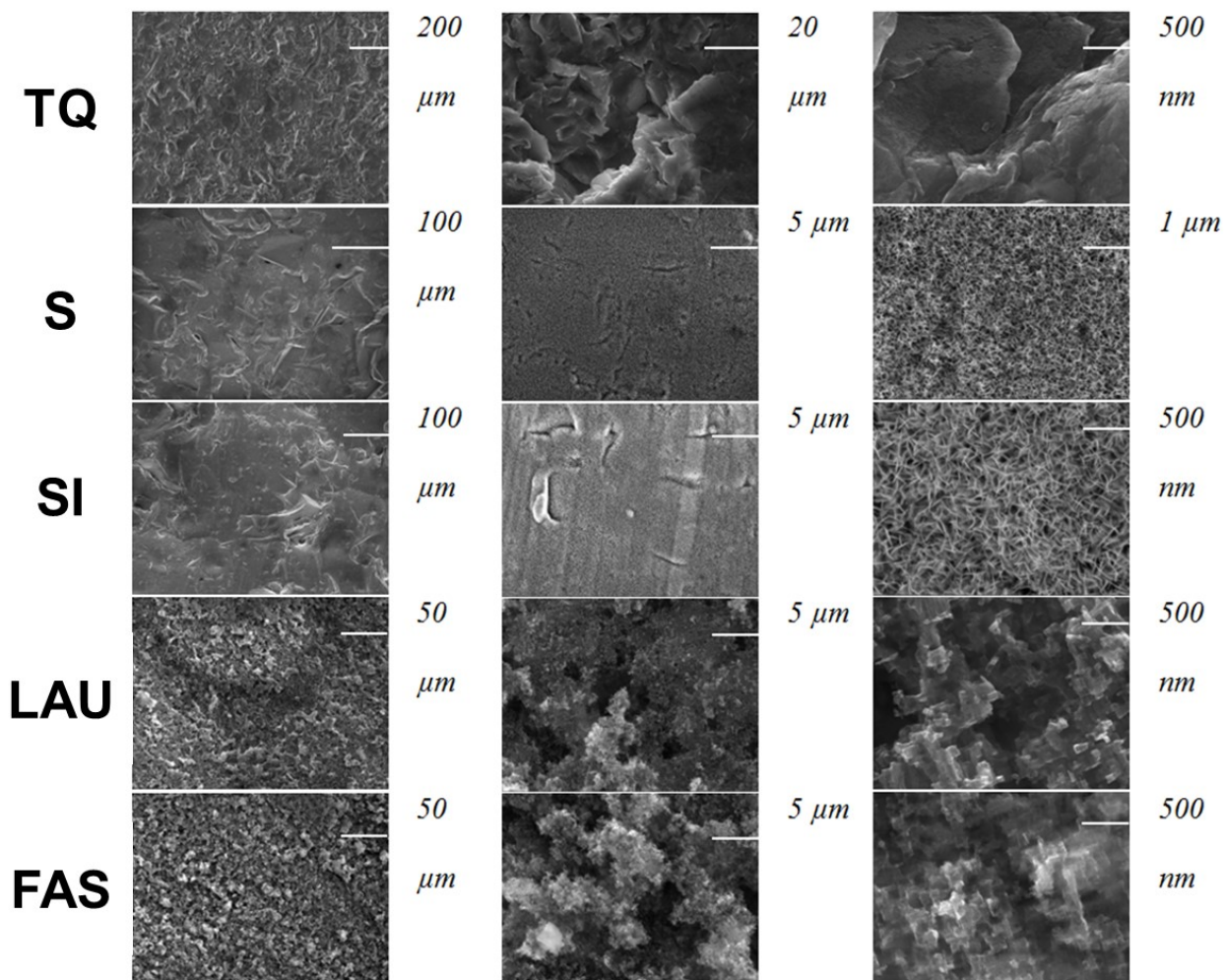


Figure 58. SEM images of the five tested surfaces at increasing magnification from left to right. Scale bars are reported in the top right corner of each image.

Roughness data shown in Figure 60 displayed relevant differences between sandblasted, boehmite-coated samples (S, SI) and etched surfaces (LAU, FAS): the former had lower average roughness values ( $S_a$ ,  $S_q$ ) but higher peaks ( $S_v$ ,  $S_z$ ). Comparing these values to those of the reference TQ surface, which were very similar, we concluded that the hybrid nanostructured coating has a small influence on the micrometric roughness of S and SI, while the main contribution belongs to the microstructure provided by sandblasting. Meanwhile, on LAU and FAS surfaces the etching reaction provided a rougher structure, but with shorter asperities and shallower cavities.



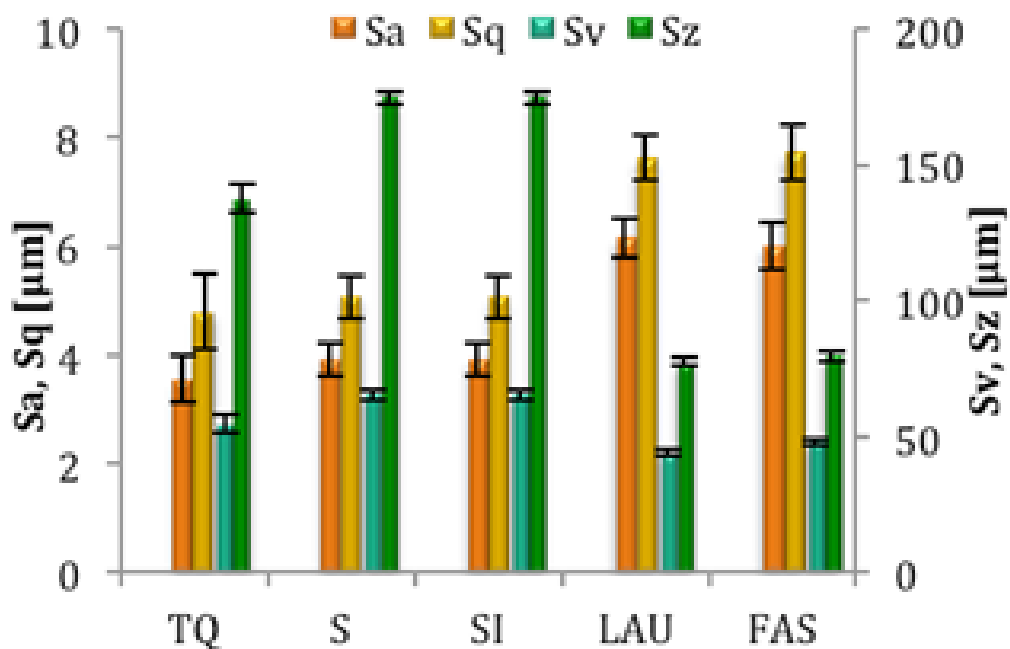


Figure 59. Roughness values (*Sa* and *Sq* on the left-hand axis, *Sv* and *Sz* on the right-hand axis) for the five tested surfaces TQ, S, SI, LAU and FAS. Standard deviations are reported as error bars.

Figure 61 reports the average values of ACA, RCA and CAH with water (top graph and table) and hexadecane (bottom) for all tested surfaces. All four functionalized surfaces had RCA > 135° and CAH < 10° with water drops, e.g. they were all superhydrophobic as per the definition by Malavasi *et.al* [195]. On the contrary, reference TQ surface was slightly hydrophilic (ACA < 90°) and has high CAH.

The picture with hexadecane drops was radically different. As predictable from the much lower surface tension of hexadecane ( $\gamma = 27.5 \text{ mN/m}$  at  $T = 20^\circ\text{C}$ ) compared to that of water ( $\gamma = 72.8 \text{ mN/m}$ ), overall contact angle values were smaller. Only 3 out of 4 surfaces proved oleophobic, e.g. had a RCA > 90°, while TQ and LAU surfaces were totally oleophilic. On the latter samples, hexadecane drops spread very easily, forming very low ACA and hindering a proper measurement of RCA and CAH. The oleophilic behavior of LAU surfaces was predictable by considering the chemical nature of the coating. Indeed, lauric acid chains grafted to the surface are extremely similar to hexadecane in terms of composition, e.g. they both have long alkyl chains. Furthermore, it is known from the literature that very low surface energy is necessary to fabricate an oleophobic surface. Alkyl chains cannot reach a surface energy low enough, while fluoroalkyl moieties are the best choice for oleophobic surfaces. However, S, SI and FAS surfaces had RCA > 120°, while the latter also had CAH < 10°. Therefore, we expected to observe

significant differences in drop impact outcome between these surfaces and LAU, as predicted by Antonini *et al.* [191].

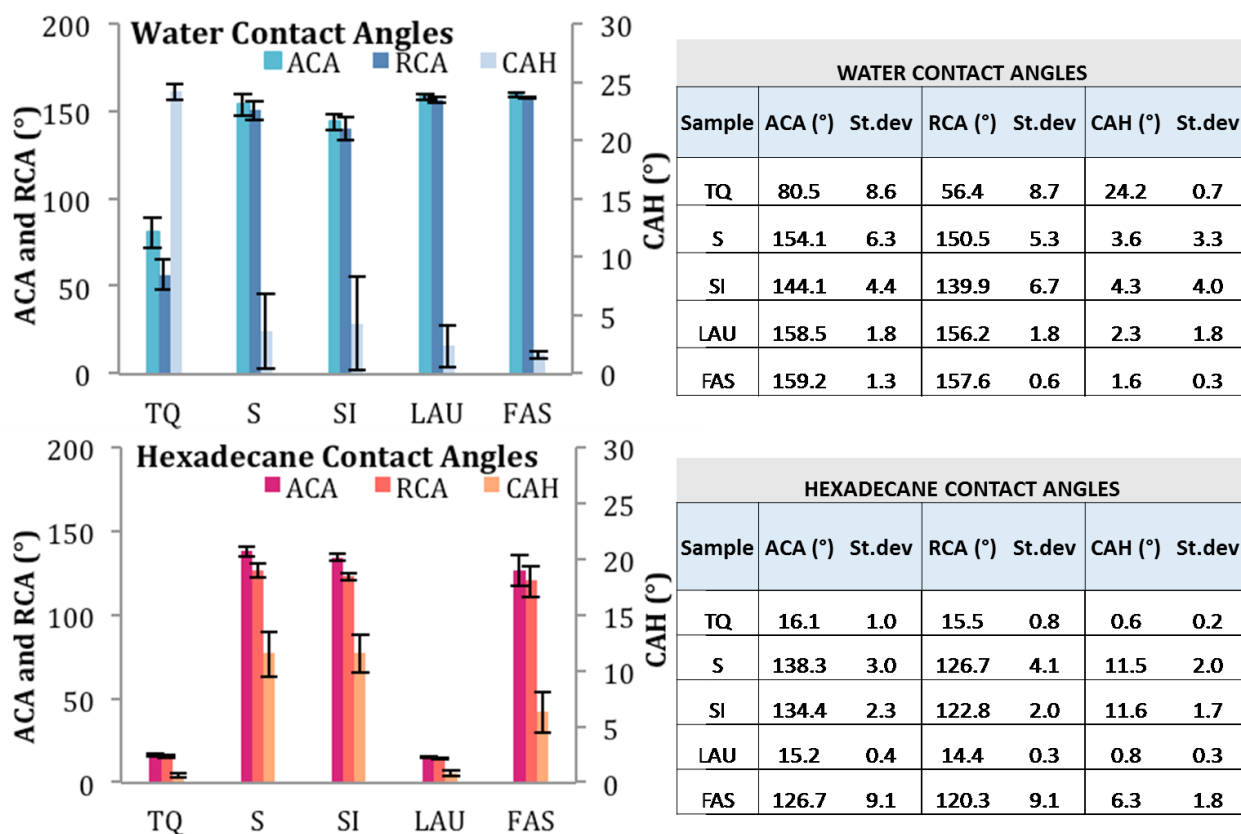


Figure 60. Average contact angle values with water (top) and hexadecane (bottom) for the five tested surfaces. In each graph, ACA and RCA values are referred to the left-hand axis, while CAH is referred to the right-hand axis. Standard deviations are reported as error bars.

The results of drop impact experiments are summarized in Table 17 and in Figure 62. Five main regimes were observed: complete rebound, partial rebound, prompt splash, receding breakup, and deposition. In water drop impact experiments, all the functionalized surfaces (S, SI, LAU and FAS) were able to generate a rebound of the drops, whether complete or partial. Reference TQ surface promoted either drop deposition for  $We \leq 200$  or receding breakup for higher  $We$ . This behavior from TQ surfaces was expected because of their hydrophilic behavior. Remarkably, surfaces S and SI were able to repel the water drops throughout the entire range of  $We$ , as no splash was observed even for the maximum investigated  $We$  value of 620. This result is unprecedented in the literature and proves that the Cassie-Baxter state on the nanostructured, hybrid coating here discussed is stable even with drops impacting at high speed. On the other hand, LAU and FAS showed a transition from complete rebound to partial rebound at high  $We$ , with part of the water drop sticking to the surface after impact and retraction. Interestingly, this transition occurs sooner (e.g. at lower  $We$ ) for FAS than for LAU, notwithstanding their

identical surface topography and wetting properties. The only difference between the two surfaces lies in their chemical composition, which surprisingly could have played a role in the drop impact outcome. This evidence has never been observed before and would provide a new edge on the prediction of drop impact behavior for non-wetting surfaces.

Surface type	We (WATER)							We (HEXADECANE)						
	< 1.5	16 ÷35	40 ÷75	65 ÷100	150 ÷215	270 ÷360	500 ÷620	10 ÷20	30 ÷40	60 ÷75	85 ÷125	205 ÷275	325 ÷485	545 ÷635
TQ	D	D*	D	D	D	RB	RB	D	D	D	D	D	PS	PS
S	R	R	R	R	R	R	R	D	D	D	D	PS	PS	PS
SI	R	R	R	R	R	R	R	D	D	D	D	PS	PS	PS
LAU	R	R	R	R	R	R	PR	D	D	D	D	D	PS	PS
FAS	R	R	R	R	PR/R**	PR	PR	D*	D	D/RB**	D/RB**	D/RB**	RB	RB

Table 17. Summary of the outcomes of the drop impact tests. R = rebound, PR = partial rebound, PS = prompt splash, RB = receding breakup, D = deposition. \*Singular jet. \*\* Transition region.

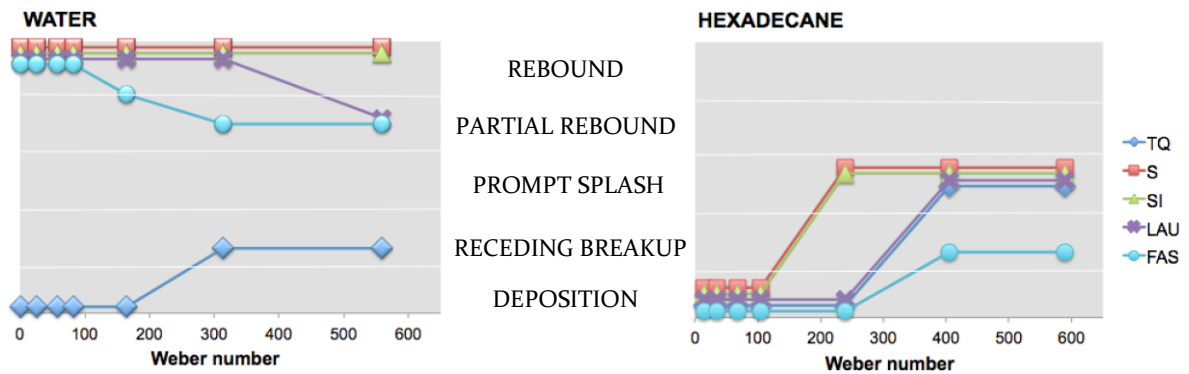


Figure 61. Schematic representation of the drop impact test outcomes with water (left) and hexadecane drops (right), respectively. In the graphs, the mean values of each We interval are reported.

In the case of hexadecane, rebound did not occur for any of the surfaces, even for oleophobic surfaces like S, SI and FAS, which had high RCA and low CAH. Furthermore, prompt splash was the most frequent outcome for  $We > 200$ . FAS surfaces exhibited peculiar behavior, as hexadecane generated a singular jet [196] after impact at very low  $We$  and showed receding breakup behavior for the higher investigated  $We$ . Image sequences of water and hexadecane liquid drops impacting the tested surfaces are shown in Figures 63 and 64, respectively. Interestingly, generation of a singular jet was also observed for water drops impacting in TQ surfaces at  $We \approx 21$ , as shown in Figure 65.

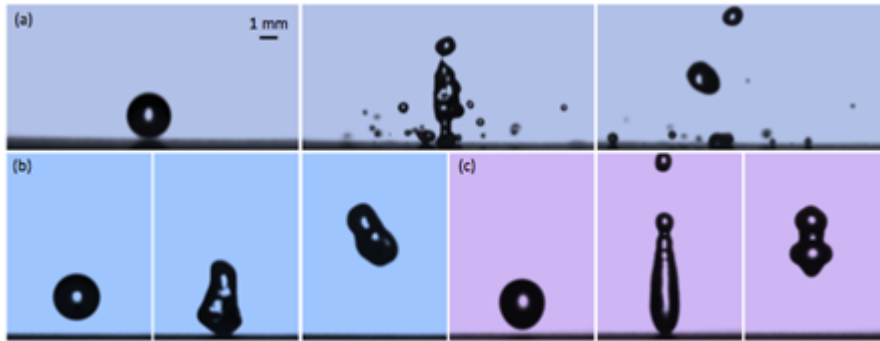


Figure 62. Image sequences of water drops (average diameter  $D_0 = 2.45$  mm) impacting on three functionalized surfaces: (a) partial rebound with fragmentation on FAS sample at  $We = 312$  at  $t = 0$ , 14.6 ms and 31.2 ms after impact; (b) rebound on SI sample at  $We = 54$  at  $t = 0$ , 11.5 ms and 31.2 ms after impact; (c) rebound on S sample at  $We = 21$  at  $t = 0$ , 14.0 ms and 21.6 ms after impact. The scale bar in (a) is valid for all images.

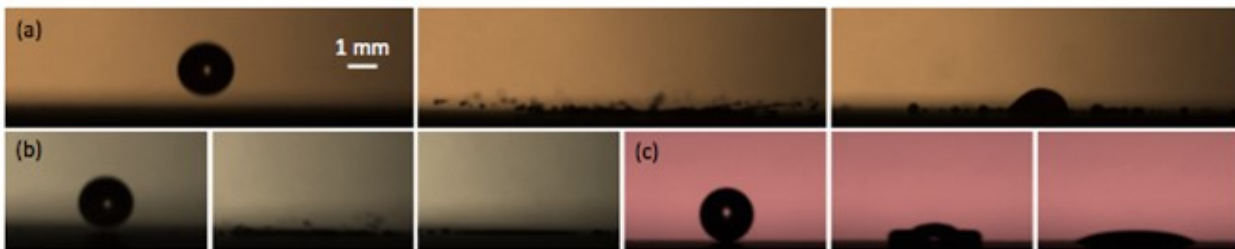


Figure 63. Image sequences of hexadecane drops (average diameter  $D_0 = 1.66$  mm) impacting on three functionalized surfaces displaying different behavior: (a) receding breakup on FAS sample at  $We = 560$ ; (b) splash on SI sample at  $We = 580$ ; (c) deposition on LAU sample at  $We = 17$ . For every surface, images at  $t = 0$ , 2.0 ms and 17.6 ms after impact are reported. The scale bar in (a) is valid for all images.

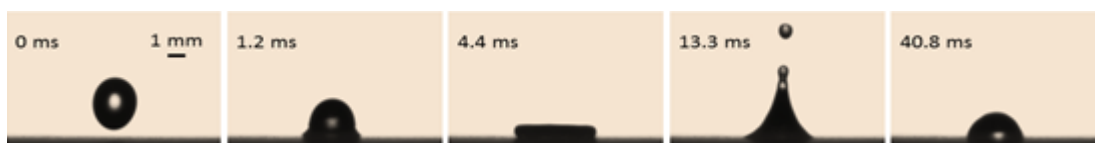


Figure 64. Image sequence of water drop (average diameter  $D_0 = 2.35$  mm) impacting on TQ surface at  $We = 21$ . Deposition occurs with the generation of a secondary drop (singular jet). The scale bar in the first frame is valid for all images.

For a better comprehension of the drop spreading and retraction dynamics, we plotted the evolution of drop diameter for water and hexadecane drop impacts, as shown in Figure 66. More specifically, we plotted the dimensionless diameter of the liquid film, called the spread factor  $\xi(t) = D(t)/D_0$  (i.e. the contact diameter at time  $t$ , made dimensionless by dividing it by the initial drop diameter), as a function of time. Different outcomes generated different  $\xi$  vs.  $t$  trends. For SHSs for which water drop rebound was observed (left side graph in Figure O),  $\xi$  quickly increased then fell to zero, meaning that the drop had completely detached from the surface, therefore  $D(t)$  and  $\xi(t)$  equal 0. The higher the slope of the fall of  $\xi$ , the faster the retraction of the drop and the shorter the rebound time. However, when deposition occurred (e.g. for water drops on TQ surface), retraction was slower and incomplete, thus  $\xi$

reaches a plateau rather than dropping to zero. The graph related to water drops also shows subsequent rebounds of the drop, in which a much lower maximum  $\xi$  was achieved as well as longer rebound times due to kinetic energy dissipation.

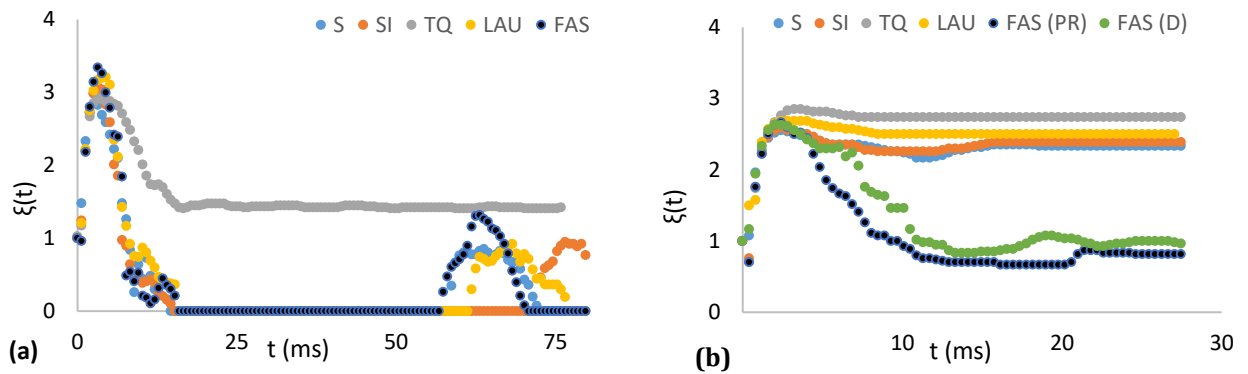


Figure 65. Spread factor time evolution,  $\xi(t)=D(t)/D_0$ , for the tested samples (single runs). (a) Water test conditions:  $V = 1.6$  m/s,  $D_0 = 2.5$  mm, and  $We \approx 90$ . (b) Hexadecane test conditions:  $V = 1.5$  m/s,  $D_0 = 1.7$  mm, and  $We \approx 110$ .

Drop impact dynamics was radically different when hexadecane drops were used (right side graph in Figure O). More precisely, on S and SI samples the drop did not retract and  $\xi$  did not change from its maximum value. Surprisingly, the same behavior was observed for LAU surfaces, notwithstanding the much lower RCA (they were oleophilic). On the other hand, FAS surface displayed a different behavior, leading to either partial rebound (with  $\xi$  reaching a value close to one due to the pinned part of the drop, then slightly increasing when the secondary drop fell back to join the primary one) or deposition at a lower plateau of  $\xi$  compared to S and SI. The time evolution of the spread factor suggests that the drop impact dynamics does not depend only on RCA because, contrary to what was reported by Antonini *et al.* [191], even for surfaces with  $RCA > 120^\circ$  like S, SI and FAS complete drop rebound did not occur and different behavior was observed for surfaces with similar RCAs.

The fact that a surface is superhydrophobic is not enough to ensure a complete rebound because impalement can occur. In other terms, liquid drops can penetrate the surface features of SHSs if their kinetic energy is high enough. Such phenomenon is also called Cassie-to-Wenzel transition (CWT) [197], as drops achieve a state of high adhesion to the surface. Therefore, it is crucial to determine when impalement occurs, impeding bouncing. Impalement is usually described using four different pressure mechanisms alternately: the water hammer pressure  $P_{WH}$ , the dynamic spreading pressure  $P_{SD}$  [198], the capillary or antiwetting pressure  $P_C$  [199], and the gas-layer pressure  $P_{GL}$  [55]. This last pressure term comes out by considering the compression effects of the gas under the drop rather than the liquid

compressibility. The initial impact of the droplet on the surfaces generates a water hammer pressure  $P_{WH}$  due to the compression of the liquid [54] [199] [200]. Water hammer pressure is defined as:

$$P_{WH} = \rho CU$$

$\rho$  is liquid droplet density,  $C$  is the velocity of sound in water, and  $U$  is the droplet impact velocity normal to the wall. However, the actual pressure acting on the surface is reduced because of the complex interactions between the drop and the surface, thus water hammer pressure is usually reduced of a factor of  $k$ , which has been experimentally evaluated over in a very broad range (e.g. from 0.2 for Deng *et al.* [54] to 0.002 for Maitra *et al.* [55]). The real value of the impact pressure due to the liquid compressibility is called the effective water hammer pressure  $P_{EWH}$  here. In the spreading stage, a liquid jump overtakes the outward-moving contact line [201]. At this stage, the spreading process implies a dynamic pressure  $P_{SD}$ :

$$P_{SD} = \frac{1}{2} \rho V^2$$

$V$  is the spreading velocity. For normal impact,  $P_{EWH}$  is supposed to be greater than  $P_{SD}$ . On the contrary, the capillary pressure is an anti-wetting pressure: it can be defined as the liquid pressure level that must be overcome in order to squeeze a droplet through a cavity on surface topology. Capillary pressure  $P_C$  can be written as:

$$P_C \approx \frac{\sigma(-\cos \theta_A)}{r_p}$$

$\sigma$  is the surface tension,  $\theta_A$  is the advancing contact angle of the corresponding smooth surface, and  $r_p$  is the length scale of the surface cavities.

In addition to these four pressure terms, the analysis of droplet impact on textured surfaces performed by Maitra *et al.* [55] showed that compressibility of the air layer between the droplet and the substrate plays a key role in the impalement. Actually, meniscus penetration is probably linked to the

compressibility of the draining air, rather than the water hammer pressure effect of the liquid. Therefore, instead of  $P_{EWH}$ , the authors defined a pressure term related to the gas layer compressibility,  $P_{GL}$ :

$$P_{GL} = \frac{0.88(R\mu_g^{-1}U^7\rho^4Ca)^{1/3}}{St^{4/9}}$$

$R$  is droplet radius,  $\mu_g$  is air viscosity,  $Ca$  is the capillary number, and  $St$  is the Stokes number. When the impacting drop exerts a  $P > P_{GL}$ , Cassie-to-Wenzel transition occurs.

Furthermore, different levels of impalement exist. The impalement can be total, in case the liquid completely penetrates the surface topology and wets the entire surface structure, or partial, when the liquid is not able to wet completely the surface and some air is retained beneath the features. More in detail, we can depict three regimes: the Wenzel regime, where impalement occurs and is present until the final deposition, with the liquid imbibed into the surface structure; the fakir (or Cassie–Baxter) regime, when no impalement and no imbibition occur for the entire duration of drop impact (from the early stages until the possible rebound or deposition); the partially impaled state, when penetration of the liquid beneath surface features is not complete. The interplay of the pressure terms previously described determines which regime is established: in the case of  $P_{EWH} > P_C > P_{SD}$ , the fluid penetrates during the contact stage, thus impalement occurs; if  $P_C > P_{EWH} > P_{SD}$ , the surface structure resists wetting throughout the impact process, leading to a fakir state. However, the fakir state is not sufficient to determine drop rebound: it is also necessary for the liquid lamella to have sufficient energy at the end of the recoiling phase to promote drop detachment from the surface, i.e. it is necessary to have enough impact kinetic energy. This condition will be satisfied only if the kinetic energy of the impinging droplet is larger than the surface energy dissipated during the retraction stage, e.g. if  $We$  is above a minimum value  $We_{r,min}$ . This scenario is labelled as bouncing fakir droplet B [198] [202]. Otherwise, if the kinetic energetic is not sufficient, the drop will not rebound (non-bouncing fakir state, NB). Moreover, the partially impaled state can manifest in two ways: the partially penetrated bouncing droplet state (PPB) occurs at higher drop impact velocity, while at low impact velocity the second non-bouncing droplet (2NB) state is observed [199].

With such a complex scenario, there is still an open debate on the criteria for impalement because, even if it is clear that impalement will appear when the antiwetting pressure  $P_C$  is lower than a pressure linked to the impact dynamics (e.g.  $P_{EWH}$ ,  $P_{GL}$ , or  $P_{SD}$ ), the actual threshold values are still unknown.

Maitra *et al.* [55] suggested that  $P_{GL} > 80 P_c$  should be used as threshold pressure value for impalement. From this expression, the critical Weber number above which complete rebound cannot occur can be evaluated:

$$We_{cr,imp} = 18.2R^{1/2}\mu_g^{2/7}\rho^{-1/7}\sigma^{-1/7}(\cos\theta_A)^{9/14}r_p^{-9/14}$$

From this equation, we can infer that the smaller the cavity size, the higher the impact velocity above which impalement occurs. This is in qualitative agreement with the different output we observed at high  $We$  on surfaces with different morphologies: S and SI samples have nanoscale cavities on their surfaces, hence a  $We_{cr,imp}$  higher than the maximum  $We$  investigated in these experiments ( $We_{cr,imp} > 620$ ). Instead, LAU and FAS surfaces displayed only submicrometric voids that provided a smaller  $We_{cr,imp}$ ; therefore, CWT can be observed at  $We \approx 550$  for LAU and  $We \approx 200$  for FAS. However, it is very difficult to estimate the  $We_{cr,imp}$  for surfaces having a stochastic roughness, such as those used in the present work. Moreover, Quan and Zhang [203] demonstrated how the initial and operating conditions, including the geometrical shape of the microstructural features on superhydrophobic surfaces, will significantly influence the bouncing ability of an impinging droplet on textured surfaces. From the above equations, it is also evident that  $We_{cr,imp}$  is increasing with the surface tension, i.e., low surface tension liquids will have a lower threshold for impalement. Hence, for a given impact velocity, a drop tends to deposit rather than to rebound when a low surface tension liquid like hexadecane is involved.

It is also important to stress that another important dimensionless number, namely the Ohnesorge number  $Oh$  which accounts for viscous dissipation, may influence drop rebound. For the water drops here utilized,  $Oh \approx 0.0024$ , but for hexadecane drops it is 7 times higher ( $Oh \approx 0.0177$ ). The viscous dissipation prevents the liquid from rising back from partial penetration to a Cassie-Baxter regime and hinders rebound [204]. However, the effect of viscosity is realized only during the retraction phase if rebound is still possible [205] [206]. In our case, we were not able to achieve rebound with hexadecane drops because of too low  $We_{cr,imp}$ , thus the contribution of viscosity could not be estimated. The overall picture of these experiments is that rebound may happen for a given  $We$  range  $We_{r,min} < We < We_{r,max}$ , with  $We_{r,max} = We_{cr,imp}$  [193] [198] [207].

Finally, so far in the literature the chemistry of the surface and of the liquid has never been considered to be a crucial factor in determining the occurrence of CWT. However, from the results here obtained it becomes clear that the chemistry of the surface and the physico-chemical interactions with the liquid drops also play important roles in determining  $We_{cr,imp}$ . For water drops with  $We = 150 \div 360$ , indeed,



different outputs were observed for LAU and FAS surfaces notwithstanding their identical morphology and wetting properties (see Figures 59 and 61). The difference between these surfaces must lie in their chemical composition. LAU surfaces were functionalized with nonpolar alkyl chains, while FAS samples exposed polar fluorinated groups. Murase and Fujibayashi [208] demonstrated that water forms hydrogen bonds with such fluorinated moieties on hydrophobic surfaces. Therefore, we may consider that these interactions cause kinetic energy dissipation in the drop. Nakajima *et al.* [209] calculated that this dissipation depends on the contact area between the drop and the surface. At  $We < 150$ , drop spreading is limited, thus the water-surface contact area is small and the interaction is negligible. With increasing impact speed, drop spreading and contact area, hydrogen bonds start to play a role, causing dissipation and hindering rebound. When  $We > 500$ , water drops penetrate the terracelike morphology of both LAU and FAS samples, with partial rebound as outcome. In such scenario, the role of chemistry is no longer relevant. Instead, for hexadecane drops no influence of the surface chemistry could be recognized: the very low surface tension makes it more probable to either splash at high  $We$  or deposit at low  $We$ , when the kinetic energy is insufficient to break the drop. Only a small influence of the surface structure is observed, causing the splash-deposition transition to shift to lower  $We$  values for the S and SI samples with flower-like surface morphology. This is the first time that this influence of chemistry on the drop impact behavior on textured surfaces is reported. However, other explanations can be evoked as well, like a more inhomogeneous grafting of FAS chains on unexposed parts of the surface topology with respect to LAU molecules. Static or quasi-static wetting measurements might not highlight such differences in surface chemical composition, whereas impinging drops could “touch” these areas and cause a retention of the drop. For instance, if a wettability gradient along the surface asperities was formed, then that would cause a different drop-surface interaction. Future work will extend the comprehension of such phenomena, possibly adding molecular dynamics modeling of the interactions between the surface and the drop.

## Conclusions

In this study, we evaluated the normal impact of water and hexadecane drops on dry, rigid, superhydrophobic surfaces with different surface morphology and chemical composition. The results highlighted that it is not possible to easily correlate contact angles (receding, advancing, and hysteresis) and drop impact dynamics of liquids on different surfaces. The Cassie-to-Wenzel transition was observed even on statically repellent surfaces. To explain the observed phenomena, physical and chemical characteristics of both the liquid drops and the surface have to be taken into account. Surface morphology is crucial in defining the critical velocity over which impalement occurs: the smaller the surface cavities, the higher the  $We_{cr,imp}$ . Also, chemical interactions such as hydrogen bonding between

surface functional groups and molecules in the liquid phase can lower  $We_{cr,imp}$  and favor impalement, especially if wettability gradients along the surface topography are present. As far as the liquid properties are concerned, in agreement with Deng *et al.* [193],  $We_{cr,imp}$  decreases with increasing viscosity and decreasing fluid surface tension. In the case of hexadecane drops, the CWT threshold was so low that no rebound was observed, even if the contact angles were well above the expected critical values obtained from previous works focusing on water drops. In summary, this work highlighted the lack of an agreed general and quantitative evaluation of the impalement criteria after a drop impact. For example, the proposed thresholds in the literature are not yet able to properly describe the results obtained using oils on amphiphobic surfaces. A direct consequence of the study is linked to the numerical simulations of drop impact on rigid and dry surfaces. Besides the liquid surface tension, they often consider models of the advancing and receding contact angles to obtain impact outcomes comparable with the experimental data [210]. However, the present study shows that all the numerical simulations of drop impact on solid, dry surfaces will never be able to capture the outcome of the impact for all the possible fluids if the surface topology and chemistry are not properly considered. Static or quasi-static wetting measurements might not highlight such differences in surface chemical composition. Furthermore, the present results emphasize how an accurate design of the surface properties must be pursued in the future research toward dynamically amphiphobic surfaces.

## 6. ASSESSMENT OF ANTI-ICING PROPERTIES

One of the main reason for the popularity of superhydrophobic surfaces lies in the wide range of potential additional properties that they can display. Amongst all, the property of delaying ice formation or facilitating its detachment is certainly one of the most appealing. In principle, if a surface does not let water drops stick, then ice formation will be avoided, or at least delayed. Such anti-icing behavior would have immensely positive consequences in a wide variety of sectors. For instance, nowadays aircrafts require frequent de-icing routines [211], usually performed by spraying large amounts of chemicals to melt the thick ice formed on wings during some moments of the flight. These processes are expensive, time-consuming and environmentally unfriendly. As an alternative, thermal routines like heating with an electrical resistance or blowing hot air can be used to melt the ice. Of course, the crucial drawbacks are massive consumption of energy and relevant costs. Similar challenges are present in other applications, such as power systems (e.g. wind turbines [212]) and electric power transmission lines [213].

All the mentioned procedures can be described as active anti-icing systems, in which energy must be provided to activate ice melting. In perspective of a reduction of energy consumption and consequent cost benefits, many scientists are investigating passive anti-icing systems to diminish or even eliminate de-icing routines. In other terms, the objective is an “icephobic” surface that does not allow ice to grow, or at least delays freezing. Superhydrophobic surfaces have been one of the first materials to be investigated for this purpose [37] [38] [39] [40]. However, many papers [41] [42] highlighted that a superhydrophobic surface is not necessarily icephobic, because its properties can radically change at freezing temperatures (e.g. below 0°C). In some cases, superhydrophobic surfaces showed no improvement compared to standard surfaces in terms of icing delay. Therefore, it is interesting to evaluate whether the outstanding water-repellent properties displayed by the nanostructured hybrid coating here described are maintained at lower temperatures. Moreover, we wanted to assess the hypothetical anti-icing properties of the coating.

In the literature, many methods have been used to evaluate the anti-icing behavior of surfaces [45] [214] [215] [216] [217] [218]. Based on the chosen technique, different aspects of the icing behavior of the surface can be addressed. For example, Differential Scanning Calorimetry (DSC) allows for the precise determination of water freezing point [219]. An icephobic surface is expected to display lower freezing point than a regular surface. However, experimental conditions in DSC (e.g. static droplet in a closed environment) are not representative of real operational conditions for many applications, like those occurring on a wing surface during flight. Thus, we chose to perform two types of test on hybrid-coated aluminum surfaces. The first one was an assessment of drop shedding by airflow in icing conditions [220] [61], comparing with the behavior at room temperature. The second test was a

measurement of drop freezing time, which is quite a common testing method for the anti-icing properties of superhydrophobic surfaces [37] [38] [218] [221] [222]. All tests were performed at the Surface Engineering and Instrumentation Lab (SEIL) headed by Professor Alidad Amirfazli at York University, Toronto, Canada.

## DROP SHEDDING IN ICING CONDITIONS

The shedding of drops lying on a substrate is a crucial phenomenon in many applications, ranging from oil recovery [223] to aircrafts [224] [225] and wind turbines [226]. Thus, the shedding phenomenon has been investigated both by simulation [227] [228] and experiments [43] [229] [230]. However, in the literature very few papers deal with drop shedding in icing conditions [220] [61].

When a sessile drop lies on a surface and airflow is activated, two forces play a role in determining whether shedding will happen or not: drag force induced by airflow and adhesion between the drop and the surface. As soon as the drag force exceeds the adhesion force, the drop starts to move. The correspondent value of airflow velocity is called critical air velocity and depends on two factors, namely drop shape and drop adhesion. The latter is dependent on the wetting characteristics of the surface, namely contact angle, contact angle hysteresis, contact line shape and size of the sessile drop [231]. Lower contact angles generally imply higher adhesion, therefore higher critical velocities [43]. In particular, many papers [232] [233] show that superhydrophobic surfaces (SHS) display very low adhesion and critical velocities in normal conditions (e.g. room temperature, low relative humidity) due to the presence of air trapped within surface micro/nano-features [49]. However, lowering the temperature down to 0°C and below causes remarkable decrease in the contact angle of a drop on a SHS [234]. At the same time, an increase in contact angle hysteresis is observed. Such behavior has been attributed to the condensation of moisture within surface features, creating a liquid water phase that favors wetting and drop adhesion [235]. The presence of micro/nanoscale features (e.g. surface roughness) favors such condensation phenomena [236] [237]. Furthermore, formation of a frost layer close to the drop-surface contact line is also favored from surface roughness [219], further favoring drop adhesion. In these high-adhesion conditions, a Cassie-to-Baxter transition is likely to occur for the sessile drop on the SHS [238]. For all these reasons, it is interesting to determine the drop shedding behavior of aluminum surfaces bearing the nanostructured hybrid coating so far described.

Another aspect we wanted to address was the effect of surface roughness on drop shedding behavior for superhydrophobic surfaces. More precisely, we deposited the nanostructured coating on aluminum

with either smooth or rough (sandblasted) surface to assess potential effects of microscale roughness on drop shedding behavior.

### Materials and methods

For drop shedding tests, we used Al 1050 99% H24 alloy foils (75 x 25 x 2 mm<sup>3</sup>) as a substrate. One of the two sides of the foil was quite smooth, with a  $R_a = 0.26 \pm 0.02 \mu\text{m}$  as determined by ContourGT-K 3D optical microscope (Bruker Nano GmbH). Meanwhile, the other side of the foil was sandblasted to reach a roughness  $R_a = 3.57 \pm 0.05 \mu\text{m}$ . These foils were coated at CNR-ISTEC with the usual procedure, taking care of both sides of each sample. As-fabricated samples were then shipped to York University for further characterization and testing.

Advancing and receding contact angles with water were measured on two points of two surfaces per type (smooth and sandblasted) with a home-made optical contact angle system, first dispensing then withdrawing a water drop with volume 25  $\mu\text{L}$ .

We performed drop shedding tests in icing conditions with the lab-scale air tunnel available at SEiL, which is schematized in Figure 67. In the tunnel, airflow was generated by a fan (maximal air flow of 12 m/s, DPP120-24-1 power supply) and its velocity was changed by providing different tension to the fan (from 0 to 5 V). Meanwhile, airflow temperature was regulated with a chiller (HAAKE KT-90, ethanol bath, range 40  $\div$  -90  $^{\circ}\text{C}$ , watercooled). An electronic sensor fitted about 7 cm downstream of the test section was used to monitor airflow temperature and velocity. The surface was placed on a Peltier cell (TE Technology, CP-031, 12 V and 5 A) to modulate surface temperature, which was monitored with a thermocouple. The test chamber (cross section 216  $\times$  470 mm), which contained the Peltier cell and the sample, was made of transparent walls and a lid for sample handling and drop dispensing. The diffused light of a lamp was used to project an image of the surface on a Phantom v4.3 high-speed camera (Vision Research Inc.), which was triggered manually to start acquisition of the shedding process with a frame rate of 500 fps and camera resolution of 43  $\mu\text{m}/\text{pixel}$ .

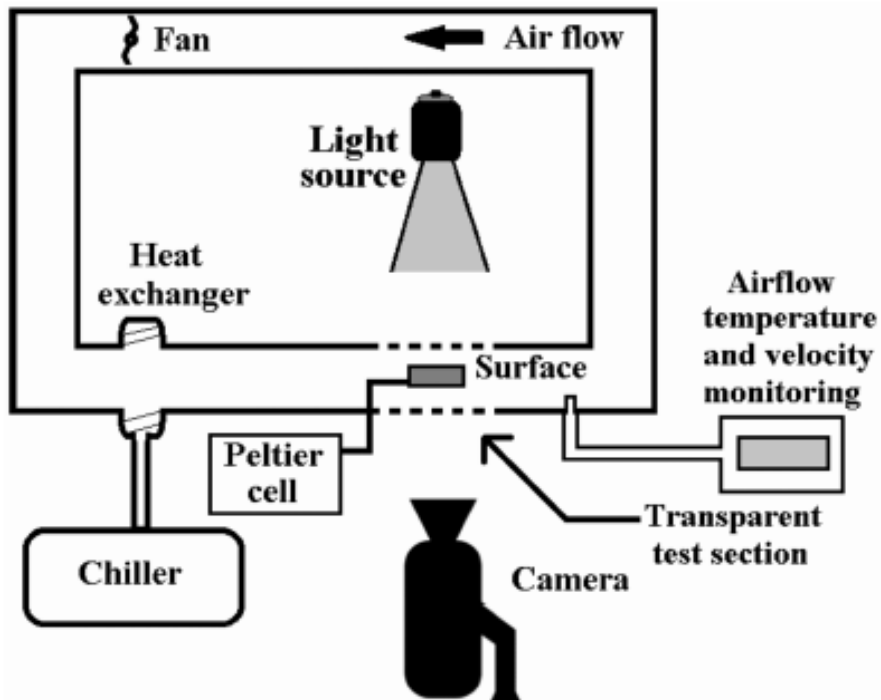


Figure 66. Schematic representation of the lab-scale wind tunnel used for drop shedding experiments in icing conditions. Image is reproduced from the paper by Mandal et al [61].

Before each test, we quickly assessed the superhydrophobic behavior of the surface by dropping water on it. We used only surfaces on which drops rolled off with no sticking. Measurements were performed according to the following procedure:

1. For measurements at low temperature, we let airflow temperature and Peltier temperature to equilibrate until they reached similar values;
2. We placed the sample on the Peltier cell and waited until temperature reached a stable value, close to that of airflow temperature. We tried to make sure that no frost had formed on the surface. However, it was very difficult to determine the presence of frost on rough surfaces due to the whitish resemblance of the samples;
3. We placed the drop in the middle of the surface with a suitable pipette or syringe and started image acquisition after few seconds;
4. We slowly increased airflow velocity until shedding occurred, then stopped image acquisition.

Recorded frames were analyzed manually with CineViewer Application (Vision Research Inc.) and ImageJ software. First, we determined the positions of the downstream contact point before shedding ( $x_{down,0}$ ). Scrolling through the frames, we selected the frame at which shedding occurred as the one in which the downstream contact point had moved by 5 pixels, as adopted by Milne and Amirfazli [43]. The correspondent positions of the downstream ( $x_{down,shed}$ ) and upstream ( $x_{up,shed}$ ) contact points were

determined to calculate the base length of the drop  $L_b$ . Furthermore, we measured drop contact angles both upstream ( $\theta_{min}$ ) and downstream ( $\theta_{min}$ ), their difference being defined as contact angle hysteresis  $\Delta\theta$ . Then, critical airflow velocity for shedding  $U_c$  was determined as the value of airflow velocity at the time when shedding occurred.

In our work, we tested two different drop volumes, namely 10  $\mu\text{L}$  and 50  $\mu\text{L}$ . It was not possible to test larger volumes as such drops immediately rolled off the surface at room temperature even for  $U = 0$  (e.g. with no airflow). As mentioned, the tests were performed at room temperature (about 24°C) and at -5°C. The experiment was repeated three times for each condition (temperature, drop volume and surface type).

### Results and discussion

Average values of advancing and receding contact angle and contact angle hysteresis are reported in Table 18. Notably, ACA and RCA values are significantly higher on smooth substrates, but it is probably due to different lighting conditions (e.g. darker image obtained for rough surfaces due to light scattering). Meanwhile, CAH is almost identical for the two types of substrate.

Surface type	ACA (°)	RCA (°)	CAH (°)
Rough	159.0	153.6	5.4
Smooth	166.9	162.2	4.7

Table 18. Average values of advancing contact angle (ACA), receding contact angle (RCA) and contact angle hysteresis (CAH) for rough and smooth aluminum substrates with nanostructured hybrid coating.

Results for drop shedding at room temperature are reported in Table 19. Four snapshots of drops at the moment of shedding are shown in Figure 68.

Surface	Vol (mL)	T (°C)		L <sub>b</sub> (mm)		θ <sub>MAX</sub> (°)		θ <sub>MIN</sub> (°)		Δθ (°)		U <sub>c</sub> (m/s)	
		Avg	St.dev	Avg	St.dev	Avg	St.dev	Avg	St.dev	Avg	St.dev	Avg	St.dev
Rough	10	23.5	0.2	1.7	0.2	160.5	5.9	154.0	4.6	6.5	1.4	0.6	0.1
Rough	50	24.1	0.6	2.9	0.1	162.6	2.6	153.2	4.9	9.4	2.6	0.5	0.1
Smooth	10	24.0	0.2	1.4	0.0	159.8	3.4	155.5	2.8	4.3	0.6	0.9	0.1
Smooth	50	25.1	0.1	2.7	0.1	163.8	1.6	156.3	1.7	7.5	2.9	0.5	0.1

Table 19. Results of drop shedding tests at room temperature on rough and smooth aluminum with hybrid coating. Reported temperature was calculated as the average between surface temperature and airflow temperature. Each value is the average of three experiments.

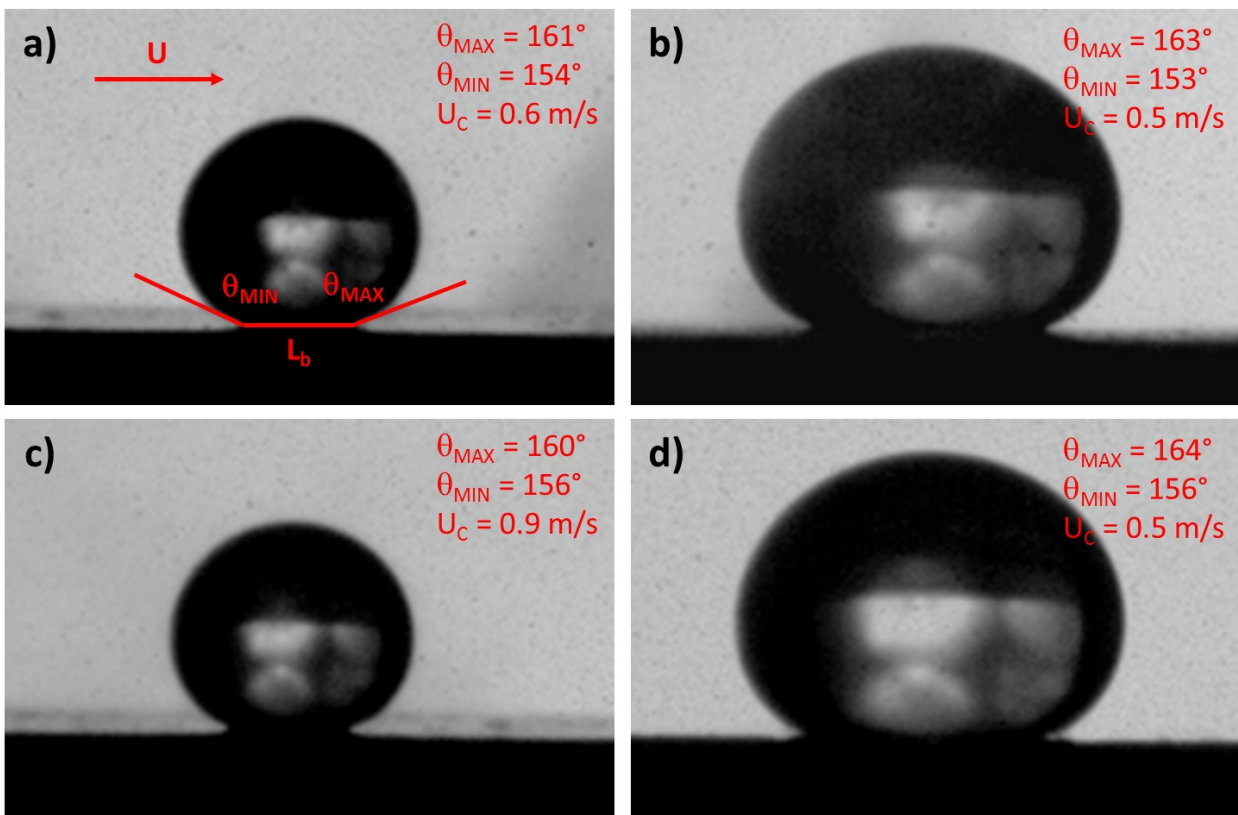


Figure 67. Drops at the moment of shedding on coated aluminum surfaces at room temperature (about 24°C): a) 10 μL drop on rough surface; b) 50 μL drop on rough surface; c) 10 μL drop on smooth surface; d) 50 μL drop on smooth surface. Upstream (θ<sub>MIN</sub>) and downstream (θ<sub>MAX</sub>) contact angles, direction of airflow U and drop base length L<sub>b</sub> are reported in panel a). In every panel, average values for θ<sub>MAX</sub>, θ<sub>MIN</sub> and critical airflow velocity U<sub>c</sub> for that experimental condition are reported.

At room temperature, drop shedding was extremely easy in all tested conditions. Shedding always occurred at  $U < 1$  m/s for both tested drop volumes. Such low  $U_c$  have never been reported before in the literature, especially for small drops (e.g. volume 10 μL) for which critical velocity is usually higher due to small drag force. In this case, there seems to be a small decrease in  $U_c$  when increasing drop volume, especially on the smooth surface, but the absolute values remain very low. Meanwhile, an



unpredicted increase in contact angle hysteresis was observed for larger volumes, but errors on the measurements were still quite high. Most remarkably, no significant difference in shedding behavior was observed between rough and smooth coated surfaces.

Drop shedding experiments at freezing temperature gave radically different results, as displayed in Table 20. One frame per surface is reported in Figure 69 to represent the observed drop behavior.

Surface	Vol (mL)	T (°C)		L <sub>b</sub> (mm)		θ <sub>MAX</sub> (°)		θ <sub>MIN</sub> (°)		Δθ (°)		U <sub>c</sub> (m/s)	
		Avg	St.dev	Avg	St.dev	Avg	St.dev			Avg	St.dev	Avg	St.dev
Rough	10	-4.8	0.2	1.6	0.1	155.2	3.1	144.8	4.6	10.4	3.1	2.5	0.2
Rough	50	-3.9	0.4	3.9	0.2	FREEZE							
Smooth	10	-2.7	0.6	1.6	0.0	163.3	1.6	144.8	4.1	18.5	5.6	3.2	0.1
Smooth	50	-1.7	0.1	4.4	0.1	134.2	3.1	89.6	6.7	44.6	9.8	6.2	0.9

Table 20. Results of drop shedding tests at freezing temperature on rough and smooth aluminum with hybrid coating. Reported temperature was calculated as the average between surface temperature and airflow temperature. Each value is the average of three experiments.

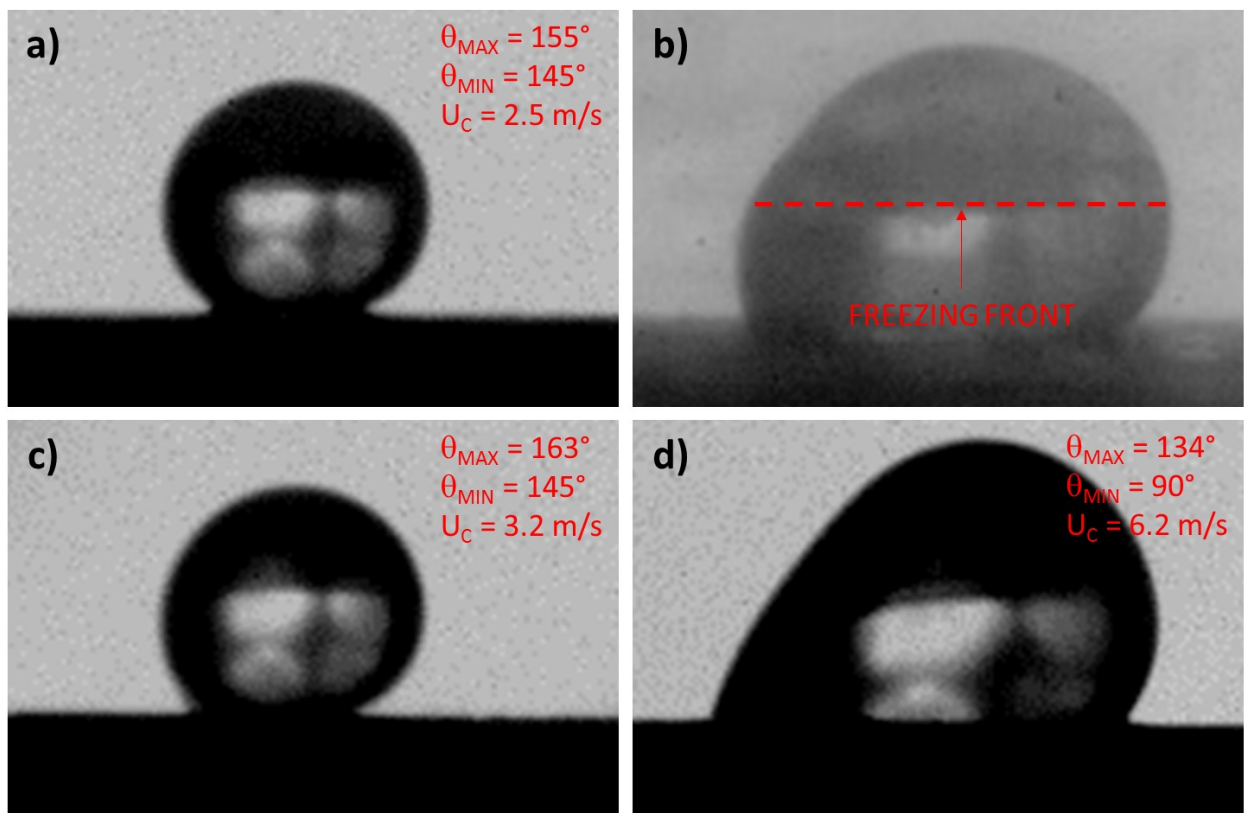


Figure 68. Drops at the moment of shedding on coated aluminum surfaces at room temperature (about 24°C): a) 10 μL drop on rough surface; b) 50 μL drop on rough surface; c) 10 μL drop on smooth surface; d) 50 μL drop on smooth surface. In every panel, average values for θ<sub>MAX</sub>, θ<sub>MIN</sub> and critical airflow velocity U<sub>c</sub> for that experimental condition are reported.

On rough surfaces, two distinct behaviors were observed depending on drop volume. Small drops (10  $\mu\text{L}$ ) were still shed by airflow, however they showed significantly higher adhesion ( $\Delta\theta = 10^\circ$ ) and critical velocity ( $U_c = 2.5 \text{ m/s}$ ) compared to room temperature experiments (Figure 69a). On the other hand, large drops (50  $\mu\text{L}$ ) did not shed at all due to freezing, as shown in Figure 69b. A freezing front propagated upward starting from the bottom of the drop, showing a heterogeneous freezing mechanism [239]. Such behavior suggests the presence of frost on the surface, even though we could not detect any clearly visible ice crystal on the surface probably due to the whitish resemblance of sandblasted aluminum. The sub-zero temperatures reached in the entire test section led to condensation of air humidity, as confirmed by the foggy view in Figure 69b, and in turn to frost formation. The presence of frost on the surface has a crucial role in heterogeneous nucleation on superhydrophobic surfaces [219]. Unfortunately, the experimental setup did not allow for control of relative humidity of the airflow, therefore such parameter is unknown. Such behavior was not observed in previous papers [220] [61], probably due to the much smaller roughness of the investigated superhydrophobic surfaces.

On smooth surface, 10  $\mu\text{L}$  drops displayed quite similar behavior with only slightly larger adhesion and  $U_c$  compared to rough surfaces. Nonetheless, shedding was observed for 50  $\mu\text{L}$  drops, but adhesion ( $\Delta\theta = 45^\circ$ ) and critical velocity ( $U_c = 6.2 \text{ m/s}$ ) hugely increased compared to room temperature experiments. It must be noted that, due to difficulties in temperature control, drop shedding experiments on smooth surfaces were performed at slightly higher temperatures compared to tests on rough surfaces. This aspect may have influenced the observed output, therefore it was hard to distinguish effects of roughness on shedding behavior. However, it is clear that shedding properties of our superhydrophobic surfaces strongly depend on temperature. Previously reported superhydrophobic surfaces [220] [61] displayed a weaker dependence of their shedding properties on temperature (e.g.  $U_c$  increased only slightly). Even though contact angle values for those surfaces were similar to those for our smooth superhydrophobic surfaces (around  $150^\circ$  at room temperature for all volumes, dependent on volume and decreasing to  $120^\circ$  at freezing T), shedding was much easier. The reason might lie in the different surface morphology: in the aforementioned papers, there is no evidence of the topography of the investigated SHS, but judging from the fabrication method (etching in concentrated HCl) a terrace-like structure is expected [9], similar to those described in the drop rebound studies [118]. Meanwhile, the SHS here described possess a flower-like nanostructure. The two types of SHS have similar roughness ( $R_a$  about 0.3  $\mu\text{m}$ ), therefore surface texture is likely to play a significant role in drop shedding at freezing temperature. However, this is just a hypothesis that requires deeper investigations, for example a comparative study of drop shedding properties at freezing temperatures for SHS with analogous wetting properties but different surface structure.

Whatever the substrate (rough or smooth aluminum), in all tested samples a nanostructured coating was present. In a previous paper [61], Mandal *et al.* showed that nanostructured, superhydrophobic surfaces have a drop shedding behavior which is strongly dependent on temperature. The authors compared drop shedding behavior for surfaces with different wetting properties, including smooth hydrophobic and nanostructured superhydrophobic surfaces (SHS). It emerged that, while at room temperature SHS displayed the lowest  $U_c$  of all samples and it did not depend on drop volume, at  $T = -5^\circ\text{C}$  critical velocity for SHS was higher than for smooth hydrophobic surfaces. Such behavior is due to increased adhesion, as confirmed by the increase in contact angle hysteresis. In fact, adhesion force  $F_{adh}$  can be calculated as:

$$F_{adh} = \gamma L_b (\cos \theta_{min} - \cos \theta_{max})$$

In this equation,  $\gamma$  is water surface tension. When lowering temperature, for 10  $\mu\text{L}$  drops base length does not change significantly and only  $\theta_{MIN}$  is sensibly decreased (from  $155^\circ$  at  $T = 24^\circ\text{C}$  to  $145^\circ$  at  $T = -5^\circ\text{C}$ ). However, for 50  $\mu\text{L}$  drops overall contact angles become smaller, resulting into larger  $L_b$  (from less than 3 mm at  $T = 24^\circ\text{C}$  to about 4 mm at  $T = -5^\circ\text{C}$ ). In such conditions, adhesion will be largely increased. Moreover, lower contact angles have effect on the drag force exerted by airflow. The authors wrote an equation to define drag force  $F_{drag}$  on a sessile drop at shedding point (e.g. when  $F_{adh} = F_{drag}$ ):

$$F_{drag} = \frac{1}{2} C_D \rho U_c^2 A$$

In this equation,  $C_D$  is drag coefficient,  $\rho$  is air density and  $A$  is drop frontal area. Briefly,  $C_D$  decreases with decreasing drop height and frontal area, with both parameters depending on contact angles.

## Conclusions

We performed drop shedding experiments on superhydrophobic surfaces with different roughness at two temperatures, namely  $24^\circ\text{C}$  and  $-5^\circ\text{C}$ . While at room temperature critical velocity is extremely low (below 1 m/s, the smallest value ever reported) and almost non-dependent on drop volume, at freezing temperature shedding became much harder. Contact angles decreased, especially for large drop volumes, causing higher adhesion force and lower drag coefficient. The result was a much higher  $U_c$ .

Comparing these results to those in the literature, we hypothesized a relevant role of surface texture on such drop shedding behavior, but further studies are needed to confirm it.

Furthermore, on rough surfaces the presence of a frost layer became relevant, causing drop freezing in large drops before they could be shed. This effect could not be avoided in the available setup, thus strongly hindering a reliable evaluation of drop shedding at freezing temperatures on rough surfaces.

These results highlight that superhydrophobic surfaces might not maintain their properties in all conditions. Therefore, it is necessary to evaluate their properties in real operational conditions in order to improve the design and the fabrication processes.

## DROP FREEZING TIME

One of the easiest ways to quantify the anti-icing properties of a surface is to measure the time in which a sessile, supercooled drop freezes [37] [38] [218] [221] [222]. If experimental conditions are controlled properly, such drop freezing time will depend only on surface properties. The longer the drop freezing time, the more difficult will be for ice to form, e.g. the more “icephobic” will be surface. In the aforementioned papers, the authors measured drop freezing time on SHS and compared them to smooth surfaces with various wetting properties, from hydrophilic to hydrophobic. SHS displayed the longest freezing time and it was attributed to high contact angles, which imply small surface-drop contact area and minimized heat exchange between the liquid drop and the solid phase. Furthermore, for drops in the Cassie-Baxter wetting state, air pockets trapped within surface features act as thermal insulators, further reducing thermal exchange between solid and liquid phases [139]. However, the role of SHS roughness is still unclear. In fact, a paper by Jung *et al.* [240] showed that hydrophilic surfaces with nano-scale roughness have longer drop freezing times than SHS with hierarchical structure. Surface roughness should be comparable to or smaller than critical ice nucleus radius (e.g. the minimum size that a growing ice crystal needs to reach in order to maintain a stable freezing process) to be effective in delaying drop freezing [40]. Moreover, the presence of frost on the surface strongly limits anti-icing properties of materials [237], as already discussed in the drop shedding tests at freezing temperature.

For all these reasons, we chose to perform drop freezing time measurements on our nanostructured, superhydrophobic coatings in order to assess their potential anti-icing properties in static conditions. We addressed the roughness issue by comparing three different surfaces, namely the nanostructured superhydrophobic coating on smooth or rough (sandblasted) aluminum and Teflon coating on smooth aluminum. Furthermore, we measured drop freezing times for two different liquids, namely deionized

water (DI) and synthetic seawater (SW, prepared as per ASTM D1141 standard), to assess possible differences in behavior determined by the presence of solutes in water. In applications such as offshore wind turbines, surfaces get in contact with salty water, thus their behavior in such environments needs to be addressed.

## Materials and methods

For drop freezing time tests, we used the same superhydrophobic surfaces mentioned in the section about drop shedding tests in icing conditions. Briefly, Al 1050 99% H24 alloy foils ( $75 \times 25 \times 2 \text{ mm}^3$ ) were used as substrates, with one smooth side ( $R_a = 0.26 \pm 0.02 \text{ }\mu\text{m}$ ) and one rough side ( $R_a = 3.57 \pm 0.05 \text{ }\mu\text{m}$ ). The nanostructured hybrid coating was fabricated at CNR-ISTEC with the usual procedure, taking care of both sides of each sample, then shipped to York University for the tests. As all samples were fabricated in a single batch, we did not repeat contact angle measurements on the surfaces used for these tests and adopted those reported in Table 18. Meanwhile, Teflon coated surface were prepared according to the method reported by Mandal *et al.* [61]. An aluminum sheet with the same surface area (thickness 1 mm instead of 2 mm) was cleaned with water and acetone and used as substrate. A solution of FC-75 (3-M) and Teflon AF (Dupont) in 5:1 v/v ratio was spin-coated on the surface, then the sample was placed in a vacuum chamber for 1 hour for drying. Analogous Teflon-coated smooth surfaces reported in the literature [219] have  $ACA = 121.9^\circ \pm 1.6^\circ$  and  $RCA = 108.5^\circ \pm 2.0^\circ$ .

We performed drop freezing time measurements with the same lab-scale air tunnel used for drop shedding tests in icing conditions, which is schematized in Figure 67. In this case, Phantom v4.3 high-speed camera (Vision Research Inc.) was operated at a much slower frame rate (24 fps) in order to have sufficient acquisition time. Prior to each test, we dropped DI water on the surface to assess their superhydrophobic behavior (only for smooth and rough SHS). We used only surfaces on which drops rolled off with no sticking. Measurements were performed according to the following procedure:

1. We let airflow temperature and Peltier temperature to equilibrate until they reached similar values, as close as possible to  $-10^\circ\text{C}$ . The airflow was maintained at minimum speed  $U \approx 2 \text{ m/s}$  to keep airflow at freezing temperature;
2. We placed the sample on the Peltier cell and waited until temperature reached a stable value. We tried to make sure that no frost had formed on the surface;
3. We placed the drop in the middle of the surface with a suitable pipette or syringe and started image acquisition after few seconds;
4. We waited until drop freezing occurred, then stopped image acquisition.

Recorded frames were analyzed manually with CineViewer Application (Vision Research Inc.) and ImageJ software. We set  $t = 0$  as the moment in which the drop detached from the needle of the dispensing system and  $t = t_{freeze}$  when an area of the drop changes its aspect from transparent to opaque due to ice formation. Furthermore, we measured drop contact angles at the two sides of the drop profile and calculated their average  $\theta_{avg}$ . We also determined whether freezing started from the liquid-solid interface (heterogeneous nucleation) or from the liquid-air interface (homogeneous nucleation) [241].

In our work, we tested two different drop volumes, namely 10  $\mu\text{L}$  and 50  $\mu\text{L}$ . The experiment was repeated from 3 to 5 times for each condition (liquid, drop volume and surface type).

## Results and discussion

Drop freezing data for DI water are reported in Table 21, together with  $\theta_{avg}$  measured during the experiments.

Substrate	Experiment N°	T(°C)	Volume ( $\mu\text{L}$ )	$\theta_{avg}$ (°)	Mechanism	$t_{freeze}$ (s)
Rough	1	-10.4	10	150.5	Hom.	654.956
Rough	2	-10.3	10	152.6	Hom.	116.542
Rough	3	-10.0	10	151.4	Hom.	662.289
Rough	4	-10.1	10	152.3	Hom.	38.541
Rough	1	-11.0	50	148.6	Het.	3.292
Rough	2	-10.5	50	129.3	Hom.	191.500
Rough	3	-10.5	50	128.2	Hom.	101.625
Rough	4	-10.2	50	126.5	Hom.	162.999
Smooth	1	-10.2	10	142.9	Hom.	72.75
Smooth	2	-10.0	10	144.8	Hom.	112.833
Smooth	3	-10.0	10	148.1	Hom.	95.667
Smooth	1	-10.1	50	129.6	Hom.	79.958
Smooth	2	-9.9	50	123.9	Hom.	54.208
Smooth	3	-9.9	50	125.0	Hom.	221.291
Teflon	1	-10.2	10	116.6	Hom.	168.75

Teflon	2	-10.1	10	114.0	Hom.	55.833
Teflon	3	-9.9	10	125.6	Hom.	247.499
Teflon	1	-10.0	50	120.4	Hom.	67.291
Teflon	2	-10.3	50	119.3	Hom.	116.083
Teflon	3	-10.2	50	109.0	Hom.	246.916

Substrate	T(°C)	Volume (μl)	$\theta_{avg}$ (°)	St.dev	$t_{freeze}$ (s)	St.Dev
Rough	-10.2	10	151.7	1.0	368	337
Rough	-10.5	50	133.1	10.4	115	83
Smooth	-10.0	10	145.2	2.7	94	20
Smooth	-10.0	50	126.2	3.0	118	90
Teflon	-10.1	10	118.7	6.1	157	79
Teflon	-10.2	50	116.2	6.3	143	76

Table 21. Raw data (upper table) and average values (lower table) for DI water drop freezing experiments.

I chose to report also the raw experimental data to better represent the high scattering of observed drop freezing times. The first remarkable result is that, in all cases except one, we observed homogeneous nucleation of ice (Figure 70): the drop quickly freezes starting from the upstream side of the drop-air interface, then another slower freezing process occurs from the drop-surface interface upwards (heterogeneous freezing). Homogeneous freezing is caused by evaporative cooling at the drop-air interface, due to non-zero airflow velocity [241]: a supercooled water droplet in an unsaturated gas will undergo evaporation, which reduces the liquid temperature locally, at the gas-liquid interface. This will lead to probable ice nucleation. The occurring of homogeneous freezing makes it difficult to establish the surface influence in the freezing process.

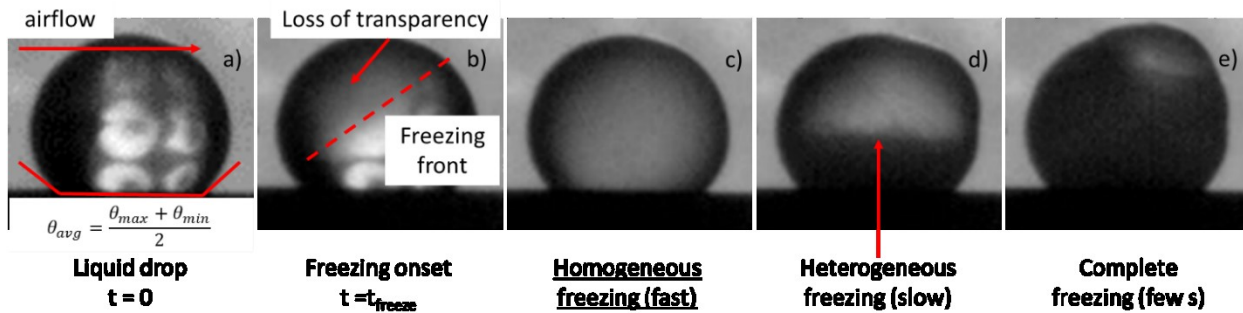


Figure 69. Freezing of a 10  $\mu\text{l}$  drop on a SHS: a) liquid drop at  $t = 0$  with contact angle  $\theta_{avg}$ ; b) homogeneous freezing onset with loss of transparency and formation of a freezing front (dashed line) at the drop-air interface at  $t = t_{freeze}$ ; c) completion of homogeneous freezing in less than 1 s (few frames); d) propagation of heterogeneous nucleation front from the bottom upwards (indicated by the arrow); e) completion of freezing in few s.

Looking at  $t_{freeze}$  values, their very large scattering must be considered. Such values fall in a three orders of magnitude span on the same surface, making it extremely difficult to compare average values due to huge standard deviations. However, if we look at the single measured freezing times, the highest values were observed for 10  $\mu\text{l}$  drops on rough SHS, with two values exceeding 600 s. However, surfaces of the same type also gave much smaller values (e.g. less than 40 s). Calculating average freezing times for 10  $\mu\text{l}$  drops, we obtained a much higher value for rough SHS compared to other tested surfaces, but the huge standard deviation cannot be neglected. On the other hand, 50  $\mu\text{l}$  drops showed very similar freezing times on all tested surfaces. This is expected, as homogeneous freezing is even more favored for drops with large surface area. Another interesting result is that contact angle on SHS decreases with increasing drop volume, while it remains constant on Teflon surface. This behavior has already been reported in the literature [242].

We tried to extrapolate useful trends by plotting freezing time versus drop volume (Figure 71) and average contact angle (Figure 72).



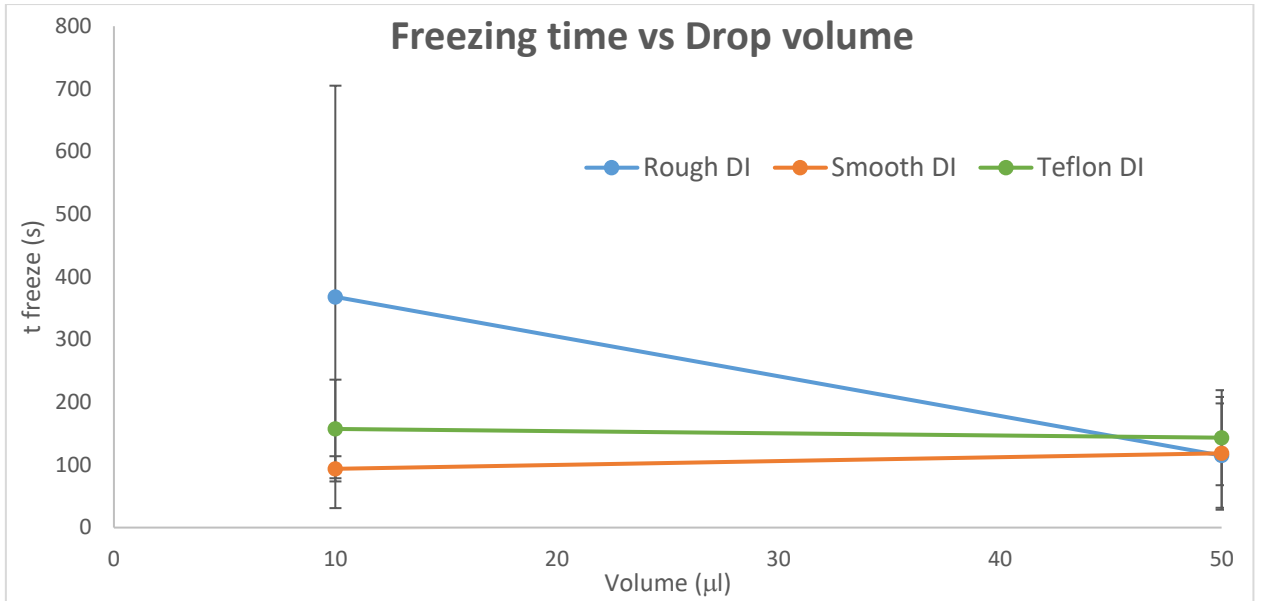


Figure 70. Freezing time versus drop volume for DI water drop freezing experiments on smooth (orange) and rough (blue) superhydrophobic surfaces, as well as on Teflon hydrophobic surfaces (green). Standard deviations are used as error bars. Lines are just a guide to the eye.

The  $t_{\text{freeze}}$  vs drop volume plot (Figure 71) confirms that rough SHS show the highest  $t_{\text{freeze}}$  for 10  $\mu\text{l}$  drops, while smooth SHS and hydrophobic Teflon surfaces have analogous drop freezing times. Concerning 50  $\mu\text{l}$  drops, such difference vanishes as  $t_{\text{freeze}}$  becomes identical for all tested surfaces.

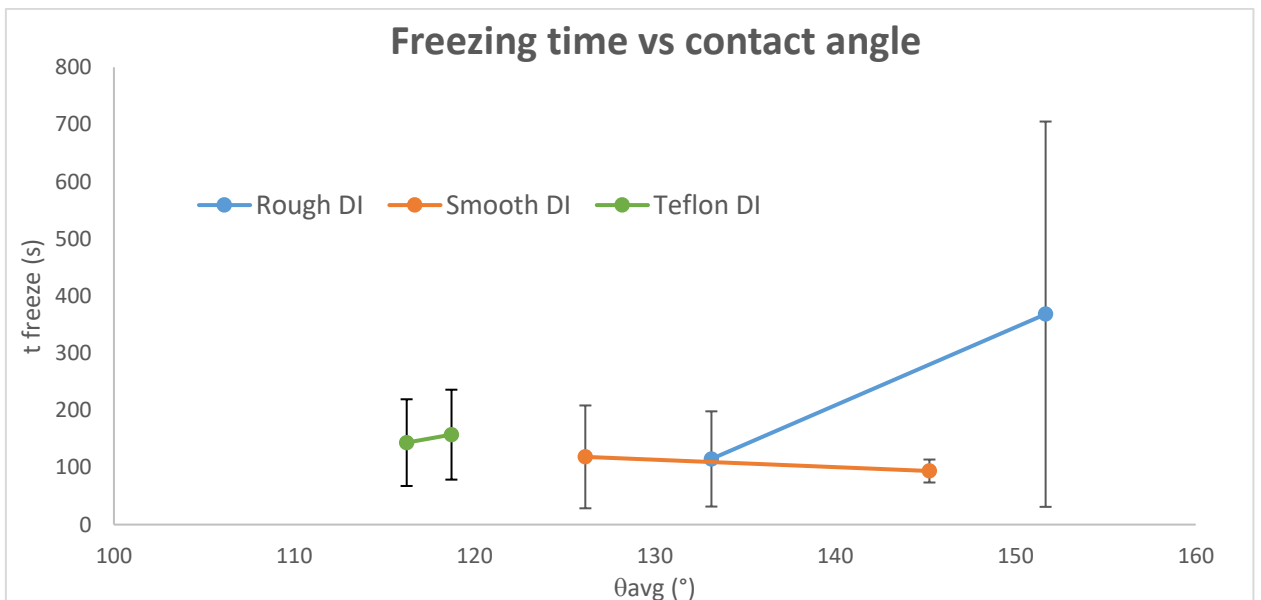


Figure 71. Freezing time versus average contact angle for DI water drop freezing experiments on smooth (orange) and rough (blue) superhydrophobic surfaces, as well as on Teflon hydrophobic surfaces (green). Standard deviations are used as error bars. Lines are just a guide to the eye.

From the  $t_{\text{freeze}}$  vs  $\theta_{\text{avg}}$  plot (Figure 72), it seems that a contact angle above  $150^\circ$  is necessary to observe a delay in drop freezing time, while surfaces with lower  $\theta_{\text{avg}}$  yield analogous  $t_{\text{freeze}}$ . However, it is worth to remember that homogeneous nucleation occurred in almost all cases, therefore the influence of surface wetting properties on drop freezing time must be evaluated carefully. Moreover, extremely large standard deviations must be taken into account.

The same experiments were repeated using synthetic seawater as liquid phase. Results are listed in Table 22.

Substrate	Experiment N°	T(°C)	Volume ( $\mu\text{l}$ )	$\theta_{\text{avg}}$ (°)	Mechanism	$t_{\text{freeze}}$ (s)
Rough	1	-9.4	10	141.5	Hom.	259.625
Rough	2	-9.7	10	150.0	Hom.	55.708
Rough	3	-9.3	10	144.6	Hom.	78.208
Rough	4	-9.2	10	143.8	Hom.	51.458
Rough	5	-9.1	10	150.4	Hom.	51.000
Rough	1	-9.3	50	132.9	Hom.	11.458
Rough	2	-9.1	50	136.1	Hom.	10.751
Rough	3	-9.3	50	115.3	Hom.	31.000
Rough	4	-9.5	50	125.0	Het.	16.249
Rough	5	-8.8	50	119.4	Het.	6.624
Smooth	1	-9.3	10	152.9	Hom.	5.292
Smooth	2	-9.1	10	132.0	Hom.	215.458
Smooth	3	-9.4	10	145.7	Hom.	14.917
Smooth	4	-9.5	10	143.9	Hom.	39.75
Smooth	5	-9.0	10	141.4	Hom.	36.916
Smooth	1	-9.1	50	110.7	Hom.	16.043
Smooth	2	-9.6	50	115.2	Het.	0.541
Smooth	3	-9.3	50	102.3	Hom.	10.666
Smooth	4	-9.1	50	118.2	Het.	53.708
Smooth	5	-9.0	50	123.1	Hom.	39.459
Teflon	1	-9.5	10	119.4	Hom.	281.541

Teflon	2	-9.3	10	117.9	Hom.	755.331
Teflon	3	-9.2	10	118.7	Hom.	40.666
Teflon	1	-9.7	50	124.0	Hom.	213.499
Teflon	2	-9.6	50	105.0	Hom.	80.291
Teflon	3	-9.5	50	119.3	Hom.	168.625

Substrate	T(°C)	Volume (μl)	$\theta_{avg}$ (°)	St.dev	$t_{freeze}$ (s)	St.Dev
Rough	-9.3	10	146.0	3.9	99	90
Rough	-9.2	50	125.7	8.8	15	9
Smooth	-9.2	10	143.2	7.6	62	87
Smooth	-9.2	50	113.9	7.9	24	22
Teflon	-9.3	10	118.7	0.8	359	297
Teflon	-9.6	50	116.1	9.9	154	55

Table 22. Raw data (upper table) and average values (lower table) for seawater drop freezing experiments.

Even with seawater drops, homogeneous nucleation was favored over heterogeneous nucleation (represented in Figure 73), which occurred only 4 times out of 10 measurements with 50 μl drops on SHS (both rough and smooth) and never on Teflon. Once again,  $t_{freeze}$  values were very scattered, causing large standard deviation. Remarkably, the highest measured freezing time values were observed for Teflon surfaces, as well as the highest average for both tested volume. Moreover, average  $t_{freeze}$  on all surfaces decreased with increasing drop volume.

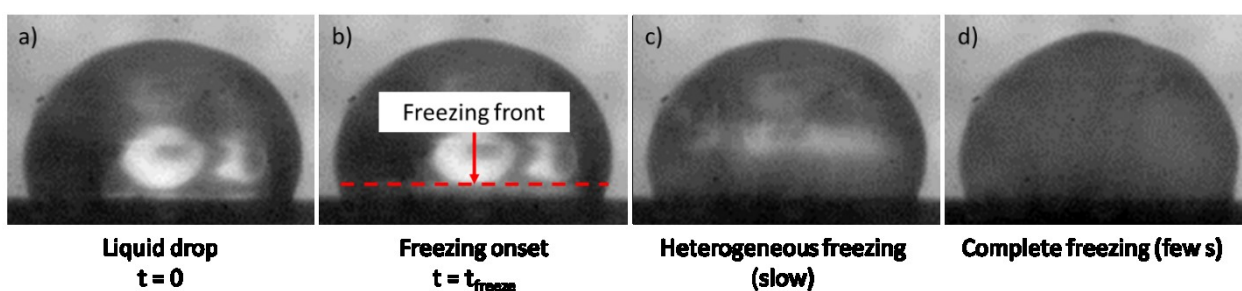


Figure 72. Freezing of a 50 μl drop on a SHS: a) liquid drop at  $t = 0$ ; b) heterogeneous freezing onset with loss of transparency and formation of a freezing front moving from the drop-solid interface upwards (dashed line) at  $t = t_{freeze}$ ; c) heterogeneous freezing with slow propagation of the freezing front over a timespan of few s; d) completion of drop freezing.

We plotted freezing time versus drop volume (Figure 74) and average contact angle (Figure 75) also for seawater experiments.

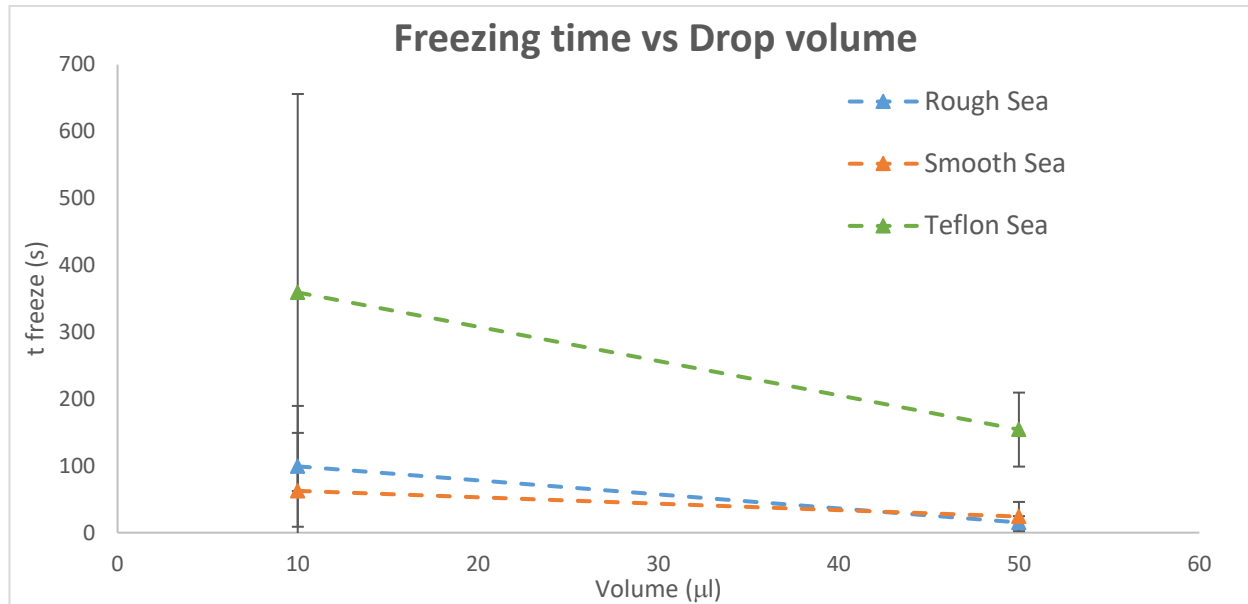


Figure 73. Freezing time versus drop volume for seawater drop freezing experiments on smooth (orange) and rough (blue) superhydrophobic surfaces, as well as on Teflon hydrophobic surfaces (green). Standard deviations are used as error bars. Lines are just a guide to the eye.

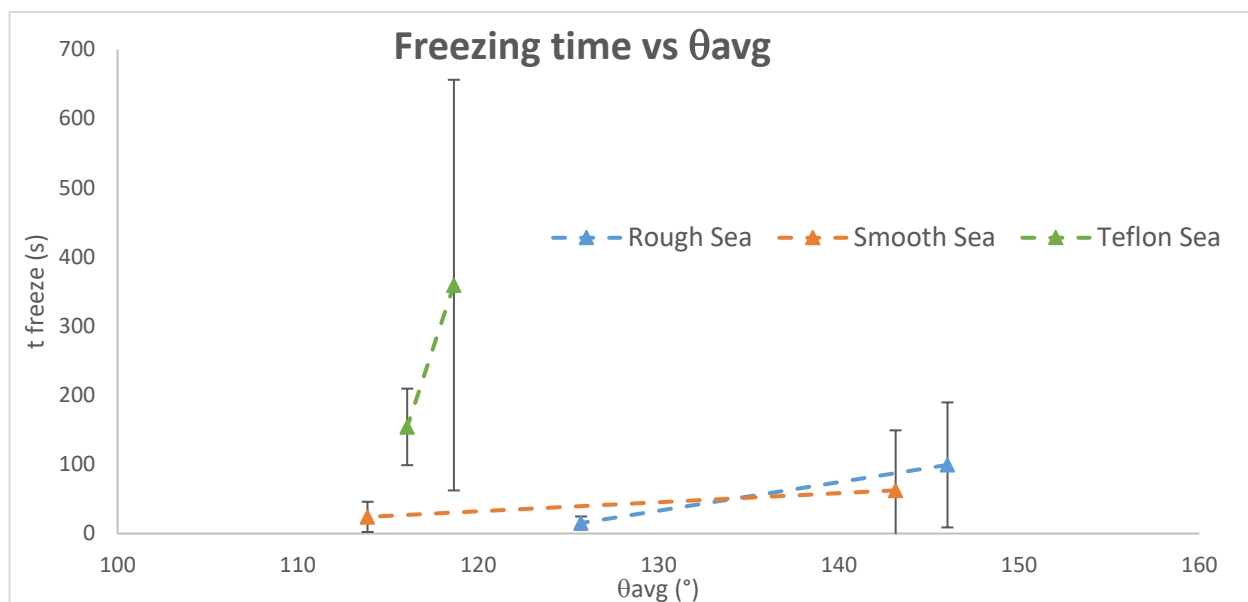


Figure 74. Freezing time versus average contact angle for seawater drop freezing experiments on smooth (orange) and rough (blue) superhydrophobic surfaces, as well as on Teflon hydrophobic surfaces (green). Standard deviations are used as error bars. Lines are just a guide to the eye.

As already mentioned, the  $t_{\text{freeze}}$  vs drop volume plot (Figure 74) confirms that Teflon surfaces show the highest  $t_{\text{freeze}}$  for both tested drop volumes. On the other hand, smooth and rough SHS have almost identical drop freezing times.

From the  $t_{\text{freeze}}$  vs  $\theta_{\text{avg}}$  plot (Figure 75), no clear correlation between these two parameters could be extrapolated for seawater experiments. In fact, Teflon surfaces have  $\theta_{\text{avg}}$  values close to those of 50  $\mu\text{l}$  drops on SHS and still their  $t_{\text{freeze}}$  was much longer. However, the occurrence of homogeneous nucleation still hinders a proper evaluation of results.

Most remarkably, the use of seawater instead of DI water did not increase  $t_{\text{freeze}}$  for any of the two SHS, while it did only for 10  $\mu\text{l}$  drops on Teflon surface. This was an unexpected result, as the depressed freezing point did not influence the homogeneous freezing that occurred in the vast majority of the experiments. In a previous paper, Fang and Amirfazli [219] showed how freezing point depression is not strictly correlated to freezing in wet environments, in which other variables such as frost formation play a relevant role.

The results described until here were not sufficient to formulate a meaningful hypothesis about drop freezing on nanostructured, hybrid-coated surfaces. The main reason for such scattered freezing time values lies in the experimental setup. The wind tunnel available at SEiL was not designed for such experiments. The long tunnel requires airflow to maintain constant temperature, but our experiments showed how homogeneous nucleation of ice becomes dominant over heterogeneous nucleation in such conditions [241]. Furthermore, Fang and Amirfazli [219] assessed the role of frost formation in drop freezing on surfaces. When hydrophilic defects are present, superhydrophobic surfaces can foster humidity condensation and frost formation, thus leading to faster drop freezing compared to smooth, hydrophobic surfaces. It is not possible to control humidity inside the wind tunnel, thus external environment has too strong of an influence on experimental conditions.

For these reasons, we tried to repeat drop freezing experiments with few changes in the setup. Inspired by Tourkine *et al.* [221], we covered the surface with a Petri dish to limit humidity condensation and frost formation on the surface. However, we still observed homogeneous freezing triggered by the airflow leaking beneath the dish. Thus, we tried to repeat the experiment disabling the airflow inside the tunnel, but surface temperature control became tricky due to massive heat exchange from the environment. Considering all these aspects, we decided to give up drop freezing experiments using the wind tunnel at SEiL. These experiments will be performed at CNR-ISTEC with a small closed chamber with controlled humidity, available as an accessory for the Drop Shape Analyzer (DSA30, Kruss GmbH).

## Conclusions

We performed drop freezing experiments on smooth and rough aluminum surfaces bearing the nanostructured hybrid coating, as well as on smooth aluminum with hydrophobic Teflon coating. We used the wind tunnel available at SEIL for the drop freezing tests, keeping the minimum airflow speed and setting both airflow and surface temperature to  $-10^{\circ}\text{C}$ . In such conditions (e.g. airflow and no control of relative humidity), homogeneous freezing occurred at the drop-gas interface, not providing useful information about the effect of surface wetting properties and roughness on drop freezing. As a result, drop freezing time values were extremely scattered and not reliable. Even tests using seawater instead of deionized water drops did not provide any clearer picture of the freezing process. We also tried to change the experimental conditions, but the setup was simply not suitable for that kind of measurements. Future activity will be performed at CNR-ISTEC to clarify the potential anti-icing properties of hybrid-coated, superhydrophobic surfaces.

## 7. CONDENSATION ON SUPERHYDROPHOBIC SURFACES

Condensation is the phase change from vapor state to liquid state. This phenomenon is almost always initiated by a temperature difference (subcooling) between the vapor phase and a solid surface [243]. This gradient causes both a heat and a mass flow between the two phases. This phenomenon is obviously fundamental in nature, but also in countless artificial processes like energy conversion, water harvesting, and thermal management systems, just to name a few. More specifically, the heat transfer related to condensation (latent heat) is very large compared to sensible heat [244], making it appealing for application in power generation [245] and heating, ventilating and air conditioning systems (HVAC) [246]. Therefore, the knowledge of condensation mechanisms is crucial to improve the efficiency of all these processes.

One of the most relevant aspects of condensation on a solid surface is whether the liquid phase forms a continuous film (filmwise condensation, FWC) or discrete drops (dropwise condensation, DWC) [247]. The favored mechanism depends on the wetting properties of the surface. Namely, liquid repellent surfaces favor DWC, which yields much larger heat transfer coefficients compared to FWC [248]. However, to have a real increase in heat exchange properties it is also necessary to implement an efficient mechanism for the removal of condensed drops, in order to sustain DWC. If drop removal did not occur, flooding or DWC-to-FWC transition would be inevitable, with related loss of efficiency. This phenomenon becomes more and more relevant for high heat flux systems [249].

Thus, superhydrophobic surfaces are extremely appealing materials for enhanced heat transfer systems. Many papers have already demonstrated that SHSs can induce dropwise condensation [250] [251] [252]. Moreover, some scientists observed coalescence-induced spontaneous motion of droplets on some superhydrophobic surfaces [253] [254]. This out-of-plane motion was attributed to the release of excess surface energy associated with the merging of the droplets [255]. In general, to achieve an efficient removal of condensed drop it is necessary for them to be in the Cassie-Baxter wetting state [255] [256]. This is not a trivial task, as many SHSs promote the formation of condensed drops in an impaled (e.g. Wenzel) state due to their roughness [257].

Therefore, we wanted to assess the behavior of the nanostructured, hybrid coating in condensing conditions. More precisely, first we studied the shedding behavior of condensed drops on SHSs in high humidity environment and in presence of an airflow with controlled speed. Second, we assessed the evolution of contact angles on surfaces with different wetting properties when exposed to high humidity environment for a certain amount of time. Both experiments were performed at the Surface

Engineering and Instrumentation Lab (SEIL) at York University, Toronto, ON, Canada, headed by Professor Alidad Amirfazli.

## DROP SHEDDING IN CONDENSING CONDITIONS

### Materials and methods

For drop shedding tests in condensing conditions, we used the same superhydrophobic surfaces mentioned in Chapter 6 about tests in icing conditions. Briefly, Al 1050 99% H24 alloy foils (75 x 25 x 2 mm<sup>3</sup>) were used as substrates, with one smooth side ( $R_a = 0.26 \pm 0.02 \mu\text{m}$ ) and one rough side ( $R_a = 3.57 \pm 0.05 \mu\text{m}$ ). The nanostructured hybrid coating was fabricated at CNR-ISTEC with the usual procedure, taking care of both sides of each sample, then shipped to York University for the tests. As these samples were fabricated together with those for tests in icing conditions, we did not repeat contact angle measurements on the surfaces used for these tests and adopted those previously reported (ACA = 159.0°, RCA = 153.6° and CAH = 5.4° for rough surfaces; ACA = 166.9°, RCA = 162.2° and CAH = 4.7° for smooth surfaces).

Figure 76 shows a sketch of the wind tunnel used for experiments in high humidity conditions.

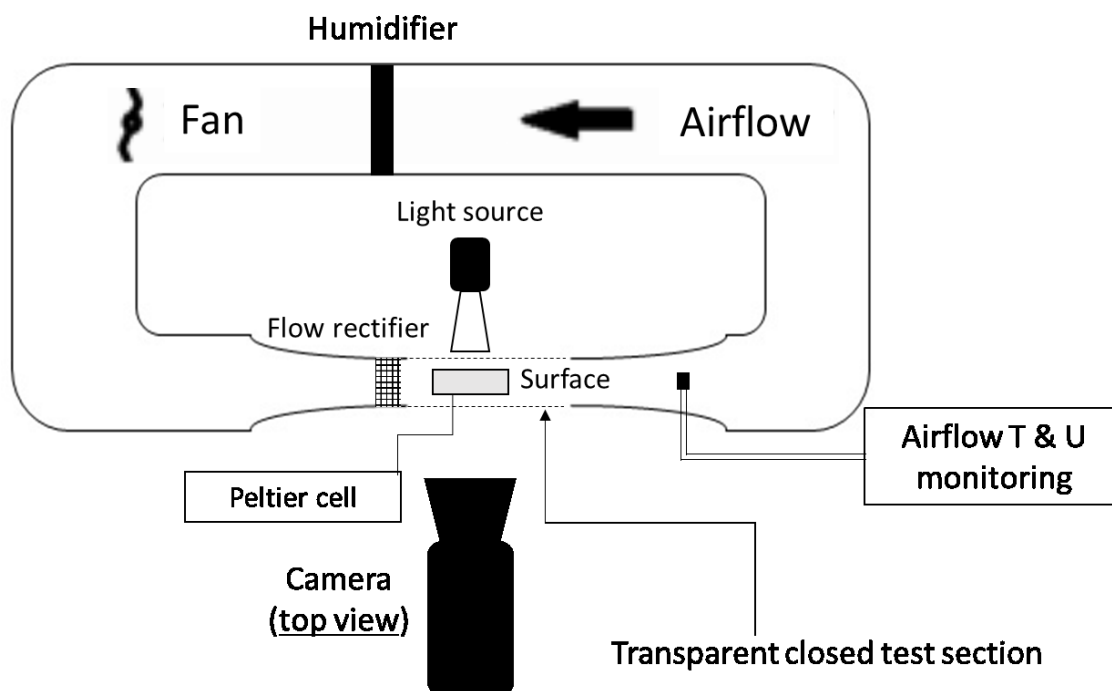


Figure 75. Schematic representation of the lab-scale wind tunnel used for drop shedding experiments in high humidity conditions.



In the tunnel, airflow was generated by a fan (model TYP4600N manufactured by Papst Motor, maximum air flow of 5.8 m/s) and its velocity was changed by providing different tension to the fan (from 0 V to 120 AC). Meanwhile, airflow temperature was regulated with a chiller (HAAKE KT-90, ethanol bath, range 40 ÷ -90 °C, watercooled) and a humidifier was used to increase relative humidity. An electronic sensor fitted downstream of the test section was used to monitor airflow temperature and velocity, while another sensor measured relative humidity of the airflow. The surface was placed on a Peltier cell (TE Technology, CP-031) to modulate surface temperature, which was monitored with a thermocouple. The test chamber, which contained the Peltier cell and the sample, was made of transparent walls and a lid for sample handling and drop dispensing. A Phantom v4.3 camera (Vision Research Inc.) was placed above the sample surface to monitor the condensation and shedding. The camera was operated at a frame rate of 2 fps and camera resolution of 116  $\mu\text{m}/\text{pixel}$ .

Before each test, we quickly assessed the superhydrophobic behavior of the surface by dropping water on it. We used only surfaces on which drops rolled off with no sticking. For all experiments, we set the temperature of the Peltier cell at 13°C (room temperature was 24°C) and the relative humidity of the chamber at 70%, corresponding to a dew point of 17°C. Therefore, in these conditions condensation must occur on the surface. Measurements were performed as per the following procedure:

1. We let the Peltier cell to reach the desired temperature,;
2. We activated airflow with a certain  $U$  to start condensation;
3. After a certain period, if shedding did not occur we would increase  $U$ .

Recorded frames were analyzed manually to check the evolution of condensed drops on the surface. The experiments were repeated at least twice to ensure reproducibility.

## Results

The first tests were run on smooth SHSs adopting a starting airflow speed  $U = 4$  m/s, quite a high value. This means that no induction period was performed. The induction period can be defined as a time in which airflow speed is voluntarily kept at values too low to cause shedding, allowing for the build-up of drops on the surface. On the contrary, by maintaining a high  $U$  from the beginning of the test, we wanted to achieve condensation and shedding with the same flow. The first evidence was that DWC was the favored condensation mechanism on the smooth SHSs, as expected from the high contact angles measured on the surface. However, shedding of condensed drops was not possible maintaining  $U$  constant to 4 m/s. Figure 77a shows a smooth SHS after 23 minutes of test. Drop sizes were quite

disperse on the surface, with diameters ranging from 100  $\mu\text{m}$  (equal to the image resolution, e.g. 1 pixel large) to almost 2 mm. We tried to provoke shedding by increasing  $U$  to the maximum value achievable by the system (about 5.8 m/s). After about 1 minute, very limited shedding was observed, as shown in Figure 77b. The shedding of the droplets over a 5 s period is shown in Figure 78.

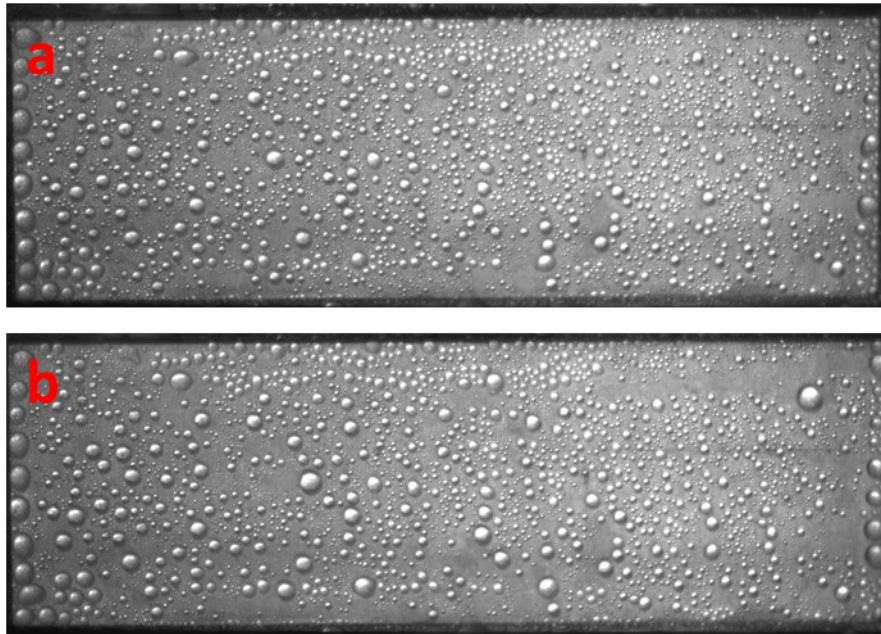


Figure 76. Smooth, hybrid-coated aluminum surface sample a) after 23 minutes in high humidity environment with airflow speed  $U = 4 \text{ m/s}$  and b) after 1 additional minute with  $U = 5.8 \text{ m/s}$ .

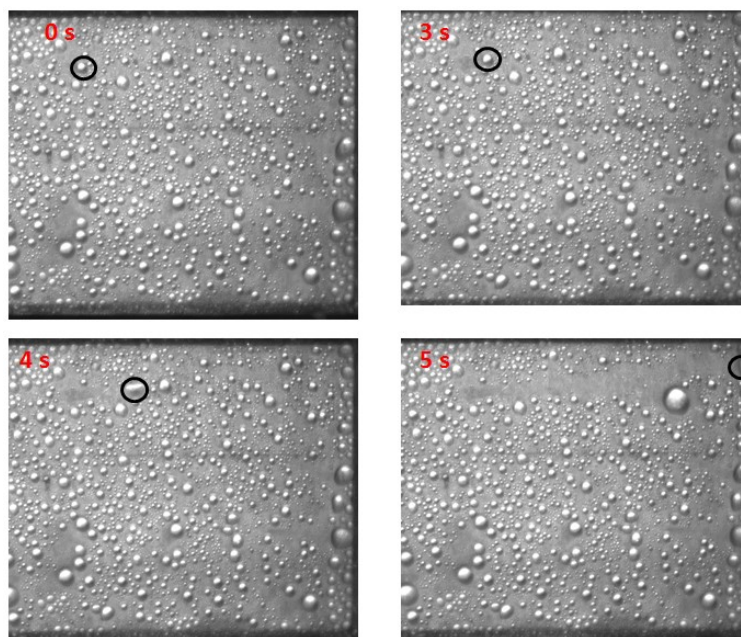


Figure 77. Sequence of a drop shedding event on a smooth, hybrid-coated aluminum surface over a 5 s period. The first frame (top left) was chosen as  $t = 0$ . The shedding drop is circled in black.

In the following tests on smooth SHSs, we performed an induction period. More precisely, we set  $U = 1$  m/s to allow for condensation at a very low rate, then increased  $U$  to achieve shedding. A smooth SHSs after an induction period of 600 s is shown in Figure 79a. The droplets were very much dispersed over the substrate, with discrete nucleation sites randomly distributed over the condensing surface. Compared to the previous tests with no induction period (see Figure 77a), nuclei were much smaller, never exceeding 500  $\mu\text{m}$  in diameter. To achieve shedding,  $U$  was subsequently increased to 5.8 m/s and substantial droplet shedding was observed within 120 s (Figure 79b) as demonstrated by the large drops on the downstream side of the surface.

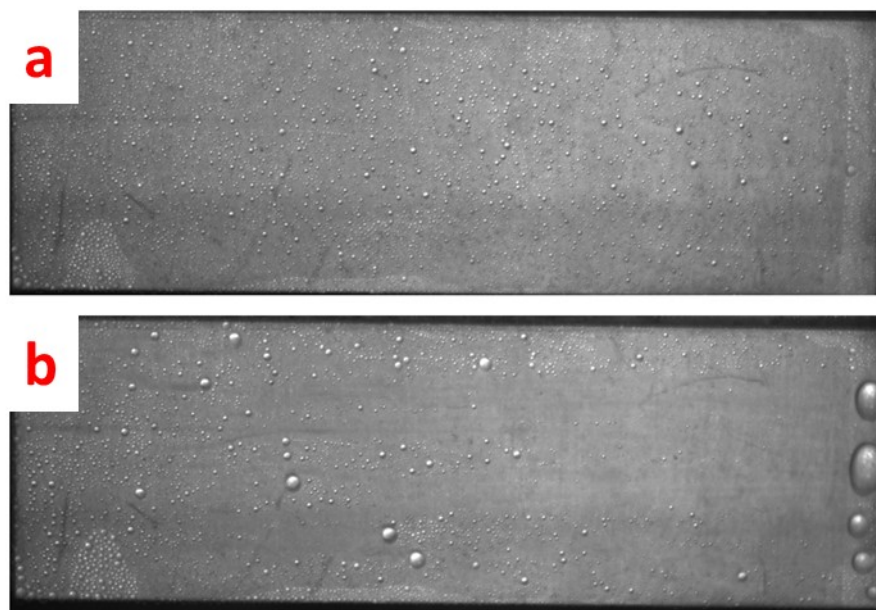


Figure 78. Smooth, hybrid-coated aluminum surface sample a) after 10 minutes in high humidity environment with airflow speed  $U = 1$  m/s (induction period) and b) after 120 additional seconds with  $U = 4$  m/s.

This behavior was in contrast with that observed in Figure 77, where induction period at low flow speed was not performed. For DWC to be sustained on nanotextured surfaces, a balance must be established among rate of condensation, discrete droplet distribution and droplet removal. Starting the experiment with a high  $U$  like 4 m/s will probably lead to the generation of droplets at a rate faster than the rate at which the droplets coalesce, thus to an increased nucleation density. Miljkovic and Wang [258] reported that, if the nucleation density is too high, condensed drops will form in a highly adhered (e.g. Wenzel) state. Moreover, Cheng *et al.* [139] also reported flooding on two-tier structured surface when the heat flux became high, thus condensed drops penetrating within surface features and reach Wenzel state. Both high nucleation density and high heat flux occur in when  $U$  is high, as when no induction period takes place. Therefore, these explanations seem plausible for the behavior here described.

We repeated the experiments also for rough, hybrid-coated aluminum surfaces. We decided to adopt an induction period to facilitate shedding. However, after an induction period of 15 minutes with  $U = 1$  m/s, no shedding occurred even when increasing  $U$  to 5.8 m/s. The rough surface after induction period is depicted in Figure 80. Many extremely small nuclei were present, all smaller than 600  $\mu\text{m}$  in diameter (except for some larger drops on the upstream edge of the foil, which reached  $\varnothing \leq 1.8$  mm). Drop growth seemed extremely slow on this surface, as even extending the induction time to 60 minutes did not increase drop size significantly. Furthermore, droplet size distribution was not as varied as the one observed during condensation on the smooth, coated surface.

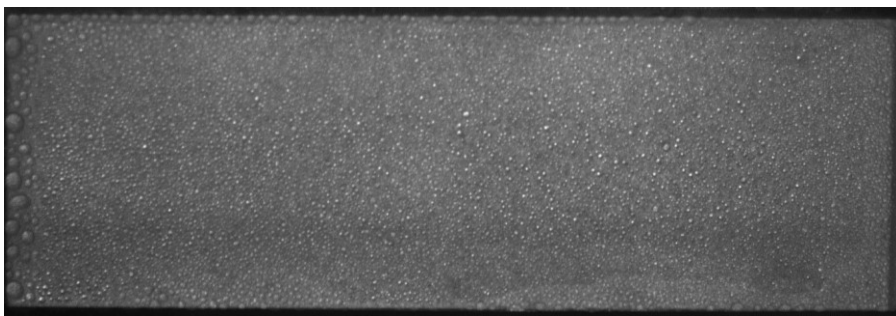


Figure 79. Rough, hybrid-coated aluminum surface sample after 15 minutes in high humidity environment with airflow speed  $U = 1$  m/s (induction period).

These results (high nucleation density, slow growth rate, high drop adhesion that hinders shedding) can be ascribed to surface roughness, which has been suggested in the literature as a promoter of nucleation density. In fact, nucleation density on a textured surface ( $N_f$ ) has been suggested to be of the form [243]:

$$N_f = fN$$

In the equation,  $f$  is a factor that expresses the degree of roughness and  $N$  is the nucleation density of a smooth surface of the same material. Moreover, the impossibility to shed condensed droplets on rough SHSs suggests that these drops had high adhesion to the surface, e.g. they were formed in a Wenzel state rather than in a Cassie state. The tendency of SHSs to form Wenzel drops with high CAH under condensing conditions is reported in the literature [259] [260].

Thus, the inability to shed the condensed droplets on the relatively rough side strongly indicates a change of state to Wenzel state, a possible decrease in in-situ water contact angle and a high increase in contact angle hysteresis. As already mentioned in Chapter 6 for drop shedding experiments in freezing conditions, contact angle hysteresis is proportional to adhesion force, thus a high CAH is certainly detrimental for drop shedding:

$$F_{adh} = \gamma L_b (\cos \theta_{min} - \cos \theta_{max})$$

For this reason, we decided to look deeper into the adhesion of condensed drops on hybrid-coated surfaces through *in situ* contact angle measurements in condensing conditions. These experiments will be discussed in the next section.

## Conclusions

We performed condensation and shedding experiments of hybrid-coated surfaces in high humidity conditions. Even though dropwise condensation always occurred, many aspects seemed to influence the behavior of condensed drops. First, we noticed that a slow nucleation rate (which we achieved by performing an induction time at low airflow speed) seemed to promote the formation of non-adherent drops, which probably were in a Cassie state. Then, we assessed the effect of surface roughness on nucleation density, thus on condensed drop adhesion. In fact, rough SHSs favored higher nucleation density and slower growth rate compared to smooth SHSs, resulting in highly adhesive drops in Wenzel state that could not be shed even at the maximum  $U$  achievable by the setup. These evidences leave wide room for further activity: it would be interesting to assess the behavior of even smoother SHSs and see if shedding was easier compared to the tested surfaces. Moreover, the different adhesion forces observed in these experiments led us to investigate the evolution of contact angle hysteresis (which is proportional to adhesion) when SHSs are in high humidity conditions.

## CONTACT ANGLE MEASUREMENTS IN HIGH HUMIDITY CONDITIONS

From the previous drop shedding experiments in condensing conditions, we understood that the shedding behavior of a single droplet placed on a superhydrophobic surface (e.g. a sessile drop) can be radically different from that of a droplet of similar size formed via condensation, especially if other

condensed drops are present on the surface. Indeed, such single drop tends to be easier to shed on a dry surface than on a surface with condensates. As already mentioned [61], the forces involved in drop shedding are the adhesion force  $F_{adh}$  and the drag force  $F_{drag}$ . The different shedding behavior could be partly due to a change in drag force when a distribution of condensed droplets is present on the surface. However,  $F_{adh}$  seems to play a major role in determining drop shedding behavior. In fact, surface roughness is a crucial parameter, as shedding is easier on a smooth surface, compared to a rougher surface with the same surface energy. In condensation theory, it is believed that droplets grow from stable nuclei [261]. On a rough surface, condensed drops were pinned, thereby extremely difficult to shed them. Contact angle hysteresis (CAH) is a good measure of  $F_{adh}$  and pinning behavior of a drop on a surface. Thus, we wanted to investigate the evolution of CAH of a sessile drop on a surface with condensates. We aimed at an assessment of the effect of condensation time on CAH.

## Materials and methods

For contact angle measurements in high humidity conditions, we used the same superhydrophobic surfaces mentioned in the previous sections, namely hybrid-coated aluminum foils with one smooth side ( $Ra = 0.26 \pm 0.02 \mu\text{m}$ ) and one rough side ( $Ra = 3.57 \pm 0.05 \mu\text{m}$ ). The nanostructured hybrid coating was fabricated at CNR-ISTEC with the usual procedure, taking care of both sides of each sample, then shipped to York University for the tests. As these samples were fabricated together with those for tests in icing conditions, we did not repeat contact angle measurements on the surfaces used for these tests and adopted those previously reported (ACA =  $159.0^\circ$ , RCA =  $153.6^\circ$  and CAH =  $5.4^\circ$  for rough surfaces; ACA =  $166.9^\circ$ , RCA =  $162.2^\circ$  and CAH =  $4.7^\circ$  for smooth surfaces). In addition, we tested hydrophobic, smooth Teflon-coated surfaces prepared as per the method reported by Mandal *et al.* [61] and used also for drop freezing measurements. Analogous Teflon-coated smooth surfaces reported in the literature [219] have ACA =  $121.9^\circ \pm 1.6^\circ$  and RCA =  $108.5^\circ \pm 2.0^\circ$

Figure 81 shows a sketch of the wind tunnel used for experiments in high humidity conditions, while Figure 82 is a picture of the real setup.

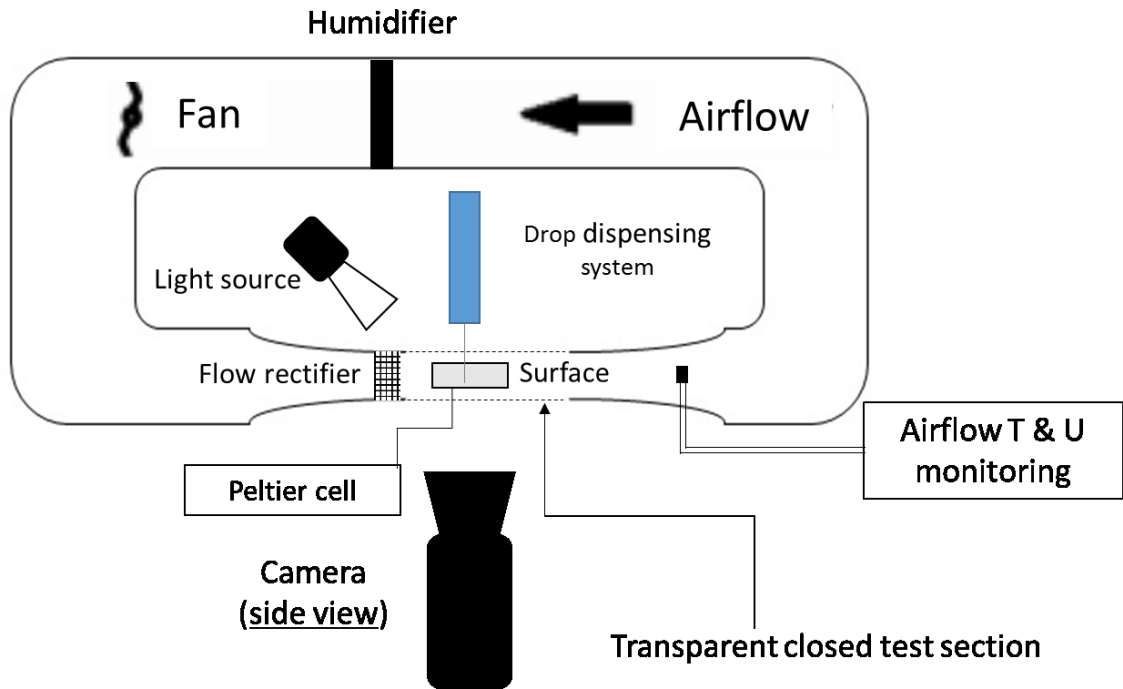


Figure 80. Schematic representation of the lab-scale wind tunnel used for contact angle measurements in high humidity conditions.

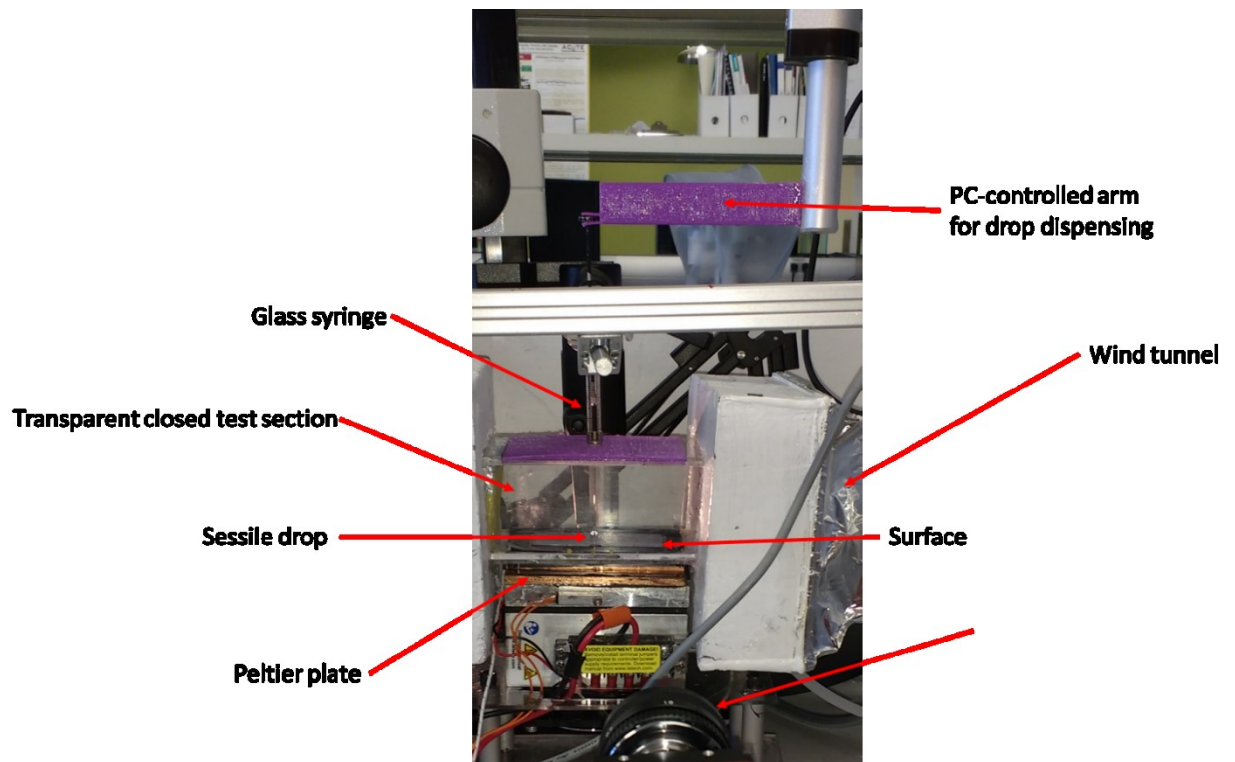


Figure 81. Picture of the test section and the dispensing system adopted for contact angle measurements in high humidity conditions.

In the tunnel, airflow was generated by a fan (model TYP4600N manufactured by Papst Motor, maximum air flow of 5.8 m/s) and its velocity was changed by providing different tension to the fan (from 0 V to 120 AC). Meanwhile, airflow temperature was regulated with a chiller (HAAKE KT-90, ethanol bath, range 40 ÷ -90 °C, watercooled) and a humidifier regulated airflow humidity. An electronic sensor fitted downstream of the test section was used to monitor airflow temperature and velocity, while another sensor measured relative humidity of the airflow. The surface was placed on a Peltier cell (TE Technology, CP-031) to modulate surface temperature, which was monitored with a thermocouple. The test chamber, which contained the Peltier cell and the sample, was made of transparent walls and a lid with a hole to host the dispensing syringe. The piston was gripped by an arm, which in turn was controlled by an Arduino interface. We used a needle with an oblique cut that generated drops from one side. A Phantom v4.3 camera (Vision Research Inc.) was used to obtain the profile of the sessile drop deposited with the syringe. The camera was operated at a frame rate of 2 fps and camera resolution of 13.6  $\mu\text{m}/\text{pixel}$ .

Before each test, we quickly assessed the superhydrophobic behavior of the surface by dropping water on it. We used only surfaces on which drops rolled off with no sticking. For all experiments, we set the temperature of the Peltier cell at 12°C (room temperature was 23°C) and the relative humidity of the chamber at 70%, corresponding to a dew point of 17°C. Therefore, in these conditions condensation must occur on the surface. Measurements were performed as per the following procedure:

1. We deposited the surface on the Peltier cell and let them reach the set T;
2. We measured advancing and receding contact angle (ACA and RCA, respectively) on the dry surface by first growing a 50  $\mu\text{l}$  drop on the surface, then withdrawing the same volume;
3. We activated airflow to start condensation on the surface;
4. After a certain condensation time, we measured ACA and RCA with the same procedure as in point 2.

Recorded frames were analyzed manually with ImageJ software to calculate advancing and receding contact angles of the sessile drop on the surface (ACA and RCA, respectively). These values were measured from the first frame in which the contact line between the drop and the surface advanced or receded, respectively.

## Results and discussion

Contact angle values measured on a Teflon surface before and after different condensation periods are reported in Figure 83.



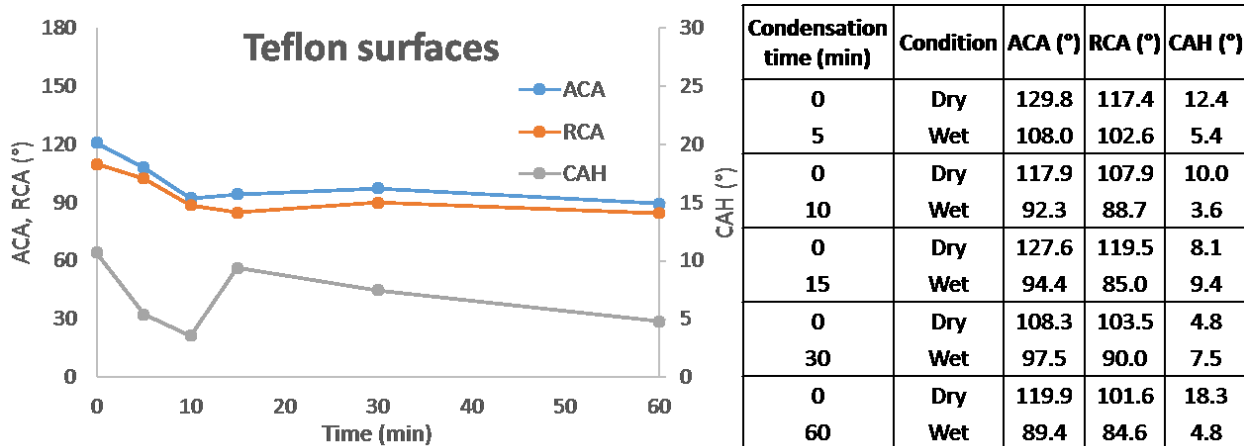


Figure 82. Advancing, receding contact angle and contact angle hysteresis (ACA, RCA and CAH, respectively) for a sessile drop on Teflon surface as a function of condensation time. The table reports the measured values.

On Teflon surfaces, both ACA and RCA slightly decreased with increasing condensation time. The trends were similar, resulting into little variations of CAH (e.g. never over 10°). This means that water drops did not increase their adhesion significantly, even though condensed drops were clearly visible on the surface.

Results for smooth, hybrid-coated aluminum surfaces are reported in Figure 84.

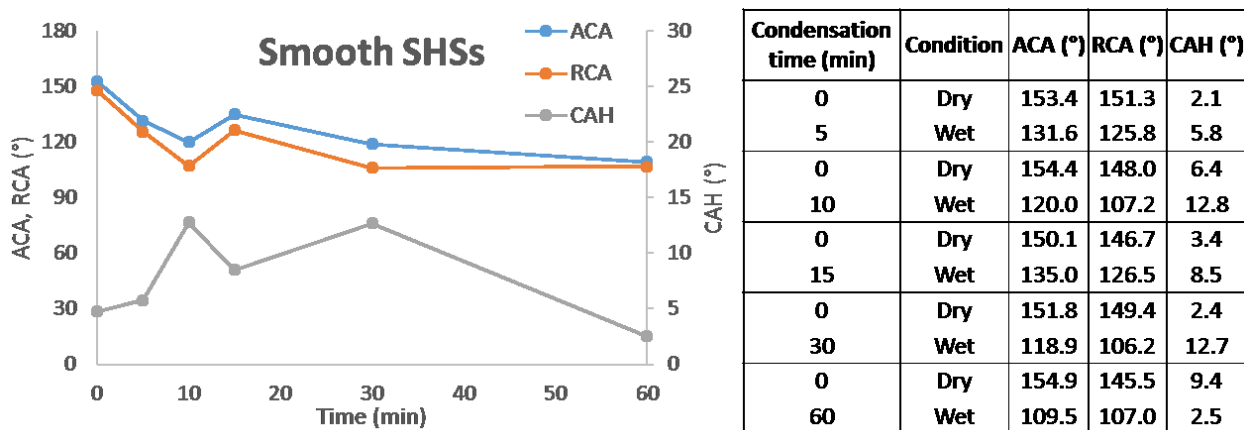


Figure 83. Advancing, receding contact angle and contact angle hysteresis (ACA, RCA and CAH, respectively) for a sessile drop on smooth, hybrid-coated superhydrophobic surfaces as a function of condensation time. The table reports the measured values.

On smooth, hybrid-coated surfaces, ACA and RCA both decreased from values higher than 150° to values lower than 110° after 60 minutes of exposition to condensing conditions. However, CAH showed an increase through the first 30 minutes (CAH > 12°), then unexpectedly dropped to very low values

after 60 minutes in high humidity environment. We tried to explain this phenomenon hypothesizing that the formation of discrete condensed drops on the surface in the first 30 minutes led to increased surface heterogeneity, which in turned resulted into higher CAH. However, for longer condensation times, a continuous liquid film could have formed on the surface, eliminating such heterogeneity and leading to lower hysteresis. Obviously, this is just a preliminary hypothesis that needs confirmation through further investigations.

A very similar behavior was observed also on rough, hybrid-coated aluminum surfaces, ad shown in Figure 85.

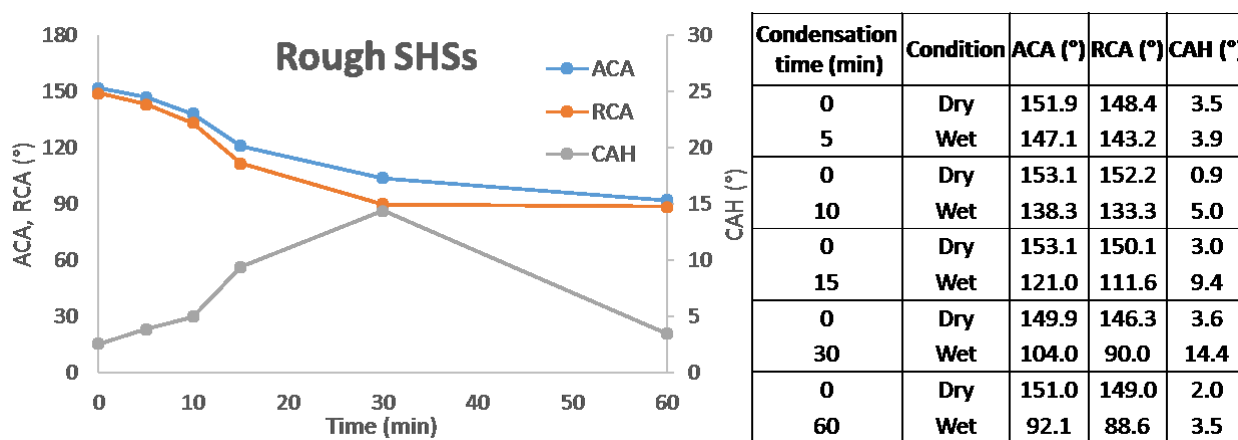


Figure 84. Advancing, receding contact angle and contact angle hysteresis (ACA, RCA and CAH, respectively) for a sessile drop on rough, hybrid-coated superhydrophobic surfaces as a function of condensation time. The table reports the measured values.

Also on rough SHSs, ACA and RCA decreased with increasing condensation time, reaching values close to 90°. Those were the lowest values observed among all the investigated surfaces. Moreover, CAH showed a similar trend compared to that of smooth SHSs, with an increase in the first 30 minutes followed by a decrease after 60 minutes to very low values. Figure 86 compares the evolution of CAH for the three investigated surface types.

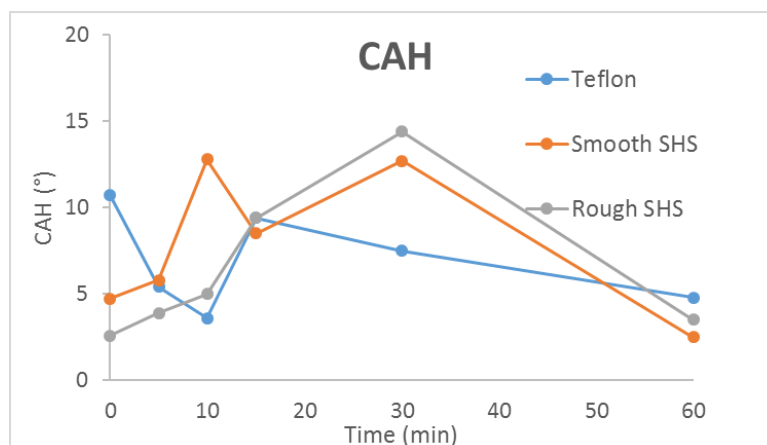


Figure 85. Contact angle hysteresis (CAH) for a sessile drop on Teflon-coated (blue), smooth superhydrophobic (orange) and rough superhydrophobic surfaces (grey) as a function of condensation time.

As already mentioned, the two investigated SHS types showed quite similar trends, with no evident influence of surface roughness on CAH evolution. Remarkably, all surfaces displayed very low CAH after 60 minutes in condensing conditions, suggesting that a liquid film was formed on all of them with no influence of wetting properties in dry conditions. Furthermore, such similar CAH values suggest that the different shedding behavior in condensing conditions observed in the previous experiments is not only related to CAH and adhesion force.

However, during these experiments some issues emerged. First of all, it was extremely difficult to obtain clear images of the drop profile close to the surface (e.g. a good view of the contact line) when condensed drops formed. Therefore, the evaluation of contact angles was quite tricky and unreliable, especially after long condensation times. Two images of sessile drops on SHSs after long condensation times are reported in Figure 87.

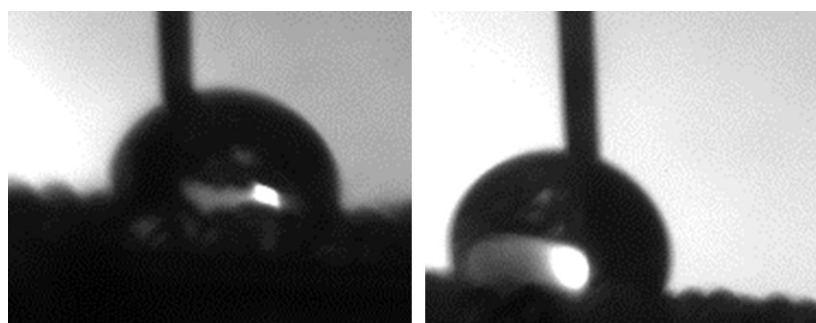


Figure 86. Frames of sessile drops on a rough SHS after 60 minutes of condensation (left) and on a smooth SHS after 30 minutes of condensation (right).

For these reason, we repeated the experiments with optimized images of the sessile drop, trying to obtain well resolved images on the dry surfaces and utilizing the same contact line also for unclear images. Moreover, contact angle values were no longer calculated on a single frame, but as the average value of all frames in which the contact line either advanced or receded. An example of this procedure is reported in Figure 88.

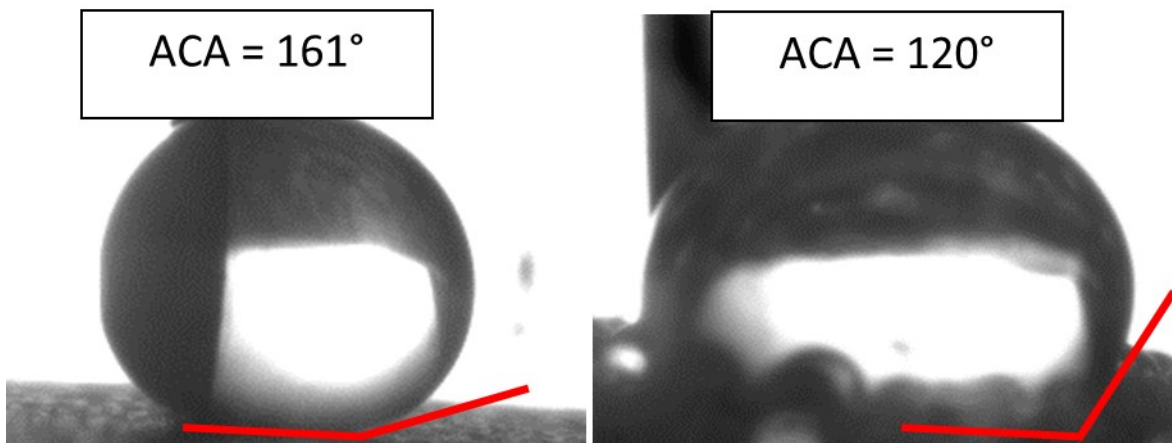


Figure 87. Evaluation of ACA of a sessile drop a rough SHS in dry state (left) and after 60 minutes of condensation (right).

We performed new tests with the improved experimental setup and calculation procedures, omitting to provide values when the contact points were not clear. Results of the second data set are reported in Figure 89.

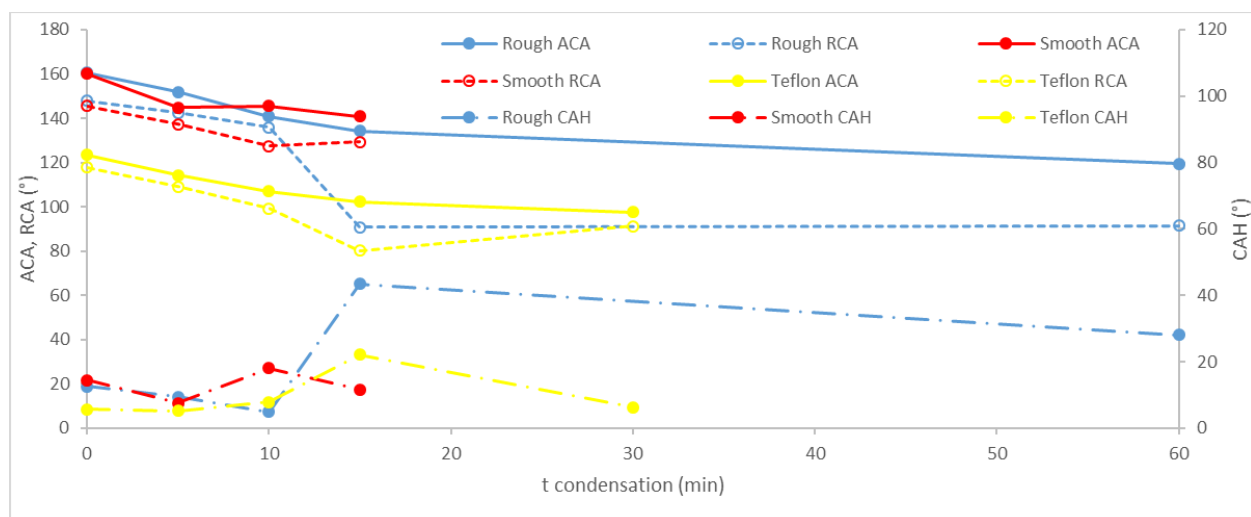


Figure 88. Advancing, receding contact angle and contact angle hysteresis (ACA, RCA and CAH, respectively) for a sessile drop on rough (blue) or smooth (red) hybrid-coated superhydrophobic surfaces and on Teflon-coated hydrophobic surfaces (yellow) as a function of condensation time.

These results seem to contradict the previous ones. Indeed, CAH increased remarkably after 15 minutes on rough SHS, reaching values as high as 40°. Meanwhile, smooth SHSs and Teflon surfaces showed similar trends, with CAH lower than 20° for the first 15 minutes. Such effect of roughness on CAH in condensing conditions was not detected in the previous data set, but is consistent with some results in the literature [238] [260].

However, such improved procedure still displayed some drawbacks, as the correct evaluation of the contact point still seemed a hard task when long condensation periods were performed. Contact angle values were still estimated manually, leading to repeatability and reliability issues. For these reason, further activity to refine this data is still in progress. We are trying to fit the drop profile with suitable calculation methods, in order to obtain a reliable contact point even when it is not visible (e.g. when condensates hinder a clear view).

Another issue was the choice of the frames useful for the calculation of contact angles. In fact, while ACA was almost constant through the entire growth of the drop, RCA values rapidly decreased as the drop became smaller. This phenomenon was probably due to the increasing influence of the needle, which caused deformation in the drop and lower RCAs when decreasing drop volume. This behavior was observed also on dry surfaces, but it was much more evident on wet surfaces. An example of such evolution is represented in Figure 90, while Figure 91 reports some significant frames. Therefore, it is necessary to establish which frames should be considered for the calculation of RCA.

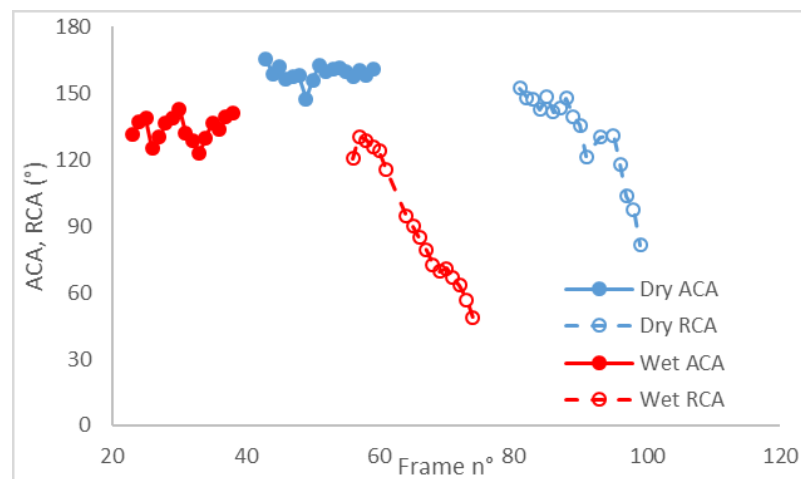


Figure 89. Evolution of ACA (solid lines) and RCA (dashed lines) on a rough SHS in the dry state (blue) and after 15 minutes in condensing conditions (red).

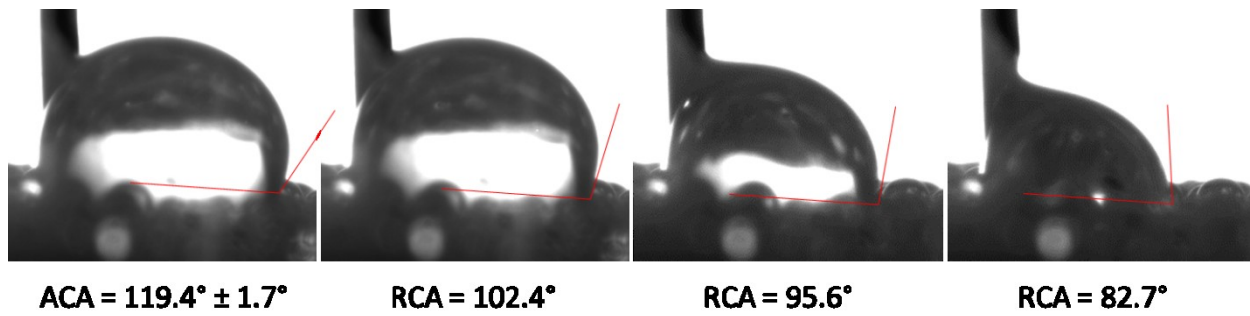


Figure 90. Measurement of ACA (first frame) and RCA (remaining frames) of a sessile drop on rough SHS after 60 minutes in condensing conditions. ACA is the average of five values, while the RCAs measured for the single frame are reported.

Considering all these limitations, we planned to perform further measurements with few experimental adjustments:

- Use larger drops (e.g. volume 100  $\mu$ l) to limit the influence of the needle on RCA values;
- Use a flat needle, which should avoid pinning phenomena thus providing two useful contact angles per frame instead of one;
- Improve the dispensing system with a stiffer arm and better software control to achieve more reliable drop volumes.

After each experiment, we also collected top-view images of condensed drops on the surface. All images are reported in Figure 92.

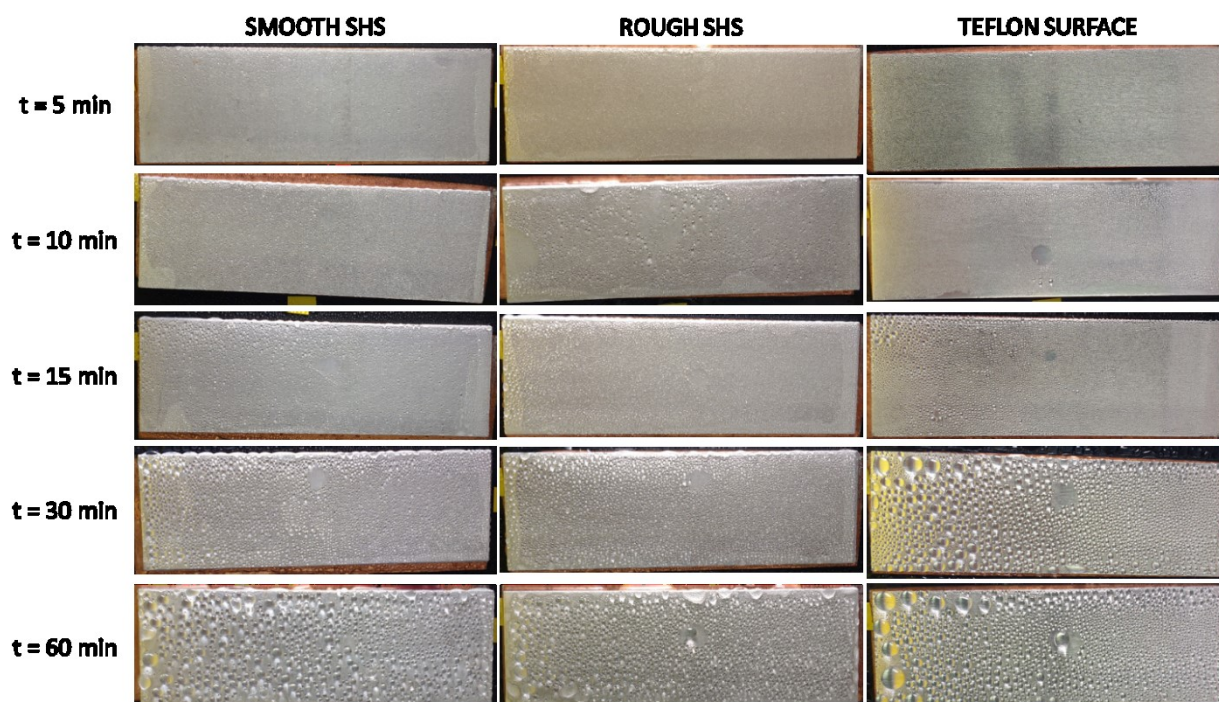


Figure 91. Top-view images of smooth SHSs (left column), rough SHSs (central column) and Teflon surfaces (right column) after exposure to high humidity conditions (condensation time increasing from the top down).

For every surface type, the size of condensed droplets increased with exposure time. However, after 60 minutes of condensation smooth SHSs and Teflon surfaces had similar droplet size distribution, while condensed drops were significantly smaller on rough SHSs. These results were consistent with those from drop shedding experiments in condensing conditions.

## Conclusions

We tried to assess the evolution of the contact angle hysteresis of a sessile drop on two SHSs (with different roughness) and a hydrophobic Teflon surface as a function of condensation time (e.g. exposure to high humidity conditions). The first data set provided surprising results, as in all cases CAH dropped to very low values after 60 minutes of condensation. This should mean that a liquid film had formed on the surface, disregarding any effect of surface roughness and wetting properties. However, the images obtained from these measurements were not good enough to provide reliable contact angle values. We repeated the experiments with an improved setup, but proper measurements were still difficult to obtain. Furthermore, a significant effect of surface roughness on CAH trend seemed to emerge, with the rough SHSs displaying the highest CAH values. Future activity is definitely necessary to clarify many aspects of the behavior of our superhydrophobic surfaces in condensing conditions.





## 8. ANTI-FRICTION PROPERTY IN AXIAL PISTON PUMPS

The last application investigated for the nanostructured, hybrid coating is in the field of mechanics. Axial piston pumps and motors are widely used in heavy-duty applications and play a fundamental role in hydrostatic and power split drives. One of their main problems is friction, which causes enormous power losses, especially when the pump (e.g. at low rotational speed or at partial displacement) works in the critical areas where the efficiency is low. Thus, a significant reduction in friction coefficient in these devices would be a huge breakthrough, with relevant positive impact in cost reduction and energy savings. In this work, we focused on one component of the pump, namely the slippers. In axial piston pumps, slippers rotate and rub against a swashplate in conditions of hydrodynamic lubrication, e.g. a meatus filled with lubricant oil separates the rotating slippers from the swashplate. In this scenario, two contrasting needs arise: the leakage of oil must be enough to maintain lubrication, while the meatus must be as small as possible to avoid volumetric losses. Standard slippers are usually extremely smooth and, most importantly, perfectly wetted by the lubricant oil to avoid seizing. In other terms, slippers are extremely oleophilic. We tried to reverse this approach: what will happen if the surface becomes oleophobic? In the project called *“Surface Nano-structured Coating for Improved Performance of Axial Piston Pumps”* (from now on defined with the acronym *SNAPP*), we investigated the potential of the nanostructured, hybrid coating on slippers surface in improving the overall efficiency of the pump through a significant reduction in fluid friction losses. Our group at CNR-ISTEC collaborated with two other CNR institutes in this project, namely CNR-IMAMOTER (composed of two units, one in Ferrara for the design and development of the test rig to simulate real working conditions and one in Turin for tribology tests) and CNR-IENI in Milan. This project led to the publication of a paper [127] and the approval of another project (*“Axial Piston Pump Prototype Assembled with Oleophobic Surfaces Components”*, also called *APPOS*) for the realization of a pump prototype with functionalized components.

### DEPOSITION OF THE OLEOPHOBIC COATING ON SLIPPERS

#### Slippers properties

The first step of the project was to study the feasibility of the coating process on the slippers. A standard slipper is shown in Figure 93.



Figure 92. Standard brass slipper clamped on a steel piston.

These samples are made of brass, namely Aeterna® VL22 alloy produced by ThyssenKrupp (CuZn37Mn3Al2PbSi alloy according to DIN EN standard). It belongs to CW713R alloy family, except for the presence of lead. This material has excellent anti-friction properties, high wear resistance, high strength and hardness, good machinability and resistance against aggressive oils. Its metallurgic composition is recapped in Table 23.

Cu	Zn	Pb	Fe	Mn	Ni	Al	Si
58	Rest	0.7	0.5	2	-	1.4	0.5

Table 23. Metallurgic composition of Aeterna VL22 alloy. The numbers reported are mass percentages reported by ThyssenKrupp.

Bare, standard slippers are mechanically machined to be as smooth as possible. Surface roughness was evaluated with a Taylor Hobson Talysurf CCI3000Å non-contact profilometer available at IMAMOTER-CNR in Turin. The average roughness was  $R_a = 0.10 \pm 0.01 \mu\text{m}$ .

As previously mentioned, the bare standard slippers were designed to be as oleophilic as possible. In the reference axial piston pump considered in *SNAPP*, namely HPP8 by HP Hydraulics SpA (Bondioli & Pavesi group), it is mandatory to use an ISO VG-46 lubricant oil, e.g. an oil with a kinematic viscosity of 46  $\text{mm}^2/\text{s}$  at  $T = 40^\circ\text{C}$ . For this reason, we used Arnica46 oil (Agip) as model oil for the characterization of the wetting behavior of the surfaces with oil drops. We measured the surface tension of Arnica46 with an OCA15plus system (Dataphysics) via pendant drop technique, obtaining  $\gamma = 29.4 \pm 0.1 \text{ mN/m}$ . For the bare standard slipper, contact angles of  $74.8^\circ$  and  $16.1^\circ$  with water and Arnica46 were observed, respectively. Notably, all wetting characterizations are referred to the outer crown of the slipper, which is the only visible area for the contact angle system and the point where friction is the highest.

### Deposition on smooth slippers

As a first attempt, we deposited alumina nanoparticles on two as-received slippers with no previous treatment (except for two cleaning steps with ultrasounds, one in soapy water and one in acetone to degrease the surface). We attempted the deposition by dip-coating with both the water-based and the alcohol-based suspension, maintaining the same conditions used for aluminum samples (immersion for 5 s, withdrawal speed 2 mm/s). Figure 94 shows the evolution of the upper surface of the slippers through the coating process. After drying overnight and thermal treatment at 400°C for 60 minutes, both slippers showed severe exfoliation in the coating, which formed transparent scales (Figure 94, column b). Of course, the coating proved extremely brittle in both cases. The darker shade of the slipper coated with the aqueous sol (Figure 94, lower row) was probably due to the presence of HNO<sub>3</sub> in the sol, which causes oxidation on the surface of the slipper.

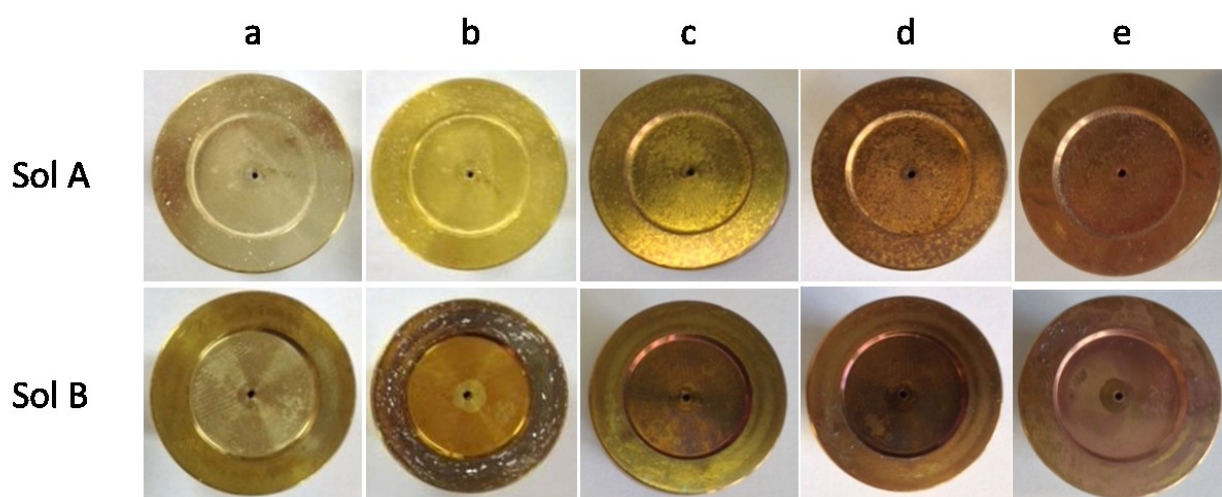


Figure 93. Smooth slippers coated with (upper row) alcohol-based and (lower row) aqueous alumina sol after each step of the coating process: a) dip coating in the suspension; b) heat treatment at 400°C for 60 minutes; c) immersion in boiling water for 30 minutes; d) heat treatment at 400°C for 10 minutes; e) chemical modification with FAS (SIVO Clear EC, Evonik).

Notwithstanding exfoliation, we still performed the entire functionalization process. Unsurprisingly, none of the slippers was either superhydrophilic after treatment with boiling water ( $WCA \geq 20^\circ$  for both slippers) or superhydrophobic/oleophobic after chemical modification with FAS (contact angles of  $120^\circ$  and  $85^\circ$  with water and lubricant oil Arnica46, respectively).

As a reference, we performed a chemical modification of smooth slippers by immersion in SIVO Clear EC for 2 minutes. Contact angles raised to  $111.2^\circ \pm 7.0^\circ$  and  $70.5^\circ \pm 6.2^\circ$  with water and Arnica46, respectively, meaning that FAS molecules were successfully deposited on the surface.

### Deposition on rough slippers

It is well known from the literature that surface roughness favors adhesion of coatings [129]. Thus, we increased surface roughness on the slippers by sandblasting, reaching roughness values of  $R_a = 1.8 \pm 0.2 \mu\text{m}$  (as measured with the Taylor Hobson Talysurf CCI3000Å non-contact profilometer at CNR-IMAMOTER in Turin). Figure 95 shows a sandblasted slipper and the SEM images of the top surface at two different magnifications. On sandblasted slippers, contact angles with water and Arnica46 were  $108^\circ$  and  $17^\circ$  respectively, showing negligible differences compared to smooth slippers in terms of oleophobicity.

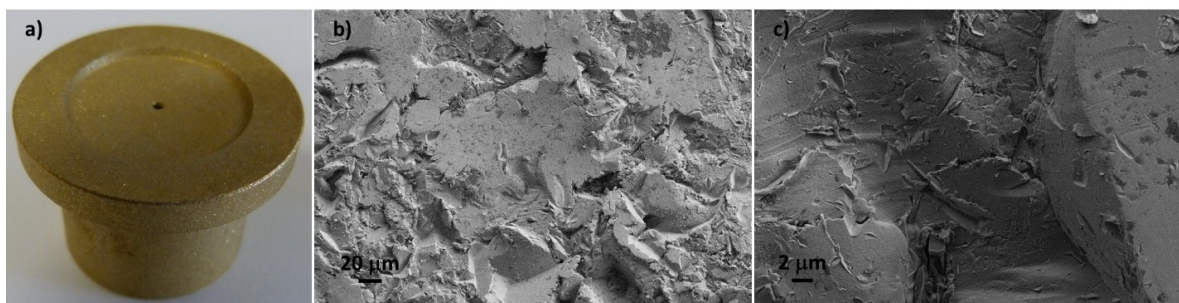


Figure 94. a) Sandblasted slipper. b) and c) SEM images of the top surface at b) 1000X and c) 10000X.

We repeated the functionalization process on rough slippers with both alumina suspensions. In these cases, no exfoliation occurred (Figure 96a and 96b). Both sols led to the formation of nanostructured alumina on the top surface of the slippers, as shown in Figure 96c. However, some defective, non-structured areas were present, especially on the edge between the outer crown and the central area (Figure 96d).

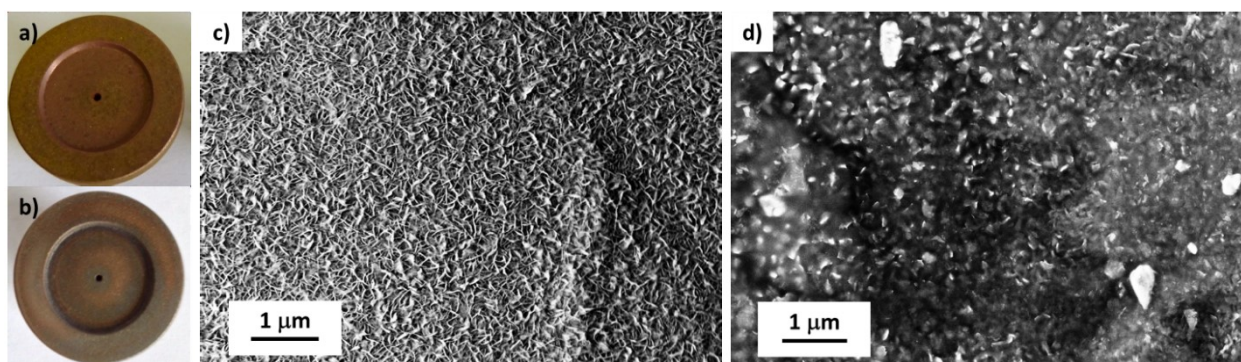


Figure 95. Sandblasted slippers with a) alcohol-based sol A and b) aqueous sol B. c) SEM image of flower-like boehmite nanostructure on the slipper surface. d) Defective, non-structured area of the coating located at the edge between the crown and the central area.

Most notably, the coated samples proved to be superhydrophobic and oleophobic, with contact angles of  $160.0^\circ \pm 17.8^\circ$  and  $150.0^\circ \pm 22.0^\circ$  with water and Arnica46, respectively. Compared to the bare component, the wetting properties of coated slippers were radically different. It must be mentioned that the edge between the crown and the central area was a defective area, with much lower contact angles with water and Arnica 46 compared to the remainder of the surface. This caused the high standard deviations in contact angle values.

From contact angle measurements and SEM observation, no significant difference was observed between the coatings derived from the alcohol-based sol and those formed by the aqueous sol. However, in later steps of the project we implemented the functionalization of blocks composed of a brass slipper clamped on a steel piston (Figure 97a). In this case, we noticed that the aqueous sol induced oxidation and rust formation on the piston, with detrimental effects on the mobility of the clamped slipper (Figure 97b). On the other hand, no rust formed when using the alcohol-based sol. For this reason, we adopted the alcohol-based sol for the remainder of the activity.

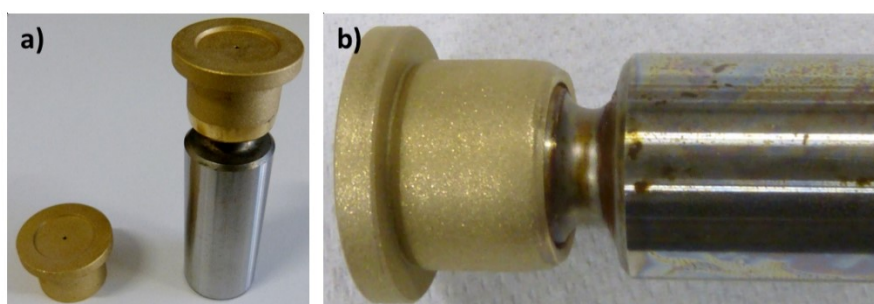


Figure 96. a) Sandblasted slipper and block composed of a sandblasted slipper clamped on a steel piston. b) Block after coating with aqueous alumina sol. Rust is evident on the steel piston.

As a reference, we grafted FAS molecules also on sandblasted slippers with no previous alumina deposition. Contact angles with water and Arnica46 were  $124.8^\circ$  and  $95.8^\circ$ , respectively. This data proves that micron-scale roughness obtained through sandblasting is not enough to achieve amphiphobic behavior, even though FAS molecules were effectively deposited on the surface. Once again, nanoscale texture proved to be a necessary condition for maximum liquid repellence.

### Spray coating

We also attempted spray coating on the slippers with Xcel automated spray system (Aurel Automation, Italy) available at CNR-ISTEC. The most appealing advantage of spray coating over dip coating is the need for smaller volumes of coating sol. Figure 98 shows the slipper in the spray system.

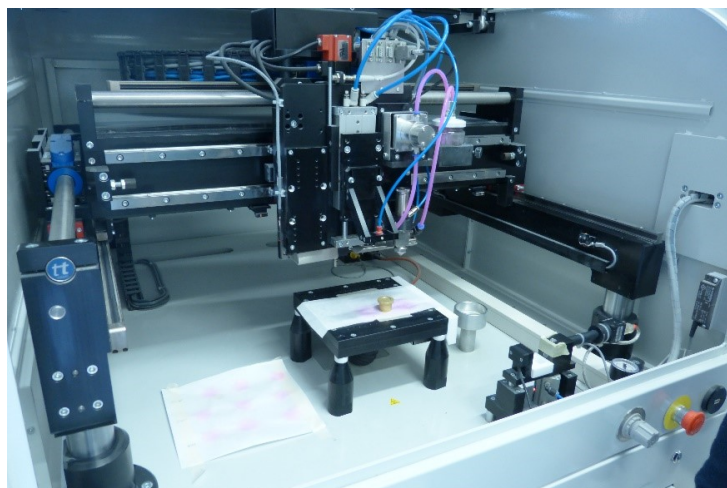
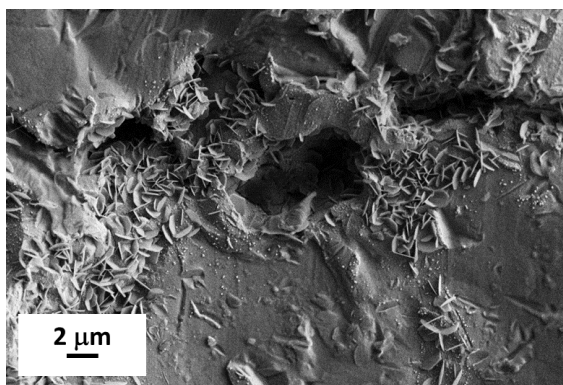


Figure 97. Slipper in the Xcel automated spray machine.

We deposited aqueous alumina suspension B on sandblasted slippers and performed the usual coating process. The Xcel system allows for control of many spraying parameters, which can strongly influence the outcome of coating process. Notably, the system does not provide an absolute value of spraying flow rate, instead it is possible to choose a level from 0 to 20. Based on previous experience with other suspensions, we chose a flow rate of 14.

SEM investigations on coated slippers revealed an inhomogeneous coating, with coexistence of nanostructured, flower-like boehmite areas and non-structured zones (Figure 99). Probably, no coating was deposited on the latter areas. Such incomplete coverage caused a limited liquid repellence on spray-coated slippers, with lower contact angles compared to dip-coated samples (see table in Figure 99).



WCA (°) Dev.st	CAH (°) Dev.st	CA Arnica (°) Dev.st
126.4 7.1	20.5 5.7	96.4 4.9

Figure 98. SEM image of the surface of a sandblasted slipper with alumina coating obtained by spray coating. In the table, water contact angle (WCA), contact angle hysteresis (CAH) and contact angle with Arnica46 (CA Arnica) and relative standard deviations for sandblasted, spray-coated slippers.

Due to such unsuccessful experiments, we abandoned spray-coating as a technique for the deposition of alumina coatings. Nevertheless, spraying remains a promising technique that requires future extensive studies and accurate optimization for its full exploitation.

## ASSESSMENT OF FUNCTIONAL PERFORMANCE IN TEST RIG

The colleagues at CNR-IMAMOTER in Ferrara designed and manufactured an experimental test rig to assess the behavior of slippers in controlled, hydrostatic conditions that simulate real operation in axial piston pumps. Here I will report only few information about the test rig and the most important results in terms of friction behavior, while more detailed information about rig design and realization can be found in the final report of *SNAPP* project [262].

### Test rig design

The design of the experimental rig for functional tests took into account the forces interacting in real piston pumps. Figure 100 schematizes the forces acting on the slippers during operation.

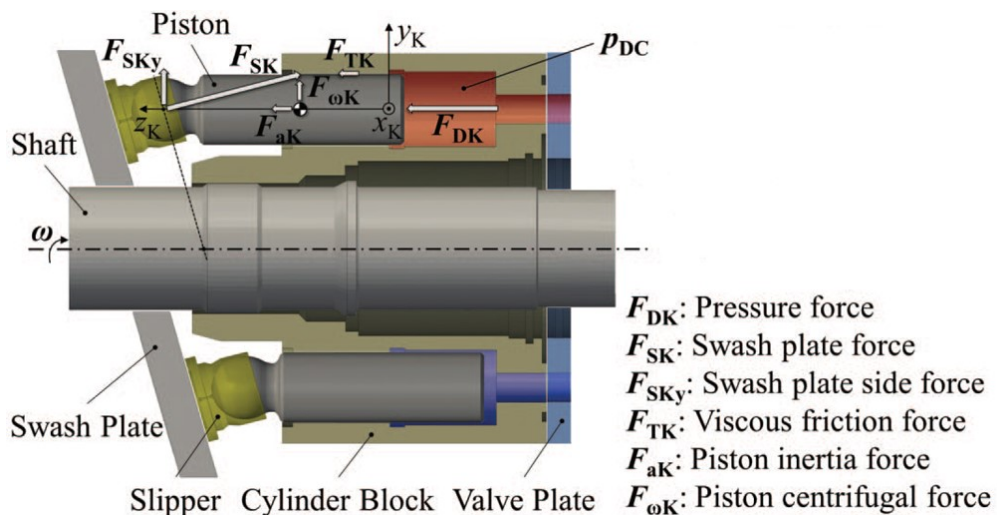


Figure 99. Scheme of axial piston machine main components and piston forces.

Each piston is connected to a slipper via a ball-joint and the slipper slides on a slipper plate which is fixed to an angled swash plate. The ball-joint ensures that the slippers are always parallel to the slipper plate.

When the pump is running, the drive shaft puts in rotation the cylinder block, thus the slippers slide over the plate. While transmitting the torque from the shaft to the mechanism, the piston is driven and a pressure is generated. When the swash plate angle is varied, variable displacement is achieved.

Slippers and swash plate can form a key friction pair, with significant influences on pump performance. Hydrostatic slipper bearing is an effective way to maintain a fluid film between slipper and swash plate during sliding motion, thereby mitigating surface-to-surface direct contact. The design of the slipper reflects such need for lubrication, as shown in Figure 101. High-pressure oil flows into the oil chamber under the slipper through damper orifice and generate hydraulic separating force, then the oil leaks from oil chamber to the shell of the pump. Proper design is necessary to maintain balance between the hydraulic separating force and pressing force that act on the slipper, forming an oil film. When the axial piston pump works, the pressing force that acts on the slipper constantly changes but, due to damping effect made by the orifice, it ensures thickness of the oil film, maintaining stability despite the variation of load. This way, reliable fluid lubrication is provided, and direct contact between the slipper and the swash plate is avoided.

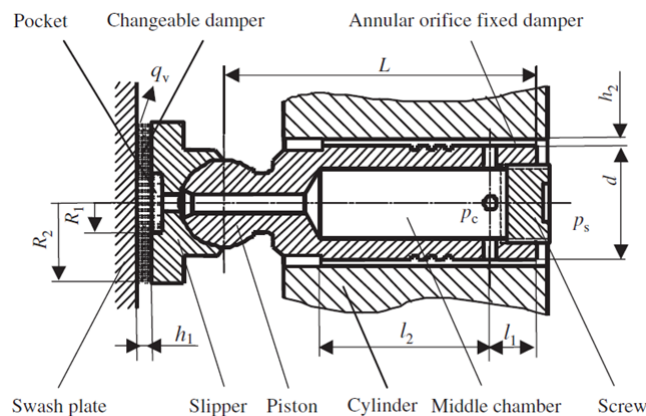


Figure 100. Hydrostatic slipper bearing with an annular orifice damper.

In this scenario, the slipper predominantly acts as a hydrostatic bearing. After careful considerations in terms of involved forces and geometrical constraints, the colleagues at CNR-IMAMOTER in Ferrara designed and assembled a test rig with the following components and depicted in Figure 102:

- Carbon steel (FE360B) frame (structural element 50x30x4);
- Hydraulic motor (HDM 30.17, Casappa) to vary oil flow by varying velocity (from 400 to 3000 rpm);
- Rotating shaft (39NiCrMo3 steel, internal diameter 35 mm);
- Phonic wheel to measure rotation speed;



- Y-bearing plummer block units, cast housing, grub screw locking (SKF - SYJ 35 TF);
- Thrust ball bearings, single direction (SKF - 51407);
- Deep groove ball bearings, single row (SKF - 61907-2RZ);
- Slippers and pistons, provided by HP Hydraulic (Bondioli & Pavesi);
- Pistons housing
- Swashplate (39NiCrMo3 steel, internal diameter 35 mm, outer diameter 160 mm);
- Pre-amplified tension load cell (CTOL 0-10)
- Weight indicator (W100)

To simulate the real working condition of hydrodynamic lubrication, the swashplate was designed and connected to the shaft, which made the swashplate rotate at the same velocity while the pistons were put into the piston housing and fixed to the shaft (see Figure 103).

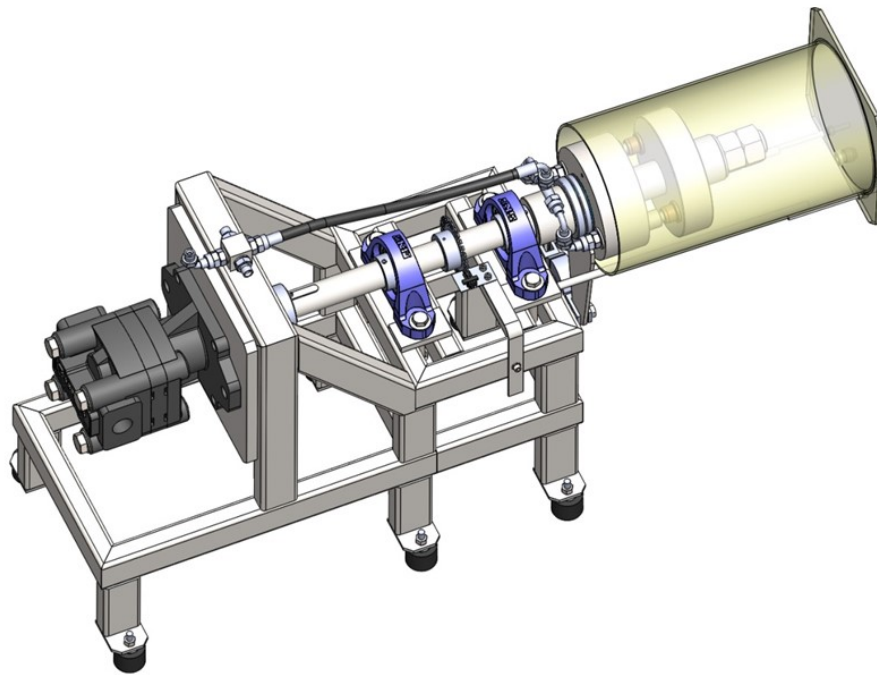


*Figure 101. Complete test bench as designed by CNR-IMAMOTER group in Ferrara.*

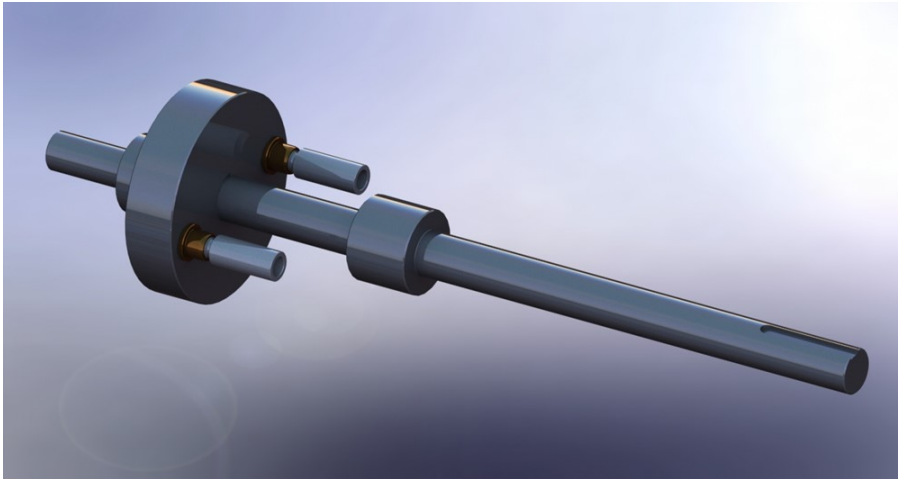


Figure 102. Contact between slippers and swash plate in the test bench.

### Tests on standard slippers

As first step, tests were performed on bare, standard samples. The experimental tests were carried out at constant speed (700rpm) and variable pressure in the range 10 ÷ 50. Table 24 shows input data for the tests on two couples of samples, while Figure 104 shows the related curves of friction and torque as a function of pressure.

<b>Input parameters</b>	<b>Magnitude</b>
Dynamic load bearing (kg)	8100
Reaction arm (m)	0.23
Frictional arm (m)	0.15
Piston diameter (mm)	22.7
Piston surface (mm <sup>2</sup> )	404.7

Table 24. Input data for experiments on bare standard slippers.

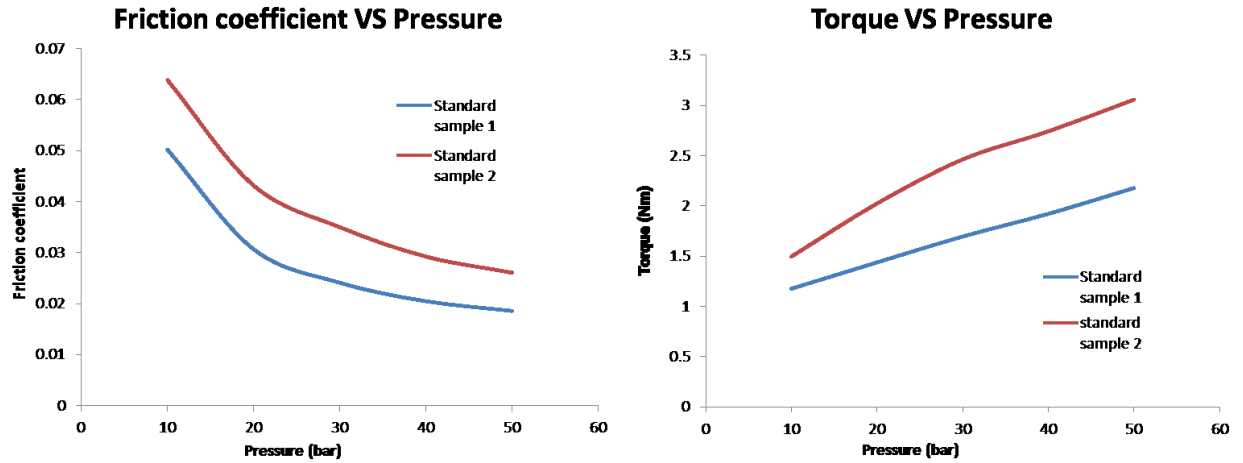


Figure 103. Curves of (left) friction coefficient and (right) torque as a function of pressure in functional tests on two couples of bare standard slippers.

Both the trends in friction coefficient and torque are similar in the two experiments, indicating good reproducibility for the test method.

### Tests on coated slippers

We repeated the tests for eight pairs of hybrid-coated, sandblasted slippers adopting the same conditions as in Table 24. Figure 105 reports the experimental trends of friction coefficient and torque versus pressure. Trends for bare standard slippers are also reported as a reference.

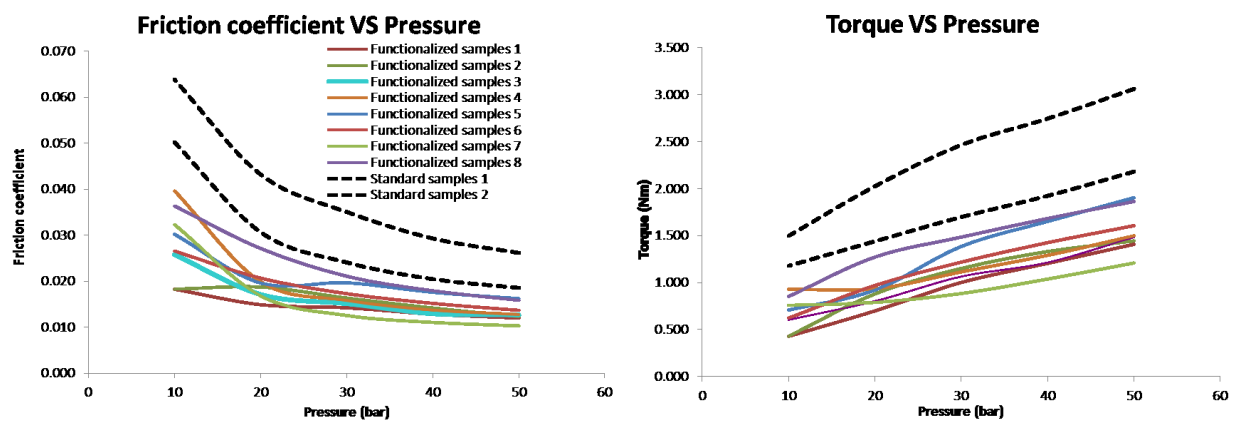


Figure 104. Curves of (left) friction coefficient and (right) torque as a function of pressure in functional tests on eight couples of hybrid-coated slippers (functionalized slippers, solid lines). Curves for two couples of bare standard slippers are also reported (dashed lines).

Most notably, all tested couples of coated slippers showed lower friction and lower torque compared to bare standard slippers. The trends were quite similar for all couples, except for the behavior observed for couple 5 at low pressures. For this reason, we calculated average values of experimental friction coefficient for coated slippers at five pressure values. Results are reported in Figure 106.

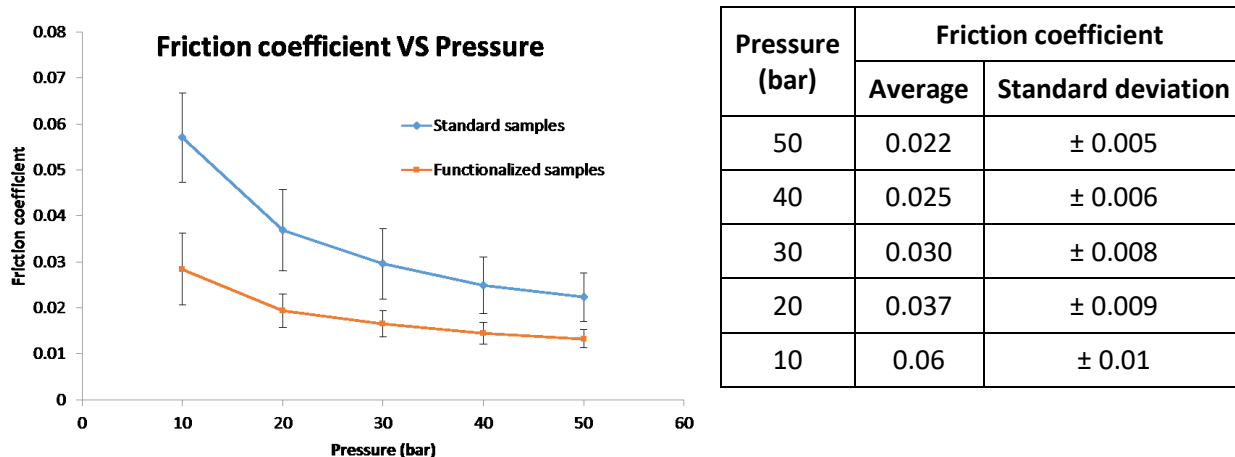


Figure 105. Average friction coefficient and related standard deviation at five pressure values for hybrid-coated slippers: (left) comparison with bare standard slippers and (right) average friction coefficient values. In the graph, standard deviations are reported as error bars. Lines are just guides to the eye.

From Figure 106, functionalized samples clearly showed smaller friction coefficient. Such effect can be attributed to the nanostructured hybrid coating. Notably, friction reduction was maximum at low pressure (e.g. 10 bars), where working conditions are the harshest.

Similarly, the absorbed torque was significantly reduced with the introduction of the nanostructured hybrid coating, as displayed in Figure 107.

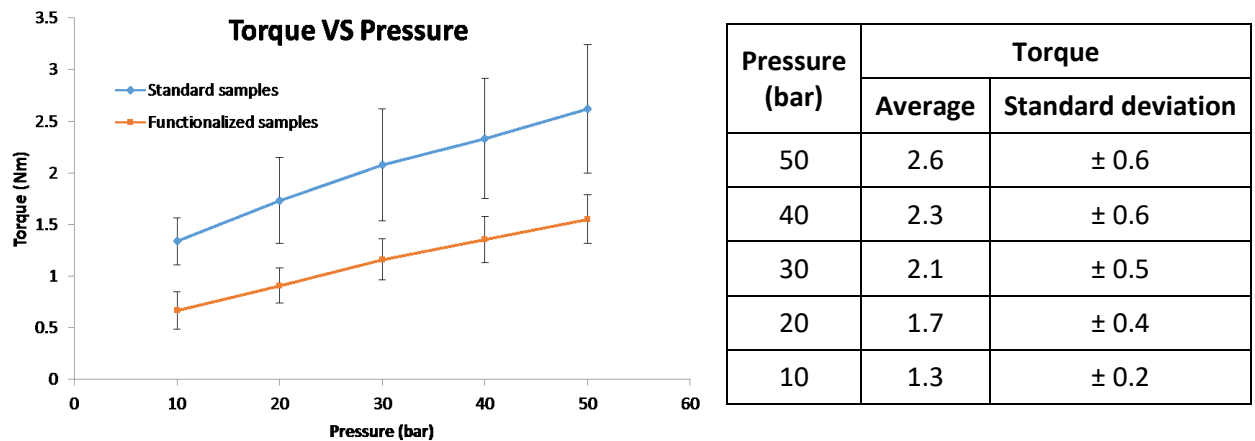


Figure 106. Average torque and related standard deviation at five pressure values for hybrid-coated slippers: (left) comparison with bare standard slippers and (right) average torque values. In the graph, standard deviations are reported as error bars. Lines are just guides to the eye.

These reductions in friction coefficient and absorbed torque might have immensely positive effects in improving efficiency in the component and, consequently, in the entire pump system.

Encouraged by these exciting results, we performed further tests on the slippers, aiming at deeper understanding of hydrodynamic lubrication in presence of a nanostructured, oleophobic surface on the slippers. The group at CNR-IMAMOTER in Ferrara improved the test rig to gain better control on experimental variables and enlarge the field of investigation.

#### Tests in low lubrication regime

Tests at variable pressure and constant speed were repeated on four couples each of standard and coated slippers in conditions of low lubrication, creating a thin meatus between slippers and swashplate (calculated thickness ranging from 43  $\mu\text{m}$  at  $P = 10$  bar down to 32  $\mu\text{m}$  at  $P = 50$  bar). The purpose was to simulate the severe conditions occurring when the pump is started and hydrodynamic lubrication is not achieved yet. Conditions were the same as for previous tests except for rotational speed, which was increased from 700 to 1000 rpm. Only average values for the two types of samples are reported in Figure 108 and Table 25 for brevity.

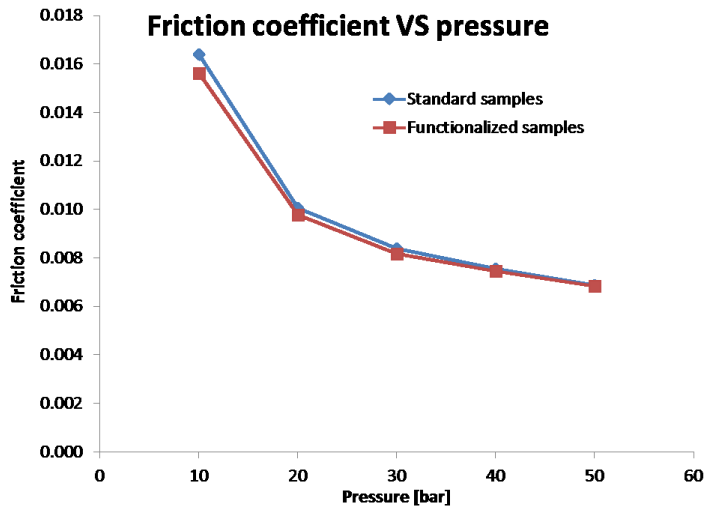


Figure 107. Average friction coefficient at five pressure values for hybrid-coated slippers (red) and bare standard slippers (blue) in low lubrication conditions. Lines are just guides for the eye.

Pressure (bar)	Average friction coefficient		
	Standard samples	Functionalized samples	Percentage gain (%)
10	0.0164 ± 0.002	0.0156 ± 0.001	4.7
20	0.01005 ± 0.0006	0.0098 ± 0.0007	2.9
30	0.0084 ± 0.0004	0.0082 ± 0.0006	2.5
40	0.0075 ± 0.0002	0.0074 ± 0.0004	1.3
50	0.0069 ± 0.0002	0.0068 ± 0.0002	0.3

Table 25. Average friction coefficient values for standard slippers and functionalized slippers at different pressure values in low lubrication conditions. Percentage gain for functionalized slippers over standard ones is also reported.

In such low lubrication conditions, the gain of coated samples over bare, standard ones became smaller, especially at  $P \geq 20$  bar when it was statistically negligible. This effect is quite obvious, as the oleophobic coating cannot express its properties when such small volume of lubricant is available, e.g. when hydrodynamic lubrication is not established.

Another type of test was performed to assess the behavior of coated slippers in low lubrication regime. Pressure was held constant at 20 bar, while rotation speed was varied from 300 to 1500 rpm. Only average values for the two types of samples are reported in Figure 109 and Table 26 for brevity.

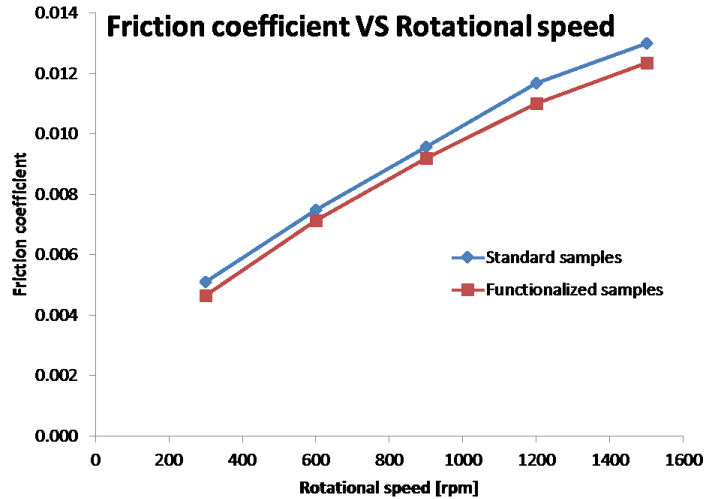


Figure 108. Average friction coefficient at five rotational speed values for hybrid-coated slippers (red) and bare standard slippers (blue) in low lubrication conditions. Lines are just guides for the eye.

Rotational speed (rpm)	Friction coefficient average		
	Standard samples	Functionalized samples	Percentage gain (%)
<b>300</b>	0.0051 ± 0.0008	0.0047 ± 0.0004	8.5
<b>600</b>	0.0075 ± 0.0007	0.0071 ± 0.0006	4.5
<b>900</b>	0.0096 ± 0.0006	0.0092 ± 0.0005	3.8
<b>1200</b>	0.0117 ± 0.0009	0.0110 ± 0.0008	5.8
<b>1500</b>	0.0130 ± 0.0009	0.0124 ± 0.0006	5.0

Table 26. Average friction coefficient values for standard slippers and functionalized slippers at different rotational speed values in low lubrication conditions. Percentage gain for functionalized slippers over standard ones is also reported.

Also in this case, the percentage gain on coated slippers was small and statistically negligible due to the low lubrication regime. No remarkable difference in friction coefficient gain was observed at different rotational speeds.

An endurance test at constant pressure (10 bar) and speed (1000 rpm) in low lubrication regime was also performed to apply very severe stress on the slippers. In fact, a real piston pump operates in such conditions only for few moments after start, but we let these tests run for 1200 minutes (20 hours). Friction coefficient on bare standard slippers was assumed constant. Results are shown in Figure 110.

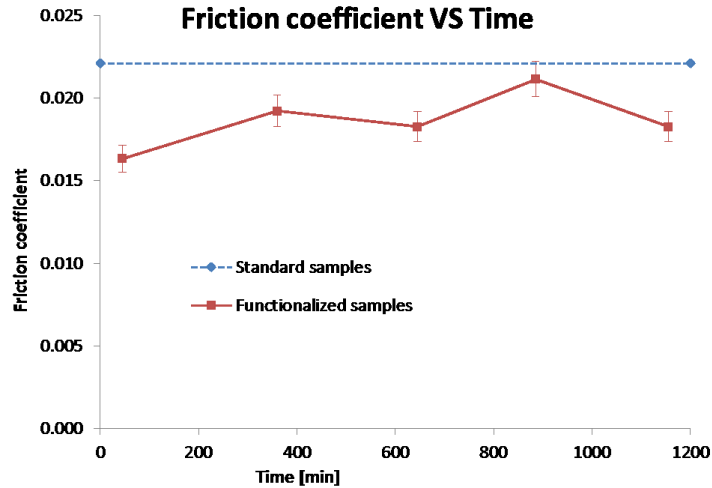


Figure 109. Average friction coefficient as a function of time for hybrid-coated slippers (red) in endurance tests (pressure 10 bar, speed 1000 rpm, low lubrication). Standard deviations are reported as error bars. Friction coefficient for bare standard slippers (blue) is assumed constant. Lines are just guides for the eye.

Remarkably, even after severe stressing for 20 hours, coated slippers still displayed considerably lower friction coefficient compared to bare standard slippers. This is an outstanding result, hinting at long-lasting friction reduction properties for the nanostructured hybrid coating. It represents a crucial property in perspective of a future application of the coating in real axial piston pumps.

#### Tests on slippers with different treatments

Previous tests have shown that hybrid-coated, oleophobic slippers display reduced friction compared to bare, oleophilic standard slippers when hydrodynamic lubrication is established. However, it was not clear whether the entire coating process was necessary to achieve such enhanced performance. Each step of the process implies an economic cost, therefore eliminating even one of them would be positive in regard of a future application on industrial scale.

For this reason, we performed all the previously mentioned tests (variable pressure, variable speed and endurance) on three types of slippers:

- Bare, smooth slippers (standard samples)
- Smooth slippers chemically modified with FAS molecules (Dynasylan SIVO Clear EC, Evonik)
- Rough, hybrid-coated slippers (functionalized samples).

All tests were performed according to the previously mentioned conditions, except for extended ranges of investigated pressure and speed. Constant-speed, variable-pressure tests showed a significant reduction of friction coefficient not only for functionalized samples, but also for smooth and chemically



modified slippers. Notably, the percentage gain in friction coefficient was almost identical, as displayed in Figure 111 and Table 27.

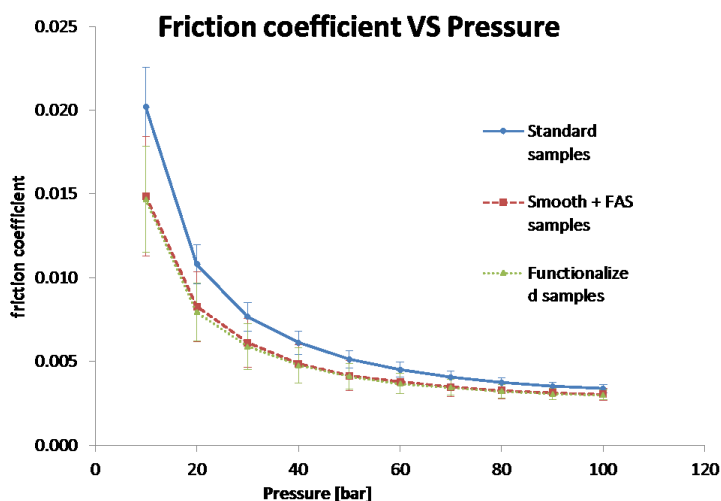


Figure 110. Average friction coefficient as a function of pressure for hybrid-coated slippers (green), smooth and FAS-grafted slippers (red) and smooth standard slippers (blue) in tests at constant speed (1000 rpm). Standard deviations are reported as error bars. Lines are just guides to the eye.

Percentage gain [%]		
Pressure (bar)	Smooth + FAS vs Standard	Functionalized vs Standard
10	26.4	27.3
20	23.4	26.4
30	20.3	23.1
40	20.9	22.0
50	19.0	19.5
60	16.1	18.3
70	14.2	14.7
80	12.8	14.1
90	11.1	12.6
100	9.7	10.8

Table 27. Percentage gain in friction coefficient for smooth, FAS-grafted slippers (central column) and rough, hybrid-coated slippers (right column) over bare, smooth slippers (standard slippers) at different pressure values.

As observed in the first tests, percentage gain on friction coefficient for functionalized slippers decreased with increasing pressure.

Functionalized and smooth, FAS-grafted slippers displayed similar percentage gains in friction coefficient also during constant-pressure, variable-speed tests. Results are shown in Figure 112 and Table 28.

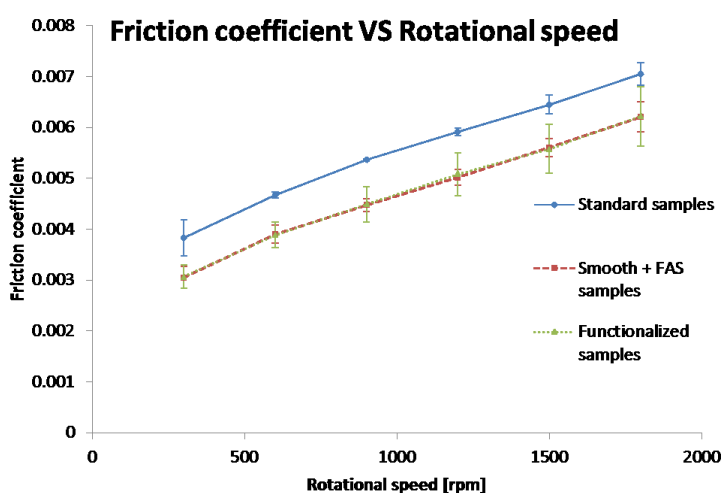


Figure 111. Average friction coefficient as a function of rotational speed for hybrid-coated slippers (green), smooth and FAS-grafted slippers (red) and smooth standard slippers (blue) in tests at constant pressure (50 bar). Standard deviations are reported as error bars. Lines are just guides to the eye.

Rotational speed (rpm)	Percentage gain (%)	
	Smooth + FAS vs Standard	Functionalized vs Standard
300	20.4	20.1
600	16.5	16.8
900	16.5	16.3
1200	15.2	14.1
1500	13.1	13.5
1800	12.0	11.8

Table 28. Percentage gain in friction coefficient for smooth, FAS-grafted slippers (central column) and rough, hybrid-coated slippers (right column) over bare, smooth slippers (standard slippers) at different rotational speed values.

The most insightful results came from endurance tests (pressure 50 bar, speed 1000 rpm, test for 1200 min), as displayed in Figure 113 and Table 29.

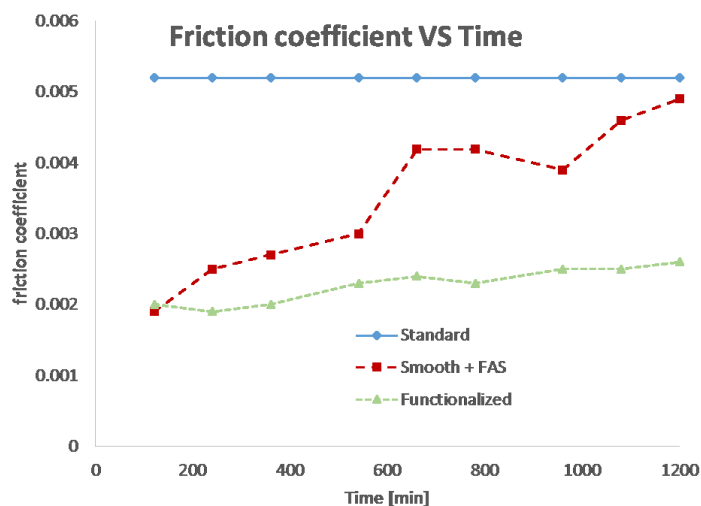


Figure 112. Average friction coefficient as a function of time for hybrid-coated slippers (green), smooth and FAS-grafted slippers (red) and smooth standard slippers (blue) in endurance tests (pressure 50 bar, rotational speed 1000 rpm). Lines are just guides to the eye.

Friction coefficient		
Time (min)	Smooth + FAS	Functionalized
120	0.0019 ± 0.0002	0.0020 ± 0.0004
240	0.0025 ± 0.0002	0.0019 ± 0.0001
360	0.0027 ± 0.0001	0.0020 ± 0.0001
540	0.0030 ± 0.0003	0.0023 ± 0.0001
660	0.00419 ± 0.00009	0.0024 ± 0.0001
780	0.00419 ± 0.00006	0.0023 ± 0.0001
960	0.0039 ± 0.0004	0.0025 ± 0.0001
1080	0.0046 ± 0.0002	0.0025 ± 0.0002
1200	0.0049 ± 0.0001	0.0026 ± 0.0001

Table 29. Friction coefficient for smooth, FAS-grafted slippers (central column) and rough, hybrid-coated slippers (right column) at different time values during endurance tests.

From Figure 113 it is clear that, even though smooth, FAS-grafted slippers and functionalized ones had identical friction coefficient at the beginning of the test, only the hybrid coating provided long-lasting reduction of friction. On “Smooth + FAS” samples, friction coefficient increased through time, reaching values similar to those on bare standard slippers after 20 hours of test. This evidence hints at a total removal of the FAS moieties due to wear. At the end of endurance tests, friction coefficient had increased by 158% on smooth, FAS-grafted slippers, while on functionalized ones it had increased only

by 30%, remaining well below the value observed on standard slippers. Such durable reduction in friction coefficient is extremely appealing for the industry and motivates further studies on the application of this coating in this field.

#### Characterization of tested samples

After such interesting results from friction tests, we wanted to evaluate the wetting behavior and the level of coating damage on tested slippers. For these reason, worn samples returned to CNR-ISTEC for SEM investigations and wetting measurements.

We found out that the level of coating damage depended on the type of test: constant-pressure and constant-speed tests were brief (few minutes each), therefore they caused limited surface erosion. As shown in Figure 114a, few scratches were visible to the naked eye, while SEM images confirmed that damaged, uncoated areas and unspoiled, flower-like boehmite coexisted. Especially in the central area of the slipper (e.g. the part that does not rub against the swashplate), nanostructured coating was still present. Such presence of coated areas guaranteed quite high contact angle values also after tests, with  $WCA = 144.0^\circ \pm 5.5^\circ$  and  $CA\ Arnica = 105.2^\circ \pm 4.5^\circ$ . On the other hand, endurance tests proved much more severe for the hybrid coating: the surface appeared almost completely deprived of the coating (Figure 114b), gaining back its original metallic resemblance. SEM investigations confirmed the clear detachment of boehmite due to abrasion, but some nanostructured areas resisted. Wetting measurements confirmed that the coating was not completely removed from the outer crown during endurance tests, as contact angles ( $WCA = 133.9^\circ \pm 7.6^\circ$  and  $CA\ Arnica = 86.6^\circ \pm 6.7^\circ$ ) remained above those of bare, uncoated slippers.

Tests in low lubrication regime proved even more stressful for the coating, which seemed severely damaged on the crown surface both by eye inspection and SEM observation (Figure 115). However, some areas preserved the nanostructured coating, probably due to protection offered by micron-sized features generated by sandblasting. As already mentioned in previous sections and in the literature [129], the presence of a dual-scale hierarchical structure has remarkably positive effects on mechanical properties of the coating. Consistently, contact angles with water and Arnica46 decreased to  $122^\circ$  and  $55^\circ$  respectively, but did not return to those observed for bare slippers. Notably, on the central area of the slippers, no significant alteration was noticed in the flower-like structure, as shown in Figure 115.

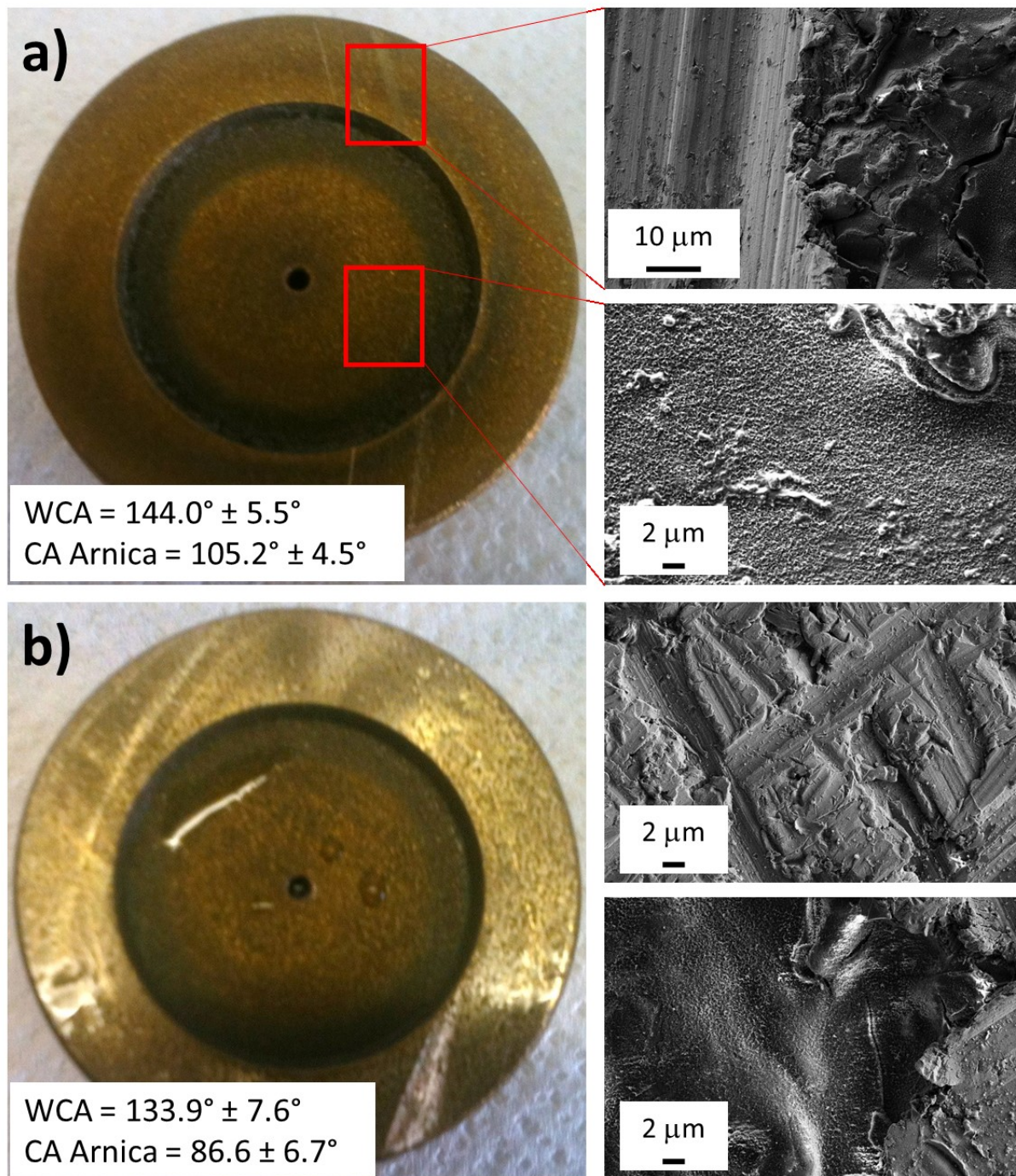


Figure 113. Functionalized slippers after tests in the bench at CNR-IMAMOTER (hydrodynamic conditions): a) after constant-speed tests, the slippers show slight wear signs on the crown (left picture). SEM observation confirmed the partial erosion of the coating on the crown (top right), while the coating on the central area was unharmed (bottom right). b) After endurance tests for 4 hours, the slipper looked damaged on the crown (left), as confirmed from the thick wear tracks in SEM images (top right). However, some areas retained the flower-like nanostructure (bottom right). Insets in the pictures show contact angle values with water (WCA) and Arnica46 (CA Arnica) measured on the crown of each type of slipper. Insets in SEM images show scale bars.

The most remarkable result of these experiments was that, even when the nanostructured coating was damaged by friction in the pump, coated slippers were still able to deliver significant friction reduction

compared to the standard, uncoated ones, as confirmed by endurance tests. This evidence suggests that even the presence of a small amount of coating is enough to obtain significant advantages in terms of efficiency. Furthermore, we also think that the presence of nanostructured coating on the central area of the slipper has positive effects in friction reduction, even if that surface is not experiencing friction against the swashplate. This hypothesis is currently under scrutiny, as CNR-IMAMOTER is performing new tests on coated samples whose crown surface was deliberately abraded with emery paper. The aim is to verify if the presence of the coating is more relevant on the center of the slipper than on the crown.

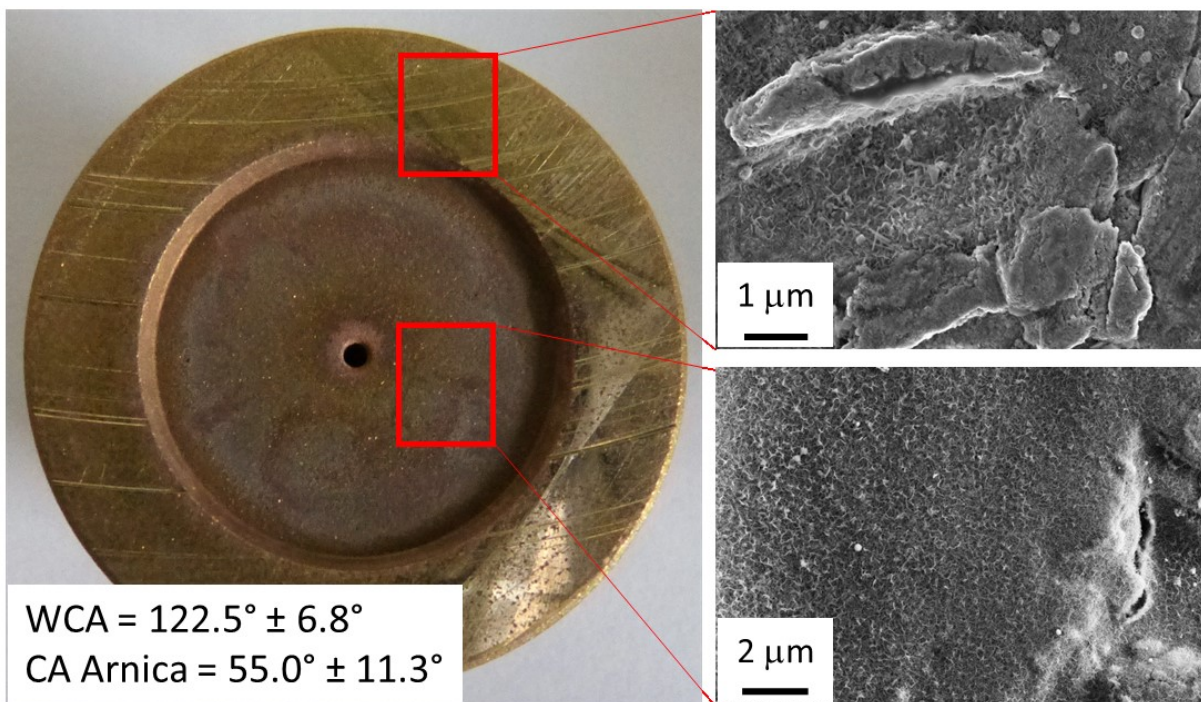


Figure 114. Functionalized slippers after tests in the bench at CNR-IMAMOTER (low lubrication regime): after endurance tests for 20 hours, the slipper looked severely scratched on the crown (left). SEM images confirmed the erosion of many areas on the surface, but some parts were still covered with flower-like boehmite (top right). Meanwhile, the center of the slipper retained the flower-like nanostructure (bottom right). Insets in the pictures shows contact angle values with water (WCA) and Arnica46 (CA Arnica) measured on the crown of each type of slipper. Insets in SEM images show scale bars.

### Tests in real axial piston pump

The final aim of SNAPP project was to validate the results from tests in experimental bench with new tests in a real axial piston pump provided by the industrial partner of the project, HP Hydraulics SpA (Bondioli & Pavesi group).

We functionalized several blocks (slipper clamped on a piston) with the usual procedure and mounted them in a HPP8 closed-circuit axial piston pump. The aim was to characterize, in terms of overall efficiency (defined as the ratio between input mechanical power and output hydraulic power), a pump

with oleophobic coated slipper mounted on, comparing the results to those obtained with uncoated standard slippers. The tests were performed by reproducing the same working conditions for standard and functionalized slippers at different flow rates (60, 90 and 120 l/min) and different working pressure, from 30 bar to 120 bar. The different flow rate was obtained by changing swash plate inclination and maintaining constant rotational speed (1500 rpm). The tests were repeated three times for each type of slipper. Results are shown in Figure 116.

Unexpectedly, the results were in contrast with those obtained in laboratory tests, as standard slippers proved better than functionalized ones in terms of friction and efficiency for all tested flow rates. This is probably due to different working conditions between the test bench and the pump. In fact, in laboratory test the slippers were pushed towards the swashplate by oil pressure, without any further mechanical action (e.g. a spring force). In such conditions, the slippers are able to develop hydrodynamic lubrication immediately, with no dry creeping between them and the plate. On the other hand, in the pump a pre-load spring and the start system transients force the slippers to creep against the plate without any lubrication during the first seconds after start-up. After very few seconds of operation in the pump, functionalized slippers showed clear signs of wear, as shown in Figure 117a. Such severe damage had never been observed before, not even after low-lubrication tests. Probably, the conditions experimented by the coating during the first seconds of operation in the pump are even harsher than those in low-lubrication tests. SEM investigation confirmed that the coating had been almost completely removed from crown surface (Figure 116b), while contact angles fell to values even below those of slippers after low-lubrication (e.g. CA Arnica = 42°, see inset in Figure 116a). Notably, also the coating on the central area of the slipper seemed damaged. SEM image in Figure 116c shows the formation of coating scales, on the surface of which nanostructured boehmite is still present (not shown). Such discontinuity in the coating might be the cause for insufficient performance in the pump.

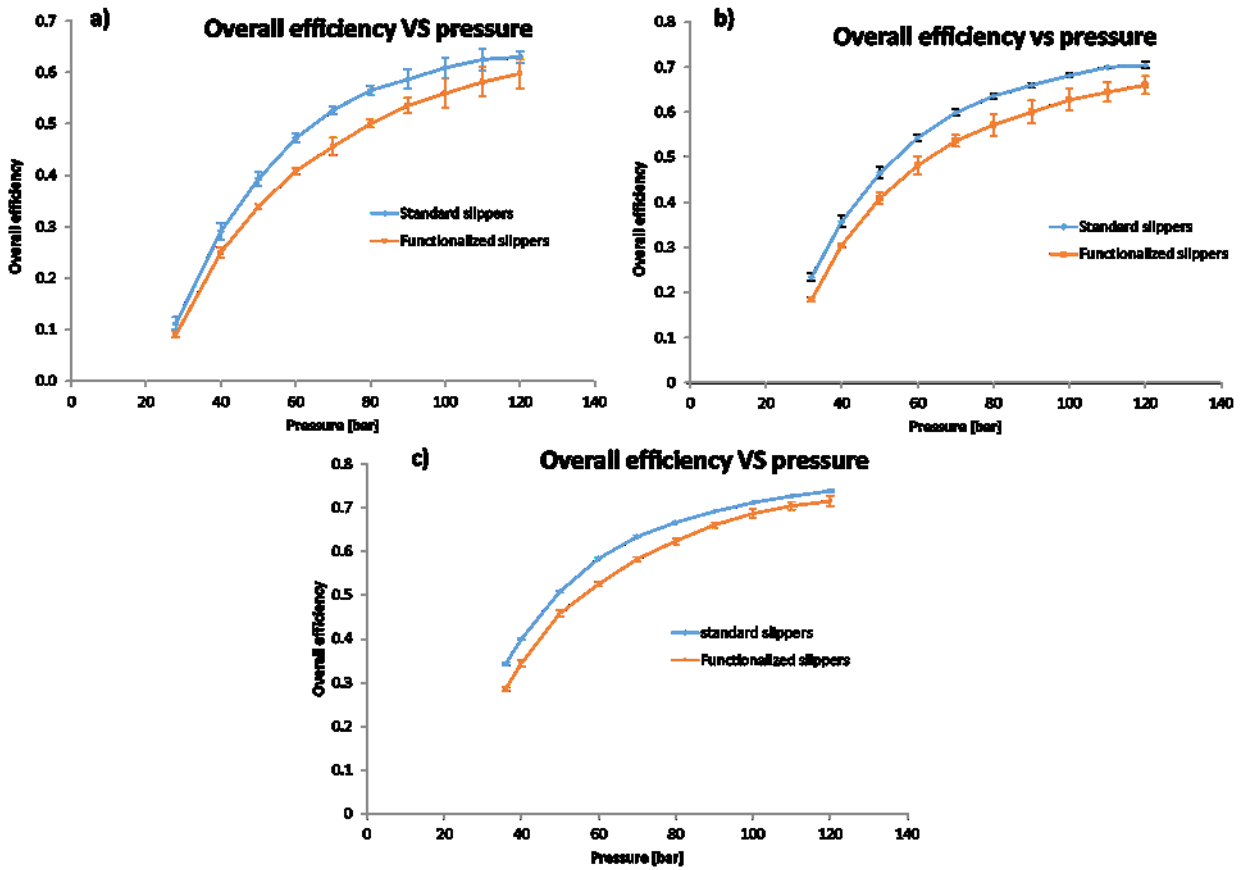


Figure 115. Overall efficiency for the HPP8 pump with standard slippers (blue) and functionalized slippers (orange) at different flow rates: a) 60 l/min, b) 90 l/min, c) 120 l/min. Lines are just guides to the eye.

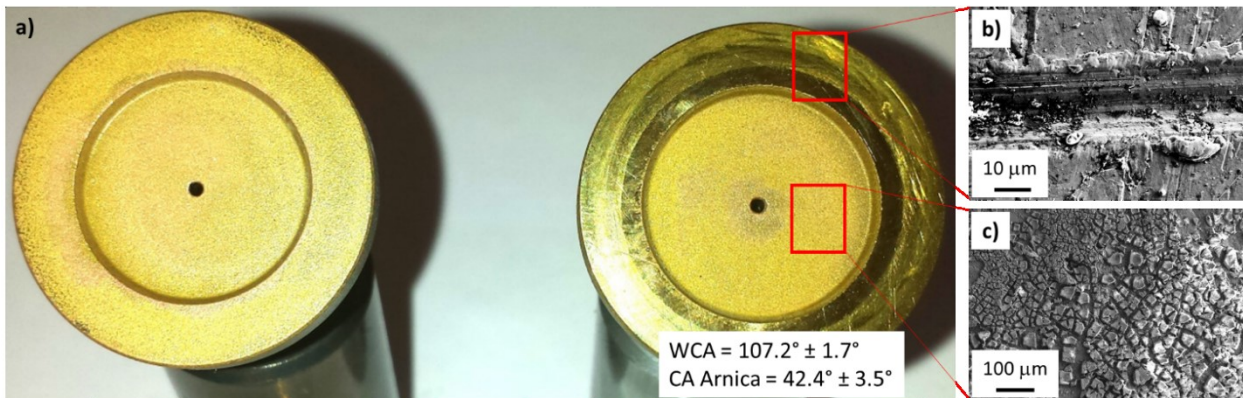


Figure 116. a) Functionalized slippers before (left) and after tests in HPP8 pump (right). Inset shows average contact angle values with water (WCA) and Arnica46 (CA Arnica) measured on the crowns of tested slippers. b) SEM image of the crown of a tested slipper. c) SEM image of the central area of a tested slipper.

These results opened new challenges that must be faced together with the pump manufacturer. Even if the project is technically expired, the network is still investigating the wear phenomena occurring in the pump in the first seconds after start. More specifically, we will install a pre-load spring in the experimental test bench to reproduce the same conditions as in the HPP8 pump. Furthermore, we will



run tests in totally dry conditions (e.g. with no lubrication at all). At the same time, we are studying the solutions to prevent wear among the various internal components of an axial piston pump when an oleophobic layer is used. Finally, we will extend the functionalization process to other components in the pump, starting with the swashplate, to evaluate potential positive effects on pump efficiency.

## TRIBOLOGICAL TESTS

We performed a characterization of the tribology properties of the superhydrophobic coating here discussed. Among the methods available for the description of tribology properties of a surface, we chose the pin-on-disc method. The pin-on-disc machine is a versatile unit designed to evaluate the wear and friction characteristics of a variety of materials exposed to sliding contacts in dry or lubricated environments [263]. The control of the test parameters such as speed, contact pressure, duration and environmental parameters such as temperature, humidity and lubricant allow to closely reproduce the real conditions of a practical wear situation.

All the tests were performed with a CSM Tribometer High temperature apparatus, available at CNR-IMAMOTER in Turin, Italy. The instrument is depicted in Figure 118, along with a table that summarizes its characteristics. In the pin-on-disc apparatus, a pin is loaded onto the test sample with a precisely known weight. The pin is mounted on a stiff lever, designed as a frictionless force transducer. Electronic sensors monitor wear and the tangential force of friction as a function of load, speed, lubrication, or environmental conditions. These parameters, as well as the acoustic emission, are measured and displayed graphically utilizing the TriboDATA software package. The deflection of the arm ensures a nearly fixed contact point and thus a stable position in the friction track. The friction coefficient is determined during the test by measuring the deflection of the arm. In order to measure sample wear behavior, depth and width of the track were measured with a Taylor Hobson Talysurf CCI3000Å non-contact profilometer also available at CNR-IMAMOTER. Furthermore, the wear tracks were inspected with a Zeiss Axio.LabA1.m optical microscope.



<b>Maximum load</b>	Up to 60 N
<b>Friction force</b>	Up to 10 N
<b>Rotation speed</b>	0.3 to 500 rpm
<b>Maximum torque</b>	450 mN
<b>Maximum temperature</b>	Up to 800°C
<b>Track depth measurement</b>	Up to 1.2 mm

Figure 117. (Left) CSM tribometer available at CNR-IMAMOTER in Turin. (Right) Table with the features of the tribometer.

Two types of test were performed with this machine: a friction test in dry conditions and a wear test in presence of a lubricant oil. The main features of these tests are summarized in Table 30.

	<b>Friction test (Dry)</b>	<b>Wear test (Wet, with oil)</b>
<b>Load</b>	10 N	10 N
<b>Speed</b>	20 cm/s	20 cm/s
<b>Temperature</b>	R.T.	R.T.
<b>Pin (diameter)</b>	18MnCr5 steel (2.4 mm)	18MnCr5 steel (2.4 mm)
<b>Laps</b>	5000	50000

Table 30. Summary of the parameters adopted in friction and wear tests performed at CNR-IMAMOTER.

The tests were performed on different samples:

- Smooth bare slipper
- Rough bare slipper
- Smooth with organic layer
- Rough with organic layer
- Rough with hybrid coating (from 5th batch)

Figure 119 reports the friction coefficients measured in the two test conditions for all samples.

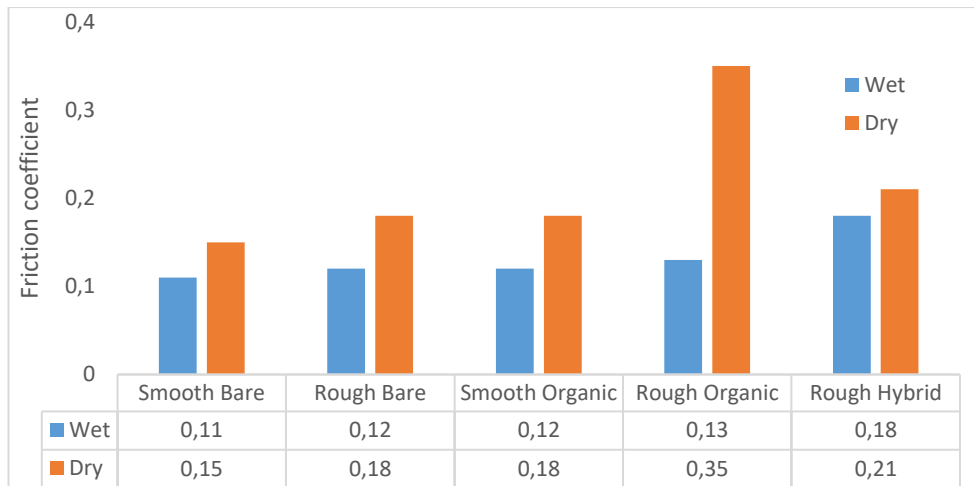


Figure 118. Friction coefficient in wet (blue columns) and dry conditions (orange columns) for five types of samples.

From the friction coefficient values, no significant difference was observed between the different surfaces. Focusing on the wear tests in wet conditions, which are closer to the real operating conditions in axial pumps, all frictions coefficients fell in the range between 0.1 and 0.2. Remarkably, the rough slipper bearing the hybrid coating showed the highest friction coefficient, in contrast to what observed in the test bench. However, it must be considered that wear tests do not reproduce the hydrodynamic flow occurring in the axial pump.

Figure 120 shows the optical microscope images of the wear tracks after test in wet conditions for the five types of surfaces. Clear signs of wear could be noticed in all cases, with exposure of the underlying brass. Judging from the images, less material was ablated from the surface when either an organic or hybrid layer is present (compare Figures 120d and 120e with Figure 120b), but this evaluation is merely qualitative.

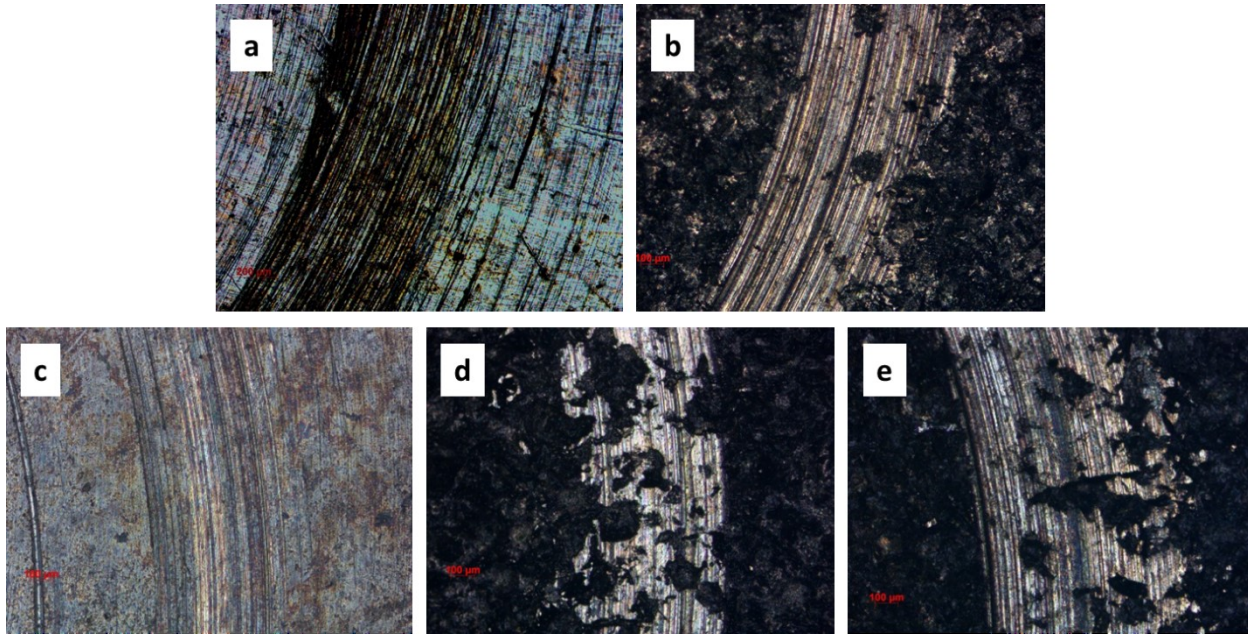


Figure 119. Wear tracks after wear tests (wet conditions) for five types of samples: a) smooth bare; b) rough bare; c) smooth with organic layer; d) rough with organic layer; e) rough with hybrid layer.

From roughness measurements on the wear tracks, it was possible to estimate the average depth of wear track for all cited surfaces. The resulting values, summarized in Table 31, confirmed the reduced track depth in presence of an organic layer for both smooth and rough substrates. However, such measurement was not possible for the hybrid-coated rough surface.

Sample	Average depth ( $\mu\text{m}$ )
Smooth Bare	3.3
Rough Bare	10.1
Smooth with organic layer	1.3
Rough with organic layer	1.4
Rough with hybrid coating	-

Table 31. Average depth of the wear track on five types of surfaces after wear tests.

These tribology tests show that coated surfaces were still sensitive to abrasion in both dry and wet conditions, if the hydrodynamic flow is not established. Once again, these results highlight the necessity for the coating to be in the proper conditions to express its friction reduction properties. Moreover,

future work must be devoted to increase friction and wear resistance in the coating, which showed severe ablation during tribology tests.

## CONCLUSIONS

During the “*Surface Nano-structured Coating for Improved Performance of Axial Piston Pumps*” project (better known with the acronym *SNAPP*), we tried to assess the effects of a superhydrophobic and oleophobic coating on axial piston pump components (e.g. slippers) in terms of friction reduction and efficiency improvement.

We successfully applied the previously described nanostructured hybrid coating on the surface of brass slippers, creating a hierarchical surface structure and shifting their wetting behavior from oleophilic to oleophobic.

The colleagues at CNR-IMAMOTER in Ferrara developed a dedicated test rig to evaluate the lubrication properties of the functionalized slippers and to compare them with standard slippers. The test rig is able to measure the friction force of the slippers in full hydrodynamic lubrication. Results showed that functionalized oleophobic coatings allow for a friction coefficient reduction between 20% and 30%, depending on working conditions. On the other hand, in low lubrication conditions the coating caused only negligible benefits to friction. This made evident that the coating needs a fully established hydrodynamic lubrication regime to bring a relevant improvement in terms of efficiency. Such evidence was confirmed by pin-on-disc tribology studies performed by the group at CNR-IMAMOTER in Turin on the functional coating. Contrary to what observed in test bench experiments, it seemed that surface functionalization did not reduce friction coefficient, even though the surface looked less worn after the tests compared to that of bare standard slippers. Even in this case, the test could not simulate the hydrodynamic lubrication condition.

Further test bench experiments were run to assess the effect of different surface treatments on friction. Even though short constant-pressure and constant-speed tests for smooth, FAS-grafted slippers and functionalized ones gave identical results, a significant difference between the two types of samples emerged in endurance tests. After 20 hours, chemically-modified smooth slippers with no nanostructured coating had friction coefficients very similar to those on standard slippers. On the other hand, functionalized slippers still showed significantly reduced friction. Thus, the nanostructured hybrid coating proved necessary for a long-lasting friction reduction in the test bench. This is an outstanding result that fosters the interest on these coatings and their friction reduction properties.

The final step of the project was to characterize a closed-circuit axial piston pump HPP8 in terms of overall efficiency, comparing the performance of standard slippers to the functionalized ones. Such tests reproduced the actual working conditions for the slippers at different flow rates and working pressures. Contrary to the expectations, standard slippers worked better than functionalized ones. We explained this behaviour with the different work conditions between the experimental test bench and the pump. In fact, in the test bench the slippers were pushed against the plate by the oil pressure, without any mechanical action (e.g. a spring force), so they could develop hydrodynamic lubrication immediately. On the contrary, in the pump a spring forces the slippers to creep against the plate without any lubrication during the first seconds of work. This wear phenomenon caused coating removal. We are planning many modifications to the test bench in order to reproduce such phenomena and extend our knowledge on wear mechanism on slippers surfaces.

In summary, *SNAPP* project was a pioneering work that studied a totally unexplored property of the nanostructured coating. Even though not all results were positive, our interest on the subject is still strong as the potential fallout of this activity could be huge.

## 9. CONCLUSIONS

The control of surface wetting properties is a relevant target in a wide range of industrial applications. More specifically, the achievement of superhydrophobicity and oleophobicity on the surface of different industrial materials has been intensively investigated by the research community in the last decades. For this reason, I chose to focus my PhD activity on the design and fabrication of a superhydrophobic and oleophobic (thus amphiphobic) hybrid coating, based on the lotus effect. The first component of the coating was an inorganic layer of randomly dispersed boehmite nanoflakes, derived from thermal treatments (including immersion in boiling water) of a film of alumina nanoparticles. I obtained such nanoparticles via sol-gel method in different media, either isopropyl alcohol or water, followed by deposition via either dip coating or spray coating. The process required a tailored optimization for materials like copper, for which treatment temperatures above 200°C proved detrimental in terms of coating adhesion and robustness due to the formation of structured CuO phases. Meanwhile, copper also favored the alcohol-based alumina suspension over the aqueous one. Boehmite nanoflakes formed a peculiar flower-like nanostructure. After chemical modification through the grafting of fluoroalkylsilanes (FAS), the as-prepared hybrid coating displayed excellent repellence towards water and many liquids with low surface tension, with high contact angles and low contact angle hysteresis. Moreover, Prof. Zanoni and his group at University La Sapienza performed a detailed analysis of the chemical composition of the coating via XPS analyses, coupled with DFT calculations to obtain more information about the organic layer. We discovered that the FAS molecules were grafted to the boehmite layer, forming an ordered monolayer that is responsible for the excellent liquid-repellent properties of the coating, together with the homogeneous boehmite nanostructure. Moreover, this technology proved suitable to different materials like metals, glass and ceramics, thus increasing its appeal for future industrial application.

However, contact angle measurements are not sufficient for a proper comprehension of surface wetting behavior in more “dynamic” situations. Thus, I performed drop impact studies on superhydrophobic surfaces in collaboration with the group of Prof. Marengo at University of Bergamo. This kind of study is relevant for application fields like sprays, ink-jet printing, fuel injection and so on. We compared the drop impact outcome of two liquids (water and hexadecane) on four superhydrophobic surfaces, with different morphology and/or chemical composition. Even though they had similar contact angles, drop impact outcomes were different. The nanostructured coating here described generated water drop rebound even for the highest investigated drop impact velocities, while on other surfaces with sub-micron features the drop could penetrate between the cavities and caused impalement. Remarkably, the critical velocity for impalement seemed to depend also on surface chemistry. It is the first time that

such an effect is reported. On the other hand, with hexadecane drops no rebound could be observed, even when contact angles were high. This result led us to reconsider the criterion for drop rebound on a surface. It is necessary to consider parameters related to both the liquid (impact velocity, surface tension, viscosity) and the solid phase (roughness, topography and chemical composition) to predict drop impact outcome.

In the literature, the anti-icing properties of superhydrophobic surfaces have been extensively investigated due to their huge potential impact on fields like aerospace, communications and renewable energies. In principle, low adhesion of water drops on the surface should lead to delayed icing (e.g. icing should occur at lower temperatures) due to easier drop shedding. However, in the literature it also reported that surface roughness enhances ice adhesion. For this reason, I studied the behavior of the superhydrophobic coating in freezing conditions at the Surface Engineering and Instrumentation Lab (SEiL) at York University (Toronto, Canada), led by Prof. Amirfazli. First, I performed drop shedding experiments on coated surfaces at room temperature and  $-5^{\circ}\text{C}$ . While in the first case sessile drops were shed at very low airflow velocities  $U$ , when lowering  $T$  shedding became much harder and required higher  $U$  due to increased adhesion to the surface. Moreover, I tried to measure the effect of the coating in delaying drop freezing, but the experimental setup was not suitable for these experiments.

At SEiL I also performed experiments in high humidity conditions. Indeed, in applications like air conditioning and automotive, surfaces are expected to favor dropwise condensation of air humidity, combined with an easy removal of the condensates for enhanced heat exchange. The behavior of liquids drops depends on the balance between adhesion forces and external ones (e.g. gravity, airflow). I performed drop shedding experiments with condensed drops on coated surfaces. Induction time proved crucial in determining drop shedding behavior in such condensing conditions, as well as surface roughness. Moreover, I evaluated the evolution through time of contact angles of sessile drops on coated surfaces kept in condensing conditions. Interestingly, CAH seemed to decrease for long condensation times on all surfaces, suggesting the formation of a liquid film and low adhesion. This unexpected finding needs further investigation as its impact could be relevant.

Another substantial part of my PhD work concerned the application of the oleophobic coating for friction reduction in axial piston pumps. We tried to reverse the wetting properties of pump components (e.g. slippers) from oleophilic to oleophobic through deposition of the nanostructured hybrid coating and investigated the effects on friction in a test rig, designed and developed by colleagues at CNR-IMAMOTER. Functional tests showed a relevant friction reduction and efficiency increase. Moreover, this behavior seemed to withstand long testing times. Notwithstanding this behavior could not be replicated in a real piston pump due to design issues, the observed phenomenon



was quite unique (no work in the literature ever reported it) and certainly deserves further investigation.

In summary, the hybrid, nanostructured coating owned remarkable liquid-repellent properties, due to the combination of flower-like morphology and grafted FAS molecules. The coating displayed excellent durability in a wide spectrum of aggressive environments and proved efficient even in dynamic conditions (e.g. drop impact, drop shedding with airflow, friction reduction). However, limitations appeared in severe conditions like high pH, high RH and freezing T. Future work must be devoted to the optimization of the coating to widen its range of potential applications.



## ACKNOWLEDGEMENTS

First, I want to thank my research group at CNR-ISTEC. Thanks to Dr.ssa Mariarosa Raimondo for believing in me and supporting my growth as a scientist. Thank you for the chance of following this PhD course, I really feel appreciated. Thanks to Aurora, Guia and Magda for teaching me everything in the lab and being patient. Thanks to Giulio for being such a precious support in my work, but even more for being a real friend. Thanks to all the colleagues and ex colleagues at ISTEC for the scientific and moral support. Special thanks to Elettra, Riccardo and Natalia for making all the breaks so fun, it is much easier to work with such great people around.

Thanks to Prof. Marco Marengo and Prof. Alidad Amirfazli for hosting me in their research groups in Bergamo and Toronto. It was an honor to attend your labs and it really made me grow up as a scientist and as a person. Thanks to Ileana, Bolarinwa, Aysan, Constantine and Chen for the support during my research activity away from home, I learned a lot from all of you.

Thanks to all the people from the groups we have collaborated with: Prof. Roberto Paoluzzi, Eng. Antonino Bonanno and their group at IMAMOTER in Ferrara; Prof. Robertino Zanoni and Alessandro Motta at University La Sapienza in Rome. It has been great to work with you and I am sure that we will continue our collaborations.

I would like to thank my family for the unconditioned support throughout my entire life, especially for encouraging me to follow my ambitions and my passions. I would like to thank my parents Anna and Angelo for being unique role models and always making me feel loved. You always gave your all for me and I am grateful. Thanks to my sister Giulia for always being on my side and providing heartfelt advice, even from a distance. I also want to thank the rest of the family: Giovanni, Nicoletta, Linda and Michele on this side of the border; Mauro, Ines and Marta in Grenoble. I have always felt your love and support and I really want to thank you for it.

Finally, I want to thank all my friends for always being with me, never letting me down and giving me help, support and much needed good times. You are way too many to name you all, but you know who you are. No matter the distance, it will always be like we saw each other yesterday.

Thank you all, once again.



## REFERENCES

- [1] T. Young, "An essay on the cohesion of fluids," *Philosophical Transactions of The Royal Society of London*, vol. 95, pp. 65-87, 1805.
- [2] R. Wenzel, "Resistance of solid surfaces to wetting by water," *Industrial & Engineering Chemistry*, vol. 28, no. 8, pp. 988-994, 1936.
- [3] A. Cassie and S. Baxter, "Wettability of porous surfaces," *Transactions of the Faraday Society*, vol. 40, pp. 546-551, 1944.
- [4] W. Barthlott and N. Ehler, "Raster-elektronenmikroskopie der epidermis-oberflächen von Spermatophyten," *Tropische und Subtropische Pflanzenwelt*, vol. 19, pp. 367-465, 1977.
- [5] W. Barthlott and C. Neinhuis, "Purity of the sacred lotus, or escape from contamination in biological surfaces," *Planta*, vol. 202, pp. 1-8, 1997.
- [6] M. T. Khorasani, H. Mirzadeh and P. G. Sammes, "Laser induced surface modification of polydimethylsiloxane as a super-hydrophobic material," *Radiation Physics and Chemistry*, vol. 47, no. 6, pp. 881-888, 1996.
- [7] X. Tian, S. Shaw, K. R. Lind and L. Cademartiri, "Thermal processing of silicones for green, scalable, and healable superhydrophobic coatings," *Advanced Materials*, vol. 28, no. 19, pp. 3677-3682, 2016.
- [8] B. Qian and Z. Shen, "Fabrication of superhydrophobic surfaces by dislocation-selective chemical etching on aluminum, copper, and zinc substrates," *Langmuir*, vol. 21, no. 20, pp. 9007-9009, 2005.
- [9] I. Bernagozzi, C. Antonini, F. Villa and M. Marengo, "Fabricating superhydrophobic aluminum: An optimized one-step wet-synthesis using fluoroalkyl silane," *Colloids and Surfaces A: Physicochemical and Engineering Aspects*, vol. 441, pp. 919-924, 2014.
- [10] H.-K. Choi, J.-H. Shin, S. Choo, S.-W. Ryu, Y.-D. Kim and H. Lee, "Fabrication of superhydrophobic and oleophobic Al surfaces by chemical etching and surface fluorination," *Thin Solid Films*, Vols. 76-80, p. 585, 2015.
- [11] N. Vandecasteele, D. Merche and F. Reniers, "XPS and contact angle study of N<sub>2</sub> and O<sub>2</sub> plasma-modified PTFE, PVDF and PVF surfaces," *Surface and Interface Analysis*, vol. 38, pp. 526-530, 2006.
- [12] E. Wohlfart, J. P. Fernández-Blázquez, E. Arzt and A. del Campo, "Nanofibrillar patterns on PET: The influence of plasma parameters in surface morphology," *Plasma Processes and Polymers*, vol. 8, no. 9, pp. 876-884, 2011.
- [13] T. Darmanin, E. Taffin de Givenchy, S. Amigoni and F. Guittard, "Superhydrophobic surfaces by electrochemical processes," *Advanced Materials*, vol. 25, pp. 1378-1394, 2013.
- [14] Z. Wang, L. Zhu, W. Li and H. Liu, "Bioinspired in situ growth of conversion films with underwater," *ACS Applied Materials & Interfaces*, vol. 5, pp. 10904-10911, 2013.

- [15] H. Wang, D. Gao, Y. Meng, H. Wang, E. Wang and Y. Zhu, "Corrosion-resistance, robust and wear-durable highly amphiphobic polymer based composite coating via a simple spraying approach," *Progress in Organic Coatings*, vol. 82, pp. 74-80, 2015.
- [16] H. S. Hwang, N. H. Kim, S. G. Lee, D. Y. Lee, K. Cho and I. Park, "Facile fabrication of transparent superhydrophobic surfaces by spray deposition," *ACS Applied Materials and Interfaces*, vol. 3, pp. 2179-2183, 2011.
- [17] L. Feng, H. Zhang, P. Mao, Y. Wang and Y. Ge, "Superhydrophobic alumina surface based on stearic acid modification," *Applied Surface Science*, vol. 257, pp. 3959-3963, 2011.
- [18] W. Ma, H. Wu, Y. Higaki, H. Otsuka and A. Takahara, "A "non-sticky" superhydrophobic surface prepared by self-assembly of fluoroalkyl phosphonic acid on a hierarchically micro/nanostructured alumina gel film," *Chemical Communications*, vol. 48, pp. 6824-6826, 2012, 48, 6824-6826.
- [19] L. Gao and J. He, "Surface hydrophobic co-modification of hollow silica nanoparticles toward large-area transparent superhydrophobic coatings," *Journal of Colloid and Interface Science*, vol. 396, pp. 152-159, 2013.
- [20] M. Manca, A. Cannavale, L. De Marco, A. S. Aricò, R. Cingolani and G. Gigli, "Durable superhydrophobic and antireflective surfaces by trimethylsilanized silica nanoparticles-based sol-gel processing," *Langmuir* 2009, 25(11), 6357-6362, vol. 25, no. 11, pp. 6357-6362, 2009.
- [21] Y. Li, L. Li and J. Sun, "Bioinspired self-healing superhydrophobic coatings," *Angewandte Chemie International Edition*, vol. 49, pp. 6129-6133, 2010.
- [22] Y. Li, S. Chen, M. Wu and J. Sun, "All spraying processes for the fabrication of robust, self-healing, superhydrophobic coatings," *Advanced Materials*, vol. 26, pp. 3344-3348, 2014.
- [23] H. Fan, S. Li, Z. Zhao, H. Wang, Z. Shi and L. Zhang, "Inhibition of brass corrosion in sodium chloride solutions by self-assembled silane films," *Corrosion Science*, vol. 53, pp. 4273-4281, 2011.
- [24] L. Yao, M. Zhen, S. He, L. Ma, M. Li and W. Shen, "Preparation and properties of ZnS superhydrophobic surface with hierarchical structure," *Applied Surface Science*, vol. 257, no. 7, pp. 2955-2959, 2011.
- [25] T. Ishizaki, J. Hieda, N. Saito and O. Takai, "Corrosion resistance and chemical stability of superhydrophobic film deposited on magnesium alloy AZ31 by microwave plasma-enhanced chemical vapor deposition," *Electrochimica Acta*, vol. 55, no. 23, pp. 7094-7101, 2010.
- [26] K. Tadanaga, T. Iwami, T. Minami and N. Tohge, "Microstructure of Al<sub>2</sub>O<sub>3</sub> xerogels and aerogels from aluminum-tri-sec butoxide modified with ethylacetoacetate," *Journal of the Ceramic Society of Japan*, vol. 103, no. 6, pp. 582-585, 1995.
- [27] K. Tadanaga, N. Katata and T. Minami, "Super-water-repellent Al<sub>2</sub>O<sub>3</sub> coating films with high transparency," *Journal of the American Ceramic Society*, vol. 80, no. 4, pp. 1040-1042, 1997.
- [28] H. Uchihashi, N. Tohge and T. Minami, "Preparation of amorphous Al<sub>2</sub>O<sub>3</sub> thin films from stabilized Al-alkoxides by the sol-gel method," *Nippon Seramikkusu Kyokai Gakujutsu Ronbunshi*, vol. 97, no. 3, pp. 396-399, 1989.

- [29] R. V. Lakshmi, P. Bera, C. Anandan and B. J. Basu, "Effect of the size of silica nanoparticles on wettability and surface chemistry of sol-gel superhydrophobic and oleophobic nanocomposite coatings," *Applied Surface Science*, vol. 20, pp. 780-786, 2014.
- [30] L. Hao, Y. Sirong, H. Xiangxiang, L. Enyang and Z. Yan, "Fabrication of superhydrophobic and oleophobic surface on zinc substrate by a simple method," *Colloids and Surfaces A: Physicochemical and Engineering Aspects*, vol. 469, pp. 271-278, 2015.
- [31] B. M. L. Koch, J. A. W. Elliott and A. Amirfazli, "Study of model superoleophobic surfaces fabricated with a modified Bosch etch method," *Langmuir*, vol. 30, pp. 14039-14047, 2014.
- [32] R. Fürstner, W. Barthlott, C. Neinhuis and P. Walzel, "Wetting and self-cleaning properties of artificial superhydrophobic surfaces," *Langmuir*, vol. 21, no. 3, pp. 956-961, 2005.
- [33] S. Nishimoto and B. Bhushan, "Bioinspired self-cleaning surfaces with superhydrophobicity, superoleophobicity, and superhydrophilicity," *RSC Advances*, vol. 3, pp. 671-690, 2013.
- [34] M. Marengo, C. Antonini, I. V. Roisman and C. Tropea, "Drop collisions with simple and complex surfaces. Curr. Opin. Colloid," *Current Opinions on Colloid and Interface Science*, vol. 16, pp. 292-303, 2011.
- [35] V. Bertola and M. Wang, "Dynamic contact angle of dilute polymer solution drops impacting on a hydrophobic surface," *Colloids and Surfaces A: Physicochemical and Engineering Aspects*, vol. 481, pp. 600-608, 2015.
- [36] A. Milionis, K. G. Krishnan and E. Loth, "Hemolymph drop impact outcomes on surfaces with varying wettability. Appl. Surf. Sci. 2015,," *Applied Surface Science*, vol. 345, pp. 36-43, 2015.
- [37] M. Song, Y. Liu, S. Cui, L. Liu and M. Yang, "Fabrication and icing property of superhydrophilic and superhydrophobic aluminum surfaces derived from anodizing aluminum foil in a sodium chloride aqueous solution," *Applied Surface Science*, vol. 283, pp. 19-24, 2013.
- [38] D. P. Singh and J. P. Singh, "Delayed freezing of water droplet on silver nanocolumnar thin film," *Applied Physics Letters*, vol. 102, p. 243112, 2013.
- [39] S. A. Kulinich and M. Farzaneh, "How wetting hysteresis influences ice adhesion strength on superhydrophobic surfaces," *Langmuir*, vol. 25, pp. 8854-8856, 2009.
- [40] L. Cao, A. Jones, W. K. Sikka, J. Wu and D. Gao, "Anti-icing superhydrophobic coatings," *Langmuir*, vol. 25, pp. 12444-12448, 2009.
- [41] S. A. Kulinich, S. Farhadi, K. Nose and X. W. Du, "Superhydrophobic surfaces: are they really ice-repellent?," *Langmuir*, vol. 27, pp. 25-29, 2010.
- [42] K. K. Varanasi, T. Deng, J. D. Smith, M. Hsu and N. Bhate, "Frost formation and ice adhesion on superhydrophobic surfaces," *Applied Physics Letters*, vol. 97, p. 234102, 2010.
- [43] A. J. B. Milne and A. Amirfazli, "Drop shedding by shear flow for hydrophilic to superhydrophobic surfaces," *Langmuir*, vol. 25, no. 24, pp. 14155-14164, 2009.
- [44] S. Moghtadernejad, M. Mohammadi, M. Jadidi, M. Tembely and A. Dolatabadi, "Shear driven

- droplet shedding on surfaces with various wettabilities," *SAE International Journal of Aerospace*, vol. 6, no. 2, pp. 459-464, 2013.
- [45] M. Wen, L. Wang, M. Zhang, L. Jiang and Y. Zheng, "Antifogging and icing-delay properties of composite micro- and nanostructured surfaces," *ACS Applied Materials & Interfaces*, vol. 6, pp. 3963-3968, 2014.
- [46] S. Moghtadernejad, M. Tembely, M. Jadidi, N. Esmail and A. Dolatabadi, "Shear driven droplet shedding and coalescence on a superhydrophobic surface," *Physics of Fluids*, vol. 27, p. 032106, 2015.
- [47] C. Gauss, *Principia generalia theoriae figurae fluidorum in statu aequilibrii*, Göttingen: Dieterichs, 1830.
- [48] E. Celia, T. Darmanin, E. Taffin de Givenchy, S. Amigoni and F. Guittard, "Recent advances in designing superhydrophobic surfaces," *Journal of Colloid and Interface Science*, vol. 402, pp. 1-18, 2013.
- [49] A. J. B. Milne and A. Amirfazli, "The Cassie equation: How it is meant to be used," *Advances in Colloid and Interface Science*, vol. 170, pp. 48-55, 2012.
- [50] S. Herminghaus, "Roughness-induced non-wetting," *Europhysics Letters*, vol. 52, no. 2, pp. 165-170, 2000.
- [51] L. Gao and T. J. McCarthy, "How Wenzel and Cassie were wrong," *Langmuir*, vol. 23, pp. 3762-3765, 2007.
- [52] R. Lipowsky, P. Lenz and P. S. Swain, "Wetting and dewetting of structured and imprinted surfaces," *Colloids and Surfaces A: Physicochemical and Engineering Aspects*, vol. 161, pp. 3-22, 2000.
- [53] J. Bico, U. Thiele and D. Quéré, "Wetting of textured surfaces," *Colloids and Surfaces A: Physicochemical and Engineering Aspects*, vol. 206, pp. 41-46, 2002.
- [54] T. Deng, K. Varanasi, M. Hsu, N. Bhate, C. Keimel, J. Stein and N. Blohm, "Nonwetting of impinging droplets on textured surfaces," *Applied Physics Letters*, vol. 94, p. 133109, 2009.
- [55] T. Maitra, M. K. Tiwari, C. Antonini, P. Schoch, S. Jung, P. Eberle and D. Poulikakos, "On the nanoengineering of superhydrophobic and impalement resistant surface textures below the freezing temperature," *Nano Letters*, vol. 14, pp. 172-182, 2014.
- [56] Y. Yuan and T. R. Lee, "Contact angle and wetting properties," in *Surface Science Techniques*, Springer, 2013, pp. 3-34.
- [57] J. F. Padday, in *Surface and Colloid Science*, vol. 1, New York, Wiley, 1968, p. 101.
- [58] A. W. Neumann and R. J. Good, in *Experimental Methods in Surface and Colloid Science*, vol. 11, New York, Plenum, 1979, p. 31-91.
- [59] A. Bateni, S. S. Susnar, A. Amirfazli and A. W. Neumann, "A high-accuracy polynomial fitting approach to determine contact angles," *Colloids and Surfaces A: Physicochemical and Engineering*



*Aspects*, vol. 219, pp. 215-231, 2003.

- [60] G. Macdougall and C. Ockrent, "Surface energy relations in liquid/solid systems. I. The adhesion of liquids to solids and a new method of determining the surface tension of liquids," *Proceedings of the Royal Society of London A: Mathematical and Physical Sciences*, vol. 180, no. 981, pp. 151-173, 1942.
- [61] D. K. Mandal, A. Criscione, C. Tropea and A. Amirfazli, "Shedding of water drops from a surface under icing conditions," *Langmuir*, vol. 31, pp. 9340-9347, 2015.
- [62] D. Bonn, J. Eggers, J. Indekeu, J. Meunier and E. Rolley, "Wetting and spreading," *Review of Modern Physics*, vol. 81, p. 739, 2009.
- [63] D. Y. Kwok and A. W. Neumann, "Contact angle measurement and contact angle interpretation," *Advances in Colloid and Interface Science*, vol. 81, pp. 167-249, 1999.
- [64] D. K. Owens and R. C. Wendt, "Estimation of the surface free energy of polymers," *Journal of Applied Polymer Science*, vol. 13, no. 8, pp. 1741-1747, 1969.
- [65] D. H. Kaelble, "Dispersion-polar surface tension properties of organic solids," *The Journal of Adhesion*, vol. 2, no. 2, pp. 66-81, 1970.
- [66] D. L. Herbertson, C. R. Evans, N. J. Shirtcliffe, G. McHale and M. I. Newton, "Electrowetting on superhydrophobic SU-8 patterned surfaces," *Sensors and Actuators A: Physical*, Vols. 130-131, pp. 189-193, 2006.
- [67] S. Y. Chou, G. Keimel and J. Gu, "Ultrafast and direct imprint of nanostructures in silicon," *Nature*, vol. 417, pp. 835-837, 2002.
- [68] B. Bhushan, K. Koch and Y. C. Jung, "Fabrication and characterization of the hierarchical structure for superhydrophobicity and self-cleaning," *Ultramicroscopy*, vol. 109, no. 8, pp. 1029-1034, 2009.
- [69] M. Qu, G. Zhao, Q. Wang, X. Cao and J. Zhang, "Fabrication of superhydrophobic surfaces by a Pt nanowire array on Ti/Si substrates," *Nanotechnology*, vol. 19, p. 055707, 2008.
- [70] W. Zhong, Y. Li., Y. Wang, X. Chen, Y. Wang and W. Yang, "Superhydrophobic polyaniline hollow bars: Constructed with nanorod-arrays based on self-removing metal-monomeric template," *Journal of Colloid and Interface Science*, vol. 365, no. 1, pp. 28-32, 2012.
- [71] Y. Fan, C. Li, Z. Chen and H. Chen, "Study on fabrication of the superhydrophobic sol-gel films based on copper wafer and its anti-corrosive properties," *Applied Surface Science*, vol. 258, pp. 6531-6536, 2012.
- [72] U. Cengiz, M. Z. Avci, H. Y. Erbil and A. S. Sarac, "Superhydrophobic terpolymer nanofibers containing perfluoroethyl alkyl methacrylate by electrospinning," *Applied Surface Science*, vol. 258, pp. 5815-5821, 2012.
- [73] D. Kim, S. Lee and W. Hwang, "Complete wetting characteristics of micro/nano dual-scale surface by plasma etching to give honeycomb structure," *Current Applied Physics*, vol. 12, pp. 219-224, 2012.

- [74] P. Pareo, G. L. De Gregorio, M. Manca, M. S. Pianesi, L. De Marco, F. Cavallaro, M. Mari, S. Pappadà, G. Ciccarella and G. Gigli, "Ultra lightweight PMMA-based composite plates with robust super-hydrophobic surfaces," *Journal of Colloid and Interface Science*, vol. 2011, pp. 668-675, 2011.
- [75] M. Psarski, J. Marczak, J. Grobelny and G. Celichowski, "Superhydrophobic surface by replication of laser micromachined pattern in epoxy/alumina nanoparticle composite," *Journal of Nanomaterials*, p. 547895, 2014.
- [76] A. Millionis, J. Languasco, E. Loth and I. S. Bayer, "Analysis of wear abrasion resistance of superhydrophobic acrylonitrile butadiene styrene rubber (ABS) nanocomposites," *Chemical Engineering Journal*, vol. 281, pp. 730-738, 2015.
- [77] X. Zhang, X. Liu, J. Laakso, E. Levänen and T. Mäntylä, "Easy-to-clean property and durability of superhydrophobic flaky g-alumina coating on stainless steel in field test at a paper machine," *Applied Surface Science*, vol. 258, pp. 3102-3108, 2012.
- [78] H. Yang, P. Pi, Z.-Q. Cai, X. Wen, X. Wang, J. Cheng and Z. Yang, "Facile preparation of superhydrophobic and super-oleophilic silica film on stainless steel mesh via sol-gel process," *Applied Surface Science*, vol. 256, pp. 4095-4102, 2010.
- [79] M. Shi, J. Xi, H. Wang and X. Wu, "A translucent and superhydrophobic surface prepared with a sol-gel method based on alumina nanoparticles," *Journal of Adhesion Science and Technology*, vol. 22, no. 3-4, pp. 311-318, 2008.
- [80] M. Faustini, B. Louis, P. A. Albouy, M. Kuemmel and D. Grosso, "Preparation of sol-gel films by dip-coating in extreme conditions," *Journal of Physical Chemistry C*, vol. 114, pp. 7637-7645, 2010.
- [81] R. V. Lakshmi, T. Bharathidasan and B. J. Basu, "Superhydrophobic sol-gel nanocomposite coatings with enhanced hardness," *Applied Surface Science*, vol. 257, pp. 10421-10426, 2011.
- [82] S.-D. Wang and S.-S. Luo, "Fabrication of transparent superhydrophobic silica-based film on a glass substrate," *Applied Surface Science*, vol. 258, pp. 5443-5450, 2012.
- [83] C. J. Brinker and G. W. Scherer, *Sol-Gel Science: The Physics and Chemistry of Sol-Gel Processing*, San Diego: Academic Press, Inc., 1990.
- [84] X. Liu, C. Niu, X. Zhen, J. Wang and X. Su, "Novel approach for synthesis of boehmite nanostructures and their conversion to aluminum oxide nanostructures for remove Congo red," *Journal of Colloid and Interface Science*, vol. 452, pp. 116-125, 2015.
- [85] C. J. Brinker, G. C. Frye, A. J. Hurd and C. S. Ashley, "Fundamentals of sol-gel dip coating," *Thin Solid Films*, vol. 201, pp. 97-108, 1991.
- [86] X. Wang, X. Zhao, C. Jing, H. Tao and J. Han, "Effects of nitric acid concentration on the stability of alumina sols," *Journal of Wuhan University of Technology - Materials Science Edition*, vol. 21, no. 1, pp. 102-105, 2005.
- [87] H. Liu, J. Chen and H. Ge, "Chemical modification of ethylacetoacetate with ASB in aqueous medium," *Journal of Wuhan University of Technology - Materials Science Edition*, vol. 24, no. 1, pp.

68-71, 2009.

- [88] Q. F. Xu, J. N. Wang and K. D. Sanderson, "Organic-inorganic composite nanocoatings with superhydrophobicity, good transparency, and thermal stability," *ACS Nano*, vol. 4, no. 4, pp. 2201-2209, 2010.
- [89] J. Sanchez and A. McCormick, "Kinetic and thermodynamic study of the hydrolysis of silicon alkoxides in acidic alcohol solutions," *The Journal of Physical Chemistry*, vol. 96, no. 22, pp. 8973-8979, 1992.
- [90] Z.-A. Qiao, L. Zhang, M. Guo, Y. Liu and Q. Huo, "Synthesis of mesoporous silica nanoparticles via controlled hydrolysis and condensation of silicon alkoxide," *Chemistry of Materials*, vol. 21, pp. 3823-3829, 2009.
- [91] D. A. Loy, B. Mather, A. R. Straumanis, C. Baugher, D. A. Schneider, A. Sanchez and K. J. Shea, "Effect of pH on the gelation time of hexylene-bridged polysilsesquioxanes," *Chemistry of Materials*, vol. 16, no. 11, pp. 2041-2043, 2004.
- [92] D. R. Ulrich, "Better ceramics through chemistry," in *Transformation of Organometallics into Common and Exotic Materials: Design and Activation*, Springer Netherlands, 1988, pp. 207-235.
- [93] Y. Wan and S.-H. Yu, "Polyelectrolyte controlled large-scale synthesis of hollow silica spheres with tunable sizes and wall thicknesses," *Journal of Physical Chemistry C*, vol. 112, pp. 3641-3647, 2008.
- [94] Y.-C. Sheen, Y.-C. Huang, C.-S. Liao, H.-Y. Chou and F.-C. Chang, "New approach to fabricate an extremely super-amphiphobic surface based on fluorinated silica nanoparticles," *Journal of Polymer Science: Part B: Polymer Physics*, vol. 46, pp. 1984-1990, 2008.
- [95] D. M. Antonelli and J. Y. Ying, "Synthesis of hexagonally packed mesoporous TiO<sub>2</sub> by a modified sol-gel method," *Angewandte Chemie International Edition*, vol. 34, no. 18, pp. 2014-2017, 1995.
- [96] C.-C. Wang and J. Y. Ying, "Sol-gel synthesis and hydrothermal processing of anatase and rutile titania nanocrystals," *Chemistry of Materials*, vol. 11, no. 11, pp. 3113-3120, 1999.
- [97] M. Shane and M. L. Mecartney, "Sol-gel synthesis of zirconia barrier coatings," *Journal of Materials Science*, vol. 25, no. 3, pp. 1537-1544, 1990.
- [98] M. N. Kamalasanan and S. Chandra, "Sol-gel synthesis of ZnO thin films," *Thin Solid Films*, vol. 288, no. 1-2, pp. 112-115, 1996.
- [99] S. A. Mahadik, M. S. Kavale, S. K. Mukherjee and A. V. Rao, "Transparent superhydrophobic silica coatings on glass by sol-gel method," *Applied Surface Science* 257 (2010) 333-339, vol. 257, pp. 333-339, 2010.
- [100] M. S. Kavale, D. B. Mahadik, V. G. Parale, P. B. Wagh, S. C. Gupta, A. V. Rao and H. C. Barshilia, "Optically transparent, superhydrophobic methyltrimethoxysilane based silica coatings without silylating reagent," *Applied Surface Science*, vol. 258, pp. 158-162, 2011.
- [101] A. Caldarelli, M. Raimondo, F. Veronesi, G. Boveri and G. Guarini, "Sol-gel route for the building up of superhydrophobic nanostructured hybrid-coatings on copper surfaces," *Surface & Coatings*

*Technology*, vol. 276, pp. 408-415, 2015.

- [102] B. J. Berne and R. Pecora, *Dynamic Light Scattering: With Applications to Chemistry, Biology, and Physics*, Mineola, New York: Dover Publications, Inc., 1976.
- [103] W. I. Goldberg, "Dynamic light scattering," *American Journal of Physics*, vol. 67, no. 12, pp. 1152-1160, 1999.
- [104] J. H. Seinfeld and S. N. Pandis, *Atmospheric Chemistry and Physics: From Air Pollution to Climate Change*, Hoboken, New Jersey: John Wiley & Sons, Inc., 2016.
- [105] G. Mie, "Beiträge zur optik trüber medien, speziell kolloidaler metallösungen," *Annalen der Physik*, vol. 330, no. 3, pp. 377-445, 1908.
- [106] H. A. Barnes and Q. D. Nguyen, "Rotating vane rheometry - a review," *Journal of Non-Newtonian Fluid Mechanics*, vol. 98, no. 1, pp. 1-14, 2001.
- [107] S. Fordham, "On the calculation on surface tension from measurements of pendant drops," *Proceedings of the Royal Society A*, vol. 194, pp. 1-15, 1948.
- [108] Y. Rotenberg, L. Boruvka and A. W. Neumann, "Determination of surface tension and contact angle from the shapes of axisymmetric fluid interfaces," *Journal of Colloid and Interface Science*, vol. 93, no. 1, pp. 169-183, 1983.
- [109] T. Okubo, "Surface tension of structured colloidal suspensions of polystyrene and silica spheres at the air-water interface," *Journal of Colloid and Interface Science*, vol. 171, pp. 55-62, 1995.
- [110] F. Ravera, E. Santini, G. Loglio, M. Ferrari and L. Liggieri, "Effect of nanoparticles on the interfacial properties of liquid/liquid and liquid/air surface layers," *Journal of Physical Chemistry B*, vol. 110, pp. 19543-19551, 2006.
- [111] M. Raimondo, M. Blosi, A. Caldarelli, G. Guarini and F. Veronesi, "Wetting behavior and remarkable durability of amphiphobic aluminum alloys surfaces in a wide range of environmental conditions," *Chemical Engineering Journal*, vol. 258, pp. 101-109, 2014.
- [112] E. Landau and B. Levich, "Dragging of a liquid by a moving plate," *Acta Physicochimica U.R.S.S.*, vol. 17, no. 1-2, pp. 142-153, 1942.
- [113] D. Grosso, "How to exploit the full potential of the dip-coating process to better control film formation," *Journal of Materials Chemistry*, vol. 21, pp. 17033-17038, 2011.
- [114] A. R. Phani and S. Santucci, "Evaluation of structural and mechanical properties of aluminum oxide thin films deposited by a sol-gel process: Comparison of microwave to conventional anneal," *Journal of Non-Crystalline Solids*, vol. 352, no. 38-39, pp. 4093-4100, 2006.
- [115] R. Nass and H. Schmidt, "Synthesis of an alumina coating from chelated aluminium alkoxides," *Journal of Non-Crystalline Solids*, vol. 121, no. 1-3, pp. 329-333, 1990.
- [116] T. Kurisu and H. Kozuka, "Effects of heating rate on stress evolution in alkoxide-derived silica gel-coating films," *Journal of the American Ceramic Society*, vol. 89, no. 8, pp. 2453-2458, 2006.

- [117] H. Kozuka, "Stress evolution on gel-to-ceramic thin film conversion," *Journal of Sol-Gel Science and Technology*, vol. 40, pp. 287-297, 2006.
- [118] I. Malavasi, F. Veronesi, M. Zani, M. Raimondo and M. Marengo, "Is a knowledge of surface topology and contact angles enough to define the drop impact outcome?," *Langmuir*, vol. 32, pp. 6255-6262, 2016.
- [119] L. Feng, H. Zhang, Z. Wang and Y. Liu, "Superhydrophobic aluminum alloy surface: Fabrication, structure, and corrosion resistance," *Colloids and Surfaces A: Physicochemical and Engineering Aspects*, vol. 441, pp. 319-325, 2014.
- [120] R.-S. Zhou and R. L. Snyder, "Structures and transformation mechanisms of the  $\eta$ ,  $g$  and  $q$  transition aluminas," *Acta Crystallographica Section B: Structural Science, Crystal Engineering and Materials*, vol. 47, pp. 617-630, 1991.
- [121] J. Ou, W. Hu, S. Liu, M. Xue, F. Wang and W. Li, "Superoleophobic textured copper surfaces fabricated by chemical etching/oxidation and surface fluorination," *ACS Applied Materials and Interfaces*, vol. 5, pp. 10035-10041, 2013.
- [122] C. D. Q. W.J. van Ooij The Department of Materials Science and Engineering University of Cincinnati, G. Prasad, S. Jayaseelan, Y. Fu and N. Teredesai, "Silane based chromate replacements for corrosion control, paint adhesion, and rubber bonding," *Surface Engineering*, vol. 16, no. 5, pp. 386-396, 2000.
- [123] X. Zhang, F. Shi, J. Niu, J. Y. and Z. Wang, "Superhydrophobic surfaces: from structural control to functional application," *Journal of Materials Chemistry*, vol. 18, pp. 621-633, 2008.
- [124] "Superhydrophobic oleophobic PDMS-silica nanocomposite coating," *Surface Innovations*, vol. 1, no. S11, pp. 40-51, 2013.
- [125] D. O'Hagan, "Understanding organofluorine chemistry. An introduction to the C-F bond," *Chemical Society Reviews*, vol. 37, pp. 309-319, 2008.
- [126] J. Yang, Z. Zhang, X. Xu, X. Zhu, X. Men and X. Zhou, "Superhydrophilic-superoleophobic coatings," *Journal of Materials Chemistry*, vol. 22, pp. 2834-2837, 2012.
- [127] G. Rizzo, G. P. Massarotti, A. Bonanno, R. Paoluzzi, M. Raimondo, M. Blosi, F. Veronesi, A. Caldarelli and G. Guarini, "Axial piston pumps slippers with nanocoated surfaces to reduce friction," *International Journal of Fluid Power*, vol. 16, no. 1, pp. 1-10, 2015.
- [128] C. E. Stauffer, "The measurement of surface tension by the pendant drop technique," *The Journal of Physical Chemistry C*, vol. 69, no. 6, pp. 1933-1938, 1965.
- [129] T. Verho, C. Bower, P. Andrew, S. Franssila, O. Ikkala and R. H. A. Ras, "Mechanically durable superhydrophobic surfaces," *Advanced Materials*, vol. 2011, pp. 673-678, 2011.
- [130] J. Liu, W. Huang, Y. Xing, R. Li and J. Dai, "Preparation of durable superhydrophobic surface by sol-gel method with water glass and citric acid," *Journal of Sol-Gel Science and Technology*, vol. 58, pp. 18-23, 2011.

- [131] X. Zhu, Z. Zhang, X. Men, J. Yang, K. Wang, X. Xu, X. Zhou and Q. Xue, "Robust superhydrophobic surfaces with mechanical durability and easy repairability," *Journal of Materials Chemistry*, vol. 21, pp. 15793-15797, 2011.
- [132] I. Takahiro, Y. Masuda and M. Sakamoto, "Corrosion resistance and durability of superhydrophobic surface formed on magnesium alloy coated with nanostructured cerium oxide and fluoroalkylsilane molecules in corrosive NaCl aqueous solution," *Langmuir*, vol. 27, pp. 4780-4788, 2011.
- [133] Z. She, Q. Li, Z. Wang, L. Li, F. Chen and J. Zhou, "Researching the fabrication of anticorrosion superhydrophobic surface on magnesium alloy and its mechanical stability and durability," *Chemical Engineering Journal*, vol. 228, pp. 415-424, 2013.
- [134] T. L. Sounart, J. Liu, J. A. Voigt, J. W. P. Hsu, E. D. Spoerke, Z. R. Tian and Y. Jiang, "Sequential nucleation and growth of complex nanostructured films," *Advanced Functional Materials*, vol. 16, pp. 335-344, 2006.
- [135] R. P. Vinci and J. J. Vlassak, "Mechanical behavior of thin films," *Annual Reviews Materials Science*, vol. 26, pp. 431-462, 1996.
- [136] W. D. Nix, "Mechanical properties of thin films," *Metallurgical Transactions A*, vol. 20A, pp. 2217-2245, 1989.
- [137] G. M. Pharr and W. C. Oliver, "Measurement of thin film mechanical properties using nanoindentation," *MRS Bulletin*, vol. 17, no. 7, pp. 28-33, 2013.
- [138] T. Arai, H. Fujita and M. Watanabe, "Evaluation of adhesion strength of thin hard coatings," *Thin Solid Films*, vol. 154, no. 1-2, pp. 387-401, 1987.
- [139] J. Cheng, A. Vandadi and C.-L. Chen, "Condensation heat transfer on two-tier superhydrophobic surfaces," *Applied Physics Letters*, vol. 101, no. 13, p. 131909, 2012.
- [140] R. L. Webb, E. R. G. Eckert and R. J. Goldstein, "Heat transfer and friction in tubes with repeated-rib roughness," *International Journal of Heat and Mass Transfer*, vol. 14, no. 4, pp. 601-617, 1971.
- [141] D. E. Aspnes, "Optical properties of thin films," *Thin Solid Films*, vol. 89, no. 3, pp. 249-262, 1982.
- [142] D. Quéré, "Wetting and roughness," *Annual Review of Materials Research*, vol. 38, pp. 71-99, 2008.
- [143] K. Stout, P. J. Sullivan, W. P. Dong, E. Mainsah, N. Luo, T. Mathia and H. Zahouani, The development of methods for the characterisation of roughness in three dimensions, 1993.
- [144] J. C. Wyant, "White light interferometry," in *Holography: A Tribute to Yuri Denisyuk and Emmett Leith*, Orlando, 2002.
- [145] J. F. Watts and J. Wolstenholme, An Introduction to Surface Analysis by XPS and AES, Wiley-VCH, 2003.
- [146] N. D. Boscher, D. Duday, S. Verdier and P. Choquet, "Single-step process for the deposition of high water contact angle and high water sliding angle surfaces by atmospheric pressure dielectric

- barrier discharge," *ACS Applied Materias and Interfaces*, vol. 5, pp. 1053-1060, 2013.
- [147] J. Li, Z. Jing, F. Zha, Y. Yang, Q. Wang and Z. Lei, "Facile spray-coating process for the fabrication of tunable adhesive superhydrophobic surfaces with heterogeneous chemical compositions used for selective transportation of microdroplets with different volumes," *ACS Applied Materials and Interfaces*, vol. 6, pp. 8868-8877, 2014.
- [148] R. Car and M. Parrinello, "Unified approach for molecular dynamics and density-functional theory," *Physical Review Letters*, vol. 55, pp. 2471-2474, 1985.
- [149] J. K. Nørskov, F. Abild-Pedersen, F. Studt and T. Bligaard, "Density functional theory in surface chemistry and catalysis," *Proceedings of the National Academy of Science of the United States of America*, vol. 108, no. 3, pp. 937-943, 2010.
- [150] A. Motta, O. Cannelli, A. Boccia, R. Zanoni, M. Raimondo, A. Caldarelli and F. Veronesi, "A mechanistic explanation of the peculiar amphiphobic properties of hybrid organic-inorganic coatings by combining XPS characterization and DFT modeling," *ACS Applied Materials & Interfaces*, vol. 7, pp. 19941-19947, 2015.
- [151] J. Humlíček, "An efficient method for evaluation of the complex probability function: The Voigt function and its derivatives," *Journal of Quantitative Spectroscopy and Radiative Transfer*, vol. 21, no. 4, pp. 309-313, 1979.
- [152] J. E. Castle, H. Chapman-Kpodo, A. A Proctor and A. M. Salvi, "Curve-fitting in XPS using extrinsic and intrinsic background structure," *Journal of Electron Spectroscopy and Related Phenomena*, vol. 106, no. 1, pp. 65-80, 2000.
- [153] C. D. Wagner, L. E. Davis, M. V. Zeller, J. A. Taylor, R. H. Raymond and L. H. Gale, "Empirical atomic sensitivity factors for quantitative analysis by electron spectroscopy for chemical analysis," *Surface and Interface Analysis*, vol. 3, pp. 211-225, 1981.
- [154] N. Phambu, "Characterization of aluminum hydroxide thin film on metallic aluminum powder," *Materials Letters*, vol. 57, no. 19, pp. 2907-2913, 2003.
- [155] G. Beamson and D. Briggs, *High Resolution XPS of Organic Polymers: The Scienta ESCA300 Database*, Chichester: John Wiley & Sons, 1992.
- [156] T. C. D. Group, "<http://www.cp2k.org>," [Online]. [Accessed 10 08 2016].
- [157] J. V. Smith and S. W. Bailey, "Second review of Al-O and Si-O tetrahedral distances," *Acta Crystallographica*, vol. 16, pp. 801-811, 1963.
- [158] N. Saleema, D. K. Sarkar, D. Gallant, R. W. Paynter and X.-G. Chen, "Chemical nature of superhydrophobic aluminum alloy surfaces produced via a one-step process using fluoroalkylsilane in a base medium," *ACS Applied Materials & Interfaces*, vol. 3, pp. 4775-4781, 2011.
- [159] D. Schondelmaier, S. Cramm, R. Klingeler, J. Morenzin, C. Zilkens and W. Ebehardt, "Orientation and self-assembly of hydrophobic fluoroalkylsilanes," *Langmuir*, vol. 18, pp. 6242-6245, 2002.
- [160] J. R. Davis, *ASM Specialty Handbook: Copper and Copper Alloys*, Ohio, USA: ASM International,

2001.

- [161] F. P. Incropera and D. P. DeWitt, *Fundamentals of Heat and Mass Transfer*, 2nd edition, New York, USA: Wiley, 1985.
- [162] D.-J. Huang and T.-S. Leu, "Condensation heat transfer enhancement by surface modification on a monolithic copper heat sink," *Applied Thermal Engineering*, vol. 75, pp. 908-917, 2015.
- [163] G. Q. Li, M. H. Alhosani, S. J. Yuan, H. R. Liu, A. Al Ghaferi and T. J. Zhang, "Microscopic droplet formation and energy transport analysis of condensation on scalable superhydrophobic nanostructured copper oxide surfaces," *Langmuir*, vol. 30, no. 48, pp. 14498-14511, 2014.
- [164] N. Miljkovic, R. Enright, Y. Nam, K. Lopez, N. Dou, J. Sack and E. N. Wang, "Jumping-droplet-enhanced condensation on scalable superhydrophobic nanostructured surfaces," *Nano Letters*, vol. 13, no. 1, pp. 179-187, 2013.
- [165] J. L. Lara and M. T. Holtzapple, "Experimental investigation of dropwise condensation on hydrophobic heat exchangers part I: Dimpled-sheets," *Desalination*, vol. 278, no. 1-3, pp. 165-172, 2011.
- [166] A. Ghosh, S. Beaini, B. J. Zhang, R. Ganguly and C. M. Megaridis, "Enhancing dropwise condensation through bioinspired wettability patterning," *Langmuir*, vol. 30, no. 43, pp. 13103-13115, 2014.
- [167] T. Liu, Y. Yin, S. Chen, X. Chang and S. Cheng, "Super-hydrophobic surfaces improve corrosion resistance of copper in seawater," *Electrochimica Acta*, vol. 52, no. 11, pp. 3709-3713, 2007.
- [168] F. Sinapi, S. Julien, D. Auguste, L. Hevesi, J. Delhalle and Z. Mekhalif, "Monolayers and mixed-layers on copper towards corrosion protection," *Electrochimica Acta*, vol. 53, no. 12, pp. 4228-4238, 2008.
- [169] S.-M. Lee, K.-S. Kim, E. Pippel, S. Kim, J.-H. Kim and H.-J. Lee, "Facile route toward mechanically stable superhydrophobic copper using oxidation-reduction induced morphology changes," *The Journal of Physical Chemistry C*, vol. 116, no. 4, pp. 2781-2790, 2012.
- [170] S. L. Shinde and K. K. Nanda, "Facile synthesis of large area porous Cu<sub>2</sub>O as super hydrophobic yellow-red phosphors," *RSC Advances*, vol. 2, pp. 3647-3650, 2012.
- [171] G. Filipič and U. Cvelbar, "Copper oxide nanowires: a review of growth," *Nanotechnology*, vol. 23, no. 19, 2012.
- [172] X. Jiang, T. Herricks and Y. Xia, "CuO nanowires can be synthesized by heating copper substrates in air," *Nano Letters*, vol. 2, no. 12, pp. 1333-1338, 2002.
- [173] F. Bayansal, S. Kahraman, G. Çankaya, H. A. Çetinkara, H. S. Güder and H. M. Çakmak, "Growth of homogenous CuO nano-structured thin films by a simple solution method," *Journal of Alloys and Compounds*, vol. 209, no. 5, pp. 2094-2098, 2011.
- [174] K. Mageshwari, Sathyamoorthy and R., "Physical properties of nanocrystalline CuO thin films prepared by the SILAR method," *Materials Science in Semiconductor Processing*, vol. 16, no. 2, pp.



337-343, 2013.

- [175] Q. B. Zhang, D. Xu, T. F. Hung and K. Zhang, "Facile synthesis, growth mechanism and reversible superhydrophobic and superhydrophilic properties of non-flaking CuO nanowires grown from porous copper substrates," *Nanotechnology*, vol. 24, no. 6, 2013.
- [176] Y. Nam and Y. S. Ju, "A comparative study of the morphology and wetting characteristics of micro/nanostructured Cu surfaces for phase change heat transfer applications," *Journal of Adhesion Science and Technology*, vol. 27, no. 20, pp. 2163-2176, 2013.
- [177] D.-J. Huang and T.-S. Leu, "Fabrication of high wettability gradient on copper substrate," *Applied Surface Science*, vol. 280, pp. 25-32, 2013.
- [178] Y. Zhang, W. Li, F. Ma, Z. Yu, M. Ruan, Y. Ding and X. Deng, "Optimum conditions for fabricating superhydrophobic surface on copper plates via controlled surface oxidation and dehydration processes," *Applied Surface Science*, vol. 280, pp. 898-902, 2013.
- [179] F. Su and K. Yao, "Facile fabrication of superhydrophobic surface with excellent mechanical abrasion and corrosion resistance on copper substrate by a novel method," *ACS Applied Materials and Interfaces*, vol. 6, no. 11, pp. 8762-8770, 2014.
- [180] P. Wang, D. Zhang, R. Qiu, Y. Wana and J. Wu, "Green approach to fabrication of a superhydrophobic film on copper and the consequent corrosion resistance," *Corrosion Science*, vol. 80, pp. 366-373, 2014.
- [181] A. Haghdoost and R. Pitchumani, "Fabricating superhydrophobic surfaces via a two-step electrodeposition technique," *Langmuir*, vol. 30, no. 14, pp. 4183-4191, 2014.
- [182] L. B. Hazell, "Quantitative XPS analysis of aluminium in the presence of copper," *Surface and Interface Analysis*, vol. 33, no. 10-11, pp. 791-795, 2002.
- [183] R. E. Johnson and R. H. Dettre, "Contact angle hysteresis. III. Study of an idealized heterogeneous surface," *The Journal of Physical Chemistry*, vol. 68, no. 7, pp. 1744-1750, 1964.
- [184] L. S. Huang, S. G. Yang, T. Li, B. X. Gu, Y. Du, Y. N. Lub and S. Z. Shi, "Preparation of large-scale cupric oxide nanowires by thermal evaporation method," *Journal of Crystal Growth*, vol. 260, no. 1-2, pp. 130-135, 2004.
- [185] M. Kaur, K. Muthe, S. Deshpande, S. Choudhury, J. Singh, N. Verma, S. Gupta and J. Yakhmi, "Growth and branching of CuO nanowires by thermal oxidation of copper," *Journal of Crystal Growth*, vol. 289, no. 2, pp. 670-675, 2006.
- [186] A. Kumar, K. A. Srivastava, P. Tiwari and R. Nandedkar, "The effect of growth parameters on the aspect ratio and number density of CuO nanorods," *Journal of Physics Condensed Matter*, vol. 16, no. 47, pp. 8531-8543, 2004.
- [187] Y. Cudennec and A. Lecerf, "The transformation of Cu(OH)<sub>2</sub> into CuO, revisited," *Solid State Sciences*, vol. 5, no. 11-12, pp. 1471-1474, 2003.
- [188] L. Gou and C. J. Murphy, "Solution-phase synthesis of Cu<sub>2</sub>O nanocubes," *Nano Letters*, vol. 3, no.

2, pp. 231-234, 2003.

- [189] B. Kasprzyk-Hordern, "Chemistry of alumina, reactions in aqueous solution and its application in water treatment," *Advances in Colloid and Interface Science*, vol. 110, no. 1-2, pp. 19-48, 2004.
- [190] M. Mazloumi, M. Attarchi, A. Lak, M. S. Mohajerani, A. Kajbafvala, S. Zanganeh and S. K. Sadrnezhad, "Boehmite nanopetals self assembled to form rosette-like nanostructures," *Materials Letters*, vol. 62, no. 26, pp. 4184-4186, 2008.
- [191] C. Antonini, F. Villa, I. Bernagozzi, A. Amirfazli and M. Marengo, "Drop rebound after impact: the role of the receding contact angle," *Langmuir*, vol. 29, pp. 16045-16050, 2013.
- [192] I. V. Roisman, A. Lembach and C. Tropea, "Drop splashing induced by target roughness and porosity: The size plays no role," *Advances in Colloid and Interface Science*, vol. 222, pp. 615-624, 2015.
- [193] X. Deng, F. Schellenberger, P. Papadopoulos, D. Vollmer and H.-J. Butt, "Liquid drops impacting superamphiphobic coatings," *Langmuir*, vol. 29, pp. 7847-7856, 2013.
- [194] T.-S. Wong, S. H. Kang, S. K. Y. Tang, E. J. Smythe, B. D. Hatton, A. Grinthal and J. Aizenberg, "Bioinspired self-repairing slippery surfaces with pressure-stable omniphobicity," *Nature*, vol. 477, pp. 443-447, 2011.
- [195] I. Malavasi, I. Bernagozzi, C. Antonini and M. Marengo, "Assessing durability of superhydrophobic surfaces," *Surface Innovations*, 2014.
- [196] D. Bartolo, C. Josserand and D. Bonn, "Singular jets and bubbles in drop impact," *Physical Review Letters*, vol. 96, p. 124501, 2006.
- [197] Z. Yoshimitsu, A. Nakajima, T. Watanabe and K. Hashimoto, "Effects of surface structure on the hydrophobicity and sliding behavior of water droplets," *Langmuir*, vol. 18, no. 15, pp. 5818-5822, 2002.
- [198] D. Bartolo, F. Bouamrine, E. Verneuil, A. Buguin, P. Silberzan and S. Moulinet, "Bouncing or sticky droplets: Impalement transitions on superhydrophobic micropatterned surfaces," *Europhysics Letters*, vol. 74, pp. 299-305, 2006.
- [199] D. H. Kwon and S. J. Lee, "Impact and wetting behaviors of impinging microdroplets on superhydrophobic textured surfaces," *Applied Physics Letters*, vol. 100, p. 171601, 2012.
- [200] S. Moulinet and D. Bartolo, "Life and death of a fakir droplet: Impalement transitions on superhydrophobic surfaces," *The European Physics Journal E*, vol. 24, pp. 251-260, 2007.
- [201] S. Mandre, M. Mani and M. P. Brenner, "Precursors to splashing of liquid droplets on a solid surface," *Physical Review Letters*, vol. 102, pp. 134502-134504, 2009.
- [202] M. Reyssat, A. Pépin, F. Marty, Y. Chen and D. Quéré, "Bouncing transitions on microtextured materials," *Europhysics Letters*, vol. 74, pp. 306-312, 2006.
- [203] Y. Quan and L. Z. Zhang, "Numerical and analytical study of the impinging and bouncing phenomena of droplets on superhydrophobic surfaces with microtextured structures," *Langmuir*,

vol. 30, pp. 11640-11649, 2014.

- [204] C. W. Extrand, "Forces, pressures and energies associated with liquid rising in nonuniform capillary tubes," *Journal of Colloid and Interface Science*, vol. 450, pp. 135-140, 2015.
- [205] J. B. Lee and S. H. Lee, "Dynamic wetting and spreading characteristics of a liquid droplet impinging on hydrophobic textured surfaces," *Langmuir*, vol. 27, pp. 6565-6573, 2011.
- [206] J. Hyvaluoma and J. Timonen, "Impact states and energy dissipation in bouncing and non-bouncing droplets," *Journal of Statistical Mechanics: Theory and Experiment*, p. P06010, 2009.
- [207] T. M. Schutzius, S. Jung, T. Maitra, P. Eberle, C. Antonini, C. Stamatopoulos and D. Poulikakos, "Physics of icing and rational design of surfaces with extraordinary icephobicity," *Langmuir*, vol. 31, pp. 4807-4821, 2015.
- [208] H. Murase and T. Fujibayashi, "Characterization of molecular interfaces in hydrophobic systems," *Progress in Organic Coatings*, vol. 31, pp. 97-104, 1997.
- [209] A. Nakajima, T. Miyamoto, M. Sakai, T. Isobe and S. Matsushita, "Comparative study of the impact and sliding behavior of water droplets on two different hydrophobic silane coatings," *Applied Surface Science*, vol. 292, pp. 990-996, 2014.
- [210] I. Malgarinos, N. Nikolopoulos, M. Marengo, C. Antonini and M. Gavaises, "VOF simulations of the contact angle dynamic during the drop spreading: standard models and a novel wetting force model," *Advances in Colloid and Interface Science*, vol. 212, pp. 1-20, 2014.
- [211] J. L. Laforte, M. A. Allaire and J. Laflamme, "State-of-the-art on power line de-icing," *Atmospheric Research*, vol. 46, pp. 143-158, 1998.
- [212] M. C. Homola, M. S. Virk, P. J. Nicklasson and P. A. Sundsbo, "Performance losses due to ice accretion for a 5 mw wind turbine," *Wind Energy*, vol. 15, pp. 379-389, 2012.
- [213] K. Szilder, E. P. Lozowski and G. Reuter, "A study of ice accretion shape on cables under freezing rain conditions," in *Journal of Offshore Mechanics and Arctic Engineering: ASME*, 2002.
- [214] S. Tarquini, C. Antonini, A. Amirfazli, M. Marengo and J. Palacios, "Investigation of ice shedding properties of superhydrophobic coatings on helicopter blades," *Cold Regions Science and Technology*, vol. 100, pp. 50-58, 2014.
- [215] Z. Zuo, R. Liao, C. Guo, Y. Yuan, X. Zhao, A. Zhuang and Y. Zhang, "Fabrication and anti-icing property of coral-like superhydrophobic aluminum surface," *Applied Surface Science*, vol. 331, pp. 132-139, 2015.
- [216] D. Mangini, C. Antonini, M. Marengo and A. Amirfazli, "Runback ice formation mechanism on hydrophilic and superhydrophobic surfaces," *Cold Regions Science and Technology*, vol. 109, pp. 53-60, 2015.
- [217] Y. Wang, X. Yao, J. Chen, Z. He, J. Liu, Q. Li, J. Wang and L. Jiang, "Organogel as durable anti-icing coatings," *Science China Materials*, vol. 58, pp. 559-565, 2015.
- [218] Y. Shen, H. Tao, S. Chen, L. Zhu, T. Wang and J. Tao, "Icephobic/anti-icing potential of

- superhydrophobic Ti6Al4V surfaces with hierachical structures," *RSC Advances*, vol. 5, pp. 1666-1672, 2015.
- [219] G. Fang and A. Amirfazli, "Understanding the anti-icing behavior of superhydrophobic surfaces," *Surface Innovations*, vol. 2, no. S12, pp. 94-102, 2014.
- [220] I. V. Roisman, A. Criscione, C. Tropea, D. K. Mandal and A. Amirfazli, "Dislodging a sessile drop by a high-Reynolds-number shear flow at subfreezing temperatures," *Physical Review E*, vol. 92, p. 023007, 2015.
- [221] P. Tourkine, M. Le Merrer and D. Quéré, "Delayed freezing on water repellent materials," *Langmuir*, vol. 25, no. 13, pp. 7214-7216, 2009.
- [222] W. Li, X. Zhang, J. Yang and F. Miao, "In situ growth of superhydrophobic and icephobic films with micro/nanoscale hierachical structures on the aluminum substrate," *Journal of Colloid and Interface Science*, vol. 410, pp. 165-171, 2013.
- [223] S. Madani and A. Amirfazli, "Oil drop shedding from solid substrates by a shearing liquid," *Colloids and Surfaces A: Physicochemical and Engineering Aspects*, vol. 441, pp. 796-806, 2014.
- [224] C. Antonini, M. Innocenti, T. Horn, M. Marengo and A. Amirfazli, "Understanding the effect of superhydrophobic coatings on energy reduction in anti-icing systems," *Cold Regions Science and Technology*, vol. 67, pp. 58-67, 2011.
- [225] S. Farhadi, M. Farzaneh and S. Kulinich, "Anti-icing performance of superhydrophobic surfaces," *Applied Surface Science*, vol. 257, pp. 6264-6269, 2011.
- [226] E. White and J. Schmucker, "A runback criterion for water drops in a turbulent accelerated boundary layer," *Journal of Fluids Engineering*, vol. 130, p. 061302-061307, 2008.
- [227] A. Theodorakakos, T. Ous, M. Gavaises, J. M. Nouri, N. Nikolopoulos and H. J. Yanagihara, "Dynamics of water droplets detached from porous surfaces of relevance to PEM fuel cells. J. Colloid," *Journal of Colloid and Interface Science*, vol. 300, pp. 673-687, 2006.
- [228] X. Zhu, P. C. Sui and N. Djilali, "Dynamic behaviour of liquid water emerging from a GDL pore into a PEMFC gas flow channel," *Journal of Power Sources*, vol. 172, pp. 287-295, 2007.
- [229] J. Fan, M. Wilson and N. Kapur, "Displacement of liquid droplets on a surface by a shearing air flow," *Journal of Colloid and Interface Science*, vol. 356, pp. 286-292, 2011.
- [230] G. Minor, N. Djilali, D. Sinton and P. Oshkai, "Flow within a water droplet subjected to an air stream in a hydrophobic microchannel," *Fluid Dynamics Research*, vol. 41, p. 045506, 2009.
- [231] F. Chini, V. Bertola and A. Amirfazli, "A methodology to determine the adhesion force of arbitrarily shaped drops with convex contact lines," *Colloids and Surfaces A: Physicochemical and Engineering Aspects*, vol. 436, pp. 425-433, 2013.
- [232] S. Moghtadernejad, M. Mohammadi, M. Jadidi, M. Tembely and A. Dolatabadi, "Shear driven droplet shedding on surfaces with various wettabilities," *SAE International Journal of Aerospace*, vol. 6, no. 2, pp. 459-464, 2013.

- [233] S. Moghtadernejad, M. Tembely, M. Jadidi, N. Esmail and A. Dolatabadi, "Shear driven droplet shedding and coalescence on a superhydrophobic surface," *Physics of Fluids*, vol. 27, p. 032106, 2015.
- [234] R. Karmouch and G. G. Ross, "Experimental study on the evolution of contact angles with temperature near the freezing point," *Journal of Physical Chemistry C*, vol. 114, pp. 4063-4066, 2010.
- [235] L. Oberli, D. Caruso, C. Hall, M. Fabretto, P. J. Murphy and D. Evans, "Condensation and freezing of droplets on superhydrophobic surfaces," *Advanced Colloid and Interface Science*, vol. 210, pp. 47-57, 2014.
- [236] K. K. Varanasi, M. Hsu, N. Bhate, W. Yang and T. Deng, "Spatial control in the heterogeneous nucleation of water," *Applied Physics Letters*, vol. 95, p. 094101, 2009.
- [237] K. K. Varanasi, T. Deng, J. D. Smith, M. Hsu and N. Bhate, "Frost formation and ice adhesion on superhydrophobic surfaces," *Applied Physics Letters*, vol. 97, p. 234102, 2010.
- [238] L. Yin, Y. Wang, J. Ding, Q. Wang and Q. Chen, "Water condensation on superhydrophobic aluminum surfaces with different low-surface-energy coatings," *Applied Surface Science*, vol. 258, pp. 4063-4068, 2012.
- [239] P. W. Wilson and A. D. J. Haymet, "Effect of solutes on the heterogeneous nucleation temperature of supercooled water: an experimental determination," *Physical Chemistry Chemical Physics*, vol. 11, pp. 2679-2682, 2009.
- [240] S. Jung, M. Dorrestijn, D. Raps, A. Das, C. M. Megaridis and D. Poulikakos, "Are superhydrophobic surfaces best for icephobicity?," *Langmuir*, vol. 27, pp. 3059-3066, 2011.
- [241] S. Jung, M. K. Tiwari, N. V. Doan and D. Poulikakos, "Mechanism of supercooled droplet freezing on surfaces," *Nature Communications*, vol. 3, p. 615, 2012.
- [242] Q. Fu, X. Wu, D. Kumar, J. W. C. Ho, P. D. Kanhere, N. Srikanth, E. Liu, P. Wilson and Z. Chen, "Development of sol-gel icephobic coatings: Effect of surface roughness and surface energy," *ACS Applied Materials and Interfaces*, vol. 6, pp. 20685-20692, 2014.
- [243] S. Khandekar and K. Muralidhar, *Dropwise Condensation on Inclined Textured Surfaces*, Springer, 2014.
- [244] D. Attinger, C. Frankiewicz, A. R. Betz, T. M. Schutzius, R. Ganguly, A. Das, C.-J. Kim and C. M. Megaridis, "Surface engineering for phase change heat transfer: A review," *MRS Energy & Sustainability : A Review Journal*, vol. 1, 2014.
- [245] J. M. Beér, "High efficiency electric power generation: The environmental role," *Progress in Energy and Combustion Science*, vol. 33, no. 2, pp. 107-134, 2007.
- [246] M. H. Kim and C. W. Bullard, "Air-side performance of brazed aluminum heat exchangers under dehumidifying condition," *International Journal of Refrigeration*, vol. 25, no. 7, pp. 924-934, 2002.
- [247] S. Pandey, "Dropwise and filmwise condensation," *International Journal of Scientific and*

*Engineering Research*, vol. 3, no. 4, pp. 2-6, 2012.

- [248] M. R. N. Reddy, M. Yohan and K. H. Reddy, "Heat transfer coefficient through dropwise condensation and filmwise condensation apparatus," *International Journal of Scientific and Research Publications*, vol. 2, no. 12, pp. 367-370, 2012.
- [249] R. W. I. Bonner, "Dropwise condensation life testing of self assembled monolayers," in *Proceedings of the 14th International Heat Transfer Conference*, 2010.
- [250] J. Feng, Z. Qin and S. Yao, "Factors affecting the spontaneous motion of condensate drops on superhydrophobic copper surfaces," *Langmuir*, vol. 28, no. 14, pp. 6067-6075, 2012.
- [251] J. Feng, Y. Pang, Z. Qin, R. Ma and S. Yao, "Why condensate drops can spontaneously move away on some superhydrophobic surfaces but not on others," *ACS Applied Materials and Interfaces*, vol. 4, no. 12, pp. 6618-6625, 2012.
- [252] C. Dietz, K. Rykaczewski, G. Fedorov and Y. Joshi, "Visualization of droplet departure on a superhydrophobic surface and implications to heat transfer enhancement during dropwise condensation," *Applied Physics Letters*, vol. 97, no. 3, pp. 33103-33104, 2010.
- [253] N. Miljkovic, R. Enright and E. N. Wang, "Modeling and optimization of superhydrophobic condensation," *Journal of Heat Transfer*, vol. 135, no. 11, p. 111004, 2013.
- [254] R. Enright, N. Miljkovic, J. Sprittles, K. Nolan, R. Mitchell and E. N. Wang, "How coalescing droplets jump," *ACS Nano*, vol. 8, no. 10, pp. 10352-10362, 2014.
- [255] J. B. Boreyko and C.-H. Chen, "Self-propelled dropwise condensate on superhydrophobic surfaces," *Physical Review Letters*, vol. 103, no. 18, p. 184501, 2009.
- [256] X. Chen, J. Wu, R. Ma, M. Hua, N. Koratkar, S. Yao and Z. Wang, "Nanograsped micropyramidal architectures for continuous dropwise condensation," *Advanced Functional Materials*, vol. 21, pp. 4617-4623, 2011.
- [257] R. Enright, N. Miljkovic, A. Al-Obeidi, C. V. Thompson and E. N. Wang, "Condensation on superhydrophobic surfaces: The role of local energy barriers and structure length scale," *Langmuir*, vol. 28, pp. 14424-14432, 2012.
- [258] N. Miljkovic and E. N. Wang, "Condensation heat transfer on superhydrophobic surfaces," *MRS Bulletin*, vol. 38, no. 5, pp. 397-406, 2013.
- [259] D. Quere, A. L. Lafuma and J. Bico, "Slippy and sticky microtextured solids," *Nanotechnology*, vol. 14, no. 10, pp. 1109-1112, 2003.
- [260] K. A. Wier and T. J. McCarthy, "Condensation on ultrahydrophobic surfaces and its effect on droplet mobility: Ultrahydrophobic surfaces are not always water repellent," *Langmuir*, vol. 22, no. 6, pp. 2433-2436, 2006.
- [261] D. (. B.-. Kaschiev, *Nucleation: Basic Theory With Applications*, Oxford: Butterworth-Heinemann, 2000.
- [262] A. Bonanno, M. Raimondo and S. Zapperi, "Surface Nano-structured Coating for Improved

Performance of Axial Piston Pumps (SNAPP) - Final Report," 2015.

- [263] H. So, "Characteristics of wear results tested by pin-on-disc at moderate to high speeds," *Tribology International*, vol. 29, no. 5, pp. 415-423, 1996.
- [264] A. W. Adamson, *Physical Chemistry of Surfaces*, Wiley, 1990.
- [265] S. Goedecker, M. Teter and J. Hutter, "Separable dual-space gaussian pseudopotentials," *Physical Review B: Condensed Matter and Materials Physics*, vol. 54, pp. 1703-1710, 1996.
- [266] J. P. Perdew, K. Burke and M. Ernzerhof, "Generalized gradient approximation made simple," *Physical Review Letters*, vol. 77, pp. 3865-3686, 1996.
- [267] S. J. Grimme, J. Antony, S. Ehrlich and H. Krieg, "A consistent and accurate Ab Initio parametrization of Density Functional Dispersion Correction (DFT-D) for the 94 elements H-Pu," *Journal of Chemical Physics*, vol. 132, p. 154104, 2010.